Khursheed Alam
Ayub Khan
R. C. Singh
Yeliz Karaca   *Editors*

Mathematical Modeling, Applied Analysis and Computational Methods

ICAIM-2023, Greater Noida, India, March 24–26

Springer

Springer Proceedings in Mathematics & Statistics

Volume 482

This book series features volumes composed of selected contributions from workshops and conferences in all areas of current research in mathematics and statistics, including data science, operations research and optimization. In addition to an overall evaluation of the interest, scientific quality, and timeliness of each proposal at the hands of the publisher, individual contributions are all refereed to the high quality standards of leading journals in the field. Thus, this series provides the research community with well-edited, authoritative reports on developments in the most exciting areas of mathematical and statistical research today.

Khursheed Alam · Ayub Khan · R. C. Singh ·
Yeliz Karaca

Editors

Mathematical Modeling, Applied Analysis and Computational Methods

ICAIM-2023, Greater Noida, India,
March 24–26

Editors
Khursheed Alam
CARAMP
Sharda University
Greater Noida, Uttar Pradesh, India

Ayub Khan
Department of Mathematics
Jamia Millia Islamia
New Delhi, Delhi, India

R. C. Singh
CARAMP
Sharda University
Greater Noida, Uttar Pradesh, India

Yeliz Karaca
Chan Medical School
University of Massachusetts (UMass)
Worcester, MA, USA

This Springer imprint is published by the registered company Springer Nature Singapore Pte Ltd.
The registered company address is: 152 Beach Road, #21-01/04 Gateway East, Singapore 189721, Singapore

If disposing of this product, please recycle the paper.

This book is dedicated to the late
Prof. Abul Hasan Siddiqi, *whose patience,*
wisdom, and encouragement made all the
difference.
This book stands as a testament to his
profound influence and lasting legacy.

Preface 1

In today's rapidly evolving world, mathematics is no longer confined to the abstract theories of academia. Instead, it has emerged as a powerful tool, guiding us through the complex challenges of the modern age. This book, a collection of 17 meticulously researched chapters from multiple authors, exemplifies this shift by showcasing the diverse and far-reaching applications of applied mathematics across various industries.

From the moment we were introduced to these contributions, we were captivated by the innovative approaches to problem-solving presented throughout the chapters. The authors have skillfully assembled a wealth of knowledge, transforming intricate mathematical concepts into practical solutions that address real-world issues. As individuals deeply immersed in the world of mathematics and its applications, we are both inspired and humbled by the breadth and depth of the work presented here.

The book sets the stage with a groundbreaking encryption method that draws from the principles of statistical physics—a testament to the creative synergy between seemingly disparate fields. This innovative approach not only enhances data security but also highlights the limitless possibilities that arise when we dare to think beyond traditional boundaries. As you journey through the subsequent chapters, you will discover how applied mathematics is being harnessed to optimize solar energy potential, improve healthcare outcomes and even decode the mysteries of our planet's natural phenomena. Each chapter serves as a testament to the transformative power of mathematics, offering readers a glimpse into how these concepts are being used to address some of the most pressing challenges of our time.

One of the most striking aspects of the book is its interdisciplinary nature. The authors have seamlessly woven together mathematics, physics, engineering, and computer science, demonstrating that the solutions to complex problems often lie at the intersection of these fields. Whether you are an academic, a practitioner or simply someone with a curiosity for how the world works, this book offers something of value. It is with great admiration that we endorse this work, not only for its scholarly merit but also for its potential to inspire the next generation of problem solvers.

The chapters contained within these pages are more than just studies; they are blueprints for innovation, each offering a unique perspective on how mathematics

can be used to improve our world. As you embark on this intellectual adventure, we encourage you to explore each chapter with an open mind and a sense of curiosity. The journey through these mathematical landscapes is sure to be as rewarding as the discoveries themselves.

Yelize Karaca
Worcester, USA

Preface 2

Applied mathematics is like a treasure map guiding us through the maze of real-world problems, and it's becoming everyone's favorite adventure! As more people discover its magic, they realize just how helpful it is in finding clever solutions to tough challenges in all sorts of industries. This book is like a collection of 17 treasure chests, each filled with exciting discoveries about how applied mathematics can make our lives easier and more interesting.

In Chapter "A New Method of Cryptography Providing Perfect Confidentiality of Information", the author introduces a groundbreaking encryption method inspired by ideas from statistical physics. This unique approach assigns distinct transformations to each piece of data, boosting its security. By drawing from the Lieb–Liniger model, which explains the behavior of particles in one-dimensional space, this fresh encryption technique offers heightened levels of protection.

Moving on to Chapter "Prediction of Solar Energy Potential with Machine Learning and Deep Learning Models", the research zeroes in on evaluating the solar energy potential of Antalya and Serik, tapping into their rich renewable energy reservoirs. This investigation intricately weaves together meteorological, geographical, and technological elements, with a particular spotlight on leveraging machine learning and deep learning models. Through this comprehensive approach, the aim is to refine solar energy forecasts and devise more effective strategies for maximizing solar power utilization.

In Chapter "Total Electron Content and Wavelet Transformation Analysis: Understanding the Role of Modelling", the research sets out to understand how variations in total electron content (TEC) within the ionosphere affect Ankara, Turkey, with a specific focus on the year 2017. It's known that solar winds and geomagnetic storms can influence TEC, which in turn can affect radio waves and satellite communications. To gain insights into these dynamics, the study employs wavelet analysis and machine learning algorithms to forecast changes in TEC levels.

Moving on to Chapter "Friction Dominated Flow in Gas-Networks: Modeling, Simulation, Optimal Control and Domain Decompositions", the study investigates the antioxidant levels in certain food powders like Acai, Camu, Beetroot, Cacao, and Coffee. Using a technique called "electron spin resonance" (ESR) spectrometry, they

measured the "g-values" of the radicals in these foods, which ranged from 2.0044 to 2.00578. These findings offer valuable insights into the antioxidant properties of these foods.

In Chapter "Free Radical, Antioxidant and Human Health", authors delve into the world of nonlinear dynamic models, which offer a powerful tool for understanding and controlling complex systems. By incorporating fractional calculus and operators, these models provide a comprehensive approach to tackling real-world challenges. Specifically, they explore a model for multi-strain tuberculosis, using a modified Atangana–Baleanu–Caputo fractional derivative. This innovative approach enables more accurate numerical approximations, helping to unravel the complexities of such problems.

Turning to Chapter "Algebraic Properties of Doubt ω-Fuzzy CI-Sub algebras and Ideals in CI-Algebra", authors introduce the intriguing concept of doubt (ω)-fuzzy CI-subalgebras (doubt ω-FCI-SA) and embarks on an exploration of doubt triangular norm (ω)-fuzzy CI-subalgebras. Through the study, they verify the homomorphism of doubt triangular norm (ω)-fuzzy CI-algebras (doubt ω-FCI-SA) and delve into various algebraic properties, including the Cartesian product of doubt triangular norm (ω) with fuzzy CI-algebras.

In Chapter "Elastoplastic Behavior of Transversely Isotropic Piezoelectric Disc Made of Functionally Graded Material with Variable Thickness Under Rotation", the authors embark on an exploration of stress distribution and displacement in a rotating circular disc crafted from a unique material featuring variable thickness. Employing Seth's transition theory, authors derive stress components and vividly illustrate their findings through numerical and graphical analyses, shedding light on the alterations in radial stress as the thickness parameter fluctuates.

Moving forward to Chapter "Detection and Classification of Pneumonia from Chest X-rays Using Image Based Deep Learning Methods", the research takes on the critical task of assessing various convolutional neural network (CNN) models for their efficacy in diagnosing pneumonia from chest X-ray images. Through rigorous evaluation using metrics like accuracy, precision, recall, F1-score, and AUC score, the study seeks to identify the most effective model for this vital medical application.

In Chapter "Precision Agriculture Using IOT Sensors", the study aims to develop an innovative smart agriculture system. This system incorporates various features such as intelligent irrigation based on real-time field data, monitoring soil conditions, detecting animal intrusions, managing weather changes, and controlling pests. These functions can be remotely managed by using smart devices or internet-connected computers, with the integration of technologies like ESP32, Wi-Fi, actuators, and sensors.

Moving on to Chapter "On the Analysis of a Very Severe Cyclonic Storm Nilofar Over the Arabian Sea: A Numerical Weather Prediction Model Study", the authors delve into analyzing the dynamics of the severe cyclonic storm Nilofar in the Arabian Sea. Utilizing numerical simulations with the WRF model, they meticulously compare their findings with observational data to identify key factors leading to Nilofar's dissipation before making landfall. These factors include disrupted latent heat circulation, negative sea surface temperature anomalies, increasing wind shear,

and fluctuations in atmospheric stability. Their insights underscore the effectiveness of the WRF model in comprehending tropical cyclone dynamics.

In Chapter "Crypto-Encoding Communication with Graph Theory", the authors explore the intriguing realm of cryptography, the art of transforming plain text into encrypted code and vice versa. They highlight the historical significance of cryptography, which has long been employed by militaries and diplomats to safeguard sensitive information.

In Chapter "Cybersecurity Incidents in Relation to Fraudulent SIM Card Registration in Malawi", the study analyzes the relationship between cybersecurity incidents and the prevalence of mobile numbers without national identities in Malawi by using data from 2016 to 2021. It also evaluates the effectiveness of SMS OTP as a security measure, aiming to provide insights into regional cybersecurity trends and mitigate associated risks.

Chapter "On Signed Product Cordial Labeling of Pan Related Graphs" explores the signed product cordial behavior of the *m*-pan graph, focusing on path connections and merging of graph copies under specific conditions, contributing to a better understanding of its unique characteristics.

In Chapter "Supply Chain Analysis and Prediction Using Machine Learning", machine learning techniques are applied to analyze complex supply chain data. The study covers preprocessing steps, model implementation including logistic regression, SVM, and random forest and tasks such as late delivery detection, fraudulent transaction identification, sales prediction, and customer segmentation by using the RFM analysis. Visualizations aid in data interpretation, while a dedicated website showcases data preprocessing and model results for improved collaboration.

In Chapter "Optimal Transport: A Promising Technique for Causal Inference Applications", the focus is on optimal transport methods for causal inference, overcoming limitations of traditional techniques in handling high-dimensional models. Monge's problem and Kantorovich's dual formulation are explored, along with their application in methods like difference-in-differences and synthetic controls.

Chapter "Analysis of a Queueing Model with Catastrophe and First Exceptional Service" introduces a queuing model with multiple vacations and server breakdowns, employing generating function techniques to analyze performance.

In Chapter "CNN-Based Mathematical Model for Sub-classification of Non-small Cell Lung Cancer into Squamous Cell Carcinoma and Adenocarcinoma", a convolutional neural network (CNN) model is developed to accurately classify lung cancer subtypes from low-dose CT scan images, achieving impressive accuracies of 96.89% in training and 93.20% in validation.

The book covers a wide range of topics, spanning from encryption methods and solar energy potential assessment to healthcare advancements and machine learning applications. Each chapter addresses unique challenges and explores innovative solutions across various fields such as cryptography, cybersecurity, healthcare, and environmental science. The chapters demonstrate the practical applications of mathematical modeling, deep learning, and optimization techniques in solving

real-world problems, ultimately contributing to technological advancements and improving quality of life.

Greater Noida, India   Khursheed Alam
New Delhi, India   Ayub Khan
Greater Noida, India   R. C. Singh
Worcester, USA   Yeliz Karaca

Acknowledgements

This book has been a journey filled with discovery, collaboration, and immense learning. It would not have been possible without the support, guidance, and contributions from many individuals and institutions, to whom we owe our deepest gratitude.

First and foremost, we would like to express our sincere thanks to our mentor, the late Prof. Abul Hasan Siddiqi, whose wisdom, encouragement, and unwavering belief in our work have been a constant source of inspiration. His insights and advice not only shaped this book but also profoundly influenced our approach to research and problem-solving.

We are also deeply grateful to our colleagues and collaborators, who have generously contributed their expertise to the various chapters of this book. Their dedication and passion for exploring new frontiers in applied mathematics have enriched this work and brought it to life.

We finally thank the readers of this book for their embarking on this mathematical adventure with us. We hope that the knowledge and insights shared within these pages will inspire them, just as the journey of creating this book has inspired us.

Khursheed Alam
Ayub Khan
R. C. Singh
Yeliz Karaca

Contents

About the Editors

Khursheed Alam is Professor and Head of the Department of Mathematics, Sharda University, Greater Noida, Gautam Buddha Nagar, Uttar Pradesh, India. He also is a Coordinator of The A. H. Siddiqi Centre for Advance Research in Applied Mathematics and Physics (CARAMP), School of Basic Sciences and Research at Sharda University. He obtained his M.Sc. and Ph.D. degrees in Mathematics in the year 1999 and 2005, respectively, from Jamia Millia Islamia, New Delhi. He is associated with the Sharda Group of Institutions (SGI), since July 2006. With more than 17 years of teaching experience and research, his research area is fractals using wavelet, image processing, nonlinear dynamical systems, and chaos theory.

With more than 43 research papers in many Scopus- and SCI-indexed journals, he is the recipient of the Academic Excellence Awards 2021 for the Best Performer in Learning and Development, received at the International Conference and the Academic Excellence Award on Recent Innovation and Interdisciplinary Research and Global Academic Excellence Awards 2021 for the Best Young Scientist, received in National Conference and Academic Excellence Award on Recent Innovation and Interdisciplinary Research. He has published six books and many book chapters.

Ayub Khan is Professor and Head of the Department of Mathematics, Jamia Millia Islamia, New Delhi, India. Earlier, he held the position of Pro Vice-Chancellor and Vice-Chancellor (in-charge) of Maulana Azad National Urdu University, Hyderabad, Telangana, India. He was the first alumnus of the University of Delhi to hold a Ph.D. degree in Nonlinear Dynamical System. He completed his Ph.D. degree from the University of Delhi in 1995 on the topic "Chaos in Nonlinear Planar Oscillations of a Satellite in Elliptic Orbits." His research work was online to NEP 2020 even in 1995. With more than 165 research papers published in several journals of repute, he has supervised 23 Ph.D. and 12 M.Tech. students. A member of different academic bodies in the country, he has delivered a number of lectures at different forum and conferences.

R. C. Singh is Professor of Physics, Director National and International Ranking, Advisor of the Learning Resource Centre (Central Library), and Director of Online

Education at Sharda University, Greater Noida, Gautam Buddha Nagar, Uttar Pradesh, India. He earned his Ph.D. degree in Theoretical Condensed Matter Physics, B.Sc. (Hons.) and M.Sc. degrees in Physics from Banaras Hindu University, Varanasi, Uttar Pradesh, India. With more than 70 research papers and several book chapters published in peer-reviewed international journals and conference proceedings, he has an impressive publication record. He has also authored 1 book and co-edited 3 books, in addition to 11 conference proceedings. Under his guidance, five research students have successfully obtained their doctorate degrees, while five more research fellows are currently carrying out their research work under his mentorship. A reviewer for several international journals actively participates in national and international conferences, seminars, workshops, and short-term courses; he successfully completed three research projects that were sponsored by the Department of Science and Technology (the Government of India), New Delhi, with three patents granted and six patents published in collaboration with his colleagues.

Yeliz Karaca is an Associate Professor of Mathematics, and a Researcher Professor at the University of Massachusetts (UMass) Chan Medical School, Worcester, USA. She received her Ph.D. degree in Mathematics in 2012. Along with the other awards she has been conferred, she was granted the Cooperation in Neurological Sciences and Support Award by Turkish Neurology Association as the first mathematician in Türkiye. She also holds a medical card as the only mathematician entitled for it. Furthermore, she received the Outstanding Young Scientist Award in 2012 and Best Paper Awards in her specialized discipline, among the other national and international awards in different categories as well as grants. Another award of hers is Outstanding Reviewer Award (Mathematics Journal, MDPI) in 2021.

Editor-in-Chief of the book series *Systems Science and Nonlinear Intelligence Dynamics*, Dr. Karaca has been acting as the Lead Editor, Editor, and Associate Editor in many SCI-indexed journals. She has been the leading Guest Editor of several special issues, including "Fractals-Fractional AI-Based Analyses and Applications to Complex Systems (Parts IV, III, II, I)" in *Fractals Journal*. She also has active involvement with diverse projects, some of which are the Institute of Electrical and Electronics Engineers (IEEE, as Senior Member), the Organization for Women in Science for the Developing World (OWSD); Complex Human Adaptive Organizations and Systems (CHAOS), University of Perugia, Italy; International Engineering and Technology Institute (IETI, as the Member of Board of Director). Her research interests include complex systems sciences with applications in various terrains, applied mathematics, advanced computational methods, AI applications, computational complexity, fractional calculus, fractional quantum calculus, fractals and multifractals, stochastic processes, different kinds of differential and difference equations, discrete mathematics, algebraic complexity, complexity science, wavelet and entropy, solutions of advanced mathematical challenges, mathematical neuroscience, and biology as well as advanced data analysis in medicine and other related theoretical, computational, and applied domains.

A New Method of Cryptography Providing Perfect Confidentiality of Information

Mukhayo Yunusovna Rasulova [ORCID]

Abstract In this paper, using the method of statistical physics, a new encryption method is proposed that provides its own transformation for each cell of information, i.e., the perfect security of information. This new method is based on the Lieb-Liniger Model, which describes a gas of bosons in one-dimensional space.

Keywords Statistical physics · Lieb-Liniger model · Advanced encryption system · Tree-pass protocol

MSC Code 94A60

1 Introduction

From ancient times to the present, the security of information and its transmission has been an urgent problem. Interest in this problem has increased many times, due to the digitalization of the entire industry of life and activity. Unfortunately, at present, information security methods are based on probabilistic methods, which do not provide perfect information protection. Even 'The Design of Rijndael AES-The Advanced Encryption Standard" [1], which is the basis of modern Western information security, also based on probabilistic methods of information protection, is not excluded from this shortcoming.

One of the possible methods for solving the problem of ideal information security is to solve the equation for the function of n variables, where n is the number of information cells, which will give a complete set of their own transformations for each cell. At present, there are only a few such exact solvable equations. One of these equations is the Schrodinger equation, which describes a system of n particles, interacting with a potential in the form of a delta function. The solution of this

M. Y. Rasulova (✉)

Institute of Nuclear Physics, Academy of Sciences Republic of Uzbekistan, Tashkent, Republic of Uzbekistan

e-mail: rasulova@live.com

equation has the form of the form of Bethe ansatz [2], which includes the argument permutation operator. This problem was first solved by Lieb and Linigher [3].

Another problem of information security is related to the transmission of information. It is in the transmission of information that there is a process of transferring the information key from the sender of the encoded information to the addressee. This process is quite dangerous, since the key can get to a third enemy person. Therefore, it is necessary to exclude this process when transmitting information. The most promising way to solve this problem is to ensure the transfer of information without a key transfer process, creating a method of information transfer where the participants in the transfer have their own encryption e_A, e_B and decryption d_A, d_B keys and do not use the key transfer process. This method was developed by Shamir [4] in the 80s of the last century (see Fig. 1).

In this paper, we have proposed a new approach [5–8] to solving the creation of a method for ensuring perfect information protection, based on statistical mechanics, namely, the Lieb-Linigher Model. This approach allows us to fully implement the use of the Shamir information transmission method. The first chapter of the work is devoted to the introduction. In the second chapter, a method for solving the problem in the Lieb-Liniger Model is briefly indicated. The third chapter shows how the Lieb-Liniger method can be applied to information transfer. The last chapter is devoted to the conclusion.
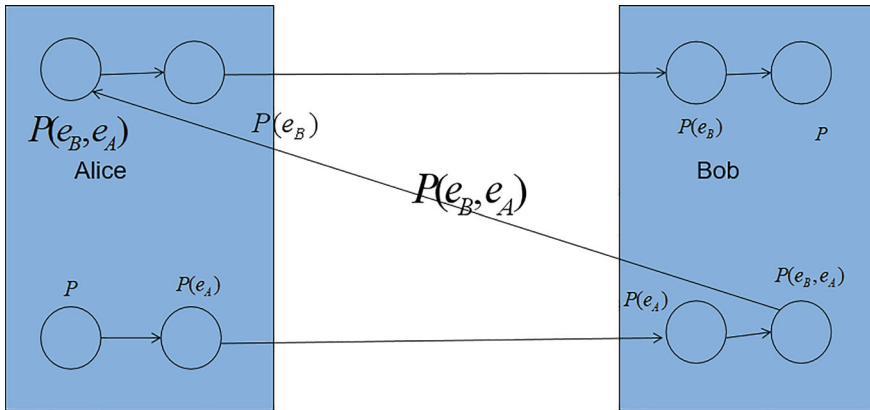
Fig. 1 Flow chart illustrating a communication process between two entities, Alice and Bob, represented by two blue sections. Each section contains circles connected by arrows, indicating the flow of information. The chart includes probability expressions such as P(eB,eA), P(eB), and P(eA), showing the relationships and dependencies between different events or states. The diagram emphasizes the interaction and data exchange between Alice and Bob

2   Bethe Ansatz for Bose Gas

Following [3], consider the solution of the time independent Schrödinger equation for s particles interacting with the potential in the form of a delta function

$$\delta(|x_i - x_j|) = \{_0^{\infty,} \quad_{if}^{if} \quad_{x_i \neq x_j}^{x_i = x_j,}.$$

in one-dimensional space R:

$$-\frac{\hbar^2}{2m} \sum_{i=1}^{s} \Delta_i \psi(x_1, x_2, ..., x_s) + 2c \sum_{1 \leq i < j \leq s} \delta(x_i - x_j)$$

$$\psi(x_1, x_2, ..., x_s) = E\psi(x_1, x_2, ..., x_s), \tag{1}$$

where the constant $c \geq 0$ and $2c$ is the amplitude of the delta function, $m = 1$- massa of boson, $\hbar = 1$-Plank constant, Δ-Laplasian, the domain of the problem is defined in R: all $0 \leq x_i \leq L$ and the wave function ψ satisfies the periodicity condition in all variables. In [3], it was proved that defining a solution ψ in $R_1 : 0 \leq x_1 \leq x_2 \leq ... \leq x_s \leq L$ is equivalent to defining a solution to the equation

$$-\sum_{i=1}^{s} \frac{1}{2m} \Delta_{x_i} \psi = E\psi,$$

with the boundary condition

$$\left(\frac{\partial}{\partial x_{j+1}} - \frac{\partial}{\partial x_j}\right)\psi\bigg|_{x_{j+1}=x_j} = c\,\psi|_{x_{j+1}=x_j}, \tag{2}$$

and the initial periodicity condition is equivalent to the periodicity conditions in

$$\psi(0, x_2, ..., x_s) = \psi(x_2, ..., x_s, L),$$

$$\frac{\partial \psi(x, x_2, ..., x_s)}{\partial x}\bigg|_{x=0} = \frac{\partial \psi(x_2, ..., x_s, x)}{\partial x}\bigg|_{x=L}.$$

Using Eq. (2) we can determine the solution of equation Eq. 1 in the form of the Bethe ansatz [2, 3, 5, 9]:

$$\psi(x_1, ..., x_s) = \sum_P a(P)P \exp(i \sum_{j=1}^{s} k_j x_j) \tag{3}$$

in the region R_1 with eigenvalue $E_s = \sum_{j=1}^{s} k_j^2$, where the summation is performed over all permutations P of the numbers $\{k\} = k_1, k_2, ..., k_s$ and $a(P)$ is a certain coefficient depending on $a(Q) = -a(P) \exp(i\theta_{i,j})$, where $\theta_{i,j} = \theta(k_i - k_j)$, $\theta(r) = -2\tan^{-1}\left(\frac{r}{c}\right)$ and when r is a real value and $-\pi \leq \theta(r) \leq \pi$.

For the case $s = 2$, one can find [3, 5–10]:

$$\psi(x_1, x_2) = a_{1,2}(k_1, k_2)e^{i(k_1 x_1 + k_2 x_2)} + a_{2,1}(k_1, k_2)e^{i(k_2 x_1 + k_1 x_2)}.$$

and

$$ik_2 a_{1,2} + ik_1 a_{2,1} - ik_1 a_{1,2} - ik_2 a_{2,1} = c(a_{1,2} + a_{2,1}),$$

or

$$a_{2,1} = -\frac{c - i(k_2 - k_1)}{c + i(k_2 - k_1)} a_{1,2}.$$

If we choose

$$a_{1,2} = e^{i(k_1 x_1 + k_2 x_2)},$$

one gets

$$e^{i(k_2 x_1 + k_1 x_2)} = -\frac{c - i(k_2 - k_1)}{c + i(k_2 - k_1)} e^{i(k_1 x_1 + k_2 x_2)} = -e^{i\theta_{2,1}} e^{i(k_1 x_1 + k_2 x_2)}. \qquad (4)$$

3 Application of Bethe Ansatz in Information Technology

Let's consider how the last equation can be used for three-stage information transfer. Let Alice encrypt information $X = e^{i(k_1 x_1 + k_2 x_2 + k_3 x_3 + k_4 x_4 + k_5 x_5 + k_6 x_6 + k_7 x_7 + k_8 x_8)}$ using the encryption key

$$e_A = e^{i\theta_{3,1}} e^{i\theta_{5,2}} e^{i\theta_{1,3}} e^{i\theta_{6,4}} e^{i\theta_{2,5}} e^{i\theta_{4,6}} e^{i\theta_{8,7}} e^{i\theta_{7,8}}$$

and send encrypted information to Bob:

$$(e_A X) = e^{i\theta_{3,1}} e^{i\theta_{5,2}} e^{i\theta_{1,3}} e^{i\theta_{6,4}} e^{i\theta_{2,5}} e^{i\theta_{4,6}} e^{i\theta_{8,7}} e^{i\theta_{7,8}} \times$$
$$e^{i(k_1 x_1 + k_2 x_2 + k_3 x_3 + k_4 x_4 + k_5 x_5 + k_6 x_6 + k_7 x_7 + k_8 x_8)}$$
$$= e^{i(k_3 x_1 + k_5 x_2 + k_1 x_3 + k_6 x_4 + k_2 x_5 + k_4 x_6 + k_8 x_7 + k_7 x_8)}.$$

Bob receives this information and encrypts it with his key:

$$e_B = e^{i\theta_{2,1}} e^{i\theta_{4,2}} e^{i\theta_{5,3}} e^{i\theta_{1,4}} e^{i\theta_{6,5}} e^{i\theta_{3,6}} e^{i\theta_{8,7}} e^{i\theta_{7,8}}$$

and sends the double-encrypted information back to Alice:

$$(e_B(e_A X)) = e^{i\theta_{2,1}} e^{i\theta_{4,2}} e^{i\theta_{5,3}} e^{i\theta_{1,4}} e^{i\theta_{6,5}} e^{i\theta_{3,6}} e^{i\theta_{8,7}} e^{i\theta_{7,8}} \times$$

$$e^{i(k_3 x_1 + k_5 x_2 + k_1 x_3 + k_6 x_4 + k_2 x_5 + k_4 x_6 + k_8 x_7 + k_7 x_8)} =$$

$$e^{i(k_2 x_1 + k_4 x_2 + k_5 x_3 + k_1 x_4 + k_6 x_5 + k_3 x_6 + k_8 x_7 + k_7 x_8)}.$$

Having received the latest information from Bob, Alice decrypts it with her key

$$d_A = e^{-i\theta_{3,1}} e^{-i\theta_{5,2}} e^{-i\theta_{1,3}} e^{-i\theta_{6,4}} e^{-i\theta_{2,5}} e^{-i\theta_{4,6}} e^{-i\theta_{8,7}} e^{-i\theta_{7,8}} :$$

$$(d_A(e_B(e_A X))) = e^{-i\theta_{3,1}} e^{-i\theta_{5,2}} e^{-i\theta_{1,3}} e^{-i\theta_{6,4}} e^{-i\theta_{2,5}} e^{-i\theta_{4,6}} e^{-i\theta_{8,7}} e^{-i\theta_{7,8}} \times$$

$$e^{i(k_2 x_1 + k_4 x_2 + k_5 x_3 + k_1 x_4 + k_6 x_5 + k_3 x_6 + k_8 x_7 + k_7 x_8)} =$$

$$e^{i(k_3 x_1 + k_5 x_2 + k_1 x_3 + k_6 x_4 + k_2 x_5 + k_4 x_6 + k_8 x_7 + k_7 x_8)}$$

and send it back to Bob. Now the information is covered by Bob's key just one time. Bob, having received this information, decrypts it with his decoder key

$$d_B = e^{-i\theta_{2,1}} e^{-i\theta_{4,2}} e^{-i\theta_{5,3}} e^{-i\theta_{1,4}} e^{-i\theta_{6,5}} e^{-i\theta_{3,6}} e^{-i\theta_{8,7}} e^{-i\theta_{7,8}} :$$

$$(d_B(d_A(e_B(e_A X)))) = (d_B(d_A(e_A(e_B X)))) =$$

$$= e^{-i\theta_{2,1}} e^{-i\theta_{4,2}} e^{-i\theta_{5,3}} e^{-i\theta_{1,4}} e^{-i\theta_{6,5}} e^{-i\theta_{3,6}} e^{-i\theta_{8,7}} e^{-i\theta_{7,8}} \times$$

$$e^{-i\theta_{3,1}} e^{-i\theta_{5,2}} e^{-i\theta_{1,3}} e^{-i\theta_{6,4}} e^{-i\theta_{2,5}} e^{-i\theta_{4,6}} e^{-i\theta_{8,7}} e^{-i\theta_{7,8}} \times$$

$$e^{i\theta_{3,1}} e^{i\theta_{5,2}} e^{i\theta_{1,3}} e^{i\theta_{6,4}} e^{i\theta_{2,5}} e^{i\theta_{4,6}} e^{i\theta_{8,7}} e^{i\theta_{7,8}} \times$$

$$e^{i\theta_{2,1}} e^{i\theta_{1,2}} e^{i\theta_{6,3}} e^{i\theta_{2,4}} e^{i\theta_{3,5}} e^{i\theta_{5,6}} e^{i\theta_{8,7}} e^{i\theta_{7,8}} \times$$

$$e^{i(k_1 x_1 + k_2 x_2 + k_3 x_3 + k_4 x_4 + k_5 x_5 + k_6 x_6 + k_7 x_7 + k_8 x_8)} =$$

$$e^{-i\theta_{2,1}} e^{-i\theta_{4,2}} e^{-i\theta_{5,3}} e^{-i\theta_{1,4}} e^{-i\theta_{6,5}} e^{-i\theta_{3,6}} e^{-i\theta_{8,7}} e^{-i\theta_{7,8}} \times$$

$$e^{i\theta_{2,1}} e^{i\theta_{4,2}} e^{i\theta_{5,3}} e^{i\theta_{1,4}} e^{i\theta_{6,5}} e^{i\theta_{3,6}} e^{i\theta_{8,7}} e^{i\theta_{7,8}} \times$$

$$e^{i(k_1 x_1 + k_2 x_2 + k_3 x_3 + k_4 x_4 + k_5 x_5 + k_6 x_6 + k_7 x_7 + k_8 x_8)} =$$

$$e^{i(k_1 x_1 + k_2 x_2 + k_3 x_3 + k_4 x_4 + k_5 x_5 + k_6 x_6 + k_7 x_7 + k_8 x_8)}.$$

so in binary $k_1 = 1$, $k_2 = 0$, $k_3 = 1$, $k_4 = 0$, $k_5 = 1$, $k_6 = 1$, $k_7 = 0$, $k_8 = 0$.

The latest information matches the information that Alice wanted to send to Bob.

To adapt the results obtained in Chap. 3 for modern computers, which are based on matrix coding, we introduce a permutation operator P, which we denote as follows:

$$e^{i(k_2 x_1 + k_1 x_2)} = \sum_{i=0}^{\infty} \frac{i^n}{n!}(k_2 x_1 + k_1 x_2)^n = \sum_{i=0}^{\infty} \frac{i^n}{n!}\left([x_1 x_2]\begin{bmatrix} k_2 \\ k_1 \end{bmatrix}\right)^n =$$
$$\sum_{i=0}^{\infty} \frac{i^n}{n!}\left([x_1 x_2] P \begin{bmatrix} k_2 \\ k_1 \end{bmatrix}\right)^n,$$

where

$$P = \begin{bmatrix} 0 & 1 \\ 1 & 0 \end{bmatrix}$$

From last equation, after taking the logarithm, we obtain:

$$e_A = \begin{bmatrix} 0 & 0 & 1 & 0 & 0 & 0 & 0 & 0 \\ 0 & 0 & 0 & 0 & 1 & 0 & 0 & 0 \\ 1 & 0 & 0 & 0 & 0 & 0 & 0 & 0 \\ 0 & 0 & 0 & 0 & 0 & 1 & 0 & 0 \\ 0 & 1 & 0 & 0 & 0 & 0 & 0 & 0 \\ 0 & 0 & 0 & 1 & 0 & 0 & 0 & 0 \\ 0 & 0 & 0 & 0 & 0 & 0 & 0 & 1 \\ 0 & 0 & 0 & 0 & 0 & 0 & 1 & 0 \end{bmatrix} \quad e_B = \begin{bmatrix} 0 & 1 & 0 & 0 & 0 & 0 & 0 & 0 \\ 0 & 0 & 0 & 1 & 0 & 0 & 0 & 0 \\ 0 & 0 & 0 & 0 & 1 & 0 & 0 & 0 \\ 1 & 0 & 0 & 0 & 0 & 0 & 0 & 0 \\ 0 & 0 & 0 & 0 & 0 & 1 & 0 & 0 \\ 0 & 0 & 1 & 0 & 0 & 0 & 0 & 0 \\ 0 & 0 & 0 & 0 & 0 & 0 & 0 & 1 \\ 0 & 0 & 0 & 0 & 0 & 0 & 1 & 0 \end{bmatrix}$$

$$d_A = \begin{bmatrix} 0 & 0 & 1 & 0 & 0 & 0 & 0 & 0 \\ 0 & 0 & 0 & 0 & 1 & 0 & 0 & 0 \\ 1 & 0 & 0 & 0 & 0 & 0 & 0 & 0 \\ 0 & 0 & 0 & 0 & 0 & 1 & 0 & 0 \\ 0 & 1 & 0 & 0 & 0 & 0 & 0 & 0 \\ 0 & 0 & 0 & 1 & 0 & 0 & 0 & 0 \\ 0 & 0 & 0 & 0 & 0 & 0 & 0 & 1 \\ 0 & 0 & 0 & 0 & 0 & 0 & 1 & 0 \end{bmatrix} \quad d_B = \begin{bmatrix} 0 & 0 & 0 & 1 & 0 & 0 & 0 & 0 \\ 1 & 0 & 0 & 0 & 0 & 0 & 0 & 0 \\ 0 & 0 & 0 & 0 & 0 & 1 & 0 & 0 \\ 0 & 1 & 0 & 0 & 0 & 0 & 0 & 0 \\ 0 & 0 & 1 & 0 & 0 & 0 & 0 & 0 \\ 0 & 0 & 0 & 0 & 1 & 0 & 0 & 0 \\ 0 & 0 & 0 & 0 & 0 & 0 & 0 & 1 \\ 0 & 0 & 0 & 0 & 0 & 0 & 1 & 0 \end{bmatrix}$$

Matrices e_A and e_B are commutative:

$$e_A \times e_B = \begin{bmatrix} 0&0&1&0&0&0&0&0 \\ 0&0&0&0&1&0&0&0 \\ 1&0&0&0&0&0&0&0 \\ 0&0&0&0&0&1&0&0 \\ 0&1&0&0&0&0&0&0 \\ 0&0&0&1&0&0&0&0 \\ 0&0&0&0&0&0&0&1 \\ 0&0&0&0&0&0&1&0 \end{bmatrix} \times \begin{bmatrix} 0&1&0&0&0&0&0&0 \\ 0&0&0&1&0&0&0&0 \\ 0&0&0&0&1&0&0&0 \\ 1&0&0&0&0&0&0&0 \\ 0&0&0&0&0&1&0&0 \\ 0&0&1&0&0&0&0&0 \\ 0&0&0&0&0&0&0&1 \\ 0&0&0&0&0&0&1&0 \end{bmatrix} =$$

$$e_B \times e_A = \begin{bmatrix} 0&1&0&0&0&0&0&0 \\ 0&0&0&1&0&0&0&0 \\ 0&0&0&0&1&0&0&0 \\ 1&0&0&0&0&0&0&0 \\ 0&0&0&0&0&1&0&0 \\ 0&0&1&0&0&0&0&0 \\ 0&0&0&0&0&0&0&1 \\ 0&0&0&0&0&0&1&0 \end{bmatrix} \times \begin{bmatrix} 0&0&1&0&0&0&0&0 \\ 0&0&0&0&1&0&0&0 \\ 1&0&0&0&0&0&0&0 \\ 0&0&0&0&0&1&0&0 \\ 0&1&0&0&0&0&0&0 \\ 0&0&0&1&0&0&0&0 \\ 0&0&0&0&0&0&0&1 \\ 0&0&0&0&0&0&1&0 \end{bmatrix} =$$

$$= \begin{bmatrix} 0&0&0&0&1&0&0&0 \\ 0&0&0&0&0&1&0&0 \\ 0&1&0&0&0&0&0&0 \\ 0&0&1&0&0&0&0&0 \\ 0&0&0&1&0&0&0&0 \\ 1&0&0&0&0&0&0&0 \\ 0&0&0&0&0&0&1&0 \\ 0&0&0&0&0&0&0&1 \end{bmatrix}$$

We can also show that $d_A = e_A^{-1}$ is inverse to e_A and:

$$d_A \times e_A = \begin{bmatrix} 0&0&1&0&0&0&0&0 \\ 0&0&0&0&1&0&0&0 \\ 1&0&0&0&0&0&0&0 \\ 0&0&0&0&0&1&0&0 \\ 0&1&0&0&0&0&0&0 \\ 0&0&0&1&0&0&0&0 \\ 0&0&0&0&0&0&0&1 \\ 0&0&0&0&0&0&1&0 \end{bmatrix} \times \begin{bmatrix} 0&0&1&0&0&0&0&0 \\ 0&0&0&0&1&0&0&0 \\ 1&0&0&0&0&0&0&0 \\ 0&0&0&0&0&1&0&0 \\ 0&1&0&0&0&0&0&0 \\ 0&0&0&1&0&0&0&0 \\ 0&0&0&0&0&0&0&1 \\ 0&0&0&0&0&0&1&0 \end{bmatrix} =$$

$$= \begin{bmatrix} 1&0&0&0&0&0&0&0 \\ 0&1&0&0&0&0&0&0 \\ 0&0&1&0&0&0&0&0 \\ 0&0&0&1&0&0&0&0 \\ 0&0&0&0&1&0&0&0 \\ 0&0&0&0&0&1&0&0 \\ 0&0&0&0&0&0&1&0 \\ 0&0&0&0&0&0&0&1 \end{bmatrix}$$

Similarly, $d_B = e_B^{-1}$ and:

$$
d_B \times e_B
\begin{bmatrix}
0\,0\,0\,1\,0\,0\,0\,0 \\
1\,0\,0\,0\,0\,0\,0\,0 \\
0\,0\,0\,0\,0\,1\,0\,0 \\
0\,1\,0\,0\,0\,0\,0\,0 \\
0\,0\,1\,0\,0\,0\,0\,0 \\
0\,0\,0\,0\,1\,0\,0\,0 \\
0\,0\,0\,0\,0\,0\,0\,1 \\
0\,0\,0\,0\,0\,0\,1\,0
\end{bmatrix}
\times
\begin{bmatrix}
0\,1\,0\,0\,0\,0\,0\,0 \\
0\,0\,0\,1\,0\,0\,0\,0 \\
0\,0\,0\,0\,1\,0\,0\,0 \\
1\,0\,0\,0\,0\,0\,0\,0 \\
0\,0\,0\,0\,0\,1\,0\,0 \\
0\,0\,1\,0\,0\,0\,0\,0 \\
0\,0\,0\,0\,0\,0\,0\,1 \\
0\,0\,0\,0\,0\,0\,1\,0
\end{bmatrix}
=
$$

$$
=
\begin{bmatrix}
1\,0\,0\,0\,0\,0\,0\,0 \\
0\,1\,0\,0\,0\,0\,0\,0 \\
0\,0\,1\,0\,0\,0\,0\,0 \\
0\,0\,0\,1\,0\,0\,0\,0 \\
0\,0\,0\,0\,1\,0\,0\,0 \\
0\,0\,0\,0\,0\,1\,0\,0 \\
0\,0\,0\,0\,0\,0\,1\,0 \\
0\,0\,0\,0\,0\,0\,0\,1
\end{bmatrix}
$$

Let the initial information in a binary representation have the form:

$$
X =
\begin{bmatrix}
1 \\ 0 \\ 1 \\ 0 \\ 1 \\ 1 \\ 0 \\ 0
\end{bmatrix}.
\quad Then \quad
e_A X =
\begin{bmatrix}
0\,0\,1\,0\,0\,0\,0\,0 \\
0\,0\,0\,0\,1\,0\,0\,0 \\
1\,0\,0\,0\,0\,0\,0\,0 \\
0\,0\,0\,0\,0\,1\,0\,0 \\
0\,1\,0\,0\,0\,0\,0\,0 \\
0\,0\,0\,1\,0\,0\,0\,0 \\
0\,0\,0\,0\,0\,0\,0\,1 \\
0\,0\,0\,0\,0\,0\,1\,0
\end{bmatrix}
\times
\begin{bmatrix}
1 \\ 0 \\ 1 \\ 0 \\ 1 \\ 1 \\ 0 \\ 0
\end{bmatrix}
=
\begin{bmatrix}
1 \\ 1 \\ 1 \\ 1 \\ 0 \\ 0 \\ 0 \\ 0
\end{bmatrix}
$$

$$
(e_B(e_A X)) =
\begin{bmatrix}
0\,1\,0\,0\,0\,0\,0\,0 \\
0\,0\,0\,1\,0\,0\,0\,0 \\
0\,0\,0\,0\,1\,0\,0\,0 \\
1\,0\,0\,0\,0\,0\,0\,0 \\
0\,0\,0\,0\,0\,1\,0\,0 \\
0\,0\,1\,0\,0\,0\,0\,0 \\
0\,0\,0\,0\,0\,0\,0\,1 \\
0\,0\,0\,0\,0\,0\,1\,0
\end{bmatrix}
\times
\begin{bmatrix}
1 \\ 1 \\ 1 \\ 1 \\ 0 \\ 0 \\ 0 \\ 0
\end{bmatrix}
=
\begin{bmatrix}
1 \\ 1 \\ 0 \\ 1 \\ 0 \\ 1 \\ 0 \\ 0
\end{bmatrix}
$$

$$(d_A(e_B(e_A X))) = \begin{bmatrix} 0\,0\,1\,0\,0\,0\,0\,0 \\ 0\,0\,0\,0\,1\,0\,0\,0 \\ 1\,0\,0\,0\,0\,0\,0\,0 \\ 0\,0\,0\,0\,0\,1\,0\,0 \\ 0\,1\,0\,0\,0\,0\,0\,0 \\ 0\,0\,0\,1\,0\,0\,0\,0 \\ 0\,0\,0\,0\,0\,0\,0\,1 \\ 0\,0\,0\,0\,0\,0\,1\,0 \end{bmatrix} \times \begin{bmatrix} 1 \\ 1 \\ 0 \\ 1 \\ 0 \\ 1 \\ 0 \\ 0 \end{bmatrix} = \begin{bmatrix} 0 \\ 0 \\ 1 \\ 1 \\ 1 \\ 1 \\ 0 \\ 0 \end{bmatrix}$$

$$(d_B(d_A(e_B(e_A X)))) = \begin{bmatrix} 0\,0\,0\,1\,0\,0\,0\,0 \\ 1\,0\,0\,0\,0\,0\,0\,0 \\ 0\,0\,0\,0\,0\,1\,0\,0 \\ 0\,1\,0\,0\,0\,0\,0\,0 \\ 0\,0\,1\,0\,0\,0\,0\,0 \\ 0\,0\,0\,0\,1\,0\,0\,0 \\ 0\,0\,0\,0\,0\,0\,0\,1 \\ 0\,0\,0\,0\,0\,0\,1\,0 \end{bmatrix} \times \begin{bmatrix} 0 \\ 0 \\ 1 \\ 1 \\ 1 \\ 1 \\ 0 \\ 0 \end{bmatrix} = \begin{bmatrix} 1 \\ 0 \\ 1 \\ 0 \\ 1 \\ 1 \\ 0 \\ 0 \end{bmatrix} = X.$$

4 Conclusion

This work proposes a new encryption method based on the Lieb-Liniger model, which allows the translation to provide for each cell its own encryption transformation. For this purpose, we use the solutions of the Schrodinger equation for the boson system interacting with the potential in the form of a delta function.

The advantages of this algorithm and information transfer method:

1. Complete diffusion of component bits at each stage of information transfer.
2. The cost-effectiveness of the algorithm, since good diffusion is provided by a small number of bits. If modern programs requires 5 cells to express letters, then in our approach it is possible to express letters in one cell.
3. Equality of zero correlation between plaintext and ciphertext, which is a condition for perfect encryption.
4. The lack of a key transfer process between partners is the most danger-ous part of information transfer.
5. Possibility of programming the direction of propagation of bosons in one-dimensional space.

References

1. Daemen, J., Rijmen, V.: The Design of Rijndael AES-The Advanced Encryption Standard. Springer (2002)
2. Bethe, H.A.: On the theory of metals, I. Eigenvalues and eigenfunctions of a linear chain of atoms, (German). Zeits. Phys. **71**, 205–226 (1931)
3. Lieb, E.H., Liniger, W.: Exact analysis of an interacting Bose gas.I: the general solution and the ground state. Phys. Rev. **130**, 1605–1616 (1963)
4. Shamir, A., Rivest, R.L., Adleman, L.M.: Mental Poker. In: Klarner, D.A. (eds) The Mathematical Gardner, Wadsworth, pp. 37–43. (1981)
5. Rasulova, M.Y.: The solution of quantum kinetic equation with delta potential and its application for information technology. Appl. Math. Inf. Sci. **12**(4), 685–688 (2018)
6. Rasulova, M.Y.: The BBGKY hierarchy of quantum kinetic equations and its application in cryptography. Phys. Part. Nucl. **51**(4), 781–785 (2020)
7. Rasulova, M., Yunusov, J.: Definition of a three-pass protocol using the Lieb-Liniger Model. Appl. Math. Inf. Sci. **15**(6), 677–680 (2021)
8. Rasulova, M.Y.: Approach to cryptography from the Lieb-Liniger Model. Appl. Math. Inf. Sci. **17**(3), 431–436 (2023)
9. Craig, A., Tracy, I., Harold Widom, J.: The dynamics of the one-dimensional deltafunction Bose gas. Phys. A Math. Theor. **41**, (485204) (2008)
10. Brokate, M., Rasulova, M.Y.: The solution of the hierarchy of quantum kinetic equations with delta potential, in industrial mathematics and complex systems. In: Siddiqi, A.H. (ed.). Springer, pp. 165–170 (2017)

Prediction of Solar Energy Potential with Machine Learning and Deep Learning Models

Buket İşler ⓘ**, Uğur Şener** ⓘ**, Ahmet Tokgözlü** ⓘ**, Zafer Aslan** ⓘ**, and Peter Baumann** ⓘ

Abstract Replacing fossil fuel-based energy with carbon-free sources is essential for achieving climate neutrality in Europe, aligned with the European Green Deal. The southern regions of Turkey, especially Serik, Antalya, are well-suited to support this strategy due to their significant solar energy potential. This research investigates the solar energy potential of Serik, a region with one of Turkey's highest renewable energy reservoirs. Accurately forecasting solar energy potential requires understanding meteorological, geographical, and technological factors, particularly advancements in machine learning and deep learning models. This study employs Nonlinear Autoregressive Neural Networks (NAR), Long Short-Term Memory (LSTM), Gated Recurrent Unit (GRU), Seasonal Autoregressive Moving Average (SARMA), and Discrete Wavelet Analysis, as well as the NARX model, incorporating Wavelet outputs as inputs. The integration of Discrete Wavelet Transform with neural networks has significantly enhanced forecast accuracy. The SARMA model also performed well over the test period. This paper serves as a

B. İşler (✉)
Department of Software Engineering, Istanbul Topkapi University, Istanbul, Türkiye
e-mail: buketisler@topkapi.edu.tr

U. Şener
Department of Computer Information Systems and Business Analytics, Metropolitan State University of Denver, Denver, CO, USA
e-mail: ugsener@msudenver.edu

A. Tokgözlü
Faculty of Science and Literature, Süleyman Demirel University, Isparta, Türkiye
e-mail: ahmettokgozlu@sdu.edu.tr

Z. Aslan
Faculty of Engineering, Department of Computer Engineering, Istanbul Aydin University, Istanbul, Türkiye
e-mail: zaferaslan@aydin.edu.tr

P. Baumann
School of Computer Science and Engineering, Constructor University, Bremen GmbH, Bremen, Germany
e-mail: pbaumann@constructor.university

guide for selecting optimal approaches to forecast medium- and long-term solar energy potential, contributing to improved strategies for solar energy utilization.

Keywords ANN · Discrete wavelet analysis · GRU · Hybrid forecasting · LSTM · Solar irradiance forecasting

MSC Code 68T07

1 Introduction

Energy consumption per capita is considered a significant indicator reflecting a country's technological and economic advancement. Fossil fuels are generally relied upon to meet energy demand in the twentieth century. The climate-neutral continent objective of the European Green Deal and rising energy demand have led to a rapid rise in interest in renewable energy sources due to the limited reserves and environmental impacts of carbon-based energy production. In this context, many countries have been increasing their clean and renewable energy production [1–3]. Solar panels exhibit a distinctive capacity to generate energy devoid of combustion processes, thereby obviating the emission of harmful gases into the atmosphere. This inherent characteristic contributes significantly to the mitigation of air pollution, thus constituting a pivotal measure in the global endeavor to combat climate change. Furthermore, the utilization of renewable energy derived from indigenous sources engenders a consequential reduction in dependency on external reservoirs of energy. This is an important step toward a cleaner and more responsible future.

Estimating the solar irradiance potential of a region is of great importance in achieving maximum efficiency from the generated energy systems. The energy obtained from solar radiation can be converted into various forms. This energy can be directly converted into electrical energy through photovoltaic (PV) panels [4], utilized for thermal energy purposes such as water heating [5], and transformed into chemical energy through the use of photoelectrochemical tools for the production of solar energy. All mentioned forms of energy require adequately mapped resources in regions where they are abundantly available. Therefore, accurate prediction of solar energy potential plays a critical role in ensuring the efficient utilization of these energy sources. There is no precise model available currently to correctly forecast the solar energy intensity. Solar radiation can be predicted using model-based and data-driven methods [6, 7]. The model-based system is based a physical foundation that utilizes weather variables to predict solar PV power. In the case of a data-driven model, techniques such as extreme learning machines, gradient-boosting regression trees, support vector machines, and artificial neural networks are utilized to construct the prediction model [8, 9].

Artificial Neural Networks (ANN), which are basically inspired by the biological thought process and can accurately predict data points outside a given data set by learning hidden trends in the training data, have emerged as an important

methodological approach in solar potential estimation [10]. This approach, which differs from traditional analysis methods, is becoming increasingly popular due to its high accuracy performance and effective modeling of complex data. As noted by Pan and Duraisamy (2018) and Thike et al. (2020), ANN can successfully capture the interactions of complex variables such as atmospheric conditions, solar radiation angle, and cloud cover. This feature increases the potential to achieve effective results in solar energy forecasting [11, 12]. In a study conducted by Kalogirou et al. (2014), ANNs were employed for predicting the performance of large solar energy systems. The research aimed to estimate the expected daily energy production and the temperature level the storage tank could reach by the end of the daily operation cycle under typical conditions [13]. In a study conducted in 2023, various machine learning models used for solar photovoltaic (PV) power prediction were examined, and the success of these models was evaluated. Among these models, regression, artificial neural networks, support vector machines, and random forests were included. The effectiveness and accuracy of these algorithms in predictions based on variables such as solar irradiation and temperature were compared in the study. Notably, artificial neural networks achieved higher accuracy rates compared to other models [14]. Maduabuchi et al. conducted a study on electricity demand forecasting using daily actual load electricity data collected over 18 months from 709 randomly selected households in Ireland. In this study, ARIMA and ANN models were applied. The findings of the study show that ANN provides superior results compared to ARIMA for non-linear load data. These results are obtained by comparing the Mean Absolute Percentage Error (MAPE) [15]. A different research focuses on finding the best surrogate performance prediction model for a solar photovoltaic-thermoelectric (PV-TE) module with different semiconductor materials. In this analysis using various ANNs, the ANN architecture with two hidden layers and five neurons in each layer was found to be the most effective [16].

Recurrent neural networks (RNN) are a subset of ANN specialized for the modeling of sequential data. Long short-term memory (LSTM) and Gated Recurrent Units (GRU) are modified RNN models that have wide applications for both academic and business purposes such as sequence modeling tasks of speech recognition, natural language processing, classification as well as univariate and multivariate forecasting of time series. An input gate, output gate, self-loop, and forget gate have been included in the classical single-layer RNN cell through its evolution to the LSTM. GRU is a more recent and simplified RNN relative to the LSTM where gates are reduced to two as reset gate and update gate in order to alleviate the burdensome computations, especially for large data sets [17, 18].

In the realm of artificial neural networks, it has been observed that pre-processing parameters prior to the prediction process can significantly enhance the model's performance. This observation is critical as data characteristics often remain hidden from forecasters; consequently, the integration of various forecasting models yields more accurate results than singular forecasting methods [19]. The application of discrete wavelet transforms (DWT) for data preparation is widely recognized. Furthermore, the amalgamation of DWT with ANN in a hybrid modeling approach effectively segments data into time and frequency components, thereby augmenting

both the preparation and feature extraction phases [20]. This methodology substantially enhances the understanding and accuracy of the predictions. In another vein, a study explored solar radiation prediction using diverse backpropagation algorithms and meteorological data, revealing that ANN models, particularly those trained with the Bayesian Regularization algorithm, outperformed alternative models in predictive efficacy [21]. A new study focuses on solar energy forecasting for large-scale renewable energy facilities, emphasizing the importance of adapting to changing weather conditions. To improve the accuracy of solar power generation forecasting, the study proposes a hybrid model that combines machine learning and statistical techniques, showing that this hybrid model outperforms traditional machine learning models in performance and cost-effectiveness [22]. As of 2023, a study was conducted to improve solar energy forecasting in Iraq's Wasit and Dhi Qar regions, comparing three different methods. Wavelet Artificial Neural Network (WANN) and Wavelet Support Vector Machine (WSVM) techniques produced similar results, with WANN outperforming WSVM. On the other hand, the Adaptive Neuro-Fuzzy Inference System (ANFIS) technique was reported to perform worse than the other two methods [23].

The analysis of solar power plant (SPPs) projects requires measuring meteorological parameters in the areas where the plants are planned to be installed. In this study, meteorological parameters obtained from the large-scale climate meteorology station owned by the General Directorate of Meteorology (MGM) in Antalya city center were evaluated. The average global solar irradiance intensities for each month were considered for 2020–2022.

We address the gap in science that a limited body of research dedicated to the estimation of solar energy potential in the research region and relatively recent deep learning models are not employed [24–28]. The primary objective of this study is to provide insights into the prospective development of solar energy potential as well as comparing the performance of statistical, machine learning, and deep learning forecast models with solar irradiance series. By scrutinizing historical meteorological data and considering factors such as solar radiation, meteorological conditions, and geographical parameters, it becomes feasible to forecast how the potential for solar energy generation in the region may evolve. This analytical effort significantly contributes to the identification of areas characterized by substantial solar energy potential and streamlines the decision-making process regarding the establishment of solar power facilities in the region. Moreover, this study introduces a hybrid model rooted in deep learning to enhance the accuracy of solar radiation forecasts. The proposed hybrid model amalgamates ANN NARX and DWT as a pre-processing step preceding the forecasting process. MATLAB (Matrix Laboratory) and the C++ programming language were employed to implement these models. Additionally, the study compares innovative approaches, including LSTM, GRU, and SARMA, to other conventional methodologies employed in estimating solar potential. This holistic approach aims to yield a more dependable and precise model for solar radiation forecasting.

2   Study Area, Data and Methodology

The broad effects of climate change on solar irradiance and solar energy potential in Turkey's Mediterranean region are the focus of this pilot project. The region selected as the study area is shown below. This section then discusses the technique and literature review.

2.1   Study Area

Antalya province is located in the southwest of Anatolia, between 29° 20′–32° 35′ east longitudes and 36° 07' - 37° 2' north latitudes. It covers an area of 20,723 square kilometers, which accounts for about 2.6% of Turkey's total area. The Taurus Mountains form the inland borders of the province. It is bordered by the Mediterranean Sea to the south, Mersin, Konya, and Karaman to the east, Isparta and Burdur to the north, and Muğla to the west. The coastal districts of the province include Merkez, Gazipaşa, Alanya, Manavgat, Serik, Kemer, Kumluca, Finike, Kale, and Kaş. The elevation ranges from 5 to 44 m mean sea level.

The highland districts include Gündoğmuş, Akseki, İbradı, Korkuteli, and Elmalı. These districts have an elevation of 900 to 1000 m mean sea level. They are all located in the western part of the Mediterranean Region, between the Antalya Gulf and the Western Taurus Mountains, Fig. 1 Antalya is the fifth largest province in Turkey in terms of population and land area. As of the end of 2022, the province's population is 2,688,004. It is known as the "capital of tourism" in Turkey. The number of tourists increases significantly, especially during the summer months. The province has a land area of 20,177 square kilometers, with a population density of 130 people per square kilometer. The most populous district is Kepez with a population of 591,895 as of 2021. The district with the highest population density is Muratpaşa with 5,429 people per square kilometer. Antalya has 19 districts and municipalities, with a total of 914 neighborhoods.

Approximately 77.8% of the province's terrain consists of mountains, 10.2% is plain, and 12% is characterized by rugged terrain. Many peaks of the Taurus Mountains, which cover three-quarters of the province's area, exceed elevations of 2500–3000 m. The western Teke region is characterized by vast plateaus and basins. In this area, which is mostly composed of limestone, karst formations such as caves, sinkholes, springs, dolines, and larger depressions called poljes, formed by the dissolution of limestone, are widespread. The topographical variation of the province creates different environments in terms of climate, agriculture, demographics, and settlements. These distinct areas are defined as the coastal and highland regions.

Antalya province generally has a Mediterranean climate. It is classified as a "Temperate Sea and Warm Sea Climate Class," characterized by hot and dry summers and mild and rainy winters. In the more inland areas, a "Cold Semi-Continental Climate" type is observed. The average temperature in summer ranges from 28 to 36 degrees
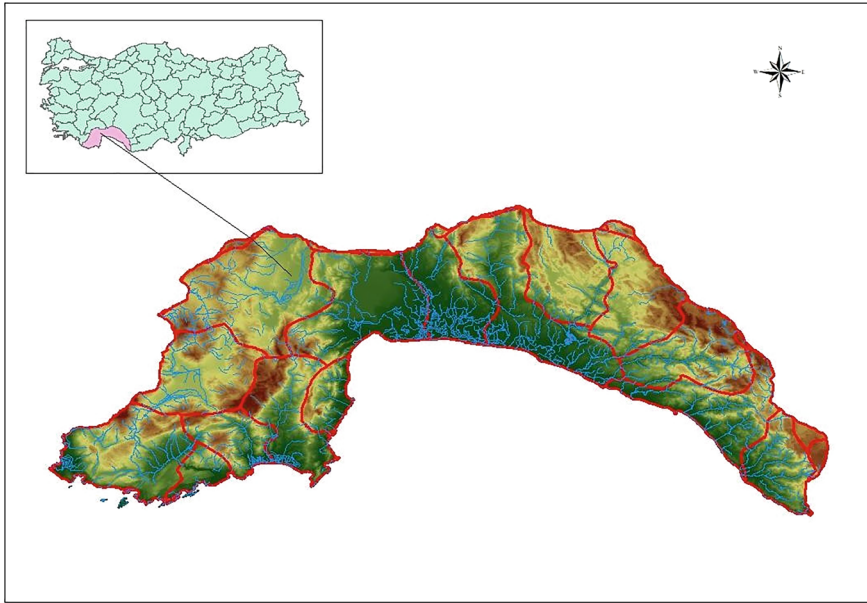
Fig. 1 Map of the research region

Celsius. During midday, the thermometer can rise above 40 degrees Celsius. In January, the temperature averages between 10 and 20 degrees Celsius. Snow is rare in the coastal areas, and frost occurs infrequently, not every winter. The average relative humidity in the province is around 64%.

The coastal region of Antalya experiences long and hot summers, while winters are relatively mild. Rainfall, which is almost absent during summers, occurs mostly in the winter months and occasionally in the early and late autumn as showers. Only about 40–50 days of the year are cloudy and rainy. Antalya enjoys an average of 300 sunny days per year, with an annual average temperature of 18.7 degrees Celsius, making it one of the few regions open to tourism year-round. The sea can be enjoyed for nine months of the year.

The highest recorded daily rainfall in Antalya was 232.8 kg/m2, the fastest wind speed was 155.5 km/h, and the highest snow depth measured was 5.0 cm.

In this study, hourly solar irradiance (cal/cm^2) between the years 1 st. January, 2020 and 31st. December, 2022 recorded in Antalya Meteorological Observatory was analysed. 18,565 hourly measurements of solar irradiance were evaluated with deep machine learning techniques.

2.2 Nonlinear Autoregressive Neural Network (NAR, NARX)

Artificial intelligence (AI) refers to a technology that aims to equip computer systems with human-like qualities, including intellectual capabilities, reasoning abilities, and the capacity to draw inferences from past experiences. Within the realm of AI, ANNs employ a network architecture comprising synthetic neurons, designed to mimic the structure of biological neural networks. These neurons, akin to their biological counterparts, are interconnected and utilize mathematical operations to process and model data. ANNs often serve as a foundational framework for deep learning models [29].

Artificial neural networks have been observed to be effective in various domains, including prediction, modeling, and classification, as commonly observed in the literature [30, 31]. Artificial neural networks are equipped with specialized network designs for time series data prediction. The nonlinear autoregressive neural network (NAR) and the nonlinear autoregressive neural network with exogenous inputs (NARX) are examples of these architectures. Numerous academic studies have regularly come across the NARX technique in artificial neural networks, indicating its successful use in simulating chaotic data [32, 33]. Additionally, NARX networks, a feedback-based artificial neural network model capable of accurate time series data prediction, demonstrate higher learning capabilities in terms of speed and efficacy when compared to traditional feedback network architectures [34].

2.3 LSTM and GRU

The recurrent neural network (RNN) works with a reverse logic compared with a feedforward neural network, while output contributes to its own input. A Long short-term memory neural network is a typical type of RNN and in general it is superior to the conventional RNN. A traditional RNN uses information from far back and loses this information quickly. RNN is improved by including more relevant information to its memory and excluding the rest. From this point of view, LSTM is better than its previous generations [17]. LSTM is founded by Hochreiter and Schmidhuber in order to improve the computational mechanism of long sequence models [18, 35]. Gated Recurrent Unit (GRU) is a more recent RNN model, where the number of gates are reduced to two for alleviating burdensome computations [17]. Besides their common applications of language processing, and speech recognition; LSTM and GRU have time series forecasting and classification abilities.

Sequence to sequence LSTM and GRU networks start with an input layer where the predicted variable is included to forecast itself. Multiple inputs are also possible in this layer. The input layer is followed by LSTM of GRU layers with a number of hidden units which is a factor determining the sophistication of the model. Then a dropout layer can be employed with a given probability to alleviate overfitting risk. It is possible to employ a fully connected layer before and/or after the dropout layer. The

fully connected layer can be followed by a regression layer for time series forecasting. Softmax and classification layers are used for classification considerations [17, 18].

2.4 Discrete Wavelet Transforms

In 1909, Alfred Haar used the term "wavelet" for the first time. Since then, the wavelet transform has advanced significantly thanks to the contributions of several illustrious academics, including Daubechies, Coifman, and Wickerhauser. In the discipline of signal processing, the wavelet transform is widely acknowledged as a common preprocessing method. The DWT is a mathematical operation used as a method to analyze data by decomposing it into smaller components in both the time and frequency domains. This method involves splitting a signal into smaller constituents and analyzing the temporal variations of chaotic data. By applying this process in multiple stages within the time-frequency domain, we can identify the underlying subcomponents that contribute to the primary modes of variability in the time series and understand their evolution over time. This transformation provides a means to represent the original data set in a format that enhances interpretability and comprehension. The discrete wavelet transform generates two complementary signals, namely the approximation (A) and detail (D) components, from the original signal denoted by the symbol S. The resulting coefficients can be examined at various frequency and resolution ranges. In the decomposition process, the approximation component encapsulates the overall properties of the original signal in a condensed form, while the detail component aids in identifying time series with rapid changes at high frequencies.

Widely used in many academic fields, particularly in the fields of signal processing, image processing, and data compression, is the DWT. It has several uses in tasks including improving data feature interpretation, lowering noise, compressing data, and stressing important information. In these disciplines, the DWT can be applied in a variety of ways [36, 37].

2.5 ARIMA

The ARIMA model combines the auto-regressive component with a finite moving average process while employing a differencing process if the data contains a trend. Auto-correlation and unit root tests can answer whether the trend exists in the series [38]. Auto-regressive component (AR) consists of lagged series of the predicted variable as explanatory variables in the model while transforming the serial-correlation problem to an asset for the model. Error series and its lagged versions are used in the moving average component which has similar properties to the exponential smoothing models but its model complexity is higher. When the differencing is applied to the ARMA models, it is called the ARIMA model [39, 40].

2.6 Model Fit Measures

The sum of squares-based error measures of the sum of squares (SSE), mean square error (MSE), and root mean square error (RMSE) are used in all regression-based models for both model fitting and comparing forecast models. RMSE is preferable for the latter purpose because it is on the same level as the actual observation after the square root operation is applied. Mean absolute percentage error (MAPE) is used to compare different forecast models even with different data sets while it measures the absolute error relative to the predicted variable. Mean percentage error (MPE) is used to determine whether the model underestimates or overestimates the level of the predicted variable. Significantly positive MPE values indicate that the forecast is lower than the actual observation in general and vice versa. R-Square shows the percentage of explained variance relative to the total variance in the predicted variable.

3 Results

In this study, a data set comprising 26,280 hourly measurements of solar irradiance between the years 2020 and 2022 was utilized where 2020–2021 period is selected for training, 2022 is selected as the test period and future forecasting is done for 2023. The absence of any missing values in the data set serves as an indication of the reliability of the data. LSTM, GRU, SARMA and NAR models are used as singular forecast models. In order to enhance the prediction performance, a hybrid model was developed, where the data underwent preprocessing using the wavelet transform method. The preprocessed data was then reanalyzed using the NARX-Wavelet methods. The best model was determined based on fixed R2 values. While 60% of the data set was used for training, the remaining 40% were allocated for validation and testing purposes. The number of neurons in the hidden layer was adjusted according to the network's performance. The optimal performance in both models was achieved when the hidden layer had 3 neurons. All error measures indicated that the SARMA (1,0,8) (1,1,1) models outperformed all other alternatives. The results section provides an overview of the accuracy of predictions made by both models.

In the study, various artificial intelligence methods were employed to predict solar irradiance, and one of these methods was the ANN NARX approach. The performance of the network was evaluated by comparing the R test results. The study found that the best R performances were 0.95 for training, 0.96 for validation, and 0.95 for test values. The analysis results, including graphical prediction outcomes, were presented in Fig. 2.

2020, 2021, and 2022 average annual solar irradiance were determined as 24.3 cal/cm2, 24.5 cal/cm2, and 24.8 cal/cm2, respectively. It shows, slightly an increasing trend. According to the results obtained using the NARX-Wavelet method, the average for 2023 is predicted to be 24.8 cal/cm2. The results of the NAR model
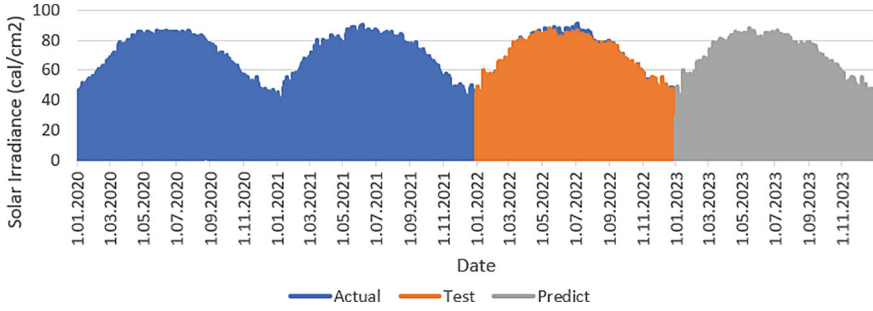
Fig. 2 Temporal solar irradiance variation of ANN model between 2020 and 2023 in Antalya

suggest that no significant change in solar irradiance is expected for the Antalya region in 2023 compared to 2022.

In this study, hybrid approaches are proposed to improve the prediction results of solar irradiance variations. The hybrid method is developed using wavelet transform and NARX. Initially, the solar irradiance data are subjected to wavelet analysis and decomposed into sub-components. The d4 wavelet, known for producing effective results in the literature, is utilized to partition the data into three levels. The study identifies the influence of large and medium-scale events in the Antalya region on solar irradiance variations. Consequently, the newly obtained data through wavelet transform are introduced to the network as input data along with the ANN data.

In the study, it was observed that the hybrid model developed using the wavelet transform method slightly improved the prediction performance compared to the model developed solely using ANN. In the hybrid study, R values of 0.96 for training, 0.96 for validation, and 0.96 for test data were obtained. Based on the hybrid model, the solar irradiance prediction for the year 2023 was determined as 24.7 ca/cal2. The results suggest a slight decrease in the average solar irradiance in 2023 compared to 2022. Fig. 3 presents the graphical and prediction outcomes obtained based on the analysis results.

Forecast accuracy measures for LSTM, GRU, NAR, NARX-Wavelet and SARMA models are presented below for the training period (2020-2021) of the data set (See
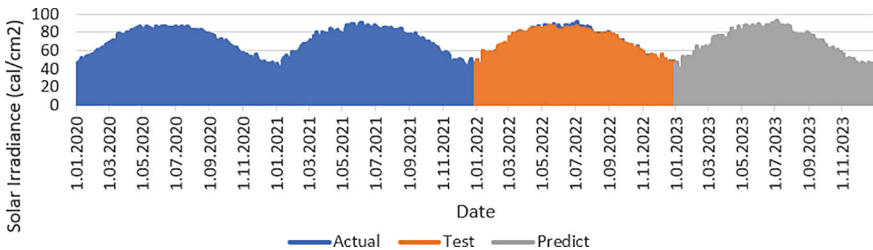

Fig. 3 Temporal solar irradiance variation of WANN model between 2020 and 2023 in Antalya

Table 1 Model fit statistics for training period (2020–2021)

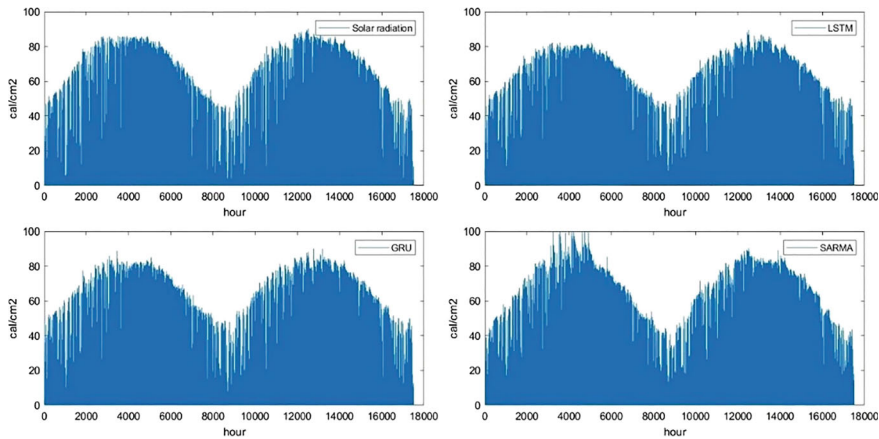| Error measure	LSTM	GRU	SARMA
SSE	1,879,860	2,107,518	858,575
MSE	72	80	33
RMSE	8.5	9	5.7
R^2	0.89	0.88	0.95

Fig. 4 Actual solar radiation, LSTM, GRU and SARMA forecasts for training period (2020–2021)

Table 1). SARMA model covered the data pattern better than other models which shows the advantage of using seasonal component for the seasonal data series.

LSTM, GRU and SARMA forecasts for the training period (2020–2021) and test period (2022) are presented at Figs. 4 and 5 respectively. All models successfully covered the seasonal pattern.

Table 2 presents the error measures for the test period of the data. SARMA model produced best predictions, while NAR and Wavelet-NARX models produced better results than deep learning models. Percentage based error measures cannot be calculated here because solar radiation has zero values at nights.

4 Discussion

The aim of this study is to perform hourly solar irradiance prediction and test the performance of hybrid forecasting models. The developed hybrid methods are utilized to assess their suitability for solar irradiance prediction and to evaluate whether they enhance prediction accuracy. The results have shown that the NARX-Wavelet model improved the learning performance only compared to the NAR model. An R- square value of 0.96 was obtained for the test data, whereas this value was
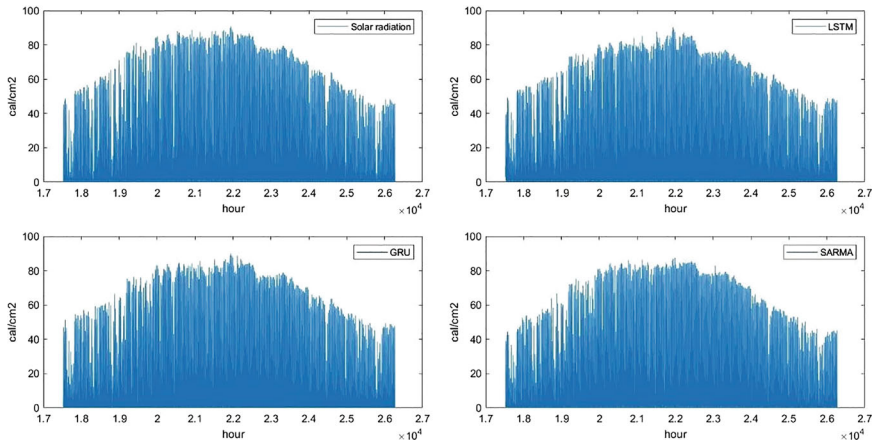
Fig. 5 Actual solar radiation, LSTM, GRU and SARMA forecasts for test period (2022)

Table 2 Model fit statistics for test period (2022)

Error measure	LSTM	GRU	SARMA	NAR	Wavelet NARX
SSE	604,580	673,810	199,992	364,044	357,024
MSE	69	77	23	59	58
RMSE	8.3	8.8	4.8	7.7	7.6
R^2	0.9	0.88	0.97	0.92	0.92

0.95 for the NAR model. This resulted in a 1% increase in prediction accuracy when using the hybrid model. Based on the results obtained from the NARX-Wavelet model, it is projected that the solar irradiance intensity for the Antalya region will decrease by 0.4% in 2023 compared to the year 2022. Compared with the machine learning and deep learning models, the SARMA model produced better results for solar radiation. Considering the seasonal impacts such as zero values at night, daily and seasonal cycles; the statistical ARIMA model with seasonal components covered the data pattern better than neural networks. By understanding the future potential of solar energy in the region, policymakers, energy companies, and investors can make informed decisions regarding the development of solar power projects, leading to a more sustainable and environmentally friendly energy landscape.

5 Conclusion

In conclusion, this study represents a significant advance in predicting solar energy potential in the Antalya region through machine learning and deep learning models. A comparative performance evaluation was conducted among various models,

including NAR, LSTM, GRU, NARX-Wavelet and SARMA. Notably, the use of DWT for data preprocessing distinctly enhanced the performance of these models, indicating its potential as a critical tool in future solar energy forecasting research.

In terms of future research, several targets are planned to be explored: i) incorporating more comprehensive meteorological and geographical data to refine model accuracy; ii) adapting the models for application in diverse geographic regions, thereby increasing their utility and relevance; iii) Continual development of more robust and efficient machine learning and deep learning algorithms, tailored explicitly for solar energy prediction, could offer further improvements in the field.

References

1. Lorenz, E., Hurka, J., Heinemann, D., Beyer, H.G.: Irradiance forecasting for the power prediction of grid-connected photovoltaic systems. IEEE J. Select. Top. Appl. Earth Observ. Remote Sens. **2**(1), 2–10 (2009)
2. Alessandrini, S., Delle Monache, L., Sperati, S., Cervone, G.: An analog ensemble for short-term probabilistic solar power forecast. Appl. Energy **157**, 95–110 (2015)
3. Van der Meer, D.W., Widén, J., Munkhammar, J.: Review on probabilistic forecasting of photovoltaic power production and electricity consumption. Renew. Sustain. Energy Rev. **81**, 1484–1512 (2018)
4. Nwaigwe, K.N., Mutabilwa, P., Dintwa, E.: An overview of solar power (PV systems) integration into electricity grids. Mater. Sci. Energy Technol. **2**(3), 629–633 (2019)
5. Tian, Y., Zhao, C.Y.: A review of solar collectors and thermal energy storage in solar thermal applications. Appl. Energy **104**, 538–553 (2013)
6. Al-Dahidi, S., Ayadi, O., Adeeb, J., Alrbai, M., Qawasmeh, B.R.: Extreme learning machines for solar photovoltaic power predictions. Energies **11**(10), 2725 (2018)
7. Das, U.K., Tey, K.S., Seyedmahmoudian, M., Mekhilef, S., Idris, M.Y.I., Van Deventer, W., Stojcevski, A.: Forecasting of photovoltaic power generation and model optimization: a review. Renew. Sustain. Energy Rev. **81**, 912–928 (2018)
8. Izgi, E., Öztopal, A., Yerli, B., Kaymak, M.K., Şahin, A.D.: Short–mid-term solar power prediction by using artificial neural networks. Sol. Energy **86**(2), 725–733 (2012)
9. Al-Dahidi, S., Ayadi, O., Alrbai, M., Adeeb, J.: Ensemble approach of optimized artificial neural networks for solar photovoltaic power prediction. IEEE Access **7**, 81741–81758 (2019)
10. Maduabuchi, C.: Thermo-mechanical optimization of thermoelectric generators using deep learning artificial intelligence algorithms fed with verified finite element simulation data. Appl. Energy **315**, 118943 (2022)
11. Pan, S., Duraisamy, K.: Long-time predictive modeling of nonlinear dynamical systems using neural networks. Complexity **2018**, 1–26 (2018)
12. Thike, P.H., Zhao, Z., Shi, P., Jin, Y.: Significance of artificial neural network analytical models in materials' performance prediction. Bull. Mater. Sci. **43**, 1–22 (2020)
13. Kalogirou, S.A., Mathioulakis, E., Belessiotis, V.: Artificial neural networks for the performance prediction of large solar systems. Renew. Energy **63**, 90–97 (2014)
14. Gaboitaolelwe, J., Zungeru, A.M., Yahya, A., Lebekwe, C.K., Vinod, D.N., Salau, A.O.: Machine learning based solar photovoltaic power forecasting: a review and comparison. IEEE Access (2023)

15. Maduabuchi, C., Nsude, C., Eneh, C., Eke, E., Okoli, K., Okpara, E., Harsito, C.: Renewable energy potential estimation using climatic-weather-forecasting machine learning algorithms. Energies **16**(4), 1603 (2023)

16. Alghamdi, H., Maduabuchi, C., Albaker, A., Alatawi, I., Alsenani, T.R., Alsafran, A.S., Alkhedher, M.: A prediction model for the performance of solar photovoltaic-thermoelectric systems utilizing various semiconductors via optimal surrogate machine learning methods. Eng. Sci. Technol. Int. J. **40**, 101363 (2023)

17. Charniak, E.: Introduction to deep learning. The MIT Press (2021)

18. Goodfellow, I., Bengio, Y., Courville, A.: Deep learning. MIT press (2016)

19. Huang, J., Koopialipoor, M., Armaghani, D.J.: A combination of fuzzy Delphi method and hybrid ANN-based systems to forecast ground vibration resulting from blasting. Sci. Rep. **10**(1), 19397 (2020)

20. Khandelwal, I., Adhikari, R., Verma, G.: Time series forecasting using hybrid ARIMA and ANN models based on DWT decomposition. Proc. Comp. Sci. **48**, 173–179 (2015)

21. Heng, S.Y., Ridwan, W.M., Kumar, P., Ahmed, A.N., Fai, C.M., Birima, A.H., El-Shafie, A.: Artificial neural network model with different backpropagation algorithms and meteorological data for solar radiation prediction. Sci. Rep. **12**(1), 10457 (2022)

22. Vennila, C., Titus, A., Sudha, T.S., Sreenivasulu, U., Reddy, N.P.R., Jamal, K., Belay, A.: Forecasting solar energy production using machine learning. Int. J. Photoenergy **2022**, 1–7 (2022)

23. Anupong, W., Jweeg, M.J., Alani, S., Al-Kharsan, I.H., Alviz-Meza, A., Cárdenas-Escrocia, Y.: Comparison of wavelet artificial neural network, wavelet support vector machine, and adaptive neuro-fuzzy inference system methods in estimating total solar radiation in Iraq. Energies **16**(2), 985 (2023)

24. Bakırcı, K.: Prediction of diffuse radiation in solar energy applications: Turkey case study and compare with satellite data. Energy **237**, 121527 (2021)

25. Koca, A., Oztop, H.F., Varol, Y., Koca, G.O.: Estimation of solar radiation using artificial neural networks with different input parameters for Mediterranean region of Anatolia in Turkey. Expert Syst. Appl. **38**(7), 8756–8762 (2011)

26. Şenkal, O., Kuleli, T.: Estimation of solar radiation over Turkey using artificial neural network and satellite data. Appl. Energy **86**(7–8), 1222–1228 (2009)

27. Sözen, A., Arcaklioğlu, E., Özalp, M.: Estimation of solar potential in Turkey by artificial neural networks using meteorological and geographical data. Energy Convers. Manage. **45**(18–19), 3033–3052 (2004)

28. Ertekin, C., Yaldiz, O.: Comparison of some existing models for estimating global solar radiation for Antalya (Turkey). Energy Convers. Manage. **41**(4), 311–330 (2020)

29. Şener, U., Kılıç, B.İ., Tokgözlü, A., Aslan, Z.: Prediction of wind speed by using machine learning. In: Gervasi, O., et al. (eds.) Computational Science and Its Applications—ICCSA 2023 Workshops. ICCSA 2023. Lecture Notes in Computer Science, vol. 14104. Springer, Cham (2023). https://doi.org/10.1007/978-3-031-37105-9_6

30. Kim, S., Choi, C.Y., Shahandashti, M., Ryu, K.R.: Improving accuracy in predicting city-level construction cost indices by combining linear ARIMA and nonlinear ANNs. J. Manag. Eng. **38**(2), 04021093 (2022)

31. Radhakrishnan, A., Belkin, M., Uhler, C.: Wide and deep neural networks achieve optimality for classification. arXiv preprint arXiv:2204.14126 (2022)

32. Fazzi, A., Chiuso, A.: Data-driven prediction and control for NARX systems. arXiv preprint arXiv:2304.02930 (2023)

33. Di Nunno, F., Granata, F., Gargano, R., De Marinis, G.: Nonlinear autoregressive exogenous (NARX) neural network models for storm tide forecasting in the Venice Lagoon. Environ. Sci. Proc. **21**(1), 93 (2023)

34. Song, Z., Sun, F., Zhang, R., Du, Y., Li, C.: Prediction of road network traffic state using the NARX neural network. J. Adv. Transp. **2021**, 1–17 (2021)

35. Hochreiter, S., Schmidhuber, J.: Long short-term memory. Neural Comput. **9**(8), 1735–1780 (1997)

36. Syed, S.H., Muralidharan, V.: Feature extraction using discrete wavelet transform for fault classification of planetary gearbox–A comparative study. Appl. Acoust. **188**, 108572 (2022)
37. Freire, P.K.D.M.M., Santos, C.A.G., da Silva, G.B.L.: Analysis of the use of discrete wavelet transforms coupled with ANN for short-term streamflow forecasting. Appl. Soft Comput. **80**, 494–505 (2019)
38. Adli, K.A., Sener, U.: Forecasting of the US Steel Prices with LVAR and VEC Models. Bus. Econ. Res. J. **12**(3), 509–522 (2021)
39. Terregrossa, S.J., Şener, U.: Employing a generalized reduced gradient algorithm method to form combinations of steel price forecasts generated separately by ARIMA-TF and ANN models. Cogent Econ. Finance **11**(1), 2169997 (2023)
40. Box, G.E.P., Jenkins, G.M., Reinsel, G.C., Ljung, G.G.: Time series analysis: forecasting and control. Hobokens (2016)

Total Electron Content and Wavelet Transformation Analysis: Understanding the Role of Modelling

Selcuk Doven and **Zafer Aslan**

Abstract Solar winds, geomagnetic storms cause significant disturbances in the upper layers of the upper atmosphere. These disturbances have adverse effects on radio waves and satellite communications. It plays an important role on the total electron emission by the great storm. The effects of solar winds can be observed even after geomagnetic activity has ceased. It takes a long time to affect the components of the ionosphere. In electron density measurement, when negative ionospheric storms are observed, the storm causes oxygen/Nitrogen depletion, triggering atmospheric disturbances. In this study, the effect of TEC (Total Electron Content) change in the ionosphere on the city of Ankara in Turkey was tried to be determined. It is concerned with the analysis and modeling of the temporal variation of the daily TEC in the ionosphere for the study region. Typically, TEC data is examined to observe and interpret the daily changes in data through graphical representation. However, in this study, it is not just about observation and interpretation; a predictive study is conducted on the data using the Wavelet analysis method and machine learning algorithms. Additionally, in the literature review conducted, no such study was found for the city of Ankara in the year 2017. In this regard, this study holds the distinction of being the first of its kind with the dataset specific to Ankara. The temporal variation of TEC data for the period January 1–December 31, 2017, has been examined and modeled. 60% of the one-year daily data was used for training, 20% for evaluation and 20% for testing. In the first part of the study, firstly, predictions were made with machine learning algorithms. In the second part of the study, wavelet transforms and large, medium and small-scale changes in TEC and precipitation data were examined. TEC data are modeled with support vector machine called

---

Selcuk Doven and Zafer Aslan are contributed equally to this work.

S. Doven (✉)
Institute of Graduate Study, Istanbul Aydin University, Istanbul, Türkiye
e-mail: selcukdoven@stu.aydin.edu.tr

Z. Aslan
Faculty of Engineering, Department of Computer Engineering, Istanbul Aydin University, Istanbul, Türkiye
e-mail: zaferaslan@aydin.edu.tr

linear regression, decision trees and machine learning based prediction methods. As a result, it has been determined that different algorithms show different success rates in the same geographical region. It has been determined that the structure of the datasets has a significant effect on the success rate of the algorithms. RMSE shows better modeling (0.02 rmse rate) for Linear Support Vector Machine (LSVM) modeling.

1 Introduction

In the present era, the utilization of data mining and machine learning spans across diverse domains, encompassing healthcare, telecommunications, education, and security. Among these domains lies the realm of TEC. The conducted studies aimed at estimating TEC play a crucial role in ensuring the seamless operation of our daily routines, particularly in satellite-based communications.

TEC is important in the following areas:

Satellite Communication: Satellite-based communication systems transmit signals through the ionosphere, (Fig. 1). TEC provides a crucial indicator of how these signals are affected in communication channels. TEC estimations can be used to prevent communication disruptions and improve the performance of satellite communication systems [1].

Satellite Navigation: Satellite-based navigation systems perform important functions such as local positioning and time synchronization. TEC indicates the impact of the ionosphere on the journey of satellite signals, (Fig. 2). Therefore, TEC estimations are used to enhance the accuracy of satellite navigation systems [2].

Space Weather: Space weather events, caused by factors like solar activity, affect the electron density in the ionosphere. TEC is an essential parameter used to monitor and forecast such events. For instance, space weather events like solar storms and magnetic storms can impact satellite systems. TEC estimations are crucial to predict the effects of such events and manage satellite operations [3].

Rainfall Forecasting: TEC can be used as an indicator of atmospheric conditions and plays a role in rainfall prediction. TEC data is incorporated into rainfall prediction models to obtain more accurate and reliable forecasts. This is important in various areas such as water resource management, agricultural planning, and flood prevention [4].

These reasons contribute to the increasing importance of TEC. Accurately estimating and analyzing the TEC parameter is crucial to enhance the performance of
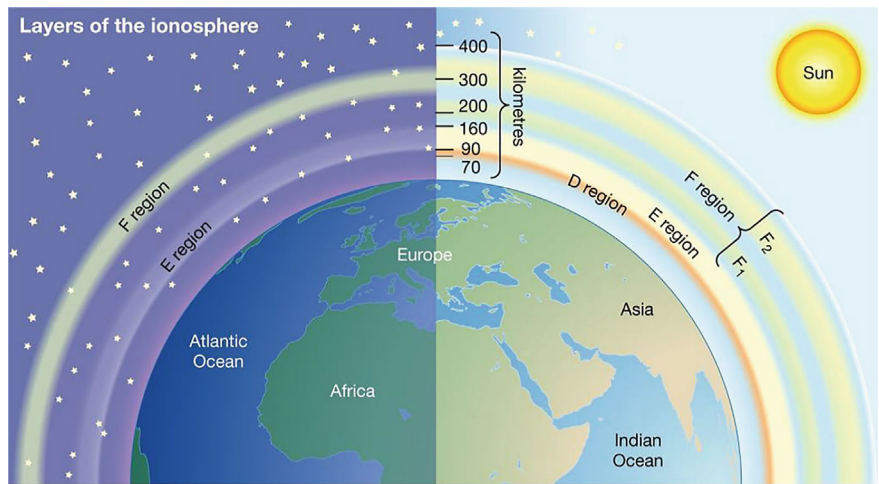
Fig. 1 Layers of the ionosphere
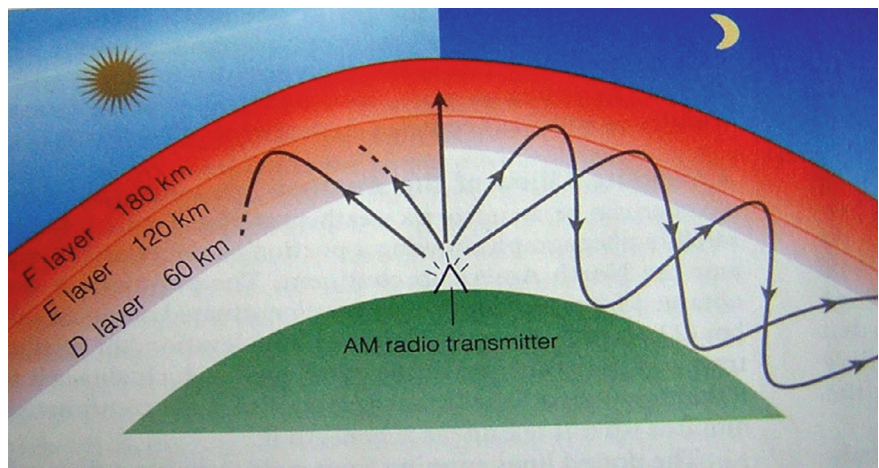
Fig. 2 Radio channels

satellite-based systems, monitor space weather events, and obtain accurate rainfall predictions.

This work differs from other studies on processing satellite and radio signals in several aspects. First of all, in this study, the changes in the ionosphere of TEC data were not made by interpreting daily data only on a graph, as is usually done in TEC studies. For this study, predictions were made with machine learning algorithms. Then, in order to increase this prediction success, the data was processed with the Wavelet signal processing method in the MATLAB program and the success rate

was increased. Hybrid method was used. As far as we researched in the literature, no other study was found for the city of Ankara in 2017. Therefore, an important area was chosen as the study area.

Other studies are listed below:

Ansari et al. in their study, accurate modeling of ionospheric total electron content (TEC) using singular spectrum analysis (SSA) was conducted on GPS-derived TEC data from the Nepal region during the low solar activity year of 2017. The diurnal plots revealed the semi-annual variability of TEC, with higher magnitudes during equinoctial seasons and lower values during solstice seasons. The analysis, including principal component analysis (PCA) and correlation coefficients, demonstrated that SSA can be a successful tool for forecasting TEC series in the region, with comparisons to empirical global ionospheric maps (GIMs) and IRI-Plas 2017 models supporting its suitability for more precise TEC forecasting [5].

Kiruthiga et al.'s study was to predict TEC and range error using low-latitude GPS data during solar flare events that occurred between January and April 2022. Various prediction models were developed and implemented to estimate TEC and range error during the specified time period. These models utilized low-latitude GPS data, which is particularly relevant for regions near the equator. The results of the study indicated that the developed prediction models were effective in estimating TEC and range error during solar flare events. This suggests that the models can be utilized to improve the accuracy of GPS-based positioning systems, particularly in low-latitude regions [6].

Sharma et al.'s study was to utilize GPS-derived TEC data collected from various stations in the Saudi Arabian region and analyzed the variations in TEC in relation to solar indices such as F10.7 and sunspot number. They investigated how these solar indices influenced the ionospheric TEC over the region. The results of the study indicated a strong correlation between TEC variability and solar indices. It was observed that higher values of solar indices were associated with increased TEC values, suggesting a direct influence of solar activity on ionospheric TEC [7].

Tang et al.'s study was to compare three methods, namely ARIMA, LSTM, and Seq2Seq, for predicting storm-time ionospheric TEC. Using TEC data collected during storm events, the models were trained and tested. The results revealed that both LSTM models outperformed the ARIMA model in accurately forecasting storm-time ionospheric TEC. This suggests that LSTM model can be an effective tool for predicting ionospheric behavior during storm events [8].

Shi et al.'s study was to investigate on ionospheric TEC prediction maps over China using the Bidirectional Long Short-Term Memory (BiLSTM) method. The study aimed to develop accurate TEC prediction models for China's ionosphere. The researchers collected TEC data from multiple GPS stations across China and trained the BiLSTM model to predict TEC values. The model utilized a bidirectional approach to capture both past and future dependencies in the TEC time series. The results of the study demonstrated that the BiLSTM method achieved high accuracy in predicting TEC values over China [9].

Liu et al.'s study was to investigate the mapping of Arctic TEC using integrated observations from Low Earth Orbit (LEO)-based GNSS-R and ground-based GNSS systems. The study aimed to assess the feasibility of utilizing these integrated observations for TEC mapping in the Arctic region. The researchers simulated the GNSS-R observations from LEO satellites and combined them with ground-based GNSS data to generate TEC maps over the Arctic area. The integrated observations were used to capture the spatial and temporal variations of TEC in the region. The results of the study demonstrated the effectiveness of the integrated approach in mapping Arctic TEC. The generated TEC maps showed a high correlation with the true TEC values, indicating the potential of using integrated LEO-based GNSS-R and ground-based GNSS observations for accurate TEC mapping in challenging Arctic conditions [10].

Younas et al.'s study aimed to investigate the ionospheric and magnetic signatures of a space weather event that occurred from 25 to 29 August 2018, which involved a Coronal Mass Ejection (CME) and High-Speed Solar Wind Streams (HSSWs). The researchers aimed to analyze the impact of these space weather events on the ionosphere and the associated magnetic disturbances. The study utilized various observational data, including ionospheric parameters obtained from ionosondes and Global Navigation Satellite System (GNSS) receivers, as well as magnetometer measurements. The data were analyzed to examine the changes in ionospheric parameters and magnetic field variations during the space weather event. The results of the study revealed significant disturbances in the ionosphere and magnetic field during the period of the CME and HSSWs. The ionospheric parameters exhibited variations, such as increased TEC and electron density irregularities. The magnetic field measurements indicated disturbances, including sudden commencement and geomagnetic storms [11].

Forootan et al. in their study, the aim was to improve the accuracy of TEC estimation by combining observed data with existing models. By assimilating the TEC data into the models, the researchers were able to refine and update the models based on real-time measurements. The results showed that the assimilation approach improved the agreement between the merged TEC estimates and independent observations, demonstrating its effectiveness in enhancing the accuracy and reliability of TEC modeling and prediction [12].

2 Data and Study Area

2.1 Dataset

This study was carried out to cover the capital city of Ankara of Turkey. The dataset contains 365 rows of daily TEC records in 2017. The dataset consists of 2 columns of daily TEC data, historical data transformed with the Wavelet technique.

Data obtained from the following link.

https://impc.dlr.de/helper-pages/search-results?tx_kesearch_pi1%5Bsword%5D=TEC+%2C+data+archive.

TEC data is taken from Germany's open source IMPC DLR (Ionosphere Monitoring and Prediction Center) site. These values are TEC values taken daily for 1 year from 01.01.2017 to 31.12.2017.

2.2 Study Area

Figure 3 shows the terrestrial and geographic and local specifications of the study area, Ankara.

The latitude and longitude information is as follows (Table 1).

3 Models and Algorithms

3.1 TEC—Total Number of Electrons

TEC refers to the quantity of free electrons per unit area within a range of up to 1000 km above the Earth's surface. Several factors influence the total number of electrons, including geographical location, seasonal variations, local time differences, magnetic activities, and changes in extreme ultraviolet radiation [13].

Fig. 3 Shows the study area, Ankara on the Map

Table 1 Geographic description of study area	No	Study area	Latitude	Longitude
	1	Ankara	39.925533° N	32.866287° E

The variation in the total number of electrons follows a specific pattern throughout the day, with the lowest values observed at midnight and the highest values at noon. Furthermore, there is a gradual increase in the total number of electrons from north to south [13].

TEC is the total number of electrons present along any path between the ground stations and GPS, with units of electrons per square meter, where 1016 electrons m^{-2} = 1 TEC unit (TECU). According to Adewale et al. (2012), the VTEC is derived from slant TEC (STEC) by using the following equation [14].

$$VTEC = [STEC - (bR + bS)]/S (E) \tag{1}$$

3.2 Methods of Completing the Missing Data

The Ankara TEC dataset is structured with two columns, where the first column represents the day information, and the second column displays the total electron count obtained from ionosphere observations. It is crucial to properly handle missing data, such as NaN (Not a Number) or unknown values, within databases.

In MATLAB, the "fillmissing" function is commonly utilized to address missing data. There are six frequently used methods in MATLAB for filling missing entries [15]:

1. "fillmissing (A, 'previous')": This method fills the missing entries with the previous entry value.
2. "fillmissing (A, movemethod, window)": It employs a moving window, typically with average or median calculations, to fill the missing entries based on neighboring values within a specified window length.
3. "fillmissing (A, fillfun, gapwindow)": This method fills the gaps of missing entries using a custom function, specified by "fillfun," and a fixed window surrounding each gap. The padding values are calculated within this window, utilizing the available sample data and missing data locations.

These methods offer flexibility in handling missing data in MATLAB, allowing for effective data completion and analysis. Table 2 shows the empty and filled versions of missing data as an example.

3.3 Machine Learning

Machine learning is a field of study that focuses on developing algorithms and models that enable computers to learn from data and make predictions or decisions without being explicitly programmed. It involves training a model on a given dataset, allowing the model to identify patterns and relationships within the data. The trained model can then be used to make predictions or classify new, unseen data [16]

Table 2 Missing data from the file

No	Tec	No	Tec
123	5,31	123	5,31
124	5,74	124	5,74
125	5,37	125	5,37
126	6,18	126	6,18
127		127	6,18
128		128	6,18
129		129	6,18
130	8,18	130	8,18
131	4,42	131	4,42
132	5,03	132	5,03
133	5,48	133	5,48
134	4,83	134	4,83
135	5,61	135	5,61
136	7,03	136	7,03

Machine learning encompasses a wide range of fields and applications, including but not limited to:

1. Pattern Recognition: Machine learning techniques are extensively used in pattern recognition tasks, such as image and speech recognition, handwriting recognition, and object detection [17].
2. Natural Language Processing: Machine learning plays a crucial role in natural language processing tasks, including language translation, sentiment analysis, text generation, and information retrieval [17, 18].
3. Data Mining: Machine learning algorithms are utilized for data mining tasks, where patterns, trends, and insights are extracted from large datasets, enabling organizations to make informed decisions and predictions [17].
4. Robotics and Control Systems: Machine learning is employed in robotics and control systems to enable robots and autonomous agents to learn from their environment, adapt to changing conditions, and make intelligent decisions [17].
5. Bioinformatics and Healthcare: Machine learning techniques are used in bioinformatics to analyze biological data, predict protein structures, and classify genes. In healthcare, machine learning is applied for disease diagnosis, drug discovery, and personalized medicine [17].
6. Financial Analysis: Machine learning algorithms are employed in financial markets for tasks such as stock market prediction, algorithmic trading, credit scoring, and fraud detection [17].
7. Recommender systems: machine learning is used in recommender systems to provide personalized recommendations for products, movies, music, and other items based on user preferences and behavior [17].

"Machine Learning: A Probabilistic Perspective" by Kevin P. Murphy explores the advantages of machine learning. Here's a concise summary [18]:

1. Pattern Extraction: Machine learning algorithms excel at identifying patterns and extracting insights from complex datasets.
2. Predictive Modeling: Machine learning enables accurate predictions and forecasts based on historical data and patterns.
3. Automation and Efficiency: Machine learning automates tasks, processes large amounts of data quickly, and streamlines operations.
4. Personalization: Machine learning allows for personalized experiences, tailored recommendations, and customized products or services.
5. Adaptability: Machine learning models continuously learn from new data, adapting and improving over time.
6. Complex Problem Solving: Machine learning tackles complex problems by processing vast amounts of data and making accurate decisions or predictions.

These are the key advantages of machine learning discussed in Kevin P. Murphy's book. It provides a comprehensive understanding of machine learning techniques and their applications.

3.4   Linear Regression Algorithm

Linear regression is a statistical method used to model the relationship between a dependent variable and one or more independent variables. It assumes a linear relationship between the variables and aims to find the best-fitting line that represents this relationship. The model is defined by an equation of the form $y = mx + b$, where y is the dependent variable, x is the independent variable, m is the slope, and b is the intercept [19].

The main objective of linear regression is to minimize the difference between the observed values and the predicted values by adjusting the values of the slope and intercept. This is typically done using the method of least squares, which finds the line that minimizes the sum of the squared residuals [19].

Linear regression has a wide range of applications in various fields, including economics, social sciences, and engineering. It is commonly used for predicting outcomes based on historical data, identifying the impact of independent variables on the dependent variable, and assessing the strength and direction of relationships [19].

Evaluation of a linear regression model involves assessing the goodness of fit and the predictive performance. Common evaluation metrics include the coefficient of determination (R-squared), which measures the proportion of the variance explained by the model, and error metrics such as root mean squared error (RMSE) and mean absolute error (MAE), which quantify the accuracy of the predictions. [19].

3.5   Support Vector Machine Algorithm (SVM)

SVM is a machine learning algorithm used for classification and regression tasks. It offers several advantages, such as its ability to handle high-dimensional data and its effectiveness in dealing with non-linear relationships through the use of kernel functions [20].

One of the main advantages of SVM is its ability to find a globally optimal solution by maximizing the margin between different classes. This leads to better generalization and robustness of the model. SVM can also handle datasets with a small number of samples, making it suitable for applications with limited data availability [20].

However, SVM has certain drawbacks as well. It can be computationally expensive, especially when dealing with large datasets. Additionally, selecting the appropriate kernel function and tuning the hyperparameters of the model can be challenging and require expert knowledge. SVM may also struggle with datasets that have overlapping classes or noisy data [20].

In conclusion, the study highlights the advantages of SVM, such as its ability to handle high-dimensional data and non-linear relationships. However, it also points out the drawbacks, including the computational complexity and the need for careful selection of hyperparameters. Understanding these advantages and drawbacks can guide researchers and practitioners in effectively utilizing SVM for their specific applications [20].

3.6   Decision Tree Algorithm

The Decision Tree algorithm is a machine learning method that utilizes the features in the dataset to construct a tree-like structure with decision nodes and branches, where each decision node contains a decision rule on a specific feature and can produce different outcomes, allowing for classification or regression by dividing the dataset into segments and leveraging the patterns within them, making it a popular choice for creating interpretable data analysis and prediction models [21].

3.7   Wavelet Method

Wavelet analysis is a mathematical technique used in time-series analysis to analyze and decompose signals into different frequency components. It involves the use of wavelet functions, which are small wave-like functions with localized properties in both time and frequency domains. Wavelets provide a flexible and adaptive approach to capture transient features and changes in a signal over time. The analysis is performed by convolving the signal with different scales and positions of

the wavelet function, resulting in a time-scale representation called a wavelet transform. This allows for the identification of localized patterns and structures in the signal. Wavelet analysis has found applications in various fields, including signal processing, image compression, denoising, feature extraction, and time-series forecasting. It offers advantages over traditional Fourier analysis by providing better time–frequency localization and the ability to capture both high and low-frequency components simultaneously [22].

The main operations we can do with wavelet are as follows [23].

Signal Processing: Wavelet transformation is used to simultaneously analyze the time and frequency characteristics of signals. In the field of signal processing, wavelets can be used in various applications such as signal compression, noise reduction, and edge detection.

Image Processing: Wavelet transformation is utilized to analyze images at different scales and orientations. In the field of image processing, wavelets find applications in tasks such as image compression, edge detection, noise removal, and feature extraction.

Data Compression: Wavelet-based data compression methods are employed to compress data into a smaller size. Wavelet compression methods are commonly used for storing and transmitting large datasets, particularly in the domains of images and audio. Figure 4 shows the hybrid model architecture given below.
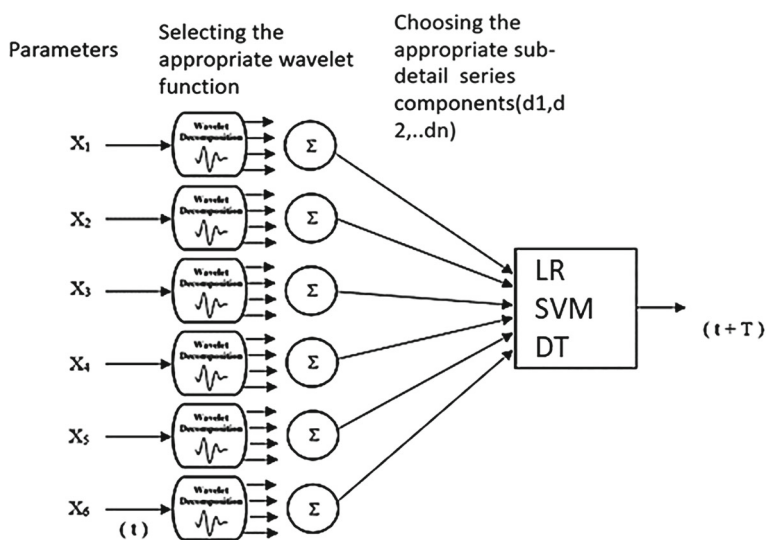

Fig. 4 Hybrid modelling

3.8 Wavelet Tool and Machine Learning Tool

In this study, a package program was used to use Wavelet features. The R2019b version of the Matlab program, which offers extensive features for the Wavelet, was used [24].

Python version 3.0 was also used in this study for machine learning algorithms. The codes were developed by coding without any package program [25].

4 Results

In this section, you can observe the results of the application for the city of Ankara. For this study area, an application was made with artificial neural networks, support vector machines, and decision tree-based estimation, which are machine learning algorithms. The r^2, mse and rmse values of each application are listed. Then, the rain data was transformed with Wavelet as d1, d2, d3. With this transformed wavelet data, machine learning algorithms work as a hybrid model to increase the success ratio. The operating architecture illustrated in Fig. 5 provides a visual representation of this example.

Figure 5 shows daily variation of TEC data in Ankara Higher waves have been received in February, April, June, July, October, November and December.

Figure 6 shows 1D wavelet analyses of TEC (daily total electron concentration) in Ankara in 2017. s, a3, d3, d2 and d1 show original signal, approximation and details (at large, meso and small scales). Winter and at the begininng of spring and autumn, TEC values show some increasing trend. In the middle term of summer, the role of large scale factors decreases, but the impact of local and meso scale events
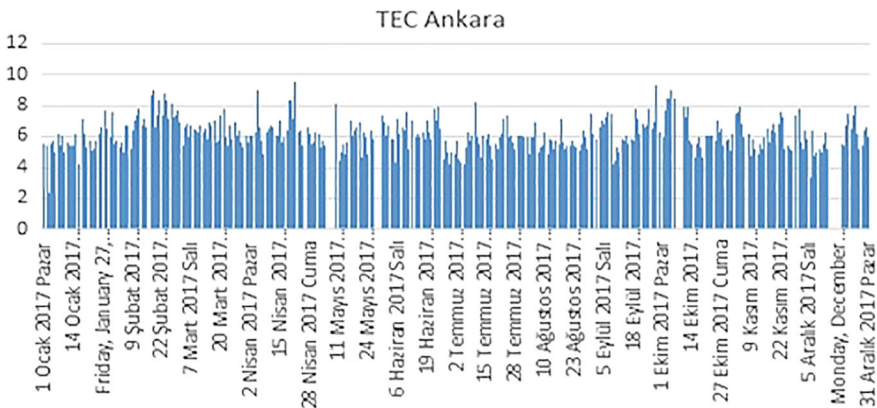

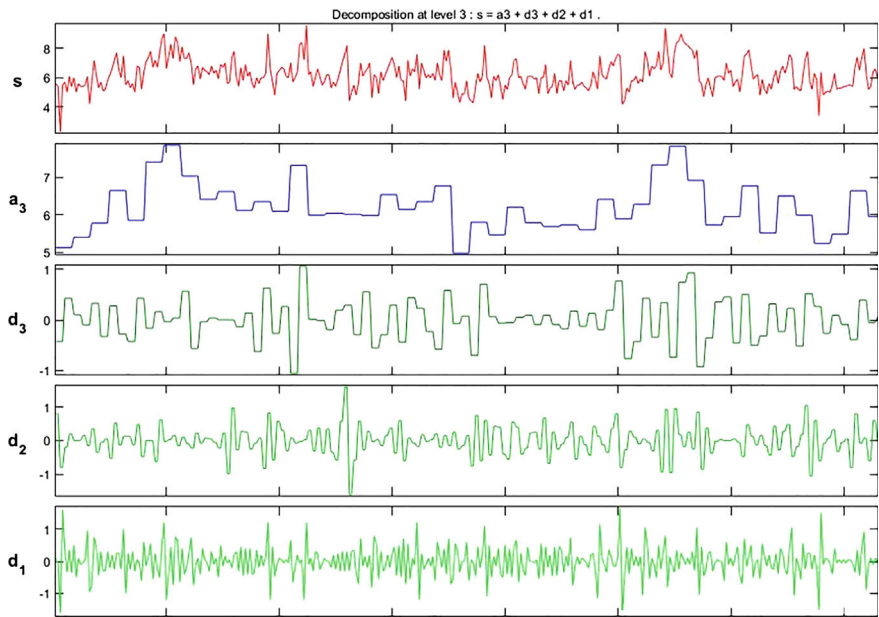**Fig. 5** Daily variation of TEC Data, 2017, Ankara

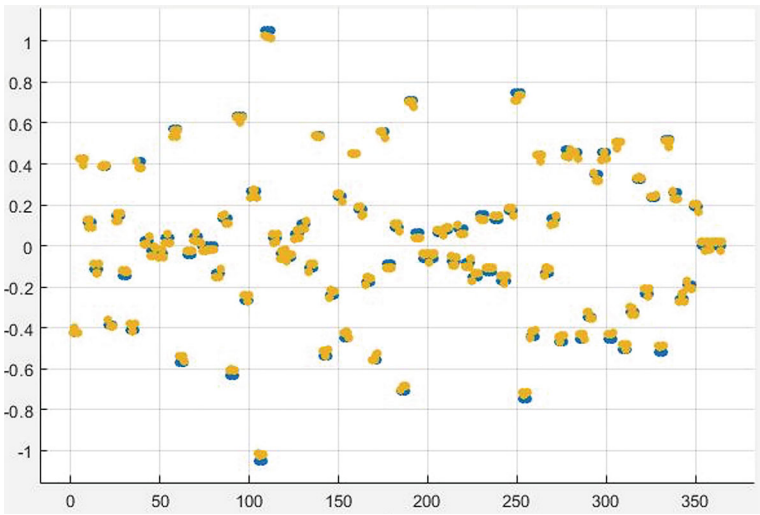**Fig. 6** 1D wavelet, TEC Data, Ankara (Level 3)

Fig. 7 Best result with wavelet D3 decision tree

increases. During whole period, d1, d2 and d3 all scale factors and their impact on daily variation of TEC are important. Figure 7 shows the best result with wavelet d3 decision tree algoritm.

Table 3 Comparison of hybrid model results for Ankara

Machine learning algorithm	Linear regression	Decision tree	Support vector machine
r2	1.00	0.98	1.00
mse	9.209	0.015	0.000
rmse	3.030	0.012	0.023
Machine learning algorithm D1	Linear regression	Decision tree	Support vector machine
r2	0.25	−0.08	−0.01
mse	0.857	0.289	0.271
rmse	0.734	0.537	0.520
Machine learning algorithm D2	Linear regression	Decision tree	Support vector machine
r2	0.00	−0.06	−0.06
mse	0.172	0.182	0.174
rmse	0.414	0.427	0.418
Machine learning algorithm D3	Linear regression	Decision tree	Support vector machine
r2	1.00	0.99	1.00
mse	8.567	0.001	0.000
rmse	2.927	0.039	0.021

Table 3 shows comparison of model results for estimating daily variation of TEC. Result of the Support Vector Machine shows better and much reliable results with rmse = 0.021.

5 Conclusions

This study was carried out for several purposes. First of all, it was desired to determine whether there is a relationship between TEC-historical data. It is aimed to predict if there is a relationship and to increase the accuracy by using the prediction rate as a mixture of Wavelet and machine learning algorithms. Finally, it has been tried to determine whether there is a certain difference on the success rates of the algorithms for the same region.

As a result of the study, it was determined that there is a linear relationship between the TEC data and the dates. This situation was determined by wavelet analysis.

In the application part, it was determined that the prediction accuracy rate increased significantly in Ankara by using the Hybrid method with machine learning algorithms and then the Wavelet signal analysis method. But this has not happened to the same extent for every algorithm.

As a result, it was observed that the linear regression algorithm did not show relation at all layers for this research. Decision tree and support vector machine algorithms were found to produce results close to each other in all layers. It was seen that both Decision tree and support vector machine algorithms produced the highest

rmse success with D3 layer. It has been seen that the support vector machine algorithm at the D3 level has higher correlation and works with the least error prediction rate with 0.021 rmse ratio.

When we examined the outputs of the application study, it was revealed that the algorithms did not show the same performance even though they worked with the same datasets for the same problem. With this result, it has been observed that different problems work with different accuracy rates by different algorithms and the success ratios of different algorithms significantly vary in the same problem.

By considering the results of this paper, further studies can be done to increase the reliability of the results. First of all, performance situations can be observed by working with different machine learning algorithms for this study area. With the same method, this study is carried out for other cities, and the prediction success ratio and the performance of the algorithms are evaluated. As another study, the 2017 dataset obtained from this study can be expanded and a larger dataset can be analyzed by using long-term results. Finally, with the expansion of the dataset, the performance conditions can be compared by working with deep learning algorithms, which is an approach covered by the field of machine learning.

References

1. Tariku, Y.A.: Patterns of GPS-TEC variation over low-latitude regions (African sector) during the deep solar minimum (2008 to 2009) and solar maximum (2012 to 2013) phases. Earth Planets Space **67**, 1–9 (2015)
2. Kunitsyn, V.E., Padokhin, A.M., Kurbatov, G.A., Yasyukevich, Y.V., Morozov, Y.V.: Ionospheric TEC estimation with the signals of various geostationary navigational satellites. GPS Solut. **20**, 877–884 (2016)
3. Alcay, S., Gungor, M.: Investigation of ionospheric TEC anomalies caused by space weather conditions. Astrophys. Space Sci. **365**, 1–15 (2020)
4. Bhardwaj, S., Chandrasekhar, E., Padiyar, P., Gadre, V.M.: A comparative study of wavelet-based ANN and classical techniques for geophysical time-series forecasting. Comput. Geosci. **138**, 104461 (2020)
5. Ansari, K., Panda, S.K., Jamjareegulgarn, P.: Singular spectrum analysis of GPS derived ionospheric TEC variations over Nepal during the low solar activity period. Acta Astronaut. **169**, 216–223 (2020)
6. Kiruthiga, S., Mythili, S., Vijay, M., Mukesh, R.: Prediction of TEC and range error using low-latitude GPS data during January to April 2022 solar flare events. Geomag. Aeron. **63**(1), 17–29 (2023)
7. Sharma, S.K., Singh, A.K., Panda, S.K., Ansari, K.: GPS derived ionospheric TEC variability with different solar indices over Saudi Arab region. Acta Astronaut. **174**, 320–333 (2020)
8. Tang, R., Zeng, F., Chen, Z., Wang, J.S., Huang, C.M., Wu, Z.: The comparison of predicting storm-time ionospheric TEC by three methods: ARIMA, LSTM, and Seq2Seq. Atmosphere **11**(4), 316 (2020)

9. Shi, S., Zhang, K., Wu, S., Shi, J., Hu, A., Wu, H., Li, Y.: An investigation of ionospheric TEC prediction maps over china using bidirectional long short-term memory method. Space Weather **20**(6), e2022SW003103 (2022)
10. Liu, L., Morton, Y.J., Wang, Y., Wu, K.B.: Arctic TEC mapping using integrated LEO-based GNSS-R and ground-based GNSS observations: a simulation study. IEEE Trans. Geosci. Remote Sens. **60**, 1–10 (2021)
11. Younas, W., Amory-Mazaudier, C., Khan, M., Fleury, R.: Ionospheric and magnetic signatures of a space weather event on 25–29 August 2018: CME and HSSWs. J. Geophys. Res. Space Phys. **125**(8), e2020JA027981 (2020)
12. Forootan, E., Kosary, M., Farzaneh, S., Schumacher, M.: Empirical data assimilation for merging total electron content data with empirical and physical models. Surv. Geophys. 1–31 (2023)
13. Şentürk, E.: Küresel İyonosfer Haritalarının Türkiye'deki Performansının GNSS Verileriyle İstatistiksel Olarak İncelenmesi. Dokuz Eylül Üniversitesi Mühendislik Fakültesi Fen ve Mühendislik Dergisi **23**(67), 247–255 (2021)
14. Bolzan, M.J.A., Tardelli, A., Pillat, V.G., Fagundes, P.R., Rosa, R.R.: Multifractal analysis of vertical total electron content (VTEC) at equatorial region and low latitude, during low solar activity. In: Annales Geophysicae, vol. 31, No. 1, pp. 127–133. Copernicus Publications, Göttingen, Germany (2013)
15. Janert, P.K.: Data analysis with open source tools: a hands-on guide for programmers and data scientists. O'Reilly Media, Inc. (2010)
16. Metlek, S., Kayaalp, K.: Makine Öğrenmesinde, Teoriden Örnek MATLAB Uygulamalarına Kadar Destek Vektör Makineleri. İksad Yayınevi (2020)
17. Flach, P.A.: On the state of the art in machine learning: a personal review. Artif. Intell. **131**(1–2), 199–222 (2001)
18. Murphy, K.P.: Machine learning: a probabilistic perspective. MIT press (2012)
19. Johnson, R., Zhang, J.: Linear regression: a comprehensive overview of theory, applications, and evaluation metrics. J. Appl. Stat. **45**(6), 1089–1108 (2020)
20. Karamizadeh, S., Abdullah, S.M., Halimi, M., Shayan, J., Javad Rajabi, M.: Advantage and drawback of support vector machine functionality. In: 2014 International Conference on Computer, Communications, and Control Technology (I4CT), pp. 63–65. IEEE (I2014)
21. Pissanetzky, S.: On the future of information: reunification, computability, adaptation, cybersecurity, semantics. IEEE Access **4**, 1117–1140 (2016)
22. Nason, G.P., Sachs, R.V.: Wavelets in time-series analysis. Philos. Trans. R. Soc. Lond. Ser. A Math. Phys. Eng. Sci. **357**(1760), 2511–2526 (1999)
23. Furati, K.M., Siddiqi, A.H. (eds.): Mathematical models and methods for real world systems. CRC Press (2005)
24. https://www.mathworks.com/support/requirements/previous-releases.html
25. https://devguide.python.org/versions/. Last accessed 10 Sep 2024

Friction Dominated Flow in Gas-Networks: Modeling, Simulation, Optimal Control, and Domain Decompositions

Günter Leugering

Abstract We consider modeling, optimization, and domain decomposition method for friction dominated flow of gas in a pipe network. The equations of motions are taken to be represented by a friction dominated model derived from the fully nonlinear isothermal Euler gas equations. This involves doubly nonlinear p-parabolic problems on a metric graph with $p = \frac{3}{2}$. We provide example of non-overlapping domain decomposition in the spirit of P.L. Lions.

Keywords Optimal control · Gas networks · p-Laplace problem on a graph · Optimality system · Domain decomposition

AMS subject classifications. 35J70 · 49J20 · 49J45 · 93C73 · 65M55 · 65N55

1 Introduction

Engineering of flow problems in pipe networks or open canal systems have attracted a lot of attention recently. Such problems appear in the context of fresh water supply networks, drainage and sewer systems, as well as in gas transportation networks. In most applications, such infrastructures are highly complex and include several thousand links, i.e., pipes or canals. Moreover, beyond the demand for accurate prediction and simulation, optimal control of such systems is the common desire. The corresponding numerical realization easily reaches the practicability on current computer systems. Moreover, real time constraints require quick responses. All this naturally leads to the desire for parallel domain decomposition methods (DDMs) for the simulation and control in this context. DDMs are, of course, well established. There are numerous textbooks available-cf. Quarteroni and Valli [40]

G. Leugering (✉)
Friedrich-Alexander-Universität Erlangen-Nürnberg (FAU), Lehrstuhl Angewandte Mathematik II, Erlangen, Germany
e-mail: guenter.leugering@fau.de

for an early contribution, Dolean et al. [10] for a more recent textbook—and the biannual proceedings of the http://www.DDM.org conferences can be seen as a regular update of the state of the art. The genuine motivation for parallel domain decomposition methods in space and time is the challenge of very large scale problems involving partial differential equations on complex domains being central in modern applications. Such methods for optimal control problems, and in particular the corresponding analysis in function spaces, are even less developed, but still, the scope would go far beyond the format of this article, see [23] for a reference, where the particular focus has been on problems on 2-d networked domains and 1-d metric graphs. The material available in the literature becomes even further confined when looking for methods covering nonlinear systems. See the recent survey article by this author [29] for an overview. We also refer to [28], where the two-link transmission problem has been discussed and a forthcoming publication [27] which will contain the *mathematical analysis* of p-type problems on metric graphs. Due to space limitations, it is not possible and with respect to the survey character also of these notes not reasonable to include the material here. For spatial domain decomposition of parabolic (i.e., $p = 2$) optimal control problems, we refer to [18, 22, 37] and the references therein. As for time-domain decomposition, we refer to [12–14, 17, 23, 34, 46]. See further [10] (and the recent update https:// hal.archives-ouvertes.fr/cel-01100932v6)). The plan of these notes is as follows. First of all, as an exemplary problem, the model of friction-dominated flow in pipes is derived from the classical Euler system in Sect. 1.1 followed by an account on the relevant literature. In Sect. 1.2, the concept of metric graphs together with—by now—standard notation is introduced. Even though maybe a bit cumbersome at the first reading it is necessary for the understanding and the appreciation of this class of problems. Section 2 provides the problem formulation (Sect. 2.1) for optimal control problems on metric graphs and in Sect. 2.2, a discretization with respect to the time is introduced. In the context of metric graphs, this results in optimal control problems for systems of ordinary differential equations of p-type on metric graphs. A further reduction is introduced in Sect. 2.3, where the rolling horizon method is applied in order to reduce the problem to a sequence of static p-type optimal control problems on the graph. Beginning with Sect. 4, domain decomposition algorithms are discussed, first at the level of the differential equations and then in Sect. 5 on optimal control problems. The article closes with conclusions and further developments in Sect. 6.

Before proceeding further, a comment on the material presented is in order. The algorithms are presented at a continuous level and are, hence, more conceptual than numerical recipes. As far as p-type problems are concerned, the only convergence proof is available in the literature for the P.L. Lions method extended to two-link problems in the context of mere simulation and optimal control [28]. This, however, will be extended to general graphs in [27]. The proofs are lengthy and rather technical and, hence, are not suitable to be given here. Nevertheless, as the survey is based at the continuous level, the known mathematical results are provided. Here, we prove for the first time a Gauß -Seidel type analogue for star-graphs using the Steklov-Poincaré map.

1.1   Modeling of Gas Flow in a Single Pipe

The Euler equations are given by a system of nonlinear hyperbolic partial differential equations (PDEs) which represent the motion of a compressible non-viscous fluid or a gas. They consist of the continuity equation, the balance of moments and the energy equation. The full set of equations is given by [7, 31, 32, 45]. Let ρ denote the density, v the velocity of the gas and p the pressure. We further denote g the gravitational constant, λ the friction coefficient of the pipe, D the diameter, a the area of the cross section. The state variables of the system are ρ and the flux $q = a\rho v$. We also denote c the the speed of sound, i.e., $c^2 = \frac{\partial p}{\partial \rho}$ (for constant entropy). For natural gas we have $c = 340 \frac{m}{sec}$. In particular, in the subsonic case ($|v| < c$), the one which we consider in the sequel, two boundary conditions have to be imposed one on the left end and one at the right end of the pipe. We consider here the isothermal case only. Thus, for horizontal pipes

$$a\frac{\partial \rho}{\partial t} + \frac{\partial}{\partial x}q = 0$$
$$\frac{\partial}{\partial t}q + \frac{\partial}{\partial x}(ap + a\rho v^2) = -\frac{\lambda}{2D}v\,|q|\,. \tag{1}$$

We may introduce a scaling parameter ϵ and the scaled time and velocity $t = \frac{\tau}{\epsilon}$, (we keep the notation t) $w = \frac{v}{\epsilon}$ and the friction $\gamma = \frac{\lambda}{2D}$. We also introduce the scaled enthalpy $h^\epsilon = \frac{\epsilon^2}{2}w^2 + P'(\rho)$ with a given potential function P. Then the scaled Euler equations become

$$a\frac{\partial \rho}{\partial t} + \frac{\partial}{\partial x}(q) = 0$$
$$\epsilon^2\frac{\partial}{\partial t}q + \frac{\partial}{\partial x}(ap + a\rho\epsilon^2 v^2) = -\gamma v\,|q|\,. \tag{2}$$

In the particular case, where we have a constant speed of sound $c = \sqrt{\frac{p}{\rho}}$ and letting $\epsilon \to 0$, we arrive at

$$a\frac{\partial p}{\partial t} + \frac{\partial}{\partial x}q = 0$$
$$\frac{\partial p^2}{\partial x} = -\gamma q\,|q|\,. \tag{3}$$

See [38] for details. We now set $y := p^2$ and obtain

$$q = -\frac{1}{\gamma}\frac{\frac{\partial y}{\partial x}}{\sqrt{\left|\frac{\partial y}{\partial x}\right|}}.$$

With $\alpha := \frac{\gamma a}{c}$ we obtain

$$\alpha \frac{\partial}{\partial t} \frac{y}{\sqrt{|y|}} - \frac{\partial}{\partial x} \frac{\frac{\partial y}{\partial x}}{\sqrt{\left|\frac{\partial y}{\partial x}\right|}} = 0. \tag{4}$$

We introduce the monotone function $\beta(s) := \frac{s}{\sqrt{|s|}}$. With this, (4) reads as

$$\alpha \frac{\partial}{\partial t} \beta(y) - \frac{\partial}{\partial x} \beta(\frac{\partial y}{\partial x}) = 0. \tag{5}$$

It is also possible to write this down in the p-Laplace format: (4) reads as

$$\alpha \frac{\partial}{\partial t} \left(|y|^{p-2} y \right) - \frac{\partial}{\partial x} \left(|\frac{\partial y}{\partial x}|^{p-2} \frac{\partial y}{\partial x} \right) = 0, \tag{6}$$

where $p = \frac{3}{2}$. Equation (6) has come to be known as doubly nonlinear parabolic equation of p-Laplace type. See, e.g., [41] for an early contribution also in higher dimensions, [42], for a general exposition and [6] for a recent treatment. Notice that $p < 2$ and that the system is, therefore, singular for $\frac{\partial}{\partial x} y(x) = 0$. For $p > 2$ such equations exhibit instead degeneration. Equations similar to (5) have been considered in the literature, see, e.g., [3, 4]. In this contribution, we aim at a discussion of such equations together with optimal control problems on networks. A more recent study of doubly nonlinear parabolic equations in the context of friction dominated flow has been provided in [1]. Equations of the type (5) are known to exhibit positive solutions and satisfy a maximum principle. As a matter of fact, to the best knowledge of the author, there are no studies on optimal control of such systems on general graphs available from the literature besides [30]. We note that the doubly nonlinear parabolic problem associated with the friction-dominated flow on a network has been considered in the thesis [38, 44]. Optimal control problems for the p-Laplace operator have been studied since the 1980s, see, e.g., [8]. Moreover, in [47] an optimal control problem for the p-Laplace equation $p \geq 2$ has been recently considered. See also [9] for a problem of optimal control in the coefficient for the p-Laplace equation, again for $p \geq 2$. We note that non-overlapping domain decompositions for p-type problems have not been considered in the literature so far with the exception of [11], where, for $p \geq 2$, a similar problem without control has been considered, however, with a different updating rule that is more related to a Gauß-Seidel-type iteration based on a Peaceman-Rachford scheme and, hence, is not completely parallel.

1.2   Network Modeling

Let $G = (V, E)$ denote the graph of the gas network with vertices (nodes) $V = \{n_1, n_2, \ldots, n_{|V|}\} = \{n_j | j \in \mathcal{J}\}$ and edges $E = \{e_1, e_2, \ldots, e_{|E|}\} = \{e_i | i \in \mathcal{I}\}$. At

a given node n_j, $j \in \mathcal{J}$, we associate to incident each edge a direction.

$$d_{ij} = \begin{cases} -1, & \text{if the the edge } e_i \text{ starts at node } n_j, \\ +1, & \text{if the edges } e_i \text{ end at node } n_j, \\ 0, & \text{else.} \end{cases}$$

For the isothermal Euler system, it is assumed that the enthalpy h_i^ϵ is continous across the multiple joints. Thus, $h_i^\epsilon(n_j)$ coincide for all $i \in \mathcal{I}_j := \{i \in 1, \ldots E | d_{ij} \neq 0\}$. Therefore, the natural nodal conditions at multiple joints, the so-called Kichhoff condition, reads $\sum_{i \in \mathcal{I}_j} d_{ij} h_i^\epsilon(n_j, t)) = 0$. This expresses the physical requirement of the balance of the internal energy. We introduce the edge degree $d_j := |\mathcal{I}_j|$. Then, the scaled Euler-system on the graph is governed by

$$
\begin{aligned}
a_i \frac{\partial \rho_i}{\partial t} + \frac{\partial}{\partial x} q_i &= 0, & i \in \mathcal{I}, \ x \in (0, \ell_i), \ t \in (0, T) \\
\epsilon^2 \frac{\partial}{\partial t} q_i + \frac{\partial}{\partial x}(a_i p_i + \epsilon^2 a_i \rho_i w_i^2) &= -\frac{\lambda_i^\epsilon}{2 D_i} w_i |q_i|, & i \in \mathcal{I}, \ x \in (0, \ell_i), \ t \in (0, T) \\
h^\epsilon(n_j, t) &= h^\epsilon(n_j, t), & \forall i, k \in \mathcal{I}_j, \ j \in \mathcal{J}^M, \ t \in (0, T) \\
\sum_{i \in \mathcal{I}_j} d_{ij} h^\epsilon(n_j, t)) &= 0, & j \in \mathcal{J}^M, \ t \in (0, T) \\
h^\epsilon(n_j, t) &= g_i(t), & i \in \mathcal{I}_j, \ j \in \mathcal{J}_D^S, \ t \in (0, T) \\
\rho_i(x, 0) = \rho_{i,0}(x), \ q_i(x, 0) &= q_{i0}(x), & x \in (0, \ell_i).
\end{aligned}
\tag{7}
$$

In the asymptotic limit, we observe the continuity conditions of the density (hence the pressure and, consequently y) read as follows:

$$y_i(n_j, t) = y_k(n_j, t), \ \forall i, k \in \mathcal{I}_j, \ d_j > 1, \tag{8}$$

while the nodal balance equation for the fluxes can be written as

$$\sum_{i \in \mathcal{I}_j} d_{ij} \beta(\partial_x y_i(n_j, t)) = 0, \ d_j > 1. \tag{9}$$

We use the d_j in order to decompose the index set for nodes $\mathcal{J}$ into $\mathcal{J} = \mathcal{J}^M \cup \mathcal{J}^S$, where $\mathcal{J}^M = \{j \in \mathcal{J} | d_j > 1\}$ represents the multiple nodes and $\mathcal{J}^S = \{j \in \mathcal{J} | d_j = 1\}$ the simple nodes. According to Dirichlet or Neumann boundary conditions a the simple nodes, we further decompose $\mathcal{J}^S = \mathcal{J}_D^S \cup \mathcal{J}_N^S$. We summarize the equations as follows:

$$\alpha_i \partial_t \beta(y_i(x,t)) - \partial_x \left(\beta(\partial_x y_i(x,t))\right) = u_i, \qquad i \in \mathcal{I}, \ x \in (0,\ell_i), \ t \in (0,T)$$

$$y_i(n_j,t) = y_k(n_j,t), \qquad\qquad\qquad \forall i,k \in \mathcal{I}_j, \ j \in \mathcal{J}^M, \ t \in (0,T)$$

$$\sum_{i \in \mathcal{I}_j} d_{ij} \beta(\partial_x y_i(n_j,t)) = 0, \qquad\qquad j \in \mathcal{J}^M, \ t \in (0,T)$$

$$y_i(n_j,t) = g_i(t), \qquad\qquad\qquad i \in \mathcal{I}_j, \ j \in \mathcal{J}^S_D, \ t \in (0,T)$$

$$d_{ij} \beta(\partial_x y_i(n_j,t)) = u_j(t), \qquad\qquad i \in \mathcal{I}_j, \ j \in \mathcal{J}^S_N, \ t \in (0,T)$$

$$p_i(x,0) = p_{i,0}(x), \ q_i(x,0) = q_{i0}(x), \qquad\qquad x \in (0,\ell_i),$$

$$\tag{10}$$

where the functions $u_i, g_i \, i \in \mathcal{I}, u_j, \, j \in \mathcal{I}_j, \, j \in \mathcal{J}^S$ serve as distributed and boundary controls, respectively. Notice that we have added inhomogeneities at the limiting on purpose.

In order to illustrate the complexity of the networks involved, we take examples from the Gaslib library https://gaslib.zib.de/. This website includes data sets for subnetworks of the German gas network that are actually used by the engineers in the German gas operations OGE https://oge.net/en. These two examples are already very complex, the first one containing 4197 pipes, including compressors, valves, and release element, while the second contains 582 such elements. The second set of figures extracts a simple model network consisting of 11 pipes, only. Nevertheless, this exemplary network is complex enough to serve as a benchmark for the purpose of mathematical research done in the DFG-funded consortium TRR154 https://www.trr154.fau.de/trr-154-en/ where continuous and integer optimization and control is investigated since 2014 in more than 20 projects. On the left, we display the network itself, while on the right, we also indicate the classification of pipes as transmission, compressor, valve- and release-type. In this article, we do not dwell on these control problems and the corresponding modeling issues. For the sake of simplicity and transparency, we use an even simpler network (with 6 nodes and 7 edges) for our experiments (Figs. 1 and 2).
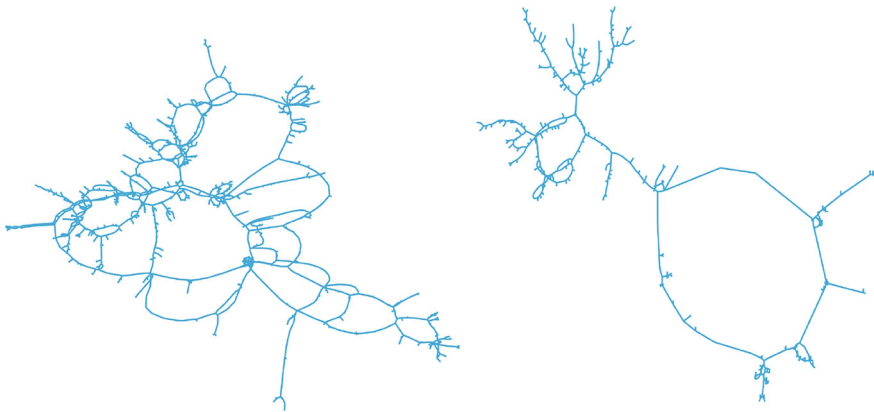

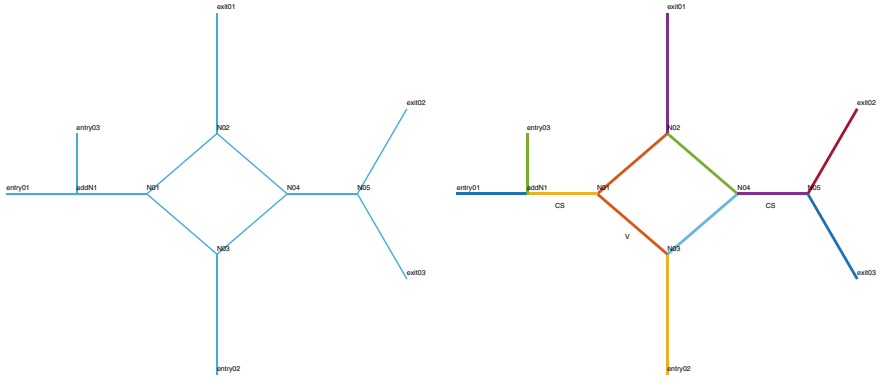**Fig. 1** Left figure: gaslib4197, right figure: gaslib 582

Fig. 2 Gaslib11: Left figure: plain network, right figure: with classified edges

Example 1 We apply the boundary conditions for the density at vertex v_1 the boundary function $h_1(t) = .2sin(2\pi \frac{t}{T})^2 + 1$ and at v_4 the input $h_4(t) = .3sin(2\pi \frac{t}{T})^3 + 1$ while the other vertices v_7, v_{10}, v_{11} are kept at the value 1. No boundary conditions are applied to the flux. This leads to an initial configuration where all densities are equal to 1, while the mass flow is uniformly zero. We set $\gamma = .5$, the diameters $a = 1$ and also the lengths of the pipes equal to 1. We first take $\epsilon = 1$ and then $\epsilon = 0$ for comparison. The numerical experiments are conducted using the codes by N. Philippi developed for her thesis [38], to which, in turn, we refer for further details. In particular, we do not dwell on the numerical realization, as this is not part of these notes. Suffice it to say that the scheme is based on a structure preserving mixed finite element method. The numerical results are shown in Figs. 3, 4, 5 and 6. We display the density ρ first with $\epsilon = 1$ in Fig. 4 and then with the asymptotic value $\epsilon = 0$ in Fig. 5. The evolution of the flux is displayed in Fig. 5 for $\epsilon = 1$ and in 1.6 for $\epsilon = 0$. Notice that the mass flow is not continuous at the joints but rather satisfies the balance law (Kirchhoff condition), while the specific energy is assumed to be continuous there. Therefore, also the density is not continuous across multiple joints for $\epsilon = 1$ but is for $\epsilon = 0$. We also remark that the mass flow can be computed from the density in case $\epsilon = 0$, as in this case the system of equations for ρ (in fact y) is decoupled.
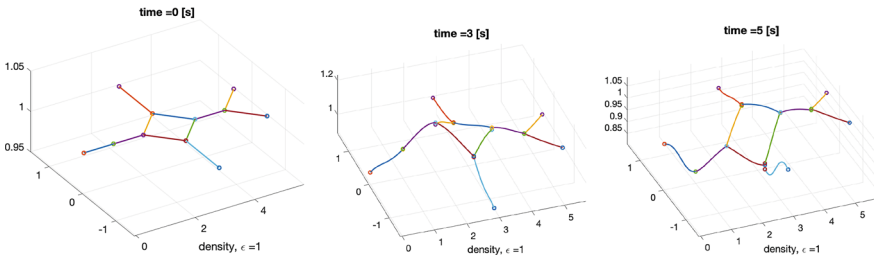

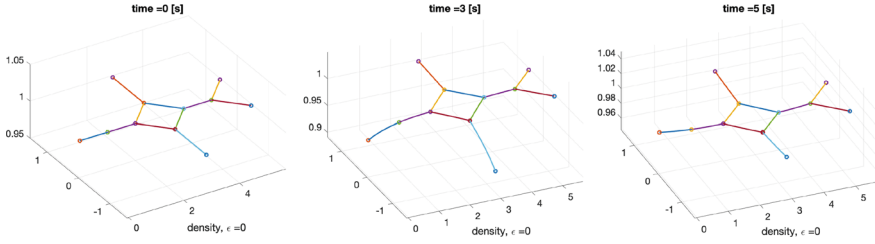**Fig. 3** Gaslib11: $\epsilon = 1$ density

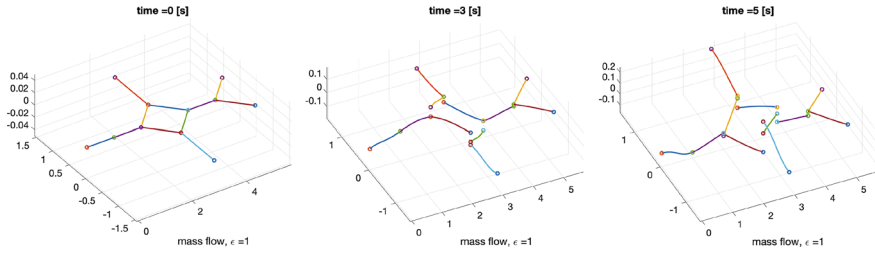**Fig. 4** Gaslib11: $\epsilon = 0$ density

Fig. 5 Gaslib11: $\epsilon = 1$ mass flow
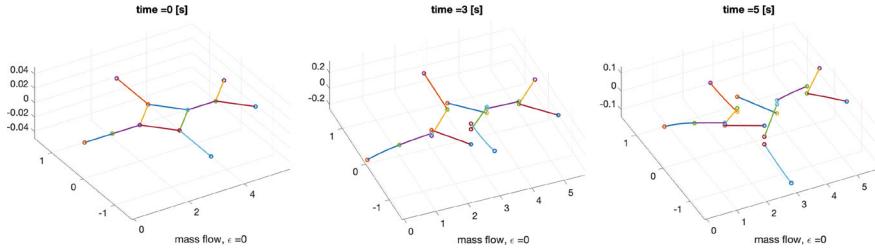
Fig. 6 Gaslib11: $\epsilon = 0$ mass flow

2 Optimal Control Problems

2.1 Problem Formulation

We are now in the position to formulate optimal control problems at the level of the networks. We first describe the general format for an optimal control problem. This involves a cost function that assigns to each admissible pair (y, u) a 'cost' $I(y, u)$, which is represented on each individual edge by a contribution on the state and the controls. The cost is chosen to include a running cost and a final cost on the state only. The typical example, the one that we will use in what follows, is given by the tracking cost

$$I_y(y) := \sum_{i \in \mathcal{I}} \int_0^T \int_0^{\ell_i} \frac{\kappa_i}{2} |y_i(x,t) - y_i^d(x,t)|^2 dx dt, \quad I_T(y(x,T)) := \sum_{i \in \mathcal{I}} \int_0^{\ell_i} \frac{\kappa_{i,T}}{2} |y_i(x,T) - y_{i,T}|^2 dx$$

$$(11)$$

for the state, while the norms of the controls are penalized as follows:

$$I_u(u) := \sum_{i \in \mathcal{I}} \frac{v_{i,d}}{2} \int_0^T \int_0^{\ell_i} |u_i(x,t)|^2 dx dt + \sum_{j \in \mathcal{J}_N^S} \frac{v_{i,b}}{2} \int_0^T |u_j(t)|^2 dt, \quad (12)$$

where $\kappa_i, \kappa_{i,T} \geq 0$, $v_{i,d}, v_{i,b} \geq 0$ serve as penalty parameters. We pose the following optimal control problem for (10)

$$\min_{(y,u)} I(y,u) := I_y(y) + I_T(y(\cdot, T)) + I_u(u)$$

$$s.t. \quad (13)$$

$$(y,u) \text{ satisfies } (1.10).$$

Remark 2.1 1. We notice that the parameters κ_i for the running cost and $\kappa_{i,T}$ for the cost of the final value as well as $v_{i,d}$, $v_{i,b}$ for the distributed and boundary controls, respectively, can be chosen individually on each edge or at the controlled Neumann nodes.
 2. Typically, problem (13) is complemented by box-constraints on the control and state variables, which we ignore here for the sake of simplicity. We remark, however, that box-constraints for the controls can be handled in a standard way using variational inequalities, even in the context of the domain decomposition techniques to be discussed below. See, e.g., [26].

Problem (13) is a prototypical example of optimal control problems for systems of fully nonlinear parabolic equations on metric graphs. The corresponding optimality system for (10) and (13) reads

$$\alpha_i \partial_t \beta(y_i(x,t)) - \partial_x \left(\beta(\partial_x y_i(x,t)) \right) = \frac{1}{v_{i,d}} p_i(x,t),$$

$$\alpha_i \beta'(y_i(x,t)) \partial_t p_i(x,t) + \partial_x \left(\beta'(\partial_x y_i(x,t)) \partial_x p_i(x,t) \right) = \kappa_i(y_i - y_i^d), \qquad i \in \mathcal{I}, \ x \in (0, \ell_i), \ t \in (0,T),$$

$$y_i(n_j,t) = y_k(n_j,t), \ p_i(n_j,t) = p_k(n_j,t), \qquad \forall i,k \in \mathcal{I}_j, \ j \in \mathcal{J}^M, \ t \in (0,T),$$

$$\sum_{i \in \mathcal{I}_j} d_{ij} \beta(\partial_x y_i(n_j,t)) = 0, \ \sum_{i \in \mathcal{I}_j} d_{ij} \beta'(\partial_x y_i(n_j,t)) \partial_x p_i(n_j,t) = 0, \qquad j \in \mathcal{J}^M, \ t \in (0,T),$$

$$y_i(n_j,t) = 0, \ p_i(n_j,t) = 0, \qquad i \in \mathcal{I}_j, j \in \mathcal{J}_D^S, \ t \in (0,T),$$

$$d_{ij} \beta(\partial_x y_i(n_j,t)) = \frac{1}{v_{i,b}} p_j(n_j,t), \ d_{ij} \beta'(\partial_x y_i(n_j,t)) \partial_x p_i(n_j,t) = 0, \qquad i \in \mathcal{I}_j, j \in \mathcal{J}_N^S, t \in (0,T),$$

$$y_i(x,0) = y_{i,0}(x), \ p_i(x,T) = -\kappa_{i,T}(y_i(x,T) - y_{iT}^d(x)), \qquad x \in (0, \ell_i),$$

$$(14)$$

where we used the common notation p for the adjoint state which, in this case, does not cause any conflicting notation.

As in these notes, the emphasis is more on the algorithms, we do not dwell on the mathematical analysis at the fully continuous level in space and time with respect to DDMs and instead resort to time- and finally space discretization, while keeping the first-optimize-then-discretize concept in mind.

2.2 Time Discretization

In order to demonstrate to which kind of system the original optimal control problem is transformed under discretization, we consider a time discretization such that $[0, T]$ is decomposed into break points $t_0 = 0 < t_1 < \cdots < t_N = T$ with widths $\Delta t_n := t_{n+1} - t_n, n = 0, \ldots, N - 1$ (we use $N + 1$ as the number of break points which is not related to N as indicating Neumann conditions). Accordingly, we denote $y_i(x, t_n) := y_{i,n}(x), n = 0, \ldots, N$ and similarly for the controls. We consider an implicit Euler scheme and a standard quadrature rule for the time integrals represented by weights ω_n. We introduce the semi-discrete cost functions

$$I_y^{\Delta t}(y_i) := \sum_{i \in \mathcal{I}} \sum_{n=1}^{N-1} \omega_n \int_0^{\ell_i} \frac{\kappa_i}{2} |y_{i,n} - y_{i,n}^d|^2 dx, \quad I_N(y_{i,N}) := \sum_{i \in \mathcal{I}} \int_0^{\ell_i} \frac{\kappa_{i,T}}{2} |y_{i,N} - y_{i,N}^d|^2 dx,$$

(15)

$$I_u^{\Delta t}(u) := \sum_{i \in \mathcal{I}} \frac{\nu_{i,d}}{2} \sum_{n=1}^{N-1} \omega_n \int_0^{\ell_i} |u_{i,n}|^2 dx + \sum_{j \in \mathcal{J}_N^S} \omega_i \frac{\nu_{i,b}}{2} \sum_1^N \omega_n |u_{j,n}|^2 \quad (16)$$

such that (13) turns into the following semi-discrete optimal control problem.

$$\min_{(y,u)} I(y, u) := I_y^{\Delta t}(y) + I_T(y(\cdot, N)) + I_u^{\Delta t}(u)$$

s.t.   (17)

$$\frac{1}{\Delta t}\beta(y_{i,n+1})(x) - \partial_x\left(\beta(\partial_x y_{i,n+1}(x))\right) = \frac{1}{\Delta t}\beta(y_{i,n})(x) + u_{i,n+1}(x), \qquad x \in (0, \ell_i),$$

$$y_{i,n+1}(n_j) = y_{k,n+1}(n_j), \qquad\qquad \forall i, k \in \mathcal{I}_j, \ j \in \mathcal{J}^M,$$

$$\sum_{i \in \mathcal{I}_j} d_{ij}\beta(\partial_x y_{i,n+1})(n_j) = 0, \qquad\qquad j \in \mathcal{J}^M,$$

$$\beta(\partial_x y_{i,n+1})(n_j) = u_{j,n+1}, \qquad\qquad d_j = 1, \ i \in \mathcal{I}_j, \ j \in \mathcal{J}_N^S,$$

$$y_{i,n+1}(n_j) = 0, \qquad\qquad i \in \mathcal{I}_j, \ j \in \mathcal{J}_D^S,$$

$$y_{i,0}(x) = y_i^0(x), \qquad\qquad i \in \mathcal{I}, \ x \in (0, \ell_i), \ i \in \mathcal{I},$$

with $n = 1, \ldots, N - 1$. For an equidistant time discretization, we may omit the weights and absorb them into the penalty parameters. Obviously, for the purpose of numerical simulation, we need a spatial discretization, too. We resort to standard
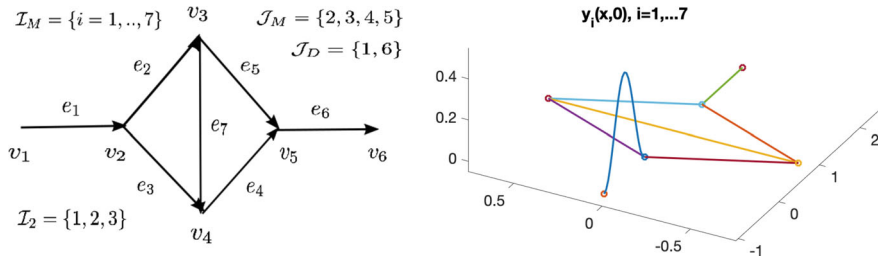
Fig. 7 Control for the diamond graph. Left: underlying network. Right: initial state

finite difference procedures (see, e.g., [3, 41]) and thereby turn the problem into a fully discrete problem. Due to space limitations, we omit the details. In fact, we consequently use professional tools, as the freely available MATLAB codes **bvp4c** for boundary value problems and **pdepe** for parabolic initial boundary value problems, as much as possible in order to underline that this survey is not at the level of numerical analysis, but rather at a conceptual level.

Example 2 We consider the problem (17) on a graph consisting of 7 edges and 6 nodes. See Fig. 7. We assume Dirichlet conditions at nodes n_1, n_7, where we apply a control at n_1 and set $y_7(\ell_7) = 0.5$. At all other vertices we have the appropriate transmission conditions. We introduce non-zero initial conditions along the edge e_2, only, and we would like to steer the solution along the edge e_7 as much as possible to the constant $y_7^d \equiv \frac{1}{2}$ in order to achieve a an almost constant pressure in that pipe. We take the penalty parameters for the running tracking cost $\kappa = 1.e4$ and the control penalty to $v = 1$. In the first experiment, we apply running cost in the second experiment, we use a tracking cost of $y_7(x, T)$ at the final time only. See Fig. 8. Moreover, we again use the standard discretization, already introduced in [3, 41]. We take 20 spatial discretization points for each edge defined on [0, 1]
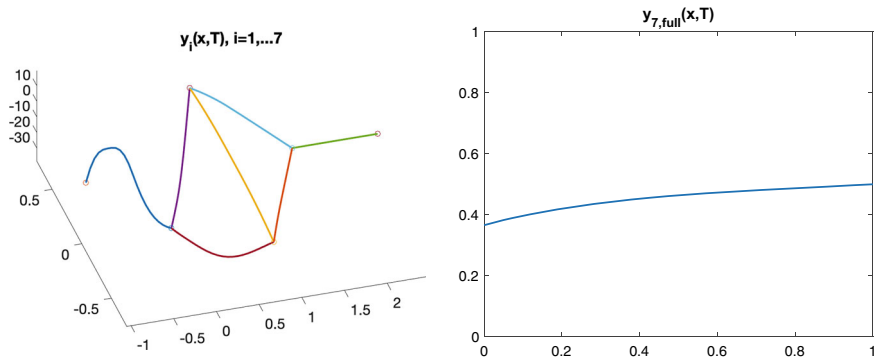

Fig. 8 Control for the diamond graph. Left: running cost control—optimal state. Right: final value control—optimal state
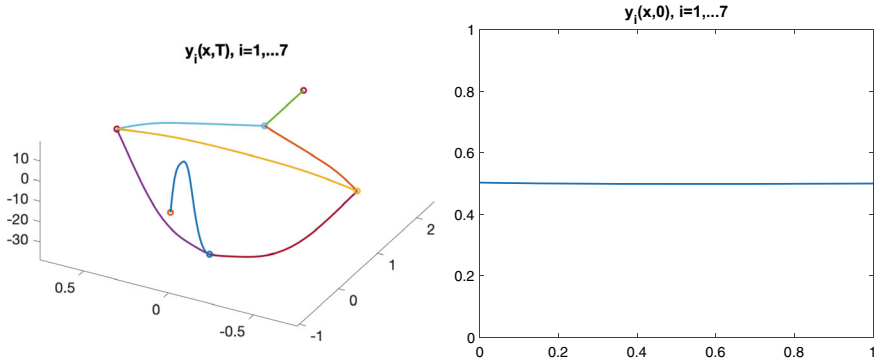
Fig. 9 Control for the diamond graph. Left: comparison of y_4 at final time T along edge 4. Lower curve: final value control; upper curve: full control. Right: controls: (.–) full control, (–) final value control vs. time

and 30 time discretization points for the time interval $[0, 1]$. Moreover, we use a $1e. - 5$ regularization of the p-Laplacian in order to avoid large condition numbers of the Jacobians involved. Again, the optimization is done using casADI with the MUMPS-solver for linear systems. See Fig. 8 (Fig. 9).

2.3 Instantaneous Control

It is clear that (17) involves all time steps in the cost functional. We would like to reduce the complexity of the problem even further. To this aim, we consider the so-called *instantaneous control* regime. This amounts to reducing the sums in the cost function of (17) to the time-level t_{n+1}. This strategy has also come to be known as *rolling horizon* approach, the simplest case of the *moving horizon* paradigm. It is now convenient to discard the actual time level $n + 1$ and redefine the states at the former time as input data. To this end, we replace $\alpha_i := \frac{1}{\Delta t}$, $f_i^1 := \alpha_i \beta(y_{i,n})$ and omit the weights ω_n. Thus, for each $n = 1, \ldots, N - 1$ and given $y_{i,n}$, we consider the cost functions at each time t_n:

$$\tilde{I}_y^{\Delta t}(y_i) := \sum_{i \in \mathcal{I}} \int_0^{\ell_i} \frac{\kappa_i}{2} |y_i - y_{i,n}^d|^2 dx, \tag{18}$$

$$\tilde{I}_u^{\Delta t}(u) := \sum_{i \in \mathcal{I}} \frac{\nu_{i,d}}{2} \int_0^{\ell_i} |u_i|^2 dx + \sum_{j \in \mathcal{J}_N^S} \frac{\nu_{i,b}}{2} |u_j|^2. \tag{19}$$

$$I(y, u) := \tilde{I}_y^{\Delta}(y) + \tilde{I}_u^{\Delta t}(u) =: \sum_{i \in \mathcal{I}} J_i(y_i, u_i). \tag{20}$$

$$\min_{(y,u)} I(y,u)$$

$$s.t.$$

$$\alpha_i \beta(y_i)(x) - \partial_x \left(\beta(\partial_x y_i(x)) \right) = u_i(x) + f_i^1(x), \qquad i \in \mathcal{I}, \ x \in (0, \ell_i),$$

$$y_i(n_j) = y_k(n_j), \qquad\qquad\qquad \forall i, k \in \mathcal{I}_j, \ j \in \mathcal{J}^M, \quad (21)$$

$$\sum_{i \in \mathcal{I}_j} d_{ij} \beta(\partial_x y_i)(n_j) = 0, \qquad\qquad\qquad j \in \mathcal{J}^M,$$

$$\beta(\partial_x y_i)(n_j) = u_j, \qquad\qquad\qquad i \in \mathcal{I}_j, \ j \in \mathcal{J}_N^S,$$

$$y_i(n_j) = 0, \qquad\qquad\qquad i \in \mathcal{I}_j, \ j \in \mathcal{J}_D^S.$$

Wellposedness of (18),(21) has been discussed in [30].

Example 3 We now use the same set-up as in Example 2, but now we perform the instantaneous control strategy. We use the same penalties as in the first experiment of Example 2. See Fig. 10 for the states and the controls, recorded for each time instant. In the second figure, Fig. 11, we display the finals state y_7 at the final time. We also
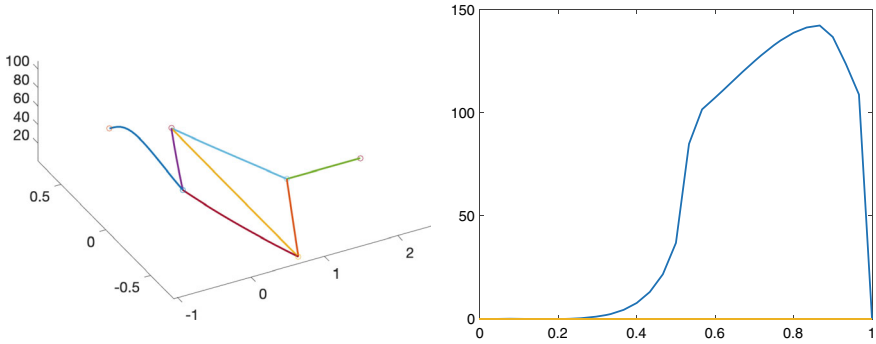

Fig. 10 Instantaneous control for the diamond graph. Left: optimal final states. Right: instantaneous control over discrete time
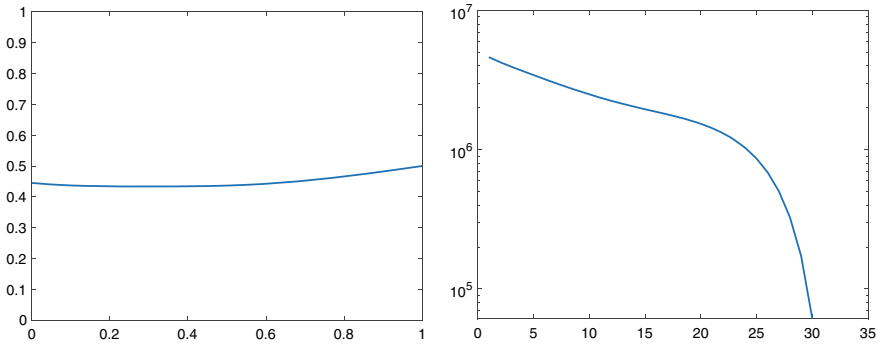

Fig. 11 Instantaneous control for the diamond graph. Left: optimal final states. Upper curve: full control problem of Example 2. Lower curve: instantaneous control Right: history of final value cost

display the history of optimal states y_7 when the instantaneous control regime is used, recorded over the time instants, i.e., the iterates. Figure 11 reveals that instantaneous controls are very effective in the neighborhood of an equilibrium. This property may turn out to be useful in the context of the turnpike phenomenon, see, e.g., [25, 39].

Theorem 2.1 ([30]) *There exists $\bar{p} \in V$ satisfying together with the optimal pair $(\bar{y}, \bar{u})$ the first order optimality condition.*

$$
\begin{aligned}
\alpha_i \beta(\bar{y}_i) - \partial_x \left(\beta(\partial_x \bar{y}_i)\right) = \bar{u}_i, && i \in \mathcal{I}, x \in (0, \ell_i), \\
\alpha_i \beta'(\bar{y}_i)\bar{p}_i - \partial_x \left(\beta'(\partial_x \bar{y}_i)\partial_x \bar{p}_i)\right) = -\kappa_i(\bar{y}_i - y_i^d), && i \in \mathcal{I}, x \in (0, \ell_i), \\
\bar{y}_i(n_j) = \bar{y}_k(n_j), \ \bar{p}_i(n_j) = \bar{p}_k(n_j), && \forall i, k \in \mathcal{I}_j, j \mathcal{J}^M, \\
\sum_{i \in \mathcal{I}_j} d_{ij}\beta(\partial_x \bar{y}_i)(n_j) = 0, && j \in \mathcal{J}^M, \\
\sum_{i \in \mathcal{I}_j} d_{ij}\beta'(\partial_x \bar{y}_i)(n_j)\partial_x \bar{p}_i(n_j) = 0, && j \in \mathcal{J}^M, \\
\beta(\partial_x \bar{y}_i)(n_j) = \bar{u}_j, && i \in \mathcal{I}_j, \ j \in \mathcal{J}_N^S, \\
\beta'(\partial_x \bar{y}_i)(n_j)\partial_x \bar{p}_i(n_j) = 0, && i \in \mathcal{I}_j, \ j \in \mathcal{J}_N^S, \\
\bar{y}_i(n_j) = 0, \ \bar{p}_i(n_j) = 0, && i \in \mathcal{I}_j, \ j \in \mathcal{J}_D^S, \\
\bar{p}_i(n_j) = v_{i,b}u_j, && i \in \mathcal{I}_j, j \in \mathcal{J}_N^S \\
\bar{p}_i = v_{i,d}u_i, && i \in \mathcal{I}, x \in (0, \ell_i).
\end{aligned}
\tag{22}
$$

One way to handle this problem is to use an iterative procedure. To this end, we introduce the common fixed point algorithm

Algorithm 1

1. *Choose u^0.*
2. *For $i = 1$ until satisfied*
3. *(a) solve for y_i*

$$
\begin{cases}
\beta_i(y_i) - \partial_x(\beta_i(\partial_x y_i) = u_i, & i = 1, 2, \ x \in I_i, \\
y_i(n_j) = y_k(n_j), & \forall i, k \in \mathcal{I}_j, j \mathcal{J}^M, \\
\sum_{i \in \mathcal{I}_j} d_{ij}\beta(\partial_x y_i)(n_j) = 0, & j \in \mathcal{J}^M, \\
\beta(\partial_x y_i)(n_j) = u_j, & i \in \mathcal{I}_j, \ j \in \mathcal{J}_N^S, \\
y_i(x_{ij}) = 0, & i \in \mathcal{I}_j, \ j \in \mathcal{J}_D^S.
\end{cases}
\tag{23}
$$

(b) Solve for p_i

$$
\begin{cases}
\beta_i'(y_i)p_i - \partial_x(\beta_i'(\partial_x y_i)\partial_x p_i) = -\kappa_i(y_i - y_i^d), & i = 1,2, \ x \in I_i, \\
p_i(n_j) = p_k(n_j), & \forall i, k \in \mathcal{I}_j, \ j \mathcal{J}^M, \\
\displaystyle\sum_{i\in\mathcal{I}_j} d_{ij}\beta'(\partial_x y_i)(n_j)\partial_x p_i(n_j) = 0, & j \in \mathcal{J}^M, \\
d_{ij}\beta_i'(\partial_x y_i(x_{ij}))\partial_x p_i(x_{ij}) = 0, & i \in \mathcal{I}_j, \ j \in \mathcal{J}_N^S, \\
p_i(n_j) = 0, & i \in \mathcal{I}_j, \ j \in \mathcal{J}_D^S.
\end{cases}
\tag{24}
$$

(c) Set $u_i = \frac{1}{v_{i,d}}p_i, \ i \in \mathcal{I}, u_j = \frac{1}{v_{i,b}}p_i(x_{ij}), \ i \in \mathcal{I}_j, j \in \mathcal{J}_N^S.$

4. *Terminate with the (approximate) fixed point* u, y, p.

Remark 2.2

1. We remark that in the iteration loop an error-based stop criterion has to be defined.
2. This algorithm is classic for linear problems. For the p-Laplace operator, this needs further arguments.
3. We remark that the analogous procedure can be used for the original optimal control problem (13) at the continuous time level.
4. With this algorithm, the DDM can be introduce on the level of the forward and backward problem, independently, on each time step.

3 Spatial Domain Decomposition of p-Laplace Problems on Metric Graphs

To fix ideas, we consider the simpler problem on the network

$$
\begin{aligned}
-\partial_x\left(\beta(\partial_x y_i(x))\right) &= f_i(x)) & i \in \mathcal{I}, \ x \in (0, \ell_i) \\
y_i(n_j) &= y_k(n_j) =: \bar{y}(n_j), & \forall i, k \in \mathcal{I}_j, \ j \in \mathcal{J}^M \\
\sum_{i\in\mathcal{I}_j} d_{ij}\beta(\partial_x y_i)(n_j) &= 0, & j \in \mathcal{J}^M \\
\beta(\partial_x y_i)(n_j) &= g_j, & d_j = 1, \ i \in \mathcal{I}_j, \ j \in \mathcal{J}_N^S \\
y_i(n_j) &= 0, & i \in \mathcal{I}_j, \ j \in \mathcal{J}_D^S.
\end{aligned}
\tag{25}
$$

The crucial point is to decompose the network at multiple joints. In this article, we employ the Steklov-Poncaré map also known as Dirichlet-to-Neumann (DtN) map. To this end, we introduce the domain decomposition method already proposed in [29], see also [11] for a two link problem. We propose the following decomposition method:

$$
-\partial_x\left(\beta_i(\partial_x y_i^{k+1})\right) = f_i, \qquad\qquad \text{in } (0, \ell_i), i \in \mathcal{I},
\tag{26}
$$

$$d_{ij}\beta_i(\partial_x y_i^{k+1})(x_{ij}) + \rho y_i^{k+1}(x_{ij}) = \rho \left(\frac{2}{d_j} \sum_{l \in \mathcal{I}_j} y_l^k(x_{lj}) - y_i^k(x_{ij}) \right)$$

$$- \left(\frac{2}{d_j} \sum_{l \in \mathcal{I}_j} d_{lj}\beta_l(\partial_x y_l^k)(x_{lj}) - d_{ij}\beta_i(\partial_x y_i^k)(x_{ij}) \right), \qquad j \in \mathcal{J}^M, i \in \mathcal{I}_j.$$

For $p = 2$ and two sub-domains, this is the classical Robin-type non-overlapping domain decomposition method introduced by P.L. Lions in [36] which is now extended to the p-Laplace problem and metric graphs. A proof of convergence for the decomposition of serial nodes is provided in [28].

Example 4 We take a tripod with edges starting at $x = 0$ and stretching out to $x = 1$. This configuration is paradigmatic for domain decomposition. We use the MATLAB routine **bvp4c** for the solutions of the corresponding Robin-type problems on the individual edges. We take $\rho = 1$ as Robin parameter. We perform two experiments, one for $p = 2$ and one for $p = 1.5$ in order to compare. See Fig. 12 and Fig. 13, respectively.

Here we follow a different approach. We look at (26) for two sub-domains, the classical P.L. Lions method extended to two p-elliptic problems. That is to say, we have a single multiple node, say at $x = 0$ such that $d = 2$ and $d_{ij} = -1, i, j = 1, 2$. Then (26) reads

$$- \partial_x \left(\beta_i(\partial_x y_i^{k+1}) \right) = f_i, \ x \in (0, 1), i = 1, 2, \tag{27}$$
$$- \beta_i(\partial_x y_i^{k+1})(0) + \rho y_i^{k+1}(0) = \rho y_j^k(0) + \beta_j(\partial_x y_j^k)(0), \ i, j = 1, 2$$
$$y_i(1) = 0, i = 1, 2.$$

If we define the DtN-maps for the two domains,

$$S_1(\bar{y}) := -\partial_x y_1(0, \bar{y}), \ S_2(\tilde{y}) = -\partial_x y_2(0, \tilde{y}), \tag{28}$$
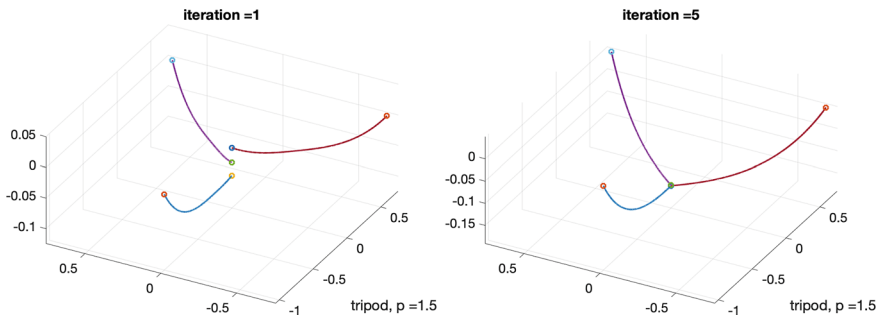

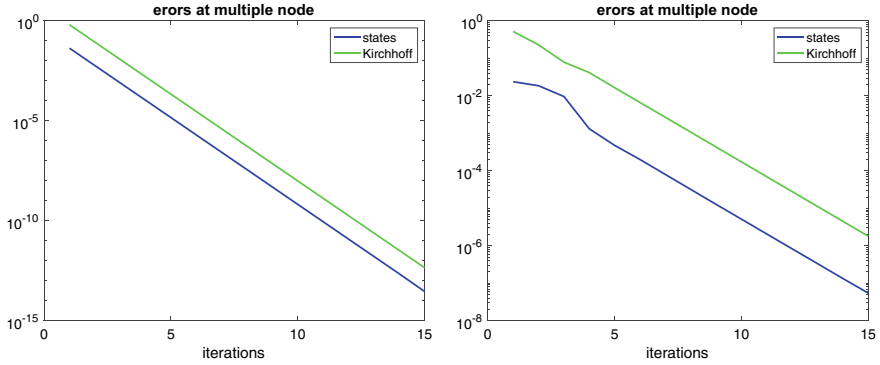**Fig. 12** Example 4. Left: 1. iteration; Right: 5. iteration

Fig. 13 Example 4. Left: errors for $p = 2$; Right: $p = 1.5$

where y_i solve the equation in $(0, 1)$ with Dirichlet boundary condition at $x = 1$ and $y_1(0) = \bar{y}$, $y_2(0) = \tilde{y}$. Then, the P.L. Lions iteration is equivalent to the iteration

$$(\rho I + S_1)\bar{y}^{k+1} = (\rho I - S_2)\tilde{y}^k, \tag{29}$$

$$(\rho I + S_2)\bar{y}^{k+1} = (\rho I - S_1)\tilde{y}^k. \tag{30}$$

We take this as the motivation to construct a domain decomposition method based on DtN-maps. We concentrate on a star graph, as the mathematical challenge is with the decomposition at multiple nodes. In fact, the two-link problem has been solved in [28] To this end, we assume that we have one multiple node n_1 with edge degree $d_1 = m$ which corresponds to $x = 0$ such that all edges meet there starting from $x = 0$ and stretch to $x = \ell_i$. Without loss of generality, we can assume that $\ell_i = 1, i = 1, \ldots, m$. Thus, the Dirichlet problem reduces to

$$
\begin{aligned}
- \partial_x \left(\beta(\partial_x y_i(x)) \right) &= f_i(x) \quad i = 1, \ldots, m, \ x \in (0, 1) \\
y_i(0) &= y_k(0) =: \bar{y}, & \forall i, k = 1, \ldots, m \\
\sum_{i \in \mathcal{I}_j} \beta(\partial_x y_i)(0) &= 0, & j \in \mathcal{J}^M \\
y_i(n_j) &= 0, & i = 1, \ldots, m.
\end{aligned}
\tag{31}
$$

The particular point of view in these notes is the usage of the DtN-map. Moreover, we select an edge, say edge #1 as the first domain and the rest of the star, in fact the edges labeled $2, \ldots, m$ coupled at the multiple node, say at $x = 0$. We start with the DtN-map for the first edge. Given $\bar{y}$, we solve

$$
\begin{aligned}
- \partial_x \left(\beta(\partial_x y_1(x)) \right) &= f_1(x) \ x \in (0, 1) \\
y_1(0) &= \bar{y}, \ y_1(1) = 0
\end{aligned}
\tag{32}
$$

and define

$$S_1(\bar{y}) := -\partial_x y_1(0, \bar{y}). \tag{33}$$

Accordingly, we solve

$$- \partial_x \left(\beta(\partial_x y_i(x)) \right) = f_i(x)), \ i = 2, \ldots, m \ x \in (0, 1) \tag{34}$$
$$y_i(0) = \bar{y}, \ y_i(1) = 0$$

and define

$$S_2(\bar{y}) := - \sum_{i=2}^{m} \partial_x y_i(0, \bar{y}). \tag{35}$$

Obviously, if we sum, the Kirchhoff condition becomes

$$S_1(\bar{y}) + S_2(\bar{y}) = 0. \tag{36}$$

The star graph problem is equivalent to solving the equation (36) for $\bar{y}$. We consider the following novel domain decomposition method, where we cluster the edges with index $i = 2, \ldots, m$. In order to iteratively decouple (38), we choose to independent variables $\bar{y}, \tilde{y}$ such that

$$y_1(0) = \bar{y}, y_i(0) = \tilde{y}, i = 2, \ldots, m. \tag{37}$$

Then the new decomposition reads

$$S_1(\bar{y})^{k+1} + \sigma \bar{y}^{k+1} = \sigma \tilde{y}^k - S_2(\tilde{y})^k$$
$$S_2(\tilde{y})^{k+1} + \sigma \tilde{y}^{k+1} = \sigma \bar{y}^k - S_1(\bar{y})^{k+1}. \tag{38}$$

Clearly, this method is consistent, as if we delete the iteration index k, hence assuming convergence, we arrive at

$$\bar{y} = \tilde{y}, \ S_1(\bar{y}) + S_2(\tilde{y}) = 0. \tag{39}$$

This is not the same as (26), as the latter is designed for the decomposition at a multiple node into each incident edge. We also notice that the scheme (38) is Gauß -Seidel type iteration, as the novel information is used in the second equation. In order to address the convergence of this method, we introduce $\eta_1 := \tilde{y}, \eta_2 = \bar{y}$ and denote by η the trace at $x = 0$ of the global solution. We, thus, consider the iteration

$$S_1(\eta_1)^{k+1} + \sigma \eta_1^{k+1} = \sigma \eta_2^k - S_2(\eta_2)^k$$
$$S_2(\eta_2)^{k+1} + \sigma \eta_2^{k+1} = \sigma \eta_1^k - S_1(\eta_1)^{k+1}. \tag{40}$$

and introduce

$$\mu^k = (\sigma I + \mathcal{S}_2)\eta_2^k, \ \mu = (\sigma I + \mathcal{S}_2)\eta \tag{41}$$
$$\lambda^k = (\sigma I + \mathcal{S}_2)\eta_2^k, \ \lambda = (\sigma I + \mathcal{S}_2)\eta.$$

We obtain

$$\frac{1}{2\sigma}(\mu^k + \lambda^k) = \eta_2^k, \ \frac{1}{2}(\mu^k - \lambda^k) = \mathcal{S}_2\eta_2^k \tag{42}$$
$$\frac{1}{2\sigma}(\mu + \lambda) = \eta, \ \frac{1}{2}(\mu - \lambda) = \mathcal{S}_2\eta = -\mathcal{S}_1\eta,$$

where we notice that the global solution satisfies the Steklov-Poincaré equation. We also infer

$$\mu^{k+1} + \lambda^k = (\sigma I + \mathcal{S}_2)\eta_2^{k+1} + (\sigma I - \mathcal{S}_2)\eta_2^k$$
$$= (\sigma I - \mathcal{S}_1^{k+1}) + (\sigma I + \mathcal{S}_1)\eta_1^{k+1} \tag{43}$$
$$= 2\sigma\eta_1^{k+1}.$$

Hence,

$$\eta_1^{k+1} = \frac{1}{2\sigma}(\mu^{k+1} + \lambda^k); \ \mathcal{S}_1\eta_1^{k+1} = \frac{1}{2}(\lambda^k - \mu^{k+1}). \tag{44}$$

This leads to

$$(\mathcal{S}_2\eta_2^k - \mathcal{S}_2\eta)(\eta_2^k - \eta) = \frac{1}{4\sigma}[(\mu^k - \mu)^2 - (\lambda^k - \lambda)^2] \tag{45}$$
$$(\mathcal{S}_1\eta_1^{k+1} - \mathcal{S}_1\eta)(\eta_1^{k+1} - \eta) = \frac{1}{4\sigma}[(\lambda^k - \lambda)^2 - (\mu^{k+1} - \mu)^2].$$

We proceed to show that the DtN-maps $\mathcal{S}_1, \mathcal{S}_2$ are monotone such that the expressions in (45) are non-negative. In fact, we will show more. Let us assume at the moment that this true, then (45) implies

$$|\mu^{k+1} - \mu|^2 \leq |\lambda^k - \lambda|^2, \ |\lambda^k - \lambda|^2 \leq |\mu^k - \mu|^2. \tag{46}$$

This implies

$$0 \leq \sum_{k=0}^{N}(|\mu^k - \mu|^2 - |\mu^{k+1} - \mu|^2 \tag{47}$$
$$= |\mu^0 - \mu|^2 - |\mu^{N+1} - \mu|^2, \ \forall N \in \mathbb{N}.$$

This, in turn, shows

$$|\mu^{N+1} - \mu| \leq |\mu^0 - \mu|^2, \ |\mu^k - \mu|^2 - |\mu^{k+1} - \mu|^2 \to 0. \tag{48}$$

Now, (46) . (48) imply

$$(S_2\eta_2^k - S_2\eta)(\eta_2^k - \eta)\frac{1}{4\sigma}[(\mu^k - \mu)^2 - (\mu^{k+1} - \mu)^2] \to 0 \qquad (49)$$

$$(S_1\eta_1^{k+1} - S_1\eta)(\eta_1^{k+1} - \eta) \le \frac{1}{4\sigma}[(\mu^k - \mu)^2 - (\mu^{k+1} - \mu)^2] \to 0.$$

Lemma 3.1 *The mappings S_i, $i = 1, 2$ are monotone. In particular, for α, $\beta \in \mathbb{R}$, let $y_{1,\alpha}$, $y_{1,\beta}$ denote the unique solutions of the p-Laplace problem (32) with $y_{1,\alpha}(0) = \alpha$, $y_{1,\beta}(0) = \beta$ and $y_{1,\alpha}$, $y_{1,\beta}$ solve (34), then we have*

$$(S_1(\alpha) - S_1(\beta))(\alpha - \beta) \ge \int_0^1 (|\partial_x y_{1,\alpha}| + |\partial_x y_{1,\beta}|)^{p-2} (\partial_x y_{1,\alpha} - \partial_x y_{1,\beta})^2 \, dx, \quad (50)$$

$$(S_2(\alpha) - S_2(\beta))(\alpha - \beta) \ge \sum_{i=2}^m \int_0^1 (|\partial_x y_{i,\alpha}| + |\partial_x y_{i,\beta}|)^{p-2} (\partial_x y_{i,\alpha} - \partial_x y_{i,\beta})^2 \, dx \quad (51)$$

Proof We have, using integration by parts,

$$
\begin{aligned}
0 &= \int_0^1 \partial_x \left((\partial_x y_{1,\alpha})^{p-2}\partial_x y_{1,\alpha} - (\partial_x y_{1,\beta})^{p-2}\partial_x y_{1,\beta}\right)(y_{1,\alpha} - y_{1,\beta})dx \\
&= -\left((\partial_x y_{1,\alpha})^{p-2}\partial_x y_{1,\alpha} - (\partial_x y_{1,\beta})^{p-2}\partial_x y_{1,\beta}\right)(0) \qquad (52) \\
&\quad - \int_0^1 \left((\partial_x y_{1,\alpha})^{p-2}\partial_x y_{1,\alpha} - (\partial_x y_{1,\beta})^{p-2}\partial_x y_{1,\beta}\right)(\partial_x y_{1,\alpha} - \partial_x y_{1,\beta})dx.
\end{aligned}
$$

However, $S_1(\alpha) = -\partial_x y_{1,\alpha}^{p-2}\partial_x y_{1,\alpha}$ and, therefore, (50) follows by the well-known monotonicity property of the function $f(s) := |s|^{p-2}s$ for $p \in (1, 2]$. A similar argument applies to S_2 by summation and, therefore, (51) follows. $\qquad\square$

Lemma 3.1 and (49) imply the following theorem.

Theorem 3.1 *Let $\tilde{y}^0$, $\bar{y}^0$ be given. Then the iteration 40 converges in $H^1(0, 1)^m$.*

4 Domain Decomposition of the Doubly Nonlinear p-Parabolic Problem on Networks

We now embark on the domain decomposition of the time-dependent problem. We notice that there is no publication available treating this case with non-overlapping domain decomposition. We take the idea from the Robin-type approach (26). More precisely, we recall system (10) and apply the analogous iterative condition as in (26).

$$\partial_t \beta_i(y^{k+1})(x,t) - \partial_x \left(\beta_i(\partial_x y_i^{k+1}(x,t))\right) = f_i(x,t), \qquad\qquad i \in \mathcal{I},\ x \in (0, \ell_i),\ t \in (0, T),$$

$$y_i^{k+1}(n_j, t) = 0, \qquad\qquad i \in \mathcal{I}_j, j \in \mathcal{J}_D^S,\ t \in (0, T),$$

$$d_{ij}\beta_i(\partial_x y_i^{k+1}(n_j, t) = 0, \qquad\qquad i \in \mathcal{I}_j, j \in \mathcal{J}_N^S,\ t \in (0, T),$$

$$\tag{53}$$

$$d_{ij}\beta_i(\partial_x y_i^{k+1})(x_{ij}, t) + \rho y_i^{k+1}(x_{ij}, t) = \rho \left(\frac{2}{d_j} \sum_{l \in \mathcal{I}_j} y_l^k(x_{lj}, t) - y_i^k(x_{ij}, t)\right),$$

$$- \left(\frac{2}{d_j} \sum_{l \in \mathcal{I}_j} d_{lj}\beta_l(\partial_x y_l^k)(x_{lj}, t) - d_{ij}\beta_i(\partial_x y_i^k)(x_{ij}, t)\right), \qquad j \in \mathcal{J}^M, i \in \mathcal{I}_j,$$

$$y_i^{k+1}(x, 0) = y_i(x);\ x \in (0, \ell_i), \qquad\qquad i \in \mathcal{I}.$$

As in [23], it is possible to apply a relaxation with a relaxation parameter $\epsilon \in [0, 1)$. This amounts to

$$d_{ij}\beta_i(\partial_x y_i^{k+1})(x_{ij}, t) + \rho y_i^{k+1}(x_{ij}, t) = \lambda_{ij}^k(t),$$

$$\lambda_{ij}^k(t) = (1 - \epsilon) \left\{ \rho \left(\frac{2}{d_j} \sum_{l \in \mathcal{I}_j} y_l^k(x_{lj}, t) - y_i^k(x_{ij}, t)\right) \right.$$

$$\left. - \left(\frac{2}{d_j} \sum_{l \in \mathcal{I}_j} \beta_l(\partial_x y_l^k)(x_{lj}, t) - \beta_i(\partial_x y_i^k)(x_{ij}, t)\right) \right\}$$

$$+ \epsilon \left\{ d_{ij}\beta_i(\partial_x y_i^k)(x_{ij}, t) + \rho y_i^k(x_{ij}, t)\right\}. \tag{54}$$

Remark 4.1 Clearly, the (under-)relaxation (54) can and will be applied to the static problem as well. The proof of convergence follows the same spirit as in [24] for linear problems and [28] for a two-link optimal control problem. The full arguments for the proof will be published in [27]. As for the analogue of the iteration (40) for the p-parabolic problem, we refer to a forthcoming publication.

In the following example, we provide a first impression of the method for doubly nonlinear p-parabolic problems. The method can be obtained from the corresponding DDM for static optimal control problems by discarding the control functions. The performance is very similar as in Example 6.

Example 5 We want to illustrate the iterative method for doubly nonlinear p-parabolic problems described by (53), (54). For the sake of simplicity, we consider a two-link serial problem, where the original domain stretches from 0 to 2 with constant load $f \equiv 1$, Dirichlet condition at $x = 0$ and Neuman condition at $x = 2$. We take $x = 1$ as interface with two edges and constant load $f_i \equiv 1$. We take $\sin(\pi x)^2$ as initial data on each link and apply a $1.e-5$ regularization for the p-Laplace operator for $p = 2$ and for $p = 3/2$. We use the MATLAB routine **pdepe** on the edges over the time interval $(0, T)$, where $T = 1$. We used the pdepe code to also compute the problem on the entire domain $(-1, 1)$. See Fig. 14, consisting of two figures, the left one for $p = 2$ and the right one for $p = \frac{3}{2}$. In each sub-figure, on the left the traces
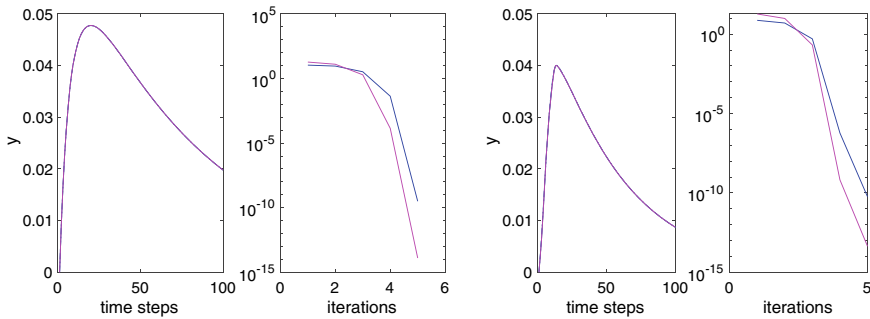
Fig. 14 P.L. Lions method for the p-parabolic problem. Left: results for p = 2, interface/errors. Right: results for p = 3/2, interface/errors

of the solutions of each link at the interface $x = 1$ are plotted together with the full solution using dashed-dotted lines. Of course, due to the precision, this is not visible in the figure. On the right, the errors of the states and the derivatives are displayed versus the iterates, respectively.

5 Non-overlapping Domain Decomposition for Optimal Control Problems: The Concept of Virtual Controls

Domain decomposition suggests itself at various levels. First of all, at the level of the optimality system, we may want to decompose the full optimality system (14) of the space-time problem, the optimality system of the semi-discrete system corresponding to (17) arising in the instantaneous control regime, or finally within Algorithm 1, the systems (23) and (24) individually. Secondly, the domain decomposition may focus on decoupling the entire graph into sub-networks, specifically into star-graphs, using either multiple or serial nodes as cutting interfaces. The decomposition may also be taken for all individual edges such that the network is iteratively decomposed into single edges. In these notes, we consider non-overlapping methods only. Indeed, at multiple nodes, overlapping methods are not obvious while at serial nodes, the classical Schwarz-type iteration may be considered.

We now embark on non-overlapping domain decomposition methods for static optimal control problems in the context of *virtual controls*. The *actual* cost-functions and the corresponding *actual* controls interfere via the penalty parameters, only. The extension of the classical P.L. Lions Algorithm to optimal control problems does not seem to be as straightforward, at least at first sight. However, at least for linear distributed controls, J. D. Benamou [5] showed that the optimality system can be recast into a complex Helmholtz problem for which, in turn, the P.L.Lions algorithm could be applied. This observation has been the basis for the development of the non-overlapping domain decompositions in space and time in the monograph by J. E. Lagnese and G. Leugering [23]. We recall the optimal control problem (10) and

the corresponding optimality system (22). We propose the following iterative domain decomposition method. With parameters $\sigma, \mu \geq 0$. The iteration (55), (57), (58) is started at $n = 0$.

Algorithm 2

1. *Given* $\lambda_{ij}^n, \rho_{ij}^n,$
2. *solve for* y_i^{n+1}, p_i^{n+1}

$$\beta_i(y_i^{n+1}) - \partial_x(\beta_i(\partial_x y_i^{n+1})) = \frac{1}{v_{i,d}} p_i^{n+1}, \qquad\qquad i \in \mathcal{I}, \, x \in I_i, \qquad (55)$$

$$\beta_i'(y_i^{n+1}) p_i^{n+1} - \partial_x(\beta_i'(\partial_x y_i^{n+1}) \partial_x p_i^{n+1}) = -\kappa_i(y_i^{n+1} - y_i^d), \qquad i \in \mathcal{I}, \, x \in I_i,$$

$$y_i^{n+1}(x_{ij}) = 0, \; p_i^{k+1}(x_{ij}) = 0, \qquad\qquad i \in \mathcal{I}_j, j \in \mathcal{J}_D^S,$$

$$d_{ij}\beta_i(\partial_x y_i^{n+1})(x_{ij}) = \frac{1}{v_{i,b}} p_i(x_{ij}), \; d_{ij}\beta_i'(\partial_x y_i^{n+1})\partial_x p_i(x_{ij}^{n+1})(x_{ij}) = 0, \qquad i \in \mathcal{I}_j, j \in \mathcal{J}_N^S, \qquad (56)$$

$$d_{ij}\beta_i(\partial_x y_i^{n+1})(x_{ij}) + \sigma y_i^{n+1}(x_{ij}) + \mu p_i^{n+1}(x_{ij}) = -\left(\frac{2}{d_j} \sum_{l \in \mathcal{I}_j} d_{lj}\beta_l(\partial_x y_l^n)(x_{lj}) - d_{ij}\beta_i(\partial_x y_i^n)(x_{ij}) \right)$$
$$\qquad\qquad (57)$$

$$+ \sigma \left(\frac{2}{d_j} \sum_{l \in \mathcal{I}_j} y_l^n(x_{lj}) - y_i(x_{ij}) \right) + \mu \left(\frac{2}{d_j} \sum_{l \in \mathcal{I}_j} p_l^n(x_{lj}) - p_i(x_{ij}) \right) =: \lambda_{ij}^n,$$

$$d_{ij}\beta_i'(\partial_x y_i^{n+1}(x_{ij}))\partial_x p_i^{n+1}(x_{ij} + \sigma p_i^{n+1}(x_{ij}) - \mu y_i^{n+1}(x_{ij})) \qquad\qquad (58)$$

$$= -\left(\frac{2}{d_j} \sum_{l \in \mathcal{I}_j} d_{lj}\beta_l'(\partial_x y_l^n(x_{lj}))\beta_l(\partial_x p_l^n)(x_{lj}) - d_{ij}\beta_i'(\partial_x y_i^n(x_{ij}))(\beta_i(\partial_x p_i^n)(x_{ij})) \right)$$

$$+ \sigma \left(\frac{2}{d_j} \sum_{l \in \mathcal{I}_j} p_l^n(x_{lj}) - p_i(x_{ij}) \right) - \mu \left(\frac{2}{d_j} \sum_{l \in \mathcal{I}_j} y_l^n(x_{lj}) - y_i(x_{ij}) \right) =: \rho_{ij}^n.$$

3. *Update* $\lambda_{ij}^{n+1}, \rho_{ij}^{n+1}$ *according to* (57), (58) *for* $n \to n + 1$.

Remark 5.1 We notice that the decomposed optimality system (55), (57), (58) at the iterate n can be seen as the optimality system for the *virtual control problem* below on each edge $e_i, i \in \mathcal{I}$, with the solution y, p updated at the iteration index $n + 1$.

Algorithm 3

1. *Given* $\lambda_{ij}^n, \rho_{ij}^n,$
2. *solve for* $y_i^{n+1}, u_i^{n+1}, u_j^{n+1}, j \in \mathcal{J}_i$

$$\min_{u,g,y} \left\{ J_i(y_i, u_i) + \frac{1}{2\mu} \sum_{j \in \mathcal{J}_i} \left[|g_i|^2 + |\mu y_i - \rho_{ij}^n|^2 \right] \right\}$$

$$s. \, t. \qquad\qquad\qquad\qquad\qquad\qquad\qquad\qquad (59)$$

$$\beta_i(y_i) - \partial_x(\beta_i(\partial_x y_i)) = u_i, \qquad\qquad i \in \mathcal{I}, \, x \in I_i,$$

$$d_{ij}\beta_i(\partial_x y_i(x_{ij})) + \sigma y_i(x_{ij}) = \lambda_{ij}^n + g_{ij}, \qquad j \in \mathcal{J}_i, i \in \mathcal{I}_j,$$

$$y_i(x_{ij}) = 0, \qquad\qquad\qquad i \in \mathcal{I}_j, j \in \mathcal{J}_D^S,$$

$$d_{ij}\beta_i(\partial_x y_i(x_{ij})) = u_j, \qquad\qquad i \in \mathcal{I}_j, j \in \mathcal{J}_N^S.$$

3. Update λ_{ij}^{n+1}, ρ_{ij}^{n+1} according to (57), (58) *for $n \to n+1$.*

We understand that the boundary control appears in (59) only if the controlled vertex n_j, $j \in \mathcal{J}_N^S$ is adjacent to the edge e_i. The equivalence of the Algorithms 2 and Algorithm 3 turns the domain decomposition method into the format of a classical PDE-constrained optimal control problem for which we can use standard software. In essence, we do not need to solve optimality systems of PDEs but rather can directly pose the corresponding PDE as equality constraints at each iteration level. We also notice, that then also box-constraints for the controls are easy to handle, which otherwise at the level of the optimality system, lead to variational inequalities. It is possible to include these in the DDM (cf. [26]), but from the point of view of PDE-numerics, this appears to be more complicated.

Convergence of the iteration (55), (57), (58) has been shown so far for a two-link network, only. The proof for the general network will appear in [27]. From [28], we cite the following result.

Theorem 5.1 ([28]) *For a two-link network $\mathcal{I} = \{1, 2\}$, let $(\hat{y}_i, \hat{p}_i)$, $i = 1, 2$ be the solution of the optimality system* (22) *and* (y_i^n, p_i^n), $i = 1, 2$ *the solution of* (55), (57), (58). *Let the errors* $(\tilde{y}_i, \tilde{p}_i) := (y_i^n, p_i^n) - (\hat{y}_i, \hat{p}_i)$ *at the interface be sufficiently small at $n = 0$. Then there are parameters σ, μ, κ, ν such that the iteration converges. Moreover, we have*

$$
\begin{aligned}
&\tilde{y}_i^n, \tilde{p}_i^n \to 0, \ n \to \infty, \ in \ H^1(I_i), \ i = 1, 2, \\
&\tilde{y}_i^n(1), \partial_x \tilde{y}_i^n(1), \tilde{p}_i^n(1), \partial_x \tilde{p}_i^n(1) \to 0, \ n \to 0, \ i = 1, 2.
\end{aligned}
\tag{60}
$$

Remark 5.2 We remark that when we take $p = 2$, then the iterative domain decomposition procedure above reduces to the well-known iteration from [23].

Example 6 In this example, we consider the static optimal control problem for a two-link model and the corresponding optimality system. The iterative decomposition is now based on the Robin-type DDM. We choose in particular a constant target function $y_d = 1$, constant Dirichlet conditions $y = 1$ at the outer ends $x = 0$, $x = 2$ and parameters $\sigma = 10, \mu = .001, \kappa = 100, \nu = .1$. We perform two experiments, one for $p = 3/2$, the case of interest in gas flow, and $p = 1.1$, which is important in, e.g., imaging, where $1 < p \le 2$ and the limiting case $p = 1$ are considered. We solve the boundary value problems arising on the full domain and the two sub-domains using the routine **bvpc4** from MATLAB with a tolerance of $1e - 14$. We have chosen a constant target because it is critical, as vanishing y and $\partial_x y$ play a special role for the p-Laplacian. For more experiments and a more detailed description, we refer to [27] (Fig. 15).
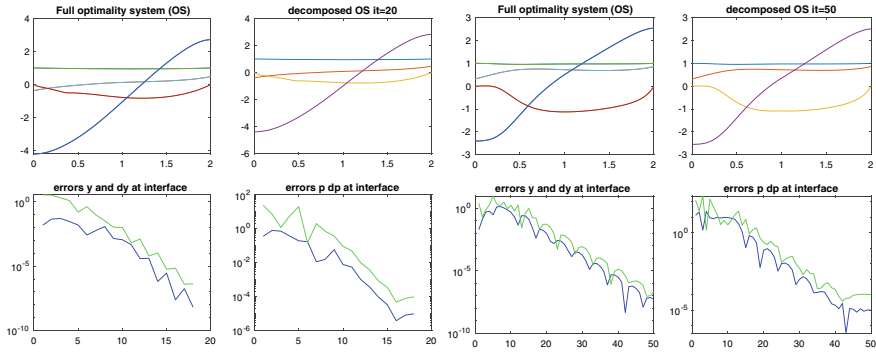
Fig. 15 Left figure: $p = 1.5, \sigma = 10, \mu = .001, \kappa = 100, \nu = .1$, right figure: $p = 1.1$, same parameters

6 Concluding Remarks and Open Problems

The methods described in this survey article are based on the paradigm of virtual controls. The corresponding DDMs can, therefore, be seen in the context of PDE-constraint optimization. This fact is useful also in the context of discrete-continuous control problems including decision making, see, e.g., [15, 16]. We refer to https://www.trr154.fau.de/trr-154-en/ for further information. To fix ideas, we concentrated on a particular set of methods, for which we have tried to provide a fairly complete account, namely, iteration methods that can be attributed to the notion of *virtual controls* in the sense of Lions and Pironneau [35]. Moreover, we presented a new Gauß -Seidel type algorithm and provide the full proof. We have seen that also the algorithm by Lions [36] can be interpreted as the result of a virtual control problem. In particular with respect to the fully doubly nonlinear p-parabolic problem, a detailed study of well-posedness of the underlying optimal control problems together with proofs of convergence at the continuous level will appear elsewhere. Time domain decomposition and the role of instantaneous control in the context of the *turnpike phenomena* is subject to further studies as well as the algorithmic realization of *reachability* or exact controllability (or the so-called nodal profile controllability) constraints. Moreover, the methods treated allow for control constraints, also. DDMs for state constraint optimal control problems appear to be widely open, at least in the continuous setting. Obviously, such problems are of importance, in particular in gas-pipe networks, where the pressure has to be limited in each pipe by box-constraints. With respect to mechanical multi-structures, further research is necessary in order to extend the algorithms provided here to 2-d and 3-d networked systems (e.g., masonry structures), see [23, 26] for 2-d networks.

Another important desire in the context of complex systems is model reduction. Clearly, domain decomposition of a network into sub-networks, a model reduction technique per se, suggests itself as a general set-up for a hierarchical decomposition in the sense that some of the sub-networks can be replaced by surrogates.

There are many ways to proceed, namely, proper orthogonal decomposition (POD), (non-)periodic homogenization and least square fits, such as by provided by so-called Physics informed neural networks (PINN). For the latter, see, e.g., [2]. More recently, transmission problems and coupled problems in general have been addressed by what is now known as the XPINN-approach, X standing for crossings or interfaces, see, e.g., [21]. Clearly, once the model is penalized using least squares, also transmission conditions can be handled using penalization. Even more, it is possible to include optimization variables and cost functions in the context of PDE-constraint optimal control by this method. See, e.g., [43]. It does not come as a surprise that domain decomposition methods have also been investigated in this context. Indeed, a deep-Schwarz overlapping domain decomposition method has been introduced in [33]. There is no space to elaborate at length on this emerging subject. In fact, we applied the P.L. Lions Robin-type approach to a two-link problem, where on one link, we used PINN, however, for the sake of brevity, we do not display the results here. The only difference to the exact Robin-approach (58), (57) is that we substitute the model-based numerical solver for the sub-domains (or one of the sub-domains) by a PINN-based solver. This approach has, to the best knowledge of the author, not been published. The interest in this non-overlapping PINN-based approach is that in the applications, in particular in the network problems we discuss here, the PINN-approach, as a surrogate, may be used in part of the complex network (say, daughter networks), while classical numerical methods are used in a parent network. This novel paradigm that we can call NETI (instead of FETI, see, e.g., the recent ML-versions of FETI [19, 20]) as NEtwork Tearing and Interconnection is the subject of further research in the CRC 154 *Mathematical modeling, simulation and optimization using the example of gas networks*, project A05, (see https://www.trr154.fau.de/trr-154-en/).

References

1. Alonso, R., Santillana, M., Dawson, C.: On the diffusive wave approximation of the shallow water equations. European J. Appl. Math. **19**(5), 575–606 (2008)
2. Bai, G., Koley, U., Mishra, S., Molinaro, R.: Physics informed neural networks (PINNs) for approximating nonlinear dispersive PDEs. J. Comput. Math. **39**(6), 816–847 (2021)
3. Bamberger, A.: Étude d'une équation doublement non linéaire. J. Funct. Anal. **24**(2), 148–155 (1977)
4. Bamberger, A., Sorine, M., Yvon, J.P.: Analyse et contrôle d'un réseau de transport de gaz. In: Computing Methods in Applied Sciences and Engineering (Proceedings of the 3rd International Symposium, Versailles, 1977), II, volume 91 of Lecture Notes in Physics, pp. 347–359. Springer, Berlin, New York (1979)
5. Benamou, J.-D.: A domain decomposition method with coupled transmission conditions for the optimal control of systems governed by elliptic partial differential equations. SIAM J. Numer. Anal. **33**(6), 2401–2416 (1996)

6. Bögelein, V., Duzaar, F., Marcellini, P., Scheven, C.: A variational approach to doubly nonlinear equations. Atti Accad. Naz. Lincei Rend. Lincei Mat. Appl. **29**(4), 739–772 (2018)
7. Brouwer, J., Gasser, I., Herty, M.: Gas pipeline models revisited: model hierarchies, non-isothermal models, and simulations of networks. Multiscale Model. Simul. **9**(2), 601–623 (2011)
8. Casas, E., Fernández, L.A.: Optimal control of quasilinear elliptic equations. In: Control of Partial Differential Equations (Santiago de Compostela, 1987), volume 114 of Lecture Notes in Control and Information Sciences, pp. 92–99. Springer, Berlin (1989)
9. Casas, E., Kogut, P.I., Leugering, G.: Approximation of optimal control problems in the coefficient for the p-Laplace equation. I. Convergence result. SIAM J. Control Optim. **54**(3), 1406–1422 (2016)
10. Dolean, V., Jolivet, P., Nataf, F.: An introduction to domain decomposition methods. In: Society for Industrial and Applied Mathematics (SIAM), Philadelphia, PA. Algorithms, Theory, and Parallel Implementation (2015)
11. Engström, E., Hansen, E.: Convergence Analysis of the Nonoverlapping Robin-Robin Method for Nonlinear Elliptic Equations (2021). https://arxiv.org/abs/2105.00649v1
12. Gander, M.J.: Analysis of the parareal algorithm applied to hyperbolic problems using characteristics. Boletin de la Sociedad Espanola de Matemática Aplicada **42**, 21–35 (2008)
13. Gander, M.J., Kwok, F.: Schwarz methods for the time-parallel solution of parabolic control problems. In: Domain Decomposition Methods in Science and Engineering XXII. volume 104 of Lecture Notes in Computational Science and Engineering, pp. 207–216. Springer, Cham (2016)
14. Gander, M.J., Vandewalle, S.: Analysis of the parareal time-parallel time-integration method. SIAM J. Sci. Comput. **29**(2), 556–578 (2007)
15. Hante, F., Krug, R., Schmidt, M.: Time-domain Decomposition for Mixed-Integer Optimal Control Problems (2021)
16. Hante, F., Schmidt, M.: Convergence of finite-dimensional approximations for mixed-integer optimization with differential equations. Control Cybern. **48**(2), 209–229 (2019)
17. Heinkenschloss, M.: A time-domain decomposition iterative method for the solution of distributed linear quadratic optimal control problems. J. Comput. Appl. Math. **173**(1), 169–198 (2005)
18. Heinkenschloss, Matthias, Herty, Michael: A spatial domain decomposition method for parabolic optimal control problems. J. Comput. Appl. Math. **201**(1), 88–111 (2007)
19. Heinlein, A., Klawonn, A., Lanser, M., Weber, J.: Combining machine learning and adaptive coarse spaces–a hybrid approach for robust FETI-DP methods in three dimensions. SIAM J. Sci. Comput. **43**(5), S816–S838 (2021)
20. Heinlein, A., Klawonn, A., Lanser, M., Weber, J.: Machine learning in adaptive FETI-DP: reducing the effort in sampling. In: Numerical Mathematics and Advanced Applications—ENUMATH 2019, volume 139 of Lecture Notes in Computational Science and Engineering, pp. 593–603. Springer, Cham (2021)
21. Jagtap, A.D., Karniadakis, G.E.: Extended physics-informed neural networks (XPINNs): a generalized space-time domain decomposition based deep learning framework for nonlinear partial differential equations. Commun. Comput. Phys. **28**(5), 2002–2041 (2020)
22. Kwok, F.: On the time-domain decomposition of parabolic optimal control problems. In: Domain Decomposition Methods in Science and Engineering XXIII, volume 116 of Lecture Notes in Computational Science and Engineering, pp. 55–67. Springer, Cham (2017)
23. Lagnese, J.E., Leugering, G.: Domain Decomposition Methods in Optimal Control of Partial Differential Equations, volume 148 of International Series of Numerical Mathematics. Birkhäuser Verlag (2004)
24. Lagnese, J.E., Leugering, G., Schmidt, E.J.P.G.: On the analysis and control of hyperbolic systems associated with vibrating networks **124**(1), 77–104
25. Lance, G., Trélat, E., Zuazua, E.: Shape turnpike for linear parabolic PDE models. Syst. Control Lett. **142**, 104733, 9 (2020)

26. Leugering, G.: Domain decomposition of constrained optimal control problems for 2D elliptic system on networked domains: convergence and a posteriori error estimates. In: Domain Decomposition Methods in Science and Engineering XVII, volume 60 of Lecture Notes in Computational Science and Engineering, pp. 119–130. Springer, Berlin (2008)
27. Leugering, G.: Domain decomposition of optimal control problems for the doubly nonlinear p-parabolic equation on metric graphs. Technical report, FAU TRR154 (2022). in preparation
28. Leugering, G.: Nonoverlapping domain decomposition for instantaneous optimal control of friction dominated flow in a gas-network. In: Proceedings of the INDAM Conference 2020. INDAM (2022)
29. Leugering, G.: Nonoverlapping Domain Decomposition and Virtual Controls for Optimal Control Problems of p-type on Metric Graphs, chapter 7. Elesevier (2023)
30. Leugering, G., Mophou, G.: Instantaneous optimal control of friction dominated flow in a gas-network. In: Shape Optimization, Homogenization and Optimal Control, volume 169 of International Series of Numerical Mathematics, pp. 75–88. Birkhäuser/Springer, Cham (2018)
31. Le Veque, R.J.: Numerical Methods for Conservation Laws. Birkhaeuser (1992)
32. Le Veque, R.J.: Finite Volume Methods for Hyperbolic Problems. Cambridge University Press (2002)
33. Li, K., Tang, K.J., Wu, T.F., Liao, Q.F.: D3m: a deep domain decomposition method for partial differential equations. IEEE ACCESS **8**, 5283–5294 (2020)
34. Lions, J.-L., Maday, Y., Turinici, G.: Résolution d'EDP par un schéma en temps "pararéel". Comptes Rendus de l'Académie des Sciences—Series I—Mathematics **332**(7), 661–668 (2001)
35. Lions, J.-L., Pironneau, O.: Algorithmes parallèles pour la solution de problèmes aux limites. C. R. Acad. Sci. Paris Sér. I Math. **327**(11), 947–952 (1998)
36. Lions, P.-L.: On the Schwarz alternating method. III. A variant for nonoverlapping subdomains. In: Third International Symposium on Domain Decomposition Methods for Partial Differential Equations (Houston. TX, 1989), pp. 202–223. SIAM, Philadelphia, PA (1990)
37. Liu, Wenyue, Ma, Keying: An iterative non-overlapping domain decomposition method for optimal boundary control problems governed by parabolic equations. IAENG Int. J. Appl. Math. **46**(3), 291–297 (2016)
38. Philipp, O.: Asymptotic Analysis and Numerical Approximation of some Partial Differential Equations on Networks. Ph.D. thesis, TU Darmstadt (2023)
39. Porretta, A., Zuazua, E.: Long time versus steady state optimal control. SIAM J. Control Optim. **51**(6), 4242–4273 (2013)
40. Quarteroni, A., Valli, A.: Domain decomposition methods for partial differential equations. Numerical Mathematics and Scientific Computation. The Clarendon Press, Oxford University Press, New York. Oxford Science Publications (1999)
41. Raviart, P.A.: Sur la résolution de certaines équations paraboliques non linéaires. J. Funct. Anal. **5**, 299–328 (1970)
42. Roubíček, T.: Nonlinear Partial Differential Equations with Applications, volume 153 of International Series of Numerical Mathematics, 2nd ed. Birkhäuser/Springer Basel AG, Basel (2013)
43. Saviz, M., Nabi, S.: Optimal control of pdes using physics-informed neural networks. Technical report (2021). arXiv:2111.09880
44. Schöbel-Kröhn, L.: Analysis and Numerical Approximation of Nonlinear Evolution Euqations on Network Structures. Ph.D. thesis, Technical University of Darmstadt (2020)
45. Smoller, J.: Shock Waves and Reaction-Diffusion Equations, volume 258 of Grundlehren der mathematischen Wissenschaften. Springer (1983)
46. Ulbrich, S.: Generalized SQP methods with "parareal" time-domain decomposition for time-dependent PDE-constrained optimization. In: Real-time PDE-constrained Optimization, volume 3 of Computational Science and Engineering, pp. 145–168. SIAM (2007)
47. Wollner, W.: An optimal control problem for equations with p-structure and its finite element discretization; DFG-SPP 1962, preprint no. 137 (2021)

Free Radical, Antioxidant, and Human Health

Muhammad S. Jahan, Afsana Sharmin, Benjamin M. Walters, and Tierney C. Crosby

Abstract Antioxidant-containing food helps to fight against free radicals that are known to produce reactive oxygen species (ROS) which, in turn, cause adverse biochemical reactions in human body. The antioxidant molecules that are particularly effective in combating ROS are known as polyphenols (PPh). When a free radical or ROS is formed in a given system, the nearby PPh molecule donates its own electron (or hydrogen atom) to repair the damage. As a result, the PPh molecule suffers a loss and it itself turns into a free radical (polyphenol radical (PPh.)). However, being relatively stable, it (PPh.) does not cause any harm to others. Measurements and analyses of the PPh. can, therefore, provide a better understanding of the antioxidant potential of the food in question. In this preliminary study, we measured free radicals (PPh.) in selected food powders that are rich in antioxidants. They are Acai, Camu, Beetroot, Cacao and Coffee. For free radical measurements, an electron spin resonance (ESR) (also known as electron paramagnetic resonance (EPR)), spectrometer was used. The g-values (spectral splitting factors) of the radicals of all antioxidant containing foods were obtained within the range from 2.0044 to 2.00578.

Keywords Free radical · Human health · Oxidative stress · Natural antioxidant · Polyphenols · Electron spin resonance (ESR)

1 Introduction

Mathematics and physics are two closely connected fields [1]. One needs to apply the physics concept as well as mathematical reasoning to describe a physical phenomenon. Without mathematics, the theory or laws of physics cannot be satisfied.

M. S. Jahan (✉) · A. Sharmin · B. M. Walters
Department of Physics and Materials Science, University of Memphis, Memphis, TN, USA
e-mail: mjahan@memphis.edu

T. C. Crosby
Research Experience for Undergraduates (REU) Participant from LeMoyne Owen College, Memphis, TN, USA

For example, Quantum Mechanics is described using mathematical analysis such as linear space [2]. Wide interdisciplinary research has been conducted on the complex function of the human body with the help of mathematical reasoning [3]. Similarly, the present study is conducted for the benefit of human health, using theories of physics and mathematical tools.

The human body is a complex system where highly organized cells make up tissues, tissues form various organs, and the organs function together within larger systems such as digestive, respiratory, and nervous systems to accomplish the specific functions necessary for sustaining life. For example, homeostasis is a self-regulating process retained in the body, while external conditions change; failure to do so may result in illness or death. Free radicals are the main cause of homeostatic disruption by the fact that, once free radicals are produced within the body, they attack important macromolecules of the cell and lead to the cell damage [4]. Free radicals are often by-products of cellular metabolism and play both positive and negative roles in physiological and pathological functioning of the human body [5]. When in moderate quantities, free radicals can play a positive role in cell signaling in the biological system [6]. However, an excessive amount of free radicals cannot be stabilized by the enzymatic antioxidants produced within the body, therefore causing oxidative stress such as damage to lipids, protein, and DNA, leading to clinical disorders or death [5]. Natural, non-enzymatic antioxidants containing micronutrients such as vitamin C, vitamin E, and polyphenols are known to provide protective effects to human health by stopping the chain reaction of free radicals. Several researchers have investigated the antioxidant behavior of such beneficial micronutrients [7]. The current study is aimed to describe the free radicals of some natural antioxidant containing foods using Electron Spin Resonance technique (ESR) techniques, while the reactions of antioxidants with harmful free radicals are of further interest.

2   Free Radicals in Human Health

Free radicals are chemical species, capable of independent existence, that contain at least one or more unpaired electrons in the outermost shell configuration [8]. In the biological system, free radicals are produced as by-products of normal cellular metabolism. Because of its odd number of electrons, the free radicals are unstable, short lived and highly reactive. Once a radical forms, it immediately reacts with another radical or molecule and pullelectrons from them to become stable. The attacked molecules then become free radicals, having lost their electrons, and repeat the chain reaction into a cascade with the adjacent molecules, finally causing widespread damage to the living cell [9]. Figure 1 shows a three-step reaction of free radicals within the biological system [10].

Free radicals are generally derived from oxygen, nitrogen, and sulfur molecules. Depending on the source molecule, the derived free radicals are grouped into three main categories: reactive oxygen species (ROS), reactive nitrogen species (RNS), and reactive sulfur species (RSS). The ROS includes some important radicals such
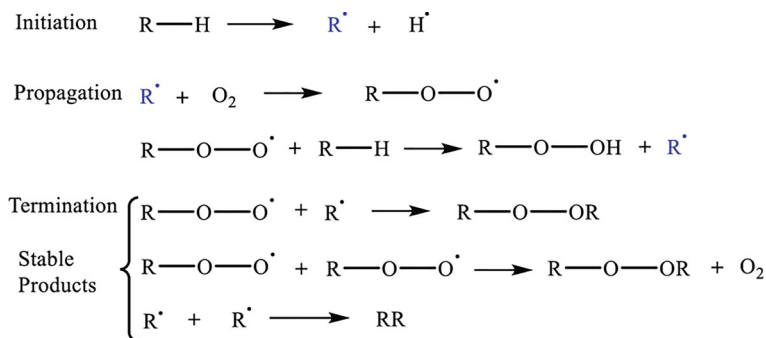
Initiation $R{-}H \longrightarrow R^{\bullet} + H^{\bullet}$

Propagation $R^{\bullet} + O_2 \longrightarrow R{-}O{-}O^{\bullet}$

$R{-}O{-}O^{\bullet} + R{-}H \longrightarrow R{-}O{-}OH + R^{\bullet}$

Termination

Stable Products

$R{-}O{-}O^{\bullet} + R^{\bullet} \longrightarrow R{-}O{-}OR$

$R{-}O{-}O^{\bullet} + R{-}O{-}O^{\bullet} \longrightarrow R{-}O{-}OR + O_2$

$R^{\bullet} + R^{\bullet} \longrightarrow RR$

Fig. 1 Three steps radical chain reaction. *Source* Ana Carolina Roveda, Magno Aparecido Gonçalves Trindade, Chap. 3, Alternative Multifunctional Additives for Biodiesel Stabilization: Perspectives for More Efficiency and More Cost-Effectiveness, Green Energy and Technology Increased Biodiesel Efficiency, Fig. 3.1, p. 59 (2018)

as hydroxyl (OH$^{\bullet}$), superoxide (O$_2^{\bullet-}$), nitric oxide (NO$^{\bullet}$), peroxyl (ROO$^{\bullet}$) as well as some non-radicals such as hypochlorous acid (HOCl), hydrogen peroxide (H$_2$O$_2$), and singlet oxygen (^{1}O$_2$) etc. [11]. RNS are derived from nitric oxide through the reaction with superoxide anion (O$_2^{\bullet-}$) to form peroxynitrite (ONOO$^-$). RSS are easily formed from thiols (R$^-$SH) by reaction with ROS [12]. Free radicals are produced in human body through normal cellular metabolism from some external sources such as pollution, cigarette smoke, radiation, and medication [13]. The rate and selectivity of free radical reactions vary, depending on the concentration of free radicals, delocalization of single electrons by radicals, and the weak bonds present in other molecules to which the radical could react with [14]. The moderate level of ROS influences different normal physiological functions of the body by governing the redox activities of the cells. If the level of ROS increases, natural enzymes in the human cells act as antioxidants by providing a defense mechanism against the elevation of ROS beyond the normal physiological levels [15, 16]. If the production of ROS overwhelms the antioxidant capacity, the term "oxidative stress" is introduced, which is thought to damage biological molecules such as DNA, proteins, carbohydrates, and lipids, leading to a wide number of clinical disorders such as diabetes mellitus, cardiovascular diseases, inflammation, obesity, cancer, neurodegenerative disorders, and hypertension [17].

2.1 Types and Effects of Free Radicals

The beneficial as well as harmful effects of some important radicals and non-radicals are discussed below.

Hydrogen peroxide (H$_2$O$_2$) is not a free radical, but an ROS which can produce hydroxyl radicals, known to be produced during normal cell metabolism and to

oxidize a number of compounds. Although H_2O_2 has been reported to promote a variety of essential cellular functions such as cell/tissue regeneration, growth, proliferation, and cell migration, at high concentrations it plays adverse effects which includes damage to proteins, lipids and nucleic acid, leading to cell death [18].

The superoxide radical ($O_2^{•-}$) is an oxygen centered radical. It has been reported that, a small increase of superoxide radicals has protective effect against H_2O_2-induced stress [19] but excess production alters the cell membranes, proteins, lipids, lipoproteins, and DNA.

The nitric oxide radical ($NO^•$) is produced by vascular endothelium, neurons, smooth muscle cells, macrophages, neutrophils, platelets, and pulmonary epithelium [20] and plays an important role for the regulation of vascular tone and blood pressure. Nitric oxide radical has been demonstrated to contribute partially in protecting the human health from malaria infection, cardiovascular diseases, and diabetes [21]. However, the relative increase of Nitric oxide and its radical causes peripheral vascular structural remodeling and loss of vascular tone that turns out pulmonary hypertension [22].
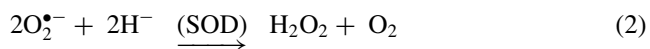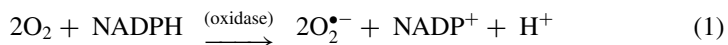
Hydroxyl radicals ($OH^•$) is a highly reactive oxygen-centered radical with a very short half-life of only 10^{-9} sec and reacts with any biological molecule resulting in the immediate formation of another radical species with lower reactivity than ($OH^•$) [23]. However, excess hydroxyl radicals may attack the cell membrane, causing membrane damage and destroying DNA base sequences [24].

The peroxyl radical ($ROO^•$) is a carbon centered radical; it is an intermediate species formed during lipid oxidation chain reaction. The peroxyl radical has been found to mediate oxidative DNA base damage and promote carcinogenesis [23, 25].

2.2 Generation of Free Radicals

Free radicals and non-radicals are generated in the human body through different reactions with the activation of different enzymes. The reaction mechanisms of few of the free radicals are shown here [26].

Superoxide anion radical ($O_2^{•-}$) is produced Eq. (1) from the rapid uptake of oxygen with activation of NADPH oxidase, and then rapidly converted to hydrogen peroxide (H_2O_2) by SOD enzymes Eq. (2).

$$2O_2 + NADPH \xrightarrow{\text{(oxidase)}} 2O_2^{•-} + NADP^+ + H^+ \tag{1}$$

$$2O_2^{•-} + 2H^- \xrightarrow{\text{(SOD)}} H_2O_2 + O_2 \tag{2}$$

Hydroxyl radicals ($^•OH$) are generated from $O_2^{•-}$ and H_2O_2 via 'respiratory burst' by a Fenton type reaction Eq. (3) and/or Haber–Weiss reaction Eq. (4),

$$H_2O_2 + Fe^{2+} \rightarrow {}^•OH + OH^- + Fe^{3+} \tag{3}$$

$$O_2{}^{\bullet-} + H_2O_2 \rightarrow {}^{\bullet}OH + OH^- + O_2 \tag{4}$$
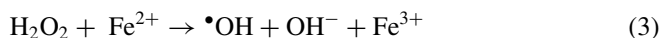
Reactive Nitrogen Species (RNS), such as nitric oxide (NO$^{\bullet}$), is produced from arginine with the activation of nitric oxide synthase enzyme Eq. (5).

$$L-Arg + O_2 + NADPH \rightarrow NO^{\bullet} + citrulline \tag{5}$$

The NO$^{\bullet}$ and O$_2{}^{\bullet-}$ react together to produce peroxynitrite (ONOO$^-$), a very strong oxidant that can attack biological molecules Eq. (6).

$$NO^{\bullet} + O_2{}^{\bullet-} \rightarrow ONOO^- \tag{6}$$

Although Singlet oxygen ($^1O_2$) not a free radial, it can be formed in some radical reactions and lead to others since it is 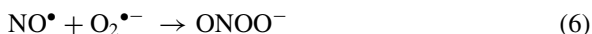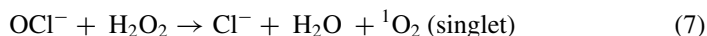one of the most active intermediates involved in chemical and biochemical reactions. One well-established reaction used in the laboratory to generate singlet oxygen is the reaction of H_2O_2 and the hypochlorite ion OCl$^-$, the ionized form of hypochlorous acid Eq. (7).

$$OCl^- + H_2O_2 \rightarrow Cl^- + H_2O + {}^1O_2 \text{ (singlet)} \tag{7}$$

3   Antioxidants

Antioxidants are natural or synthetic substances that donate electrons to stabilize the free radicals, and then become harmless stable radicals themselves (Sec 5.5). Antioxidants can be enzymatic and non-enzymatic, based on their activity in body. The enzymatic antioxidants such as superoxide dismutase (SOD), catalase (CAT), and glutathione peroxidase (GSHPx), sometimes called "First-Line Defense Antioxidants" [27], remove harmful oxidative products via conversion into hydrogen peroxide (H_2O_2), and then to water, through chemical reactions in the presence of intracellular metal cofactors. Table 1 shows some such enzymatic antioxidants, their cellular locations, substrates, and reaction mechanisms [26].

Non-enzymatic antioxidants work by stopping the progress of free radical chain reactions, and include micronutrients such as vitamin C, vitamin E, plant polyphenol, carotenoids, and glutathione. These micronutrients are not produced in the body, so they must be supplied from the diet [28]. Natural antioxidants are non-enzymatic antioxidants containing phenolic compounds and have strong anti-aging and anti-inflammatory properties. Phenolic compounds, coming primarily from fruits and vegetables [29], contain benzene rings, with one or more hydroxyl substituents, and range from single molecules to the highly polymerized ones [30]. Depending on the number of aromatic (phenolic) rings and the structural elements that bind these rings to one another, the phenolic compounds are broadly grouped into four classes: Phenolic acids, flavonoids, stilbenes, and lignans [31]. Figure 2 shows the molecular

Table 1 Location, substrate, and reaction mechanism of enzymatic antioxidant

Enzymatic antioxidant	Cellular location	Substrate	Reaction
Mn/Cu/Zn SOD	Mitochondrial matrix (Mn SOD) cytosol (Cu/Zn SOD)	$O_2^{\bullet-}$	$O_2^{\bullet-} \rightarrow H_2O_2$
CAT	Peroxisomes cytosol	H_2O_2	$2H_2O_2 \rightarrow O_2 + H_2O$
GSHPx	Cytosol	H_2O_2	$H_2O_2 + GSH \rightarrow GSSG + H_2O$
Peroxiredoxin I	Cytosol	H_2O_2	$H_2O_2 + TrxS_2 \rightarrow Trx(SH)_2 + H_2O$

Source Satish BalasahebNimse et al., Free radicals, natural antioxidants, and their reaction mechanisms, Royal Society of Chemistry Advances, Table 2, p. 4, (2015)

Phenolic acids (hydroxy-benzioc & cinnamic acids)   **Flavonoids**

Stilbenes   **Lignans**
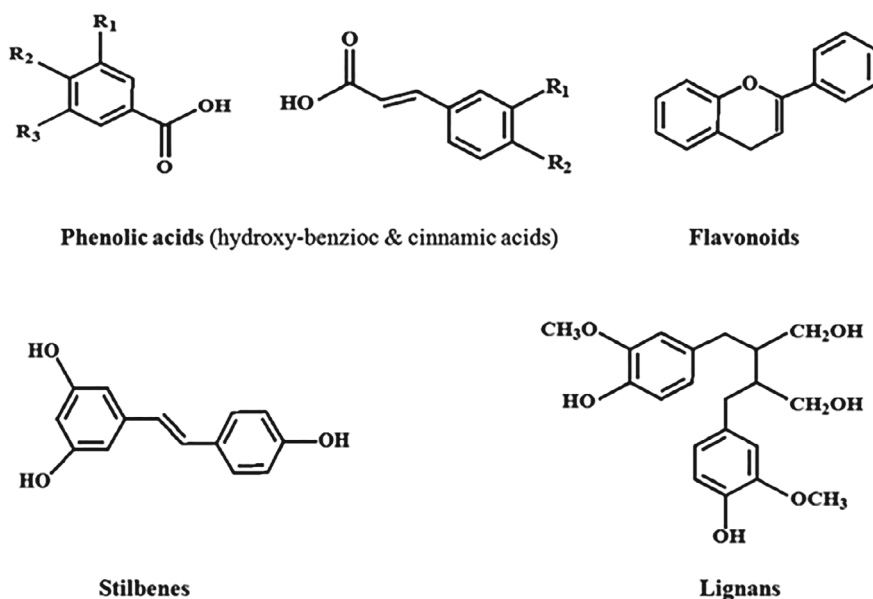
Fig. 2 Molecular structures of the different classes of polyphenols. *Source* Kanti Bhooshan Pandey, Syed ibrahimrizvi, Plant polyphenols as dietary antioxidants in human health and disease, Oxidative Medicine and Cellular Longevity, 2:5, 270–278, p. 271 (2009)

structures of different classes of polyphenols [32]. However, the plant-based natural antioxidants mainly consists of phenolic compounds/polyphenols, carotenoids, and vitamins (vitamin E and C) [33]. Figure 3 shows the reaction mechanisms by which natural polyphenols act as antioxidant through hydrogen atom transfer (HAT), single electron transfer (SET), and chelation of transition metal ions [34].
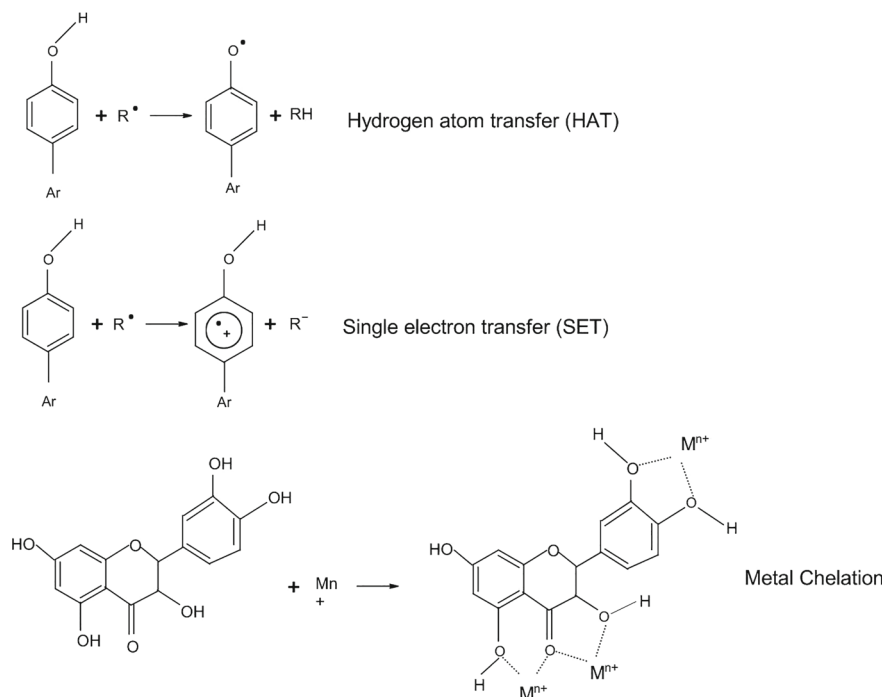
Fig. 3 Basic mechanisms through which natural polyphenols act as an antioxidant. (Ar-aryl group; R$^\bullet$-*radical*; RH- unsaturated fatty acid, and Mn$^+$- metal cation. *Source* Dimitris P. Makris, Dimitrios Boskou, Plant-derived Antioxidants as Food Additives, In book: Plants as a Source of Natural Antioxidants (pp.169–190), Edition: 1st, Chap. 9, Editors: Nawal Kishore Dubey, Fig. 9.6, p. 175 (2014)

4 Electron Spin Resonance (ESR) Technique

Electron spin resonance (ESR) spectroscopy, also known as electron paramagnetic resonance (EPR) spectroscopy, is direct and reliable technique to detect and quantify free radicals and paramagnetic species in a given material. The theory of ESR spectroscopy lies on the spin of unpaired electron and the associated magnetic moment. When a material containing unpaired electrons is exposed to an external magnetic field, the associated magnetic moment aligns parallel ($M_s = -1/2$) or antiparallel ($M_s = +1/2$) to the applied field with a specific energy causing an energy separation between the two states, which is known as the Zeeman Effect. The direction of the magnetic moment parallel to the magnetic field represents a lower energy state, while the antiparallel one represents a higher energy state. Figure 4 shows the splitting of energy states in presence of magnetic field.

Fig. 4 Splitting of energy states in an applied magnetic field (From site of EPR facility. *Source* The University of Texas at Austin, https://sites.cns.ute xas.edu/epr_facility/wha t-epr)
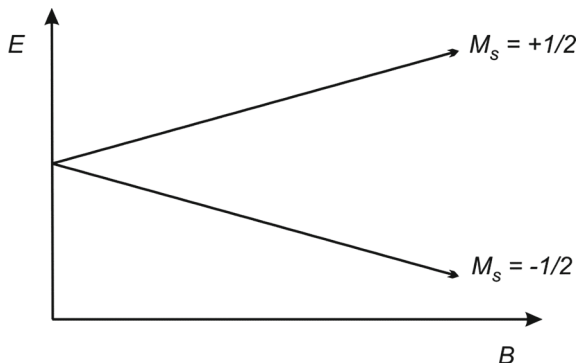
The energy of each electronic state is defined as

$$E = g\mu_B B M_s = \pm\frac{1}{2}g\mu_B B$$

where g is the spectral splitting factor, μ_B is the Bohr magneton, and B is the external magnetic field. The sign ($\pm$) is related to the direction of the magnetic moment alignment. In presence of an applied magnetic field, the energy difference between two states is defined as

$$\Delta E = g\mu_B B$$

Therefore, it can be stated that the two spin states have the same energy when there is no applied magnetic field and the energy difference between the two spin states increases linearly with increasing magnetic field strength.

In ESR spectroscopy, electromagnetic radiation is absorbed when the energy difference between two states is equal to the energy of radiation—i.e., the resonance condition. According to Planck's Law:

$$\Delta E = h\nu$$

where ΔE is the energy difference between two states, h is the Planck's constant, and ν is the frequency of the radiation (typically in the Gigahertz (GHz) range with ESR). To do this, one may try different frequencies, multiplied by Planck's constant, until it matches ΔE (the energy difference between two states); however, with ESR, the machine is tuned to a particular frequency (for example, 9.852 GHz) and then the Plank's constant cannot be varied because it is a constant, so the only other option is to vary the ΔE until it matches Planck's constant times the frequency that it is tuned to. This can be done via the aforementioned equation $\Delta E = g\mu_B B$ (therefore, also hν $= g\mu_B B$), the magnetic field (B) can be adjusted until the equation is satisfied, then resulting resonance then happens, and an absorbance occurs, which is detected by the ESR machine. A typical frequency and magnetic field combination would be using a

frequency of 9.852 GHz and checking the magnetic field around 3000–4000 Gauss. As mentioned, the "g" is the spectral splitting factor; this g is also called the g-factor, org-value, and can be used to describe particular ESR spectra and types of radicals. For a free electron, the g-value is 2.0023, and for organic radicals it ranges from 1.99 to 2.01. The g-value varies for different radicals. So, one can plug 2.0023 into the ΔE = hv=$g\mu_B B$ equation, for example, when tuned to v = 9.852 GHz, and then see that makes sense that such radicals would be detected around 3500G. The absorption of this energy causes a transition of an electron from a lower energy state to a higher energy state. This absorption signal (ESR spectrum) is detected and displayed as a first derivative of the absorption. A typical absorption signal, known as an ESR spectrum, and its first derivative are shown in Fig. 5. The peak-to-peak height (h_{pp}) is proportional to the number of radicals present in the test specimen. The radical concentration is also determined by the double integration of the first-derivative curve (ESR spectrum) [35].

Fig. 5 A typical absorption signal and its first derivative (From site of EPR facility. *Source* The University of Texas at Austin, https://sites.cns.utexas.edu/epr_facility/what-epr)
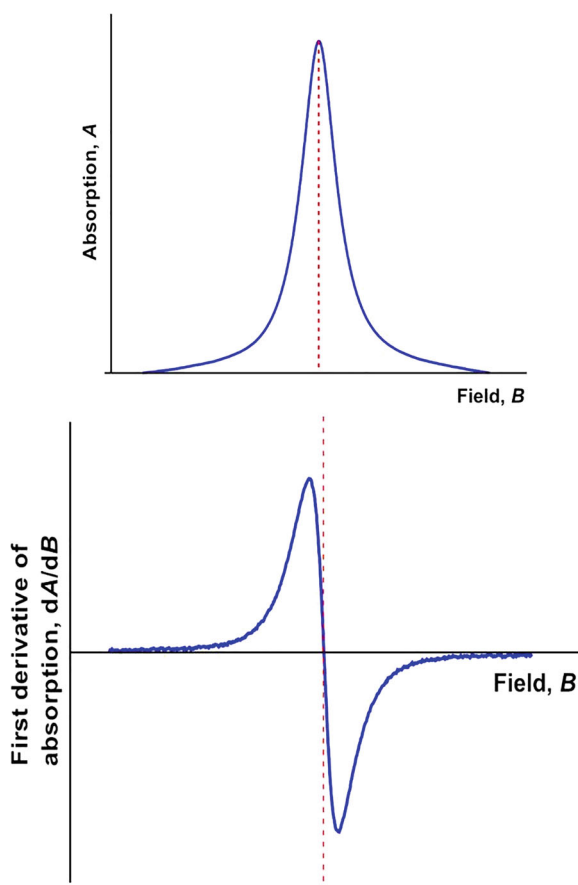
Electron spin resonance data/results presented in this chapter were obtained by using X-band (~9.8 GHz) spectrometers, EMX 300 by Bruker.

5   ESR Study of Natural Antioxidants

Free radicals and human diseases have become more researched as their importance in human health are increasingly realized. As mentioned, an antioxidant is the molecule which delays or inhibits the damaging chain reaction of free radicals through their free radical scavenging property and protects from cellular damage [36]. It has been reported that the low-molecular-weight antioxidants can safely interact with free radicals and terminate the chain reaction before vital molecules are damaged. Some of the antioxidants are produced within the body in form of enzymes, but many are from the diet as micronutrients such as vitamins E (α-tocopherol), vitamin C (ascorbic acid), and B-carotene [37]. Natural plant diets are rich sources of effective antioxidants. Phenolic compounds make many plants ideal protectors against diseases caused by oxidative stress. These natural antioxidants also offer additional benefit showing low toxicity and antimicrobial capacity [38].

Vitamin E is one of the most effective regulators of the immune system. This vitamin is often found in immune cells, and the deficiency of this vitamin may therefore impair the normal functions of the immune system in animals and humans. A deficiency may be corrected with a diet containing foods known to have vitamin E; this is better than vitamin E supplements. Foods, on the other hand, naturally contain an appropriate amount, and have other matching antioxidants, which together, have synergistic effects to make the whole better than the sum of its parts. This evolved combination is better than supplementing any individual antioxidant alone. Foods known to contain high amount of alpha-tocopherol are sunflower seeds, olive oil, and almonds. There are other naturally evolved characteristics of the actual food with advantages over supplements, such as digestive aids to help the body use them more efficiently. Supplements may be resorted to in extreme, short-term cases such as chronic deficiencies. Even then, it is unknown what the optimal dose should be for an individual at different ages, life conditions, or how well the body in different conditions will be able to utilize the supplements in the first place.

Alpha-tocopherol is a predominant form of vitamin E and plays an important role in antioxidant functions, cell signaling, and gene regulatory functions [39]. Alpha-tocopherol' effectiveness is partially due to its ability to react with lipid peroxyl radicals at a rate several orders of magnitude faster than the peroxyl radical propagation reaction [40]. Figure 6 shows the structure of vitamin E (α-Tocopherol) molecule, as well as its radical form and representative ESR spectrum [41]. The ESR spectrum of vitamin E (α-Tocopherol) indicates the existence of a stable form of the vitamin E radical, suggesting that vitamin E donates electrons to other less stable free radicals, stopping the chain reaction of free radicals, while remaining a safe and stable radical itself. It should also be noted that, while the alpha-tocopherol form of vitamin E is the most popular, other forms of vitamin E (e.g., other tocopherols and tocotrienols)

Fig. 6 Molecular structure of vitamin E (Alpha-Tocopherol) molecule and its radical, as labeled. Two first-derivative ESR spectra of the alpha-tocopherol radical before and after gamma irradiation are also shown in the figure. *Source* M. Shah Jahan et al., Book Chap. 4, Free Radical Processes in Medical Grade UHMWPE, Computational Science and its Applications, Fig. 4.12, p. 72 (2020)
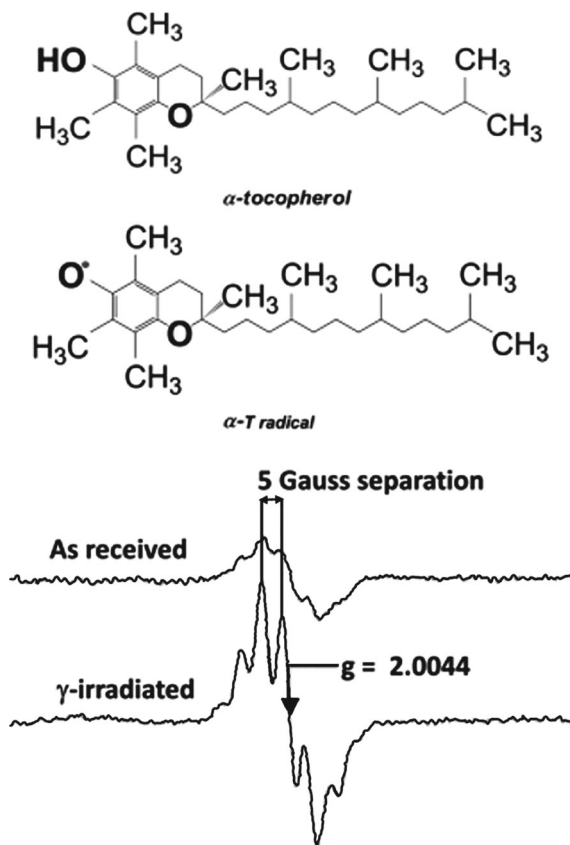
may also have beneficial functions; therefore, their study may be good future work to pursue, similar to alpha-tocopherol.

One other potent antioxidant is the palm acai berry (Euterpe oleraceae). Native to South America, acai has been revealed as a potential source of dietary phytochemicals. These phytochemicals show strong antioxidant activities, providing antimicrobial, antidiarrheal, anthelmintic, antiallergic, antispasmodic, and antiviral protection [42]. Diets rich in phytochemicals have been reported to reduce neurodegeneration and limit disease progression [43]. Carotenoids and anthocyanins are the main components of the acai fruit [44]. Figure 7 shows the molecular structure of anthocyaninand the ESR spectrum of non-irradiated Acai powder [45]. The ESR spectrum of non-irradiated organic Acai powder indicates the presence of a natural anthocyanin radical in the form of polyphenol. Such polyphenols become unreactive free radicals after electron donation to neutralize more harmful types of free radicals.

Camu-camu (Myrciariadubia), a fruit from the Amazon region, has shown effective antioxidant functionalities against human infectious diseases, thought to be primarily due to its high content of vitamin C [46]. Camu fruit is a versatile berry,
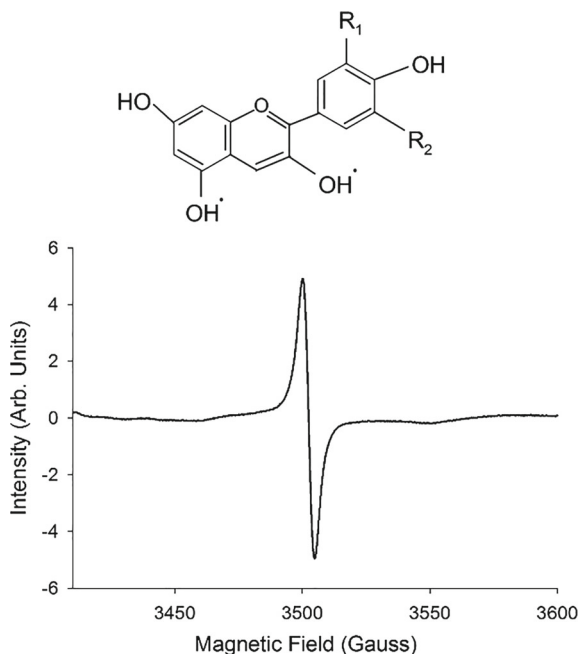
with its pulp, seeds, and skin all presenting antioxidant potential in differing degrees. The phenolic compounds found in camu-camu are quercetin, cyanidin-3-glucoside, ellagic acid, and ellagitannins. The molecular structure of phenolic compounds in the camu fruit and an ESR spectrum of organic camu powder are shown in Fig. 8. The ESR spectrum of camu powder indicates the presence of phenolic radical which is formed by donating electrons to the nearest naturally produced free radicals.

In recent years, redbeet (Beta vulgaris) has received increasing attention for its biological function toward the benefit of human health. Figure 9 shows the molecular structure of the active component betalains (betanin) and the ESR spectrum of betalains radical, which is known to remove oxidative stress, prevent DNA damage, and reduce LDL (low-density lipoprotein) cholesterol. Betalains also has antitumor properties through inhibiting cell proliferation, angiogenesis, inducing cell apoptosis, and autophagy [47, 48]. The ESR spectrum of organic redbeet powder indicates the presence of active betalains compound as antioxidant.

Theobroma Cacao seeds, commonly consumed in beverages and chocolate, have been demonstrated as an effective antioxidant and anti-inflammatory due to its content of polyphenols such as flavonoids and phenolic acids [49]. Several epidemiological studies have observed the effectiveness of cacao against disease. Report suggests that polyphenols such as resveratrol, an antioxidant of cacao, can play a role in the prevention and control of cancer [50]. The moderate consumption of chocolate has also been demonstrated to reduce cardiovascular risk [51]. Figure 10 shows the basic molecular structure of procyanidin, which is an antioxidant in cacao
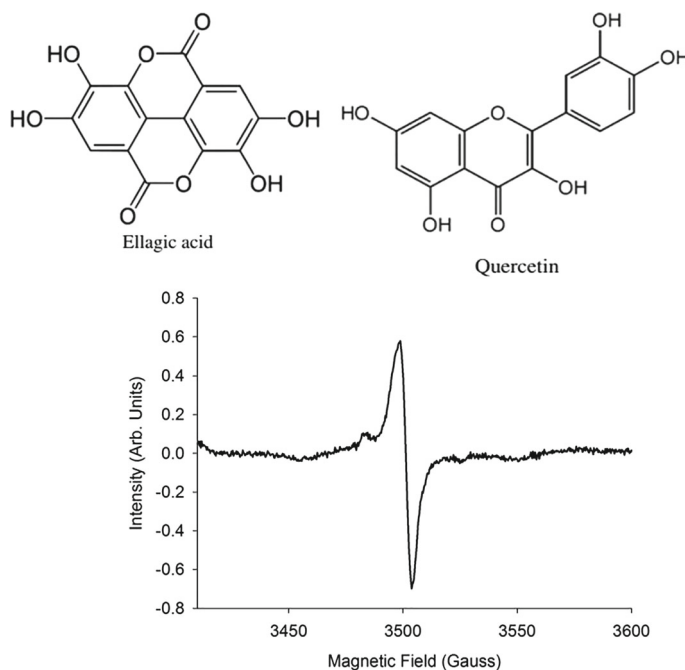
Fig. 8 Molecular structure of phenolic compounds found in camu powder and the ESR spectrum of organic camu powder as received. *Source of Molecular structure* Alice Fujita et al., Evaluation of phenolic-linked bioactives of camu-camu (Myrciariadubia Mc. Vaugh) for antihyperglycemia, antihypertension, antimicrobial properties, and cellular rejuvenation, Food Research International, 77: 194–203, Fig. 1, p. 195 (2015)

seeds [52], and the ESR spectrum produced by procyanidins radical. The excess electrons of phenolic compounds of procyanidins allow them to donate electrons to the less stable free radicals and become unreactive and stable radical itself.

Coffee contains phenolic compounds such as caffeine, chlorogenic acid, trigonelline, cafestol and kahweol. These compounds provide beneficial effect for human health by showing high antioxidant activity, antimutagenic activity, hepato-protective action, reduced incidence of type 2 diabetes mellitus, reduced risk of cardiovascular diseases, decreased incidence of inflammatory diseases, reduced menopausal symptoms, and others [53]. Figure 11 shows molecular structure of caffeine and the ESR spectrum of a typical store-bought coffee [54]. The ESR spectrum of caffeine radical confirms the antioxidant capacity of caffeine molecules.

The g-values of antioxidant (polyphenols) containing foods were also determined using ESR technique. In results, it has been observed that the g-values of antioxidant containing foods range from 2.0044 to 2.00578 which are listed in Table 2. Figure 12 shows the typical ESR spectrum of antioxidant containing food as a function of g-values.

Fig. 9 Molecular structure of betalains (the active ingredient of redbeet powder) and the ESR spectrum of organic redbeet powder as received. *Source of Molecular Structure* Bhupinder Singh, Bahadur Singh Hathan, Chemical composition, functional properties and processing of beetroot—a review, International Journal of Scientific and Engineering Research, 5 (1), p. 680 (2014)
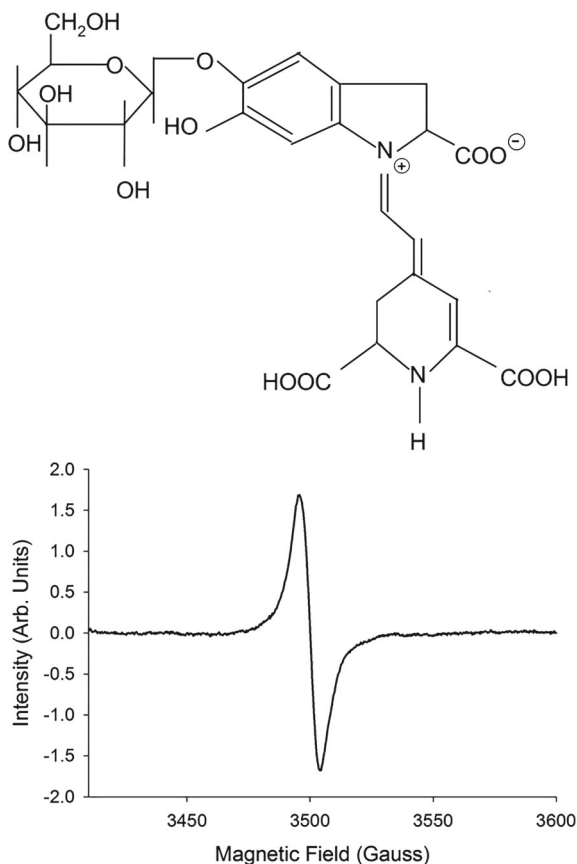
6 Summary

Human health has been an increasing interest of research along with the development of modern science. Researchers are constantly applying their innovative ideas and technologies to enhance the defensive activities of the cell immune system against the harmful factors. Since free radicals are a vital cause of cellular damage leading to disease, the study of free radicals and antioxidants is important. The current study has focused on explaining the origin, as well as the function, of free radicals in the human body and how they can be controlled by consuming the micronutrients available in the natural plant derived diets. The experimental observations suggest that all the polyphenol compounds of natural antioxidants are rich in hydrogen (H) atoms, which causes the antioxidants to donate electrons easily to the free radicals and stabilize them, while the antioxidants become safe, stable, and unreactive radicals themselves.

Fig. 10 Molecular structure of procyanidins (the active ingredient of cacao seeds) and the ESR spectrum of cacao powder as received. *Source of Molecular structure* Pubchem, National center for Biotechnology information
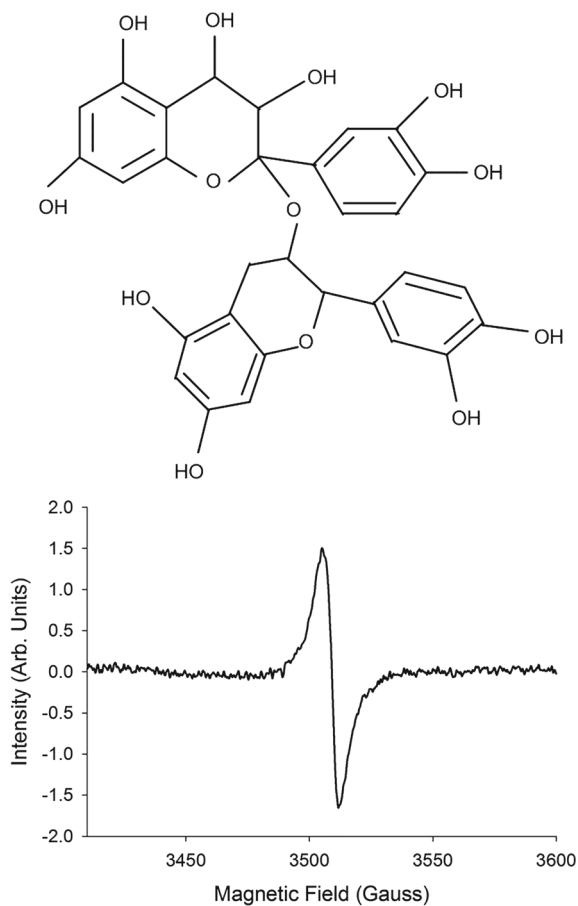
Fig. 11 Molecular structure of caffeine and the ESR spectrum of instant coffee as received. *Source of Molecular structure* Alireza Baratloo et al., The Role of Caffeine in Pain Management: A Brief Literature Review, Anesthesiology and Pain Medicine, Fig. 1, p. 2 (2016)
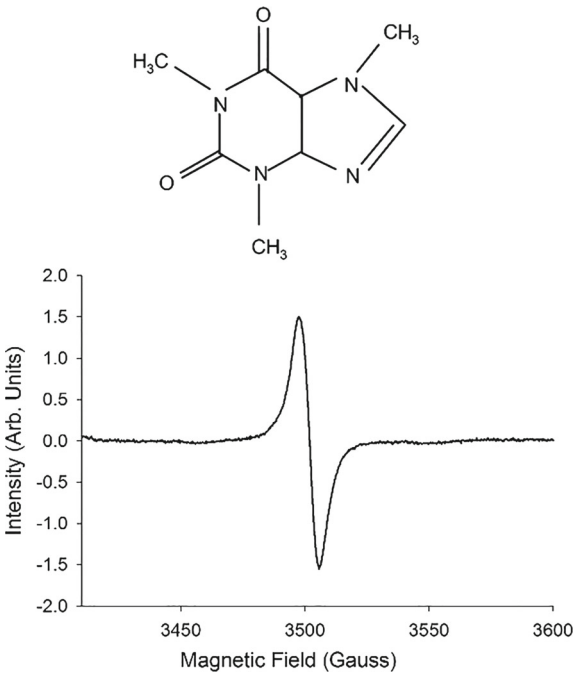
Table 2 g-values of antioxidant containing foods

Sample	g-values
Vitamin E	2.0044
Acai	2.00521
Camu	2.00559
Redbeet	2.00574
Coffee	2.00572
Cacao	2.00578

<Original to the author>

Fig. 12 ESR spectra of antioxidant containing foods as a function of g-values
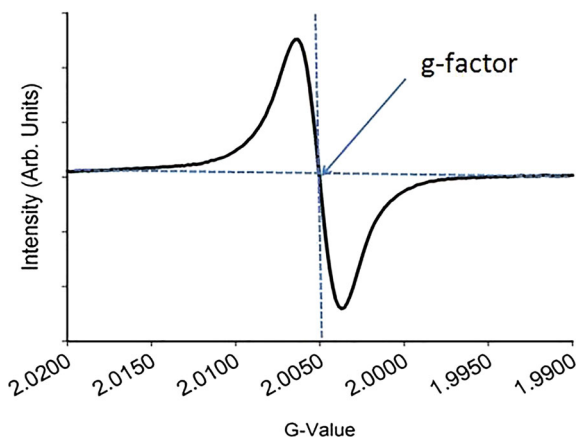
References

1. Radulović, B., Dorocki, M.: The connection between mathematics and physics from the aspect of reasoning based on proportions and errors in the conclusion. Phys. Chem. Technol. **16**(3), 257–265 (2018)
2. Dürr, D., Lazarovici, D.: Some Mathematical Foundations of Quantum Mechanics, Understanding Quantum Mechanics (2020)
3. Gorbachev, V., Nikulchev, E., Kosenkov, A.N., Sokolov, A., Zavalishin, I., Nikitin, I.: Estimating the mass of food components necessary for the utilization of free radical particles in the human body. Int J Environ Res Publ Heath **19**(23), 15574 (2022)
4. Pomatto, L.C.D., Davies, K.J.A.: Adaptive homeostasis and the free radical theory of aging, 2019. Free Radic. Biol. Med. **124**, 420–430 (2019)
5. Bardaweel, S.K., Gul, M., Alzweiri, M., Ishaqat, A., Salamat, H.A.A.L., Bashatwah, R.M.: Reactive oxygen species: the dual role in physiological and pathological conditions of the human body. Eurasian J. Med. **50**(3), 193–201 (2018)
6. Thannickal, V.J., Fanburg, B.L.: Reactive oxygen species in cell signalling. Am J Physiol-Lung Cell Mol Physiol **279**, L1005–L1028 (2018)
7. Zeb, A.: Concept, mechanism, and applications of phenolic antioxidants in foods. J. Food Biochem. **44**, 13394 (2020)
8. Di Meo, S., Venditti, P.: Evolution of the knowledge of free radicals and other oxidants. Oxid. Med. Cell. Longev. **32**, 9829176 (2020)
9. Phaniendra, A., Jestadi, D.B., Radicals, L.P.F.: Properties, sources, targets, and their implication in various diseases. Indian J. Clin. Biochem. **30**(1), 11–26 (2015)
10. Roveda, A.C., Trindade, M.A.G.: Chapter 3, Alternative multifunctional additives for biodiesel stabilization: perspectives for more efficiency and more cost-effectiveness. In: Green Energy and Technology Increased Biodiesel Efficiency, Fig: 3.1, p. 59 (2018)
11. Vajragupta, O., Boonchoong, P., Berliner, L.J.: Manganese complexes of curcuminanalogues: evaluation of hydroxyl radicalscavenging ability, superoxide dismutase activity and stability towardshydrolysis. Free Radic. Res. **38**, 303–314 (2004)
12. Giles, G.I., Jacob, C.: Reactive sulfur species: an emerging concept in oxidative stress. J. Biol. Chem. **383**, 375–388 (2002)
13. Pham-Huy, L.A., He, H., Pham-Huy, C.: Free radicals, antioxidants in disease and health. Int. J. Biomed Sci. **4**(2) (2008)
14. Lobo, V., Patil, A., Phatak, A., Chandra, N.: Free radicals, antioxidants and functional foods: impact on human health. Pharmacogn. Rev. **4**, 8 (2010)

15. Arfin, S., Jha, N.K., Jha, S.K., Kesari, K.K., Ruokolainen, J., Roychoudhury, S., Rathi, B., Kumar, D.: Oxidative stress in cancer cell, metabolism. Antioxidants **10**, 642 (2021)
16. Irshad, M., Chaudhuri, P.S.: Oxidant-antioxidant system: role and significance in human body. Indian J. Exp. Biol. **40**, 1233–1239 (2002)
17. Martemucci, G., Costagliola, C., Mariano, M., D'andrea, L., Napolitano, P., D'Alessandro, A.G.: Free radical properties, source and targets, antioxidant consumption and health. Oxygen (2022)
18. Shaji, C.A., Robinson, B.D., Yeager, A., Beeram, M.R., Davis, M.L., Isbell, C.L., Huang, J.H., Tharakan, B.: The tri-phasic role of hydrogen peroxide in blood-brain barrier endothelial cells. Sci Rep **9**(1), 133 (2019)
19. Thorpea, G.W., Reodicaa, M., Daviesb, M.J., Heerenc, G., Jarolimd, S., Pillaya, B., Breiten-bachd, M., Higginsa, V.J., Dawes, I.W.: Superoxide radicals have a protective role during H_2O_2 stress. Mol. Biol. Cell **24**(18), 2876–2884 (2013)
20. Moncada, S., Higgs, E.A.: Endogenous nitric oxide: physiology, pathology and clinical relevance. Eur. J. Clin. Invest. **21**, 361–374 (1991)
21. Palmer, R.M.J., Ashton, D.S., Moncada, S.: Vascular endothelium cell synthesize nitric oxide from L-Arginine. Nature **333**, 664–666 (1988)
22. Sim, J.Y.: Nitric oxide and pulmonary hypertension. Korean J. Anesthesiol. **58**(1), 4–14 (2010)
23. Aruoma, O.I.: Free radicals, oxidative stress, and antioxidants in human health and disease. J. Am. Oil Chem. Soc. **75**, 2 (1998)
24. Lipinski, B.: Hydroxyl radical and its scavengers in health and disease. Oxid. Med. Cell. Longev. **2011**, 9 (2011)
25. Lim, P., Wuenschell, G.E., Holland, V., Lee, D.H., Pfeifer, G.P., Rodriguez, H., Termini, J.: Peroxyl radical mediated oxidative DNA base damage: implications for lipid peroxidation induced mutagenesis. Biochemistry **43**(49), 15339–15348 (2004)
26. Nimse, S.B., and Dal, D.: Free radicals, natural antioxidants, and their reaction mechanisms. R. Soc. Chem. Adv. (2015)
27. Ighodaro, O.M., Akinloye, O.A.: First line defence antioxidants-superoxide dismutase (SOD), catalase (CAT) and glutathione peroxidase (GPX): their fundamental role in the entire antioxidant defencegrid. Alexandria J. Med. **54**(4), 287–293 (2018)
28. Kraemer, K., Badham, J., Christian, P., Hyun Rah, J. (eds.): Micronutrients; macro impact, the story of vitamins and a hungry worldexternal icon. Sight and Life Press (2015)
29. Balasundram, N., Sundram, K., Samman, S.: Phenolic compounds in plants and agri-industrial by-products: antioxidant activity, occurrence, and potential uses. Food Chem. **99**, 191–203 (2006)
30. Lin, D., Xiao, M., Zhao, J., Li, Z., Xing, B., Li, X., Kong, M., Li, L., Zhang, Q., Liu, Y., Chen, H., Qin, W., Wu, H., Chen, S.: An overview of plant phenolic compounds and their importance in human nutrition and management of type 2 diabetes molecules. Molecules **21**(10), 1374 (2016)
31. Khan, J., Deb, P.K., Priya, S., Medina, K.D., Devi, R., Walode, S.G., Rudrapal, M.: Dietary flavonoids: cardioprotective potential with antioxidant effects and their pharmacokinetic, toxicological and therapeutic concerns. Molecules **26**(13) (2021)
32. Pandey, K.B., Rizvi, S.I.: Plant polyphenols as dietary antioxidants in human health and disease. Oxid. Med. Cell. Longev. **2**(5), 270–278 (2009)
33. Dong-Ping, X., Li, Y., Meng, X., Zhou, T., Zhou, Y., Zheng, J., Zhang, J.-J., Li, H.-B.: Natural antioxidants in foods and medicinal plants: extraction, assessment and resources. Int. J. Mol. Sci. **18**(1), 96 (2017)
34. Makris, D.P., Boskou, D.: Plant-derived antioxidants as food additives. In: Plants as a Source of Natural Antioxidants, 1st edn, pp.169–190. Editors, Nawal Kishore Dubey (2014)
35. Jahan, M.S.: ESR insights into macroradicals in UHMWPE. Elsevier, UHMWPE Biomaterials Handbook (2016)
36. Halliwell, B.: How to characterize an antioxidant-an update. Biochem. Soc. Symp. **61**, 73–101 (1995)

37. Shi, H.L., Noguchi, N., Niki, N.: Comparative study on dynamics of antioxidative action of α-tocopheryl hydroquinone, ubiquinol. Free Radic. Biol. Med. **27**(3–4), 334–46 (1999)
38. Lewis, E.D., Meydani, S.N., Wu, D.: Regulatory role of vitamin e in the immune system and inflammation. IUBMB J. **71**(4), 487–494 (2019)
39. Tuckera, J.M., Townsend, D.M.: Alpha-tocopherol: roles in prevention and therapy of human disease. Biomed. Pharmacother. **59**(7), 380–387 (2005)
40. Dutta, A., Dutta, S.K.: Vitamin E and its role in the prevention of atherosclerosis and carcinogenesis: a review. J. Am. College Nutr. **22**, 258–68 (2003)
41. Jahan, M.S., Walters, B., Sharmin, A., Gomrok, S.: Book chapter 4, Free Radical Processes in Medical Grade UHMWPE. Computational Science and its Applications (2020)
42. Kumar, A., Kumar, N.P.M., Jose, A., Tomer, V., Oz, E., Proestos, C., Zeng, M., Elobeid, T., Sneha, K., Fatih, O.Z.: Major phytochemicals: recent advances in health benefits and extraction method. Molecules **28**(2), 887 (2023)
43. ALNasser, M.N., Mellor, I.R., Carter, W.G.: A preliminary assessment of the nutraceutical potential of acai berry (Euterpe sp.) as a potential natural treatment for Alzheimer's disease. Molecules **27**, 4891 (2022)
44. Darnet, S., Serra, J.L., Rodrigues, A.C., et al.: A highperformance liquid chromatography method to measure tocopherols in assai pulp (Euterpe oleracea). Food Res. Int. **44**(7), 2107–2111 (2011)
45. Peris, C.S., Caiado, R.R., Souza Lima-Filho, A.A., Rodrigues, E.B., Farah, M.E., Gonçalves, M.B., de Queiroz Alves, B., Palma Urushima, J.G., Ragazzi, R., Maia, M.: Analysis of anthocyanins extracted from the acai fruit (euterpe oleracea): a potential novel vital dye for chromovitrectomy. J Ophthalmol **9** (2018)
46. Fujita, A., Sarkar, D., Wu, S., Kennelly, E., Shetty, K., & Genovese, M.I.: Evaluation of phenolic-linked bioactives of camu-camu (Myrciariadubia Mc. Vaugh) for antihyperglycemia, antihypertension, antimicrobial properties and cellular rejuvenation. Food Res. Int. **77**, 194–203 (2015)
47. Chen, L., Zhu, Y., Hu, Z., Wu, S., Jin, C.: Beetroot as a functional food with huge health benefits: antioxidant, antitumor, physical function, and chronic metabolomics activity. Food Sci. Nutr. **9**(11), 6406–6420
48. Bhupinder, S., Bahadur, S.H.: Chemical composition, functional properties and processing of beetroot—a review. Int. J. Sci. Eng. Res. **5**(1) (2014)
49. Ebuehi, O.A.T., Anams, C., Gbenle, O.D., Ajagun-Ogunleye, M.O.: Hydro-ethanol seed extract of Theobroma cacao exhibits antioxidant activities and potential anticancer property. J. Food Biochem. **43**, e12767 (2019)
50. Chen, Q., Ganapathy, S., Singh, K.P., Shankar, S., Srivastava, R.K.: Resveratrol induces growth arrest and apoptosis through activation of FOXO transcription factors in prostate cancer cells. PLoS ONE **5**(12), e15288 (2010)
51. Gianfredi, V., Salvatori, T., Villarini, M., Moretti, M.: Can chocolate consumption reduce cardio-cerebrovascular risk? A system atic review and meta-analysis. Nutrition **46**, 103–114 (2018)
52. Scapagnini, G., Davinelli, S., Di Renzo, L., De Lorenzo, A., Olarte, H.H., Micali, G., Cicero, A.F., Gonzalez, S.: Cocoa bioactive compounds: significance and potential for the maintenance of skin health. Nutrients **6**, 3202–3213 (2014)
53. Del Castillo, M.D., Iriondo-DeHond, A., Fernández-Gómez, B., Martinez-Saez, N., Rebollo-Hernanz, M., Martín-Cabrejas, M.A., Farah, A.: Coffee antioxidants in chronic diseases. R. Soc. Chem. (UK) (2019)
54. Baratloo, A., Rouhipour, A., Forouzanfar, M.M., Safari, S., Amiri, M., Negida, A.: The role of caffeine in pain management: a brief literature review. Anesthesiol. Pain Med. (2016)
55. Green, U., Shenberger, Y., Aizenshtat, Z., Cohen, H., Ruthstein, S.: Exploring the radical nature of a carbon surface by electron paramagnetic resonance and a calibrated gas flow. J. Visual. Exp. (86):51548 (2014)

Algebraic Properties of Doubt ω-Fuzzy CI-Subalgebras and Ideals in CI-Algebra

M. Premkumar, Priya Shirley Muller, S. Maheswari, J. Juliet Jeyapackiam, A. Prasanna, Y. Prakash, and Salim Al Hudafi

Abstract In this research, we studied the new notion of Doubt (ω)-Fuzzy CI-Subalgebras $Doubt. \omega - FCI - SA$) and described the new idea of Doubt Triangular Norm (ω)-Fuzzy CI-Subalgebras and verified homomorphism of Doubt Triangular Norm (ω)-Fuzzy CI-Algebras $Doubt. \omega - FCI - SA$). Additionally, numerous algebraic properties including the Cartesian product of the Doubt Triangular Norm (ω) with Fuzzy CI-Algebras were studied.

Keywords CI-Algebra · Fuzzy Set (FS) · Fuzzy CI-Ideal ($FCI - I$) · Fuzzy CI-Subalgebra ($FCI - SA$) · Homomorphism of fuzzy CI-Algebra ($Hom - FCI - A$) · Endomorphism of a fuzzy CI-Algebra ($En - FCI - A$) · Epimorphism of fuzzy CI-Algebra ($Epi - FCI - A$) · Doubt ω Fuzzy Set ($Doubt \omega - ST$) · Doubt ω Fuzzy CI-Subalgebra ($Doubt \omega - FCI - SA$) · Doubt ω Fuzzy CI-Ideals ($Doubt \omega - FCI - Is$)

Mathematics Subject Classification MSC2020-zbMATH-03B52

M. Premkumar (✉) · P. S. Muller · S. Maheswari
Department of Mathematics, Sathyabama Institute of Science and Technology (Deemed To Be University), Chennai, Tamilnadu, India
e-mail: mprem.maths3033@gmail.com

J. Juliet Jeyapackiam
Department of Mathematics, Jayaraj Annapackiam CSI College of Engineering, Nazareth, Tuticorin, India

A. Prasanna
PG and Research Department of Mathematics, Jamal Mohamed College (Autonomous), (Affiliated to Bharathidasan University), Tiruchirappalli, Tamilnadu, India

Y. Prakash
CSI College of Engineering, Ketti, India

S. Al Hudafi
Department of Mathematics and IT, Center for Preparatory Studies, Sultan Qaboos University, Muscat, Oman
e-mail: salimsaid@squ.edu.om

1 Introduction

The idea of fuzzy sets was first developed by Zadeh [11] in 1965 In 2010, Meng [3] developed the idea of CI-algebras. 2014 saw a review of the theory of the Cartesian product of BE/ CI-algebras by Pathak et al. [6]. In 2016, Pulak Sabhapandit et al. [9] investigated the anti-fuzzy ideals notation for CI-algebras. In 2012, Sithar Selvam et al. [10] described the homomorphism of CI-algebras and anti-fuzzy subalgebras. In 2010, Meng [4] pioneered the idea of the closed filters in CI-algebras. In 2018, Chanwit Prabpayak [2] first discussed the idea of N-Fuzzy D-Subalgebras of D-Algebras. Year 2019 saw the introduction of N-Fuzzy BH-Subalgebras of BH-Algebras by Anitha and Kandaraj [1]. The notion of D-Algebras was first presented in 1999 by Neggers and Kim [5]. In 2022, Ismail et al. [7] introduced the concept of On Product of Doubt ψ-$\overline{Q}$- Fuzzy Subgroup, and in 2022, Premkumar et al. [8] detailed the new notation of a doubt ~~K~~-Q-Bipolar fuzzy BCI-Ideals and Fuzzy BCI-Implicative Ideals in 2022.

In this paper, we introduced the concept of Doubt Triangular Norm (ω)-Fuzzy CI-Subalgebras (*Doubt $\omega - FCI - SAs$*) and Homomorphism of CI-Algebras established some of its results in details.

2 Preliminaries

Definition 2.1 ([9]) Let X be a CI-algebra. A $FS \mu$ in X is called a $FCI - I$ of X if.

(i) $\mu(\hat{a}' * \hbar) \geq \mu(\hat{a}'), \forall \hat{a}', \hbar \in X$

(ii) $\mu((\hat{a}' * (\hbar * \check{c})) * \check{c}) \geq \min\{\mu(\hat{a}'), \mu(\hbar)\}, \forall x, y, \check{c} \in X$

Definition 2.2 ([10]) A *FS* μ in a CI-algebra X is called a $FCI - SA$ of X if $\mu(\hat{a}' * \hbar) \geq \min\{\mu(x), \mu(\hbar)\}, \forall \hat{a}', y \in X$.

Definition 2.3 It is a function $N : [0, 1]^2 \rightarrow [0, 1]$ satisfying the following properties.

(i) $N(\hat{a}', 1) = \hat{a}'$

(ii) $N(\hat{a}', \hbar) = N(\hbar, \hat{a}')$

(iii) $N(\hat{a}', N(\hbar, \check{c})) = N(N(\hat{a}', \hbar), \check{c})$

(iv) $N(\hat{a}', \hbar) \leq N(\hat{a}', \check{c})$ whenever $\hbar \leq \check{c}, \forall \hat{a}', \hbar, \check{c} \in [0, 1]$.

3 Triangular Norm (ω)-Fuzzy CI-Subalgebras in CI-Algebras

Definition 3.1 A Doubt *FS* ξ in a CI-Algebra of κ. Then ξ is called a *DoubtFCI − SA* of κ with respect to a *Doubtω − FCI − SA* of κ if the following conditions are satisfied:

$$\xi(\pi * \vartheta) \leq \{\xi(\pi)\omega\xi(\vartheta)\}, \forall \pi, \vartheta \in \kappa.$$

Example 3.1.1 Let $\kappa = \{0, a, b, c\}$ be a set.

*	0	a	b	c
0	0	0	0	0
a	a	0	0	a
b	b	b	0	0
c	c	c	c	0

Define a *Doubt FS* ξ of κ by $\xi(0) = 0.6$ and $\xi(\pi) = 0.3 \ \forall \pi \neq 0$.
We define a Triangular Norm,
$\omega : [0, 1]^2 \to [0, 1]$ by $\omega(\pi, \vartheta) = min\{\pi + \vartheta - 1, 0\}, \forall \pi, \vartheta \in \kappa.$

Theorem 3.2 *If κ be a CI-Algebra, let ξ be a Doubt $\omega - FCI - SA$ of κ and $\eta' \in [0, 1]$, then we have the following conditions:*

(i) *Let $\eta' = 1$, then the upper level of ξ in κ, $\Delta(\xi, \eta')$ is either empty or a CI-SA of κ.*
(ii) *Let $\omega = \wedge$, then $\Delta(\xi, \eta')$ is either empty or a Doubt FCI − SA of κ.*
(iii) *Let $\omega = \wedge$, then $\xi(0) \leq \xi(\pi), \forall \pi \in \kappa$.*

Proof

(i) Assume that $\Delta(\xi, 1)$ is not empty.

Let $\pi, \vartheta \in \Delta(\xi, 1)$. Thus, we have $\xi(\pi) \leq 1$ and $\xi(\vartheta) \leq 1$.
Since ξ is a *Doubt $\omega - FCI - SA$* of κ,
now

$$\xi(\pi * \vartheta) \leq \{\xi(\pi)\omega\xi(\vartheta)\}$$
$$\leq \{1\omega1\}$$
$$= 1.$$

$\Rightarrow \pi * \vartheta \in \Delta(\xi, 1)$.
$\therefore \Delta(\xi, 1)$ is a FCI-SA.

(ii)   Let us assume that $\Delta\big(\xi, \eta'\big)$ is not empty.

Let $\pi, \vartheta \in \Delta\big(\xi, \eta'\big)$. Then we have $\xi(\pi) \leq \eta'$ and $\xi(\vartheta) \leq \eta'$.
This follows that

$$\xi(\pi * \vartheta) \leq \{\xi(\pi)\omega\xi(\vartheta)\}$$
$$\leq \{\xi(\pi) \wedge \xi(\vartheta)\}$$
$$\leq \{\pi \wedge \pi\} = \pi$$

$\Rightarrow \pi * \vartheta \in \Delta\big(\xi, \eta'\big),$
   $\therefore \Delta\big(\xi, \eta'\big)$ is a CI-SA.

(iii)   Let $\pi * \pi = 0$, we have

$$\xi(0) = \xi(\pi * \pi)$$
$$\leq \{\xi(\pi) \ \omega \ \xi(\pi)\}$$
$$= \{\xi(\pi) \wedge \ \xi(\pi)\}$$
$$= \xi(\pi).$$

$$\Rightarrow \xi(0) \leq \xi(\pi), \forall \pi \in \kappa$$

∎

Theorem 3.3 *If ξ be a Doubt FS of CI-Algebra κ is a Doubt $\omega - FCI - SA$ iff for every $\eta' \in [0, 1]$, $\xi^{\eta'}$ is either empty or a SA of κ.*

Proof Let ξ be a *Doubt $\omega - FCI - SA$* of κ and $\xi^{\eta'} \neq \emptyset$.
   Then, for all, $\vartheta \in \xi^{\eta'}$,
   we have

$$\xi(\pi * \vartheta) \leq \{\xi(\pi) \ \omega \ \xi(\vartheta)\} \leq \eta'.$$

$\therefore \pi * \vartheta \in \xi^{\eta'}$. Hence, $\xi^{\eta'}$ is a *Doubt $\omega - FCI - SA$* of κ.
   Converse.
   Assume that $\pi * \vartheta \in \kappa$.
   Take $\eta' = \{\xi(\pi)\omega\xi(\vartheta)\}$.
   Then, by assumption, $\xi^{\eta'}$ is a *Doubt $\omega - FCI - SA$*

$$\therefore \xi(\pi * \vartheta) \leq \eta' = \{\xi(\pi) \ \omega \ \xi(\vartheta)\}.$$

$\therefore \xi$ is a *Doubt $\omega - FCI - SA$* of κ.

4 Homomorphism of Doubt Triangular Norm (ω)-Fuzzy CI-Subalgebras and Ideals in CI-Algebra

Definition 4.1 Let $\psi :' \Omega \to' Y$ be an endomorphism and ξ be a *Doubt $\omega - FS$* in κ. We define a *Doubt $\omega - FS$* in κ by ξ_ψ inδ as $\xi_\psi(\pi) = \xi(\psi(\pi))$, $\forall \pi \in \kappa$.

Definition 4.2 Let ψ be a mapping on a set κ, and ξ be a *Doubt $\omega - FS$* of $\psi(\kappa)$. Then the Doubt ω-FS ξ_ψ is called preimage of ξ under ψ.

Definition 4.3 Let κ be a CI-algebra. A Doubt FS ξ in κ is called a *Doubt $\omega - FCI - I$* of κ if

(i) $\xi(\pi * \vartheta) \le \xi(\vartheta)$, $\forall \pi, \vartheta \in \kappa$
(ii) $\xi((\pi * (\vartheta * \tau)) * \tau) \le \{\xi(\pi)\omega\xi(\vartheta)\}$, $\forall \pi, \vartheta, \tau \in \kappa$.

Definition 4.4 Let $('\Omega, *, \nu)$ and $('Y, \circ, \nu')$ be CI-algebras. A mapping $\psi :' \Omega \to' Y$ is said to be a homomorphism if $\psi(\pi * \vartheta) = \psi(\pi)^\circ \psi(\vartheta)$, $\forall \pi, \vartheta \in \kappa$.

Lemma 4.4 *The epimorphism preimage of a Doubt $\omega - FCI - SA$ of κ is a Doubt $\omega - FCI - SA$.*

Theorem 4.5 *If $\psi :' \Omega \to' Y$ be an $Epi - FCI - A$ and ξ be a Doubt $\omega - FCI - SA$ of Y, then ξ_ψ is a Doubt $\omega - FCI - SA$ of κ.*

Proof Let $\psi :' \Omega \to' Y$ be an $Epi - FCI - A$ and ξ_ψ is obviously a *Doubt $\omega - FS$* of κ.

Let $\pi, \vartheta \in \kappa$. Then $\xi_\psi(\pi * \vartheta) = \xi(\psi(\pi * \vartheta))$

$$
\begin{aligned}
&= \xi((\psi(\pi) * \psi(\vartheta)) \\
&= \xi((\psi(\pi) * \psi(\vartheta)) \\
&\le \{\xi(\psi(x)) \, \omega \, \xi(\psi(\vartheta))\} \\
&\le \{\xi_\psi(\pi) \, \omega \, \xi_\psi(\vartheta)\}
\end{aligned}
$$

Hence, ξ_ψ is a *Doubt $\omega - FCI - SA$* of κ. ∎

Theorem 4.6 *If ψ be an $En - FCI - A$ of κ. Then ξ is a Doubt $\omega - FCI - I$ of κ, then so is ξ_ψ.*

Proof Let ψ be an $En - FCI - A$ of κ.

Let $\pi, \vartheta, \tau \in \kappa$

$$
\begin{aligned}
\xi_\psi\{(\pi * (\vartheta * \tau)) * \tau\} &= \xi\{\psi((\pi * (\vartheta * \tau)) * \tau\} \\
&= \xi\{\psi(\pi * (\vartheta * \tau)) * \psi(\tau)\} \\
&= \xi\{(\psi(\pi) * \psi(\vartheta * \tau)) * \psi(\tau)\} \\
&= \xi\{(\psi(\pi) * (\psi(\vartheta) * \psi(\tau))) * \psi(\tau)\}
\end{aligned}
$$

$$\leq \{\xi(\psi(\pi))\,\omega\,\xi(\psi(\vartheta))\}$$
$$= \big\{\xi_\psi(\pi)\,\omega\,\xi_\psi(\vartheta)\big\}$$
$$\therefore \xi_\psi\{(\pi * (\vartheta * \tau)) * \tau\} \leq \big\{\xi_\psi(\pi)\,\omega\,\xi_\psi(\vartheta)\big\}$$

Hence, ξ_ψ is a *Doubt* $\omega - FCI - I$ of κ. ∎

Theorem 4.7 *Let* $\psi :' \Omega \to' Y$ *be a* $Homo - FCI - A$. *If* ξ *is a* $Doubt\ \omega - FCI - I$ *of* Y *then* ξ_ψ *is a* $Doubt\ \omega - FCI - I$ *of* κ.

Proof Let $\pi, \vartheta, \tau \in \kappa$.

Now, $\xi_\psi\{(\pi * (\vartheta * \tau)) * \tau\} = \xi\{\psi((\pi * (\vartheta * \tau)) * \tau\}$

$$= \xi\{\psi(\pi * (\vartheta * \tau)) \,^\circ\, \psi(\tau)\}$$
$$= \xi\{(\psi(\pi) \,^\circ\, \psi(\vartheta * \tau)) \,^\circ\, \psi(\tau)\}$$
$$= \xi\big\{(\psi(\pi)^\circ(\psi(\vartheta)^\circ\psi(\tau)))^\circ\psi(\tau)\big\}$$
$$\leq \{\xi(\psi(\pi))\,\omega\,\xi(\psi(\vartheta))\}$$
$$= \big\{\xi_\psi(\pi)\,\omega\,\xi_\psi(\vartheta)\big\}$$

$$\therefore \xi_\psi\{(\pi * (\vartheta * \tau)) * \tau\} \leq \big\{\xi_\psi(\pi)\,\omega\,\xi_\psi(\vartheta)\big\}.$$

Hence, ξ_ψ is a *Doubt* $\omega - FCI - I$ of κ. ∎

5 Doubt Triangular Norm (ω)-Fuzzy CI-Subalgebras in Cartesian Product of CI- Algebras

Definition 5.1 An ξ_1 and ξ_2 be *Doubt* $\omega - FCI - SA$ of a CI-Algebra κ. The direct product of *Doubt* $\omega - FCI - SAs$ ξ_1 and ξ_2 defined by $\xi_1 \times \xi_2(\pi, \vartheta) = \{\xi_1(\pi)\omega\xi_2(\vartheta)\}, \forall \pi, \vartheta \in \kappa$.

Theorem 5.2 *If* ξ_1 *and* ξ_2 *be* $Doubt\ \omega - FCI - SA$ *of a CI-Algebra* κ, *let* κ *be a CI-Algebra. Then* $\xi_1 \times \xi_2$ *is a* $Doubt\ \omega - FCI - SA$ *of* κ.

Proof Let ξ_1 and ξ_2 be *Doubt* $\omega - FCI - SA$ of a CI-Algebra κ.

Put $\xi = \xi_1 \times \xi_2$, and let $\pi, \vartheta \in \kappa$.

Then, we have

$$\xi((\pi_1, \pi_2) * (\vartheta_1, \vartheta_2)) = \xi(\pi_1 * \vartheta_1, \pi_2 * \vartheta_2)$$
$$= (\xi_1 \times \xi_2)(\pi_1 * \vartheta_1, \pi_2 * \vartheta_2)$$
$$= \{\xi_1(\pi_1 * \vartheta_1)\omega\xi_2(\pi_2 * \vartheta_2)\}$$
$$\leq \{(\xi_1(\pi_1)\omega\xi_1(\vartheta_1))\omega(\xi_2(\pi_2)\omega\xi_2(\vartheta_2))\}$$

$$= \{(\xi_1(\pi_1)\omega\xi_2(\pi_2))\omega(\xi_1(\vartheta_1)\omega\xi_2(\vartheta_2))\}$$
$$= \{((\xi_1 \times \xi_2)(\pi_1, \pi_2))\omega((\xi_1 \times \xi_2)(\vartheta_1, \vartheta_2))\}$$
$$= \{\xi(\pi_1, \pi_2)\omega\xi(\vartheta_1, \vartheta_2)\}.$$

Hence, $\xi_1 \times \xi_2$ is a *Doubt $\omega - FCI - SA$* of κ. ∎

6 Conclusion

Hence, we have discussed the Doubt Triangular Norm (ω)-Fuzzy CI-Subalgebras in CI-Algebra, which adds another dimension to the defined Homomorphism of Doubt Triangular Norm (ω)-Fuzzy CI-Subalgebras and Ideals in CI-Algebra and Cartesian Product of Doubt Triangular Norm (ω)-Fuzzy CI-Subalgebras in CI-Algebra. This concept can further be generalized to fuzzy translation and multiplication of Doubt Triangular Norm (ω)-Fuzzy CI-Subalgebra of CI-Algebra in our future work.

References

1. Anitha, K., Kandaraj, N.: N-Fuzzy BH-Subalgebras of BH-Algebras. Int. J. Sci. Res. **8**, 26–27 (2019)
2. Prabpayak, C.: N-Fuzzy D-Subalgebras of D-Algebras. Int. J. Manag. Appl. Sci. **4**, 70–72 (2018)
3. Meng, B.L.: CI—algebras. Sci. Math. Japon. **71**, 11–17 (2010)
4. Meng, B.L.: Closed filters in CI—algebras. Sci. Math. Japon. **71**, 367–372 (2010)
5. Neggers, J., Kim, H.S.: On d-algebras. Math. Slovaca **49**, 19–26 (1999)
6. Pathak, K., Sabhapandit, P., Chetia, B.C.: Cartesian product of BE/CI—algebras with essences and atoms. Acta Ciencia Indica **3**, 271–279 (2014)
7. Mohamed Ismail, A., Premkumar, M., Prasanna, A., Ismail Mohideen, S., Kumar Shukla, D.: On Product of Doubt $\psi - \overline{Q} -$Fuzzy Subgroup, IOT with Smart Systems, Smart Innovation, Systems and Technologies, vol. 312, pp. 412–416 (2023). https://doi.org/10.1007/978-981-19-3575-6_41
8. Premkumar, M., Girija Bai, H., Kumar Shukla, D., Garg, A.K., Prasanna, A., Ismail Mohideen, S.: A Doubt ₭-Q-Bipolar fuzzy BCI-ideals and doubt ₭-Q-Bipolar Fuzzy BCI-Implicative ideals in BCI-Algebra. J. Pharm. Negat. Result. **13**(3), 147–151 (2022). https://doi.org/10.47750/pnr.2022.13.S03.024
9. Sabhapandit, P., Chetia, B.C.: Anti-Fuzzy Ideals in CI-Algebras. Int. J. Math. Trends Technol. **30**, 95–99 (2016)
10. Sithar Selvam, P.M., Priya, T., Ramachandran, T.: Anti Fuzzy Subalgebras and Homomorphism of CI-Algebras. Int. J. Eng. Res. Technol. **1**, 1–6 (2012)
11. Zadeh, L.A.: Fuzzy sets, information. Inf. Control. **8**, 338–353 (1965)

Elastoplastic Behavior of Transversely Isotropic Piezoelectric Disc Made of Functionally Graded Material with Variable Thickness Under Rotation

Richa Sharma , **Vikash Ghlawat, and Khursheed Alam**

Abstract The aspiration of the present research paper is to present analysis of stresses distribution and displacement in a circular disc under the effect of rotation and of transversely isotropic piezoelectric functionally graded material with variable thickness. The stress components have been deduced analytically by using transition theory. The various components of stress are derived for the disc under rotation by applying the transition theory developed by Seth. Electrical displacement and mechanical stress equations are calculated using the stress–strain relationship. By inserting the obtained relation into the equilibrium equation, the unequal differential equation is derived. With the increasing value of thickness parameter, the radial stress changes in the intermediate surface of the rotating disk. Results have been discussed numerically and depicted graphically.

R. Sharma (✉)
Department of Mathematics, Jaypee Institute of Information Technology, Noida, Uttar Pradesh, India
e-mail: richa.sharma@mail.jiit.ac.in

V. Ghlawat · K. Alam
Department of Mathematics, School of Basic Sciences and Research, Sharda University, Greater Noida, Uttar Pradesh, India
e-mail: 2020400516.vikash@dr.sharda.ac.in

K. Alam
e-mail: khursheed.alam@sharda.ac.in

1 Introduction

In the present time, the smart materials are of vast significance in engineering and scientific research. Smart materials are defined as the materials having properties which can be changed significantly by the applications of external stimuli, for intense stress, by variation in temperature, moistness, pH, electric, or magnetic fields. Examples of smart materials are materials that exhibit piezoelectric characteristics, shape memory polymers and such type of alloys, pH sensitive polymer, magneto caloric material, pyroelectric material, and thermo-piezoelectric material. The internal generation of an electric current has a result of mechanical force applications is known as direct piezoelectric material. The material which exhibits piezoelectric effect are known as piezoelectric material. Piezoelectric material is widely used in various sensing devices, waves, shock control devices, MEMS devices, navigation, medical instruments, household kitchen appliances, and smart structures. Most commonly piezoelectric materials that we used are Quartz, Barium Titanate (BaTiO$_3$), Rochelle Salt, and polyvinylidene fluoride.

To ensure that piezoelectric devices function reliably under varying temperature conditions, it is essential to introduce temperature effects while developing mathematical models of scientific research problems. Therefore, electrothermal coupling theory and thermomechanical coupling thermoelastic theory are presented by different authors. Mindlin [1] derived a theory of piezoelectric thermoelastic materials. A few years later, Mindlin [2] developed equations for thermoelastic piezoelectric materials under the influence of high-frequency vibration. Chandrasekharaiah [3] extended Mindlin's piezoelectric theory to account for finite rates of thermal oscillations. Tauchert [4] later applied this thermoelastic theory of piezoelectric materials to composite panels. Eringen [5] included the effect of electromagnetic field in micropolar thermoelasticity. Eringen [6] derived micropolar piezoelectricity. This theory can be applied to porous electric materials and various synthetic materials also. There is great used of this theory in intelligent structure system, piezoelectric composite structure appliances, loud speakers, and ultra-sonic transducers. Iesan [7] presented linear theory of piezoelectricity for microstretch piezoelectric materials and proved uniqueness and reciprocity theorems. Marin [8] derived the expression for the solutions of elasticity problems concerned with dipolar porous materials. Migroski and Ochal [9] discussed the dynamical bilateral problem for viscoelastic piezo thermoelastic medium with the adhesion effect. Sharma and Sharma [10] discussed harmonic plane waves in an anisotropic piezoelectric thermoelastic medium. Othman and Ahmed [11] discussed the rotational effect on the piezo electric thermoelastic medium under four different theories of thermoelasticity. The fundamental governing equations for an anisotropic porous magneto-piezo thermoelastic media were introduced by Kumar and Sharma [12]. This model establishes the reciprocity theorem, the uniqueness theorem, and the variational principle. In 2016, Kumar and Sharma established the variational principle, uniqueness, and reciprocity theorems for porous magnetic piezo-thermoelastic media. Sharma and Radakovic [13] find an analytical solution of elastic–plastic stresses in thin rotating

disc composed of piezoelectric material. Eringen, A.C. [14] developed a continuous theory of microstretch elasticity subject to electromagnetic fields as a microstructural model to calculate deformations and stress fields in elastic solids with interconnected voids, microcracks, or stretchable microelements. Iesan and Quintanilla [15] investigated the effects of a concentrated heat source and a concentrated volume charge density using the linear theory of microstretch thermos piezoelectricity.

In last four decades, many scientific and engineering applications have forced the researchers to work with functionally graded materials. Atkinson and List [16] investigated steady-state crack transmission in medium with elastic moduli variation as exponentially. The plane elasticity problem for a nonhomogeneous medium with a crack was examined by Delale and Erdogan [17], who demonstrated that the thickness constraint and Poisson's ratio have a minor impact on the stress intensity factors. Noda and Jin [18] and Jin and Noda [19] also measured cracks under the effect of transient thermal loads. Recently, Gunghas et al. [20] and Kalkal et al. [21] have studied several issues of micropolar functionally graded materials.

In this present research, we have considered the piezoelectric effect and transversely isotropic properties for functionally graded material, i.e., FGMs. The dynamical problem is then solved by using analytical technique. The boundary conditions for stress components have been solved numerically. The resulting physical parameters are depicted graphically to explore the effect of piezoelectric parameter and rotation effect. In this paper, elastic and plastic parameters have been computed in a disc with rotation composed of transversely isotropic piezoelectric material with internal pressure by applying transition theory.

2   Mathematical Formulation

We take a thin disc under rotation having a & b as internal radius and external radius, respectively, and ω as angular velocity of the disc. A thin disc is assumed as we are discussing the state of plane stress, i.e., $(T_{zz} = 0)$.

Displacement components are

$$u = r(1 - \beta), v = 0, w = dz, \beta = f(r) \tag{1}$$

where β is a function of $r = \sqrt{x^2 + y^2}$ and d is some constant.

Now stress–strain relation for this problem is

$$T_{\mathrm{rr}} = (c_{11}e_{\mathrm{rr}} + (c_{11} - 2c_{66})\,e_{\Theta\Theta} + c_{13}e_{22} - e_{11}E_{\mathrm{r}}$$

$$T_{\Theta\Theta} = (c_{11} - 2c_{66})e_{\mathrm{rr}} + c_{11}e_{\Theta\Theta} + c_{13}e_{zz} - e_{12}E_{\mathrm{r}}$$

$$T_{zz} = T_{zr} = T_{r\Theta} = T_{\Theta z} = 0 \tag{2}$$

Components of strain are as follows:

$$e_{rr} = \frac{1}{n}\left[1 - (r\beta' + \beta)^n\right] = \frac{1}{n}(1 - \beta^n(1+p)^n), \ e_{\theta\theta} = \frac{1}{n}\left[1 - \beta^n\right],$$

$$e_{zz} = \frac{1}{n}\left[1 - (1-d)^n\right]E_r = \frac{1}{\eta_{11}}\left[\frac{1}{r} - \frac{e_{11}}{n}(1 - \beta^n(1+\rho)^n) - \frac{e_{12}}{n}(1 - \beta^n)\right] \tag{3}$$

For functionally graded material, the material constants are assumed as

$$c_{11} = c_{011}\left(\frac{r}{b}\right)^k, \ c_{66} = c_{066}\left(\frac{r}{b}\right)^k, \ c_{13} = c_{013}\left(\frac{r}{b}\right)^k, \ c_{12} = c_{012}\left(\frac{r}{b}\right)^k, \ h = h_0\left(\frac{r}{b}\right)^m \tag{4}$$

Equation of equilibrium for rotating disc:

$$\frac{d}{dr}(hrT_{rr}) - hT_{\theta\theta} + \rho h\omega^2 r^2 = 0 \tag{5}$$

Putting the values from Eqs. (2) to (4) in Eq. (5), we get a nonlinear differential equation in β as

$$-\left(C_{011}\beta^{n+1} + \beta^{n+1}\left(\frac{r}{b}\right)^{-k}\frac{\epsilon_{11}^2}{\eta_{11}}\right)p(1+p)^{n-1}\frac{dp}{d\beta}$$

$$= +\beta^n p\left\{(c_{011} - 2c_{066})\left(\frac{r}{b}\right)^k - \frac{e_{11}e_{12}}{\eta_{11}}\cdot\frac{1}{r}\right\}$$

$$- \frac{1}{n}(1 - \beta^n)\left\{(k+m+1)(c_{011} - 2c_{066})\left(\frac{r}{b}\right)^k + \frac{m}{r}.e_{11}e_{12} - c_{011}\left(\frac{r}{b}\right)^k - \frac{e_{12}^2}{\eta_{11}}\right\}$$

$$- \frac{1}{n}\left[1 - \beta(1+p)^n\right]\left\{(k+m)c_{011}\left(\frac{r}{b}\right)^k + \frac{e_{11}^2}{\eta_{11}}(k+1) + 2c_{066}\left(\frac{r}{b}\right)^k - \frac{e_{11}e_{12}}{\eta_{11}}\right\}$$

$$- \frac{1}{n}(1 - (1-d)^n)\left\{c_{013}(k+m)\left(\frac{r}{b}\right)^k\right\} + m\frac{e_{11}}{\eta_{11}}\cdot\frac{1}{r} - \frac{e_{12}}{\eta_{11}}\cdot\frac{1}{r} - \rho w^2 r^2 \tag{6}$$

Boundary conditions are assumed as

$$T_{rr} = -p_1 atr = a; \ T_{rr} = -p_2 atr = b \tag{7}$$

3   Transition from Elastic to Plastic State

According to transition theory, a material in an elastic state change to plastic at a critical point $P \to \pm\infty$.

For evaluation of stresses, transition function is taken as

$$R = T_{rr} + B, \text{ where B is constant} \tag{8}$$

Taking logarithmic differentiation of Eq. (8), we get

$$\frac{d}{dr}(\log R) = \frac{\splitfrac{\beta^n p \left\{ (c_{011} - 2c_{066})\left(\frac{r}{b}\right)^k - \frac{e_{11}e_{12}}{\eta_{11}} \cdot \frac{1}{r} \right\}}{}}{}$$

$$\beta^n p \left\{ (c_{011} - 2c_{066})\left(\frac{r}{b}\right)^k - \frac{e_{11}e_{12}}{\eta_{11}} \cdot \frac{1}{r} \right\}$$

$$-\frac{1}{n}(1 - \beta^n)\left\{ \begin{array}{l} (k+m+1)(c_{011} - 2c_{066})\left(\frac{r}{b}\right)^k \\[4pt] +\frac{m}{r}.e_{11}e_{12} - c_{011}\left(\frac{r}{b}\right)^k - \frac{e_{12}^2}{\eta_{11}} \end{array} \right\}$$

$$-\frac{1}{n}[1 - \beta^n(1+p)^n]\left\{ \begin{array}{l} (k+m)c_{011}\left(\frac{r}{b}\right)^k \\[4pt] +\frac{e_{11}^2}{\eta_{11}}(m+1) + 2c_{066}\left(\frac{r}{b}\right)^k - \frac{e_{11}e_{12}}{\eta_{11}} \end{array} \right\}$$

$$-\frac{1}{n}(1 - (1-d)^n)\left\{ c_{013}(k+m)\left(\frac{r}{b}\right)^k \right\} + m\frac{e_{11}}{\eta_{11}}.\frac{1}{r} - \frac{e_{12}}{\eta_{11}}.\frac{1}{r} - \rho w^2 r^2$$

$$+\frac{\beta^n p}{r}\left\{ (c_{011} - 2c_{066})\left(\frac{r}{b}\right)^k - \frac{e_{11}e_{12}}{\eta_{11}} \right\} + \frac{k}{r}\frac{c_{013}}{r}\left(\frac{r}{b}\right)^k (1 - (1-d)^n)$$

$$+\frac{e_{11}}{\eta_{11}r^2} + \frac{k}{r}\frac{c_{011}}{n}\left(\frac{r}{b}\right)^k (1 - \beta^n(1+p)^n)$$

$$\frac{+\frac{k}{r}\left(\frac{c_{011} - 2c_{066}}{n}\right)\left(\frac{r}{b}\right)^k (1 - \beta^n)}{c_{011}\left(\frac{r}{b}\right)^k.\frac{1}{n}[1 - \beta^n(1+p)^n] + \left(\frac{c_{011} - 2c_{066}}{n}\right)\left(\frac{r}{b}\right)^k (1 - \beta^n)}$$

$$+\frac{c_{013}}{n}\left(\frac{r}{b}\right)^k (1 - (1-d)^n) + \frac{e_{11}^2}{n\eta_{11}}(1 - \beta^n(1+p)^n)$$

$$+\frac{e_{11}e_{12}}{n\eta_{11}}(1 - \beta^n)\frac{-e_{11}}{\eta_{11}}.\frac{1}{r} + B \tag{9}$$

Applying $P \to \pm\infty$ in Eq. (9), we get

$$\frac{d}{dr}(\log R) = \frac{\left[k + m - \frac{k}{r}\right]c_{011} + 2c_{066} + (m+1)\left(\frac{e_{11}^2}{\eta_{11}} - \frac{e_{11}e_{12}}{\eta_{11}}\right)\left(\frac{b}{r}\right)^k}{-c_{011} - \frac{e_{11}^2}{n\eta_{11}}}$$

$$(\log R) = \frac{\left[(k+m)r - k\log r\right]c_{011} + 2rc_{066} - \frac{k}{b(m+1)\left(\frac{e_{11}^2}{\eta_{11}} - \frac{e_{11}e_{12}}{\eta_{11}}\right)\left(\frac{r}{b}\right)^{-k-1}}}{-c_{011} - \frac{e_{11}^2}{n\eta_{11}}} + \log A$$

$$R = Ae^F$$

where
$$F = \frac{\left[(k+m)r - k\log r\right]c_{011} + 2rc_{066} - k/b(m+1)\left(\frac{e_{11}^2}{\eta_{11}} - \frac{e_{11}e_{12}}{\eta_{11}}\right)\left(\frac{r}{b}\right)^{-k-1}}{-c_{011} - \frac{e_{11}^2}{n\eta_{11}}}$$

$$(10)$$

From Eqs. (3) and (10), the expressions for transitional stresses are as follows:

$$t_{rr} = Ae^F - B, \quad t_{\theta\theta} = (1+m)\left(Ae^F - B\right) + rAe^F F' + \rho w^2 r^2 \tag{11}$$

Using Eqs. (7) and (11), we have

$$A = \frac{p_2 - p_1}{\left(e^F\right)_b - \left(e^F\right)_a}, \quad B = \frac{-p_2\left(e^F\right)_a + p_1\left(e^F\right)_b}{\left(e^F\right)_b - \left(e^F\right)_a} \tag{12}$$

Using Eqs. (11) and (12), transitional stresses are

$$t_{rr} = \frac{p_2 - p_1}{\left(e^F\right)_b - \left(e^F\right)_a}e^F + \frac{-p_2\left(e^F\right)_a + p_1\left(e^F\right)_b}{\left(e^F\right)_b - \left(e^F\right)_a}$$

$$t_{\theta\theta} = (1+m)\left(\frac{p_2 - p_1}{\left(e^F\right)_b - \left(e^F\right)_a}e^F + \frac{p_2\left(e^F\right)_a - p_1\left(e^F\right)_b}{\left(e^F\right)_b - \left(e^F\right)_a}\right)$$

$$+ r\frac{p_2 - p_1}{\left(e^F\right)_b - \left(e^F\right)_a}e^F F' + \rho w^2 r^2 \tag{13}$$

Fully plastic stresses are given as

$$t_{rr} = \frac{p_2 - p_1}{\left(e^{F1}\right)_b - \left(e^{F1}\right)_a}F1 + \frac{-p_2\left(e^{F1}\right)_a - p_1\left(e^{F1}\right)_b}{\left(e^{F1}\right)_b - \left(e^{F1}\right)_a}$$

$$t_{\theta\theta} = (1+m)\left(\frac{p_2 - p_1}{\left(e^{F1}\right)_b - \left(e^{F1}\right)_a}F1 + \frac{p_2\left(e^{F1}\right)_a - p_1\left(e^{F1}\right)_b}{\left(e^{F1}\right)_b - \left(e^{F1}\right)_a}\right)$$

$$+ r\frac{p_2 - p_1}{\left(e^{F1}\right)_b - \left(e^{F1}\right)_a}e^{F1}F1' + \rho w^2 r^2$$

$$\text{where } F_1 = \frac{k/b(m+1)\left(\frac{e_{11}^2}{\eta_{11}} - \frac{e_{11}e_{12}}{\eta_{11}}\right)\left(\frac{r}{b}\right)^{-k-1}}{c_{011} + \frac{e_{11}^2}{n\eta_{11}}} \tag{14}$$

From Eq. (13), we have Tressa's yield criteria as

$$|t_{rr} - t_{\theta\theta}| = \left| \frac{p_2 - p_1}{(e^F)_b - (e^F)_a} F + \frac{-p_2(e^F)_a + p_1(e^F)_b}{(e^F)_b - (e^F)_a} + r\frac{p_2 - p_1}{(F)_b - (F)_a} F' - \rho w^2 r^2 \right| \tag{15}$$

From Eq. (15), it is evaluated that $|t_{rr} - t_{\theta\theta}|$ yields maximum value at r = a which result in

$$|t_{rr} - t_{\theta\theta}|_{r=a} = \left| \begin{array}{c} m\left(\dfrac{p_2 - p_1}{(e^F)_b - (e^F)_a} F + \dfrac{p_2(e^F)_a - p_1(e^F)_b}{(e^F)_b - (e^F)_a}\right) \\[4mm] + r\dfrac{p_2 - p_1}{(e^F)_b - (e^F)_a} e^F F' + \rho w^2 r^2 \end{array} \right|_{r=a} = \gamma \tag{16}$$

Also, it has been analyzed that at r = b, Eq. (15) yields a fully plastic yielding stress as

$$|t_{rr} - t_{\theta\theta}|_{r=b} = \left| \begin{array}{c} m\left(\dfrac{p_2 - p_1}{(e^F)_b - (e^F)_a} F + \dfrac{p_2(e^F)_a - p_1(e^F)_b}{(e^F)_b - (e^F)_a}\right) \\[4mm] + r\dfrac{p_2 - p_1}{(e^F)_b - (e^F)_a} e^F F' + \rho w^2 r^2 \end{array} \right|_{r=b} = \gamma_1 \tag{17}$$

Now, the non-dimensional form of all the parameters is defined as

$$R = \frac{r}{b}, R_0 = \frac{a}{b}, t_{r1} = \frac{\sigma_{rr}}{\gamma}, t_{\theta1} = \frac{\sigma_{\theta\theta}}{\gamma}, t_{r2} = \frac{\sigma_{rr}}{\gamma_1}, t_{\theta2} = \frac{\sigma_{\theta\theta}}{\gamma_1}, \Omega = \frac{\rho\omega^2 a^2}{\gamma},$$

$$\Omega_1 = \frac{\rho\omega^2 b^2}{\gamma_1}, P_f = \frac{p_1}{Y_1} = P_{f1}\frac{p_2}{Y_1} = P_{f2}, \frac{p_1}{Y} = P_{i1}, \frac{p_2}{Y} = P_{i2} \tag{18}$$

From Eq. (14), non-dimensional form of transitional stresses is given as

$$t_{r1} = \frac{P_{i2} - P_{i1}}{(e^F)_b - (e^F)_a} e^F + \frac{P_{i2}(e^F)_a - P_{i1}(e^F)_b}{(e^F)_b - (e^F)_a}$$

$$t_{\theta 1} = (1 + m)\left(\frac{P_{i2} - P_{i1}}{(e^F)_b - (e^F)_a}e^F + \frac{P_{i2}(e^F)_a - P_{i1}(e^F)_b}{(e^F)_b - (e^F)_a}\right)$$
$$+ r\frac{P_{i2} - P_{i1}}{(e^F)_b - (e^F)_a}e^F F\prime + \Omega \tag{19}$$

Fully plastic stresses in non-dimensional form of Eq. (19) are

$$t_{r2} = \frac{P_{i2} - P_{i1}}{(e^{F1})_b - (e^{F1})_a}e^{F1} + \frac{P_{i2}(e^{F1})_a - P_{i1}(e^{F1})_b}{(e^{F1})_b - (e^{F1})_a}$$

$$t_{\theta 2} = (1 + m)\left(\frac{P_{i2} - P_{i1}}{(e^{F1})_b - (e^{F1})_a}e^{F1} + \frac{P_{i2}(e^{F1})_a - P_{i1}(e^{F1})_b}{(e^{F1})_b - (e^{F1})_a}\right)$$

$$+ r\frac{P_{i2} - P_{i1}}{(e^F)_b - (e^F)_a}e^{F1}F1' + \Omega_1$$

$$\text{where} F_1 = \frac{k/b(m + 1)\left(\frac{e_{11}^2}{\eta_{11}} - \frac{e_{11}e_{12}}{\eta_{11}}\right)(R)^{-k-1}}{c_{011} + \frac{e_{11}^2}{n\eta_{11}}} \tag{20}$$

4 Numerical Discussions

Figures 1, 2, 3, and 4 are drawn for transitional hoop and radial stresses with different values of radii ratios, angular velocity, and pressure for piezoelectric materials BaTiO4 and PZT4. Figures 1a and b are drawn with internal pressure 5, external pressure 10, and angular velocity 5. It is observed from the figure that the radial stress increases with increasing value of the radius ratio and is maximum at the outer surface of the disc. Circumferential stresses decreases with radii ratios and attains their maximum value at the internal surface of the disc, also the stress is maximum for k = 3. Hoop stresses are maximum for piezoelectric material BaTiO4. These stresses increase with the increasing value of angular velocity as can be seen from Figs. 2a, b. It is observed from the Fig. 3a, b that radial stresses are increasing with the radio ratio and hoop stresses are decreasing with the radio ratios. Hoop stresses are maximum at the internal surface. These stresses increase with increasing value of angular velocity as observed from Fig. 4a, b.

Figures 5, 6, 7, and 8 are drawn for fully plastic hoop and radial stresses with different values of radii ratios, angular velocity, and pressure for piezoelectric materials BaTiO4 and PZT4. Fully plastic hoop stresses are maximum at the internal surface and radial stresses are maximum at the outer surface of the disc as can be seen from Fig. 5a, b. These stresses increase with increasing value of angular velocity. It is observed from Fig. 7a, b that radial stresses are increasing with the radio ratio
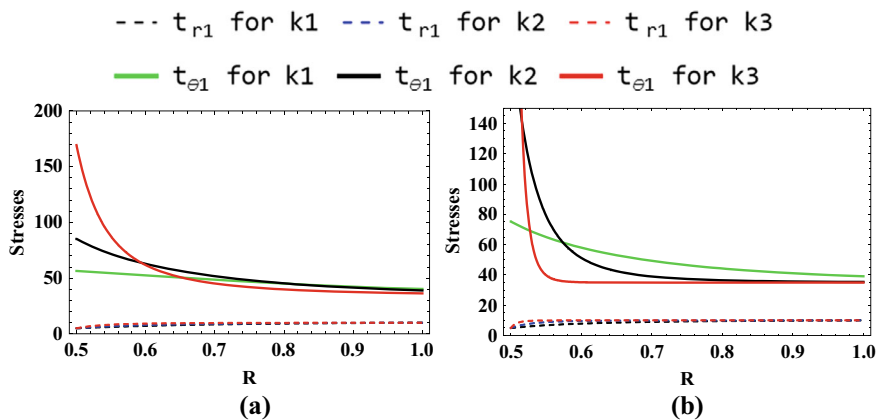
Fig. 1 Radial and hoop stresses for piezoelectric materials with $\Omega = 5; p_1 = 5; p_2 = 10$
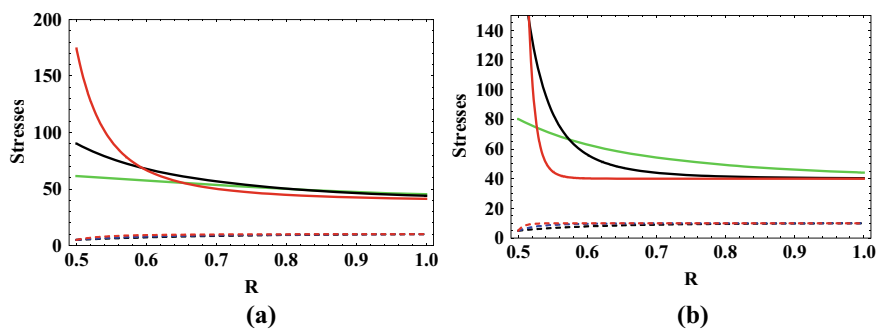
Fig. 2 Radial and hoop stresses for piezoelectric materials with $\Omega = 10; p_1 = 5; p_2 = 10$
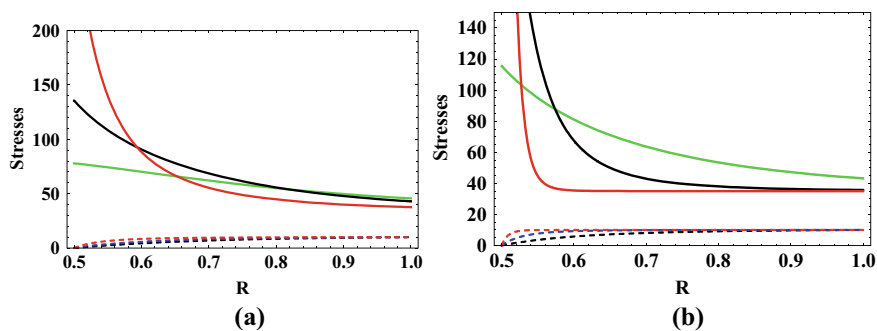
Fig. 3 Radial and hoop stresses for piezoelectric materials with $\Omega = 5; p_1 = 0; p_2 = 10$
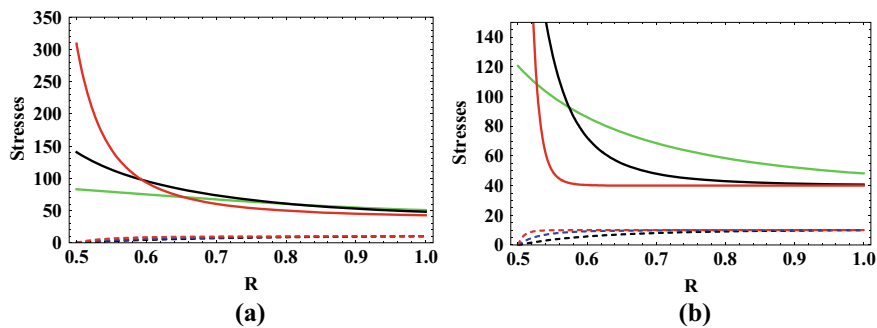
Fig. 4 Radial and hoop stresses for piezoelectric materials with $\Omega = 10$; $p_1 = 0$; $p_2 = 10$
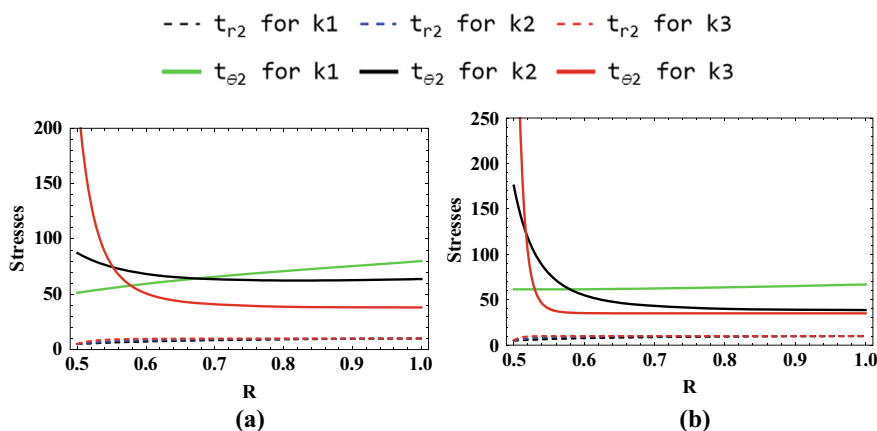
Fig. 5 Fully plastic stresses for piezoelectric materials with $\Omega = 5$; $p_1 = 5$; $p_2 = 10$

and hoop stresses are decreasing with the radio ratios. Hoop stresses are maximum at the internal surface. These stresses increase with increasing value of angular velocity as observed from Fig. 8a, b.

Fig. 6 Fully plastic stresses for piezoelectric materials with $\Omega = 10$; $p_1 = 5$; $p_2 = 10$

Fig. 7 Fully plastic stresses for piezoelectric materials with $\Omega = 5$; $p_1 = 0$; $p_2 = 10$

Fig. 8 Fully plastic stresses for piezoelectric materials with $\Omega = 10$; $p_1 = 0$; $p_2 = 10$
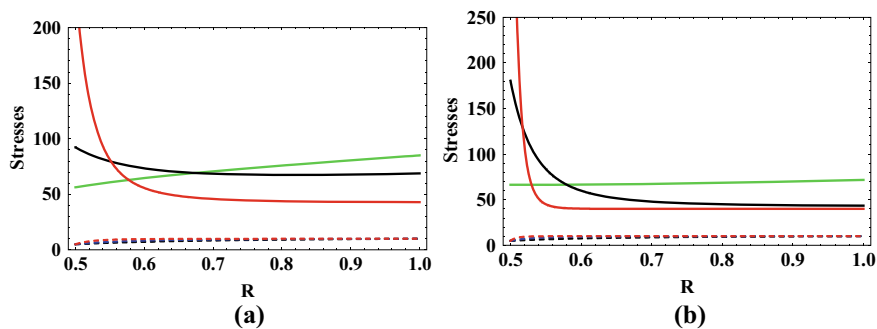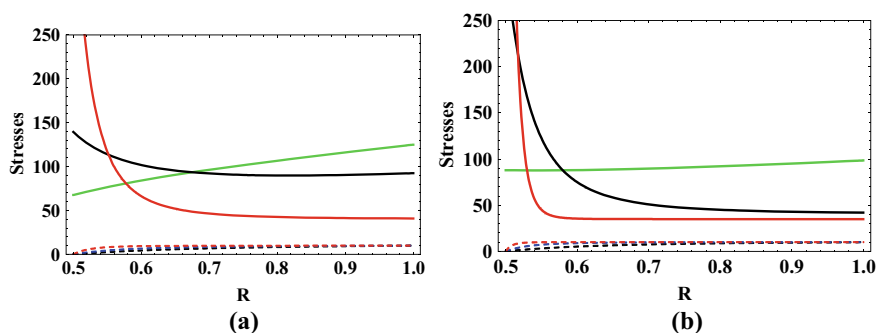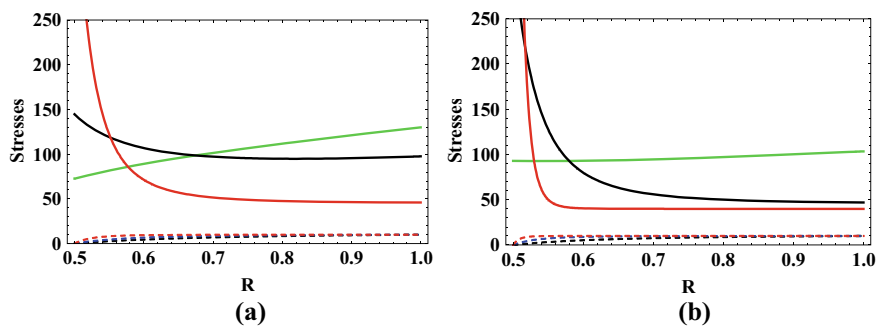
5   Conclusion

The deformations in a thin circular disc made of Barium Titanate (BaTiO$_3$) and PZT-4 (piezoceramic) materials are studied. The disc is subjected to angular velocity, temperature, and pressure. Based on all numerical calculations and graphs, it is observed that rotation and temperature have significant effect on disc. There is a significant increase in radial and circumferential stresses with the increase in temperature and angular velocity. So, the disc made of piezoelectric material PZT-4 (piezoceramic) is better than Barium Titanate (BaTiO$_3$). The results obtained can be used to design different engineering structures.

References

 1. Mindlin R.D.: On the equations of motion of piezoelectric crystals. Problems of continuum Mechanics, Muskhelishvili N.I., vol. 70, pp. 282–290 (1961)
 2. Mindlin R.D.: Equations of high frequency vibrations of thermo piezoelectric crystal plates. Int. J. Solids Struct. **10**(6), 625–637(1974)
 3. Chandrasekharaiah, D.S.: A generalized linear thermo elasticity theory for piezoelectric media. Acta Mech. **23**(1), 39–49 (1988)
 4. Tauchert, T.R.: Piezo thermoelastic behaviour of plate of crystal class 6mm a laminated plate. J. Therm. Stresses **15**, 25–37 (1992)
 5. Eringen, A.C.: Micro continuum field theories I: Foundations and Solids. Springer, New York (1999)
 6. Eringen, A.C.: Continuum theory of micromorphic electromagnetic thermoelastic solids. Int. J. Eng. Sci. **41**, 653–665 (2003)
 7. Iesan, D.: On the microstretch piezoelectricity. Int. J. Eng. Sci. **44**, 819–829 (2006)
 8. Marin, M.: Weak solutions in elasticity of dipolar porous materials. Mathematical Problems in Engineering, Hindawi Publishing Corporation **2008**, 01–08 (2008)
 9. Migorski, S., Ochal, A.: Dynamic bilateral contact problem for viscoelastic piezoelectric materials with adhesion. Nonlinear Anal. **69**, 495–509 (2008)
10. Sharma, J.N., Sharma, R.: Propagation characteristics of lamb waves in a thermoelastic plate loaded with viscous fluid layers. Int. J. Appl. Math. Mech. **6**(3), 1–20 (2010)
11. Othman, M.I.A., Ahmed, E.A.A.: The effect of rotation on piezo-thermoelastic medium using different theories. Struct. Eng. Mech. **56**(4), 649–665 (2015)
12. Kumar, R., Sharma, P.: Variational principle, uniqueness, and reciprocity theorems in porous magneto piezo thermoelastic medium. Cogent Math. **3**, 1231947 (2016)
13. Sharma, R., Radakovic, Z.: Analytical solution of elastic-plastic stresses in thin rotating disc composed of piezoelectric material. Struct. Integr. Life **20**(1), 21–25 (2020)
14. Eringen, A.C.: Electromagnetic theory of microstretch elasticity and bone modeling. Int. J. Eng. Sci. **42**, 231–242 (2004)
15. Iesan, D., Quintanilla, R.: Some theorems in the theory of microstretch thermo piezoelectricity. Int. J. Eng. Sci. **45**, 1–16 (2007)
16. Atkinson, C., List, R.D.: Steady state crack propagation into media with spatially varying elastic properties. Int. J. Eng. Sci. **16**(10), 717–730 (1978)
17. Delale, F., Erdogan, F.: The crack problem for a nonhomogeneous plane. J. Appl. Mech. **50**, 609–614 (1983)
18. Noda, N., Jin, Z.H.: A crack in functionally gradient materials under thermal shock. Arch. Appl. Mech. **64**, 99–110 (1994)

19. Jin, Z.H., Noda, N.: Transient thermal stress intensity factors for a crack in a semi-infinite plane of a functionally gradient material. Int. J. Solids Struct. **31**, 203–218 (1994)
20. Gunghas, A., Kumar, R., Deswal, S., Kalkal, K.K.: Influence of rotation and magnetic fields on a functionally graded thermoelastic solid subjected to a mechanical load. J. Math. **2019**, 1–16 (2019)
21. Kalkal, K.K., Gunghas, A., Deswal, S.: Two-dimensional magneto-thermoelastic interactions in a micropolar functionally graded solid. Mech. Based Des. Struct. Mach. **48**(3), 348–369 (2020)

Detection and Classification of Pneumonia from Chest X-rays Using Image Based Deep Learning Methods

Radhika Chanian and H. D. Arora

Abstract Artificial intelligence (AI) has progressed from splitting innovation to real world applications as deep learning methods have advanced. AI is used in illness diagnosis and therapy, care coordination, medication research and development, and precision medicine. Collaborative efforts across disciplines will be essential for developing new AI algorithms for medical applications. One suitable strategy is to utilise machine learning to help clinicians diagnose chest X-ray images. In this study, we analyze the important methodology for developing an AI model and selection of appropriate machine learning techniques, locating openly available datasets of chest X-ray images (JPEG). Training datasets, deep learning models, and analysis methodologies have been tested using freely available sets of chest X-ray images. We used chest X-ray pictures from the Chest X-Ray Images (Pneumonia) collection for our research. This dataset is connected to the work on image-based deep learning for identifying medical diagnosis and curable disorders. This dataset comprises 5,856 chest X-ray pictures classified as Normal and Pneumonia. The Pneumonia category contains graphics of pneumonia that have been identified as either bacterial or viral. Further, we examine the best Convolutional Neural Network (CNN) model for the task that has been evaluated using a test set of chest x-ray images. Several measures are used to assess the model's performance such as accuracy, precision, recall, F1 score, and AUC score.

R. Chanian · H. D. Arora (✉)
Department of Mathematics, Amity Institute of Applied Sciences, Amity University Uttar Pradesh, Noida, India
e-mail: hdarora@s.amity.edu

113

1 Introduction

All through history, viruses and physical ailments have resulted in numerous fatalities and produced severe situations which have necessitated a protracted battle for survival [1]. Pneumonia is the leading cause of infant death worldwide. Although pneumonia is frequently thought to only affect the elderly, it is truly the most prevalent infectious cause of death among children globally. Over 700,000 children under the age of five lose their lives to it annually, notably more than 153,000 new-born who are especially susceptible to infection [2].

An infection of the respiratory tract caused by microorganisms or other pathogens is termed pneumonia. Nonetheless, this common bacterial or viral infection may be successfully treated with penicillin and preventative medications. Early diagnosis of viral or bacterial pneumonia and the resulting delivery of the proper medication might occasionally significantly help to avoid the patient's health from worsening and finally resulting in a fatality [3]. If the patient was afflicted too severely, they might need oxygen treatment, which provides additional assistance for breathing. Nowadays, the strongest and most reliable method for identifying pneumonia is chest X-rays [4, 5]. Pneumonia chest x-ray images are blurry and frequently misconstrued as other illnesses or innocuous anomalies.

Because of the differences in symptoms, addressing pneumonia in children and adults is distinct. Also, the youngsters are quite susceptible to treatment. Probiotics, antiviral drugs, antifungals, relievers, and cough suppressants will be utilised in pneumonia preventative medicine. If it approaches peak form, the patient is given oxygen treatment. Also, the patient should practice self-care by resting, drinking lots of fluids, and not overstressing the body. A patient should go through these therapies to recover from pneumonia. Besides this, specialists occasionally misclassify bacterial or viral pneumonia radiographs, resulting in incorrect medicine being administered to patients and therefore deteriorating their health [6–9]. There are significant perceptual variations in physicians' judgements in identifying pneumonia. In low-resource countries (LRC), especially those with rural populations, there is also a scarcity of qualified radiologists. As a result, the development of computer-aided diagnostic (CAD) systems that can help radiologists quickly identify different types of pneumonia through chest X-ray pictures is therefore urgently needed.

Several biological issues (for example, brain tumour diagnosis, breast cancer detection, and so on) are now employing Artificial Intelligence (AI) based approaches [5, 10–12]. Convolutional neural networks (CNNs) results showed promising results in image classification and have thus been largely acknowledged by the scientific community [13]. Machine learning (ML) has been extended by deep learning. Donald Hebb initially presented machine learning in his book The Organization of Behaviour. Following that, machine learning methods were implemented. The reason deep learning machine learning accesses chest X-rays.

Kallianos et al. [14] is getting prominence is because they can be effectively employed with minimal imaging methods as well as the considerable amount of information accessible for training several various machine learning models [15, 16]. The

primary goal of CNNs is to create an artificial architecture that is similar to the visual system of the human brain. CNNs have the benefit of being able to retrieve additional meaningful information from the complete image instead of created attributes [2, 17]. Much attempts and emphasis have lately been directed into imaging technologies and deep learning in pneumonia illness.

Deep learning [18] is a neural network architecture that consists of five layers, which include input, pooling layers, convolution layers, fully inter linked layers, and an output dense layer [19]. Considering this framework, deep learning models outperformed earlier up-to-date approaches in the identification and classification of pneumonia illness and depicted high precision [20].

2 Background of Deep Learning Algorithms

2.1 *Convolution Neural Network (CNN)*

CNNs are a form of neural network that is extensively employed in the identification of images and computational vision applications. They are based on the structure and roles of the brain's visual cortex, which interprets visual data hierarchically. The convolutional component is the foundation of a CNN, and it employs an array of filters (also known as kernels or weights) on the input image in order to identify significant characteristics [21]. To create an additional characteristic mapping, the filters glide over the provided image and execute component-wise amplification and summing. Convolution is the name given to this procedure.

Pooling layers, which minimize the attributes of maps to lower their dimensions spatially and boost their resilience to tiny fluctuations in the input, are also common in CNNs. Max pooling is the most frequent pooling procedure, which picks the largest value inside a pooling interval. Eventually, the convolutional and pooling layer result is routed via one or more fully connected layers that conduct regression or classification procedures on the retrieved attributes. When programming a CNN, backpropagation is employed to adjust the balance of the filtering and fully linked layers having the goal of minimising a specific type of function of loss. CNNs have demonstrated cutting-edge performance in various recognition of image applications, involving detecting objects, differentiation, and classification [22].

CNNs are a form of neural network that is extensively employed in the identification of images and computational vision applications. They are based on the structure and roles of the brain's visual cortex, which interprets visual data hierarchically. The convolutional component is the foundation of a CNN, and it employs an array of filters (also known as kernels or weights) on the input image in order to identify significant characteristics [21]. To create an additional characteristic mapping, the filters glide over the provided image and execute component-wise amplification and summing. Convolution is the name given to this procedure.

Pooling layers, which minimize the attributes of maps to lower their dimensions spatially and boost their resilience to tiny fluctuations in the input, are also common in CNNs. Max pooling is the most frequent pooling procedure, which picks the largest value inside a pooling interval. Eventually, the convolutional and pooling layer result is routed via one or more fully connected layers that conduct regression or classification procedures on the retrieved attributes. When programming a CNN, backpropagation is employed to adjust the balance of the filtering and fully linked layers having the goal of minimising a specific type of function of loss. CNNs have demonstrated cutting-edge performance in various recognition of image applications, involving detecting objects, differentiation, and classification [22].

2.2 Transfer Learning

Transfer learning [23] is a deep learning approach that includes applying the understanding obtained by a model that was previously trained to an unknown assignment. It enables the transmission of information from a big and complicated dataset to a smaller or less complex one, allowing the development of algorithms capable of solving novel issues with a little quantity of data to train. A pre-trained model from a bigger set of data is typically utilised as the foundation for training on an unknown dataset in deep transfer learning.

The pre-trained model is often generated on a huge set of images labelled with many different classes, such as ImageNet [24]. The new layers are linked to the final result of the model that has been pre-trained, which provides the data to be fed to the newly created layers. Transfer learning has been demonstrated to be extremely successful in a vast scope of applications, including image identification, audio recollection, natural language processing, and even drug development [25] (Fig. 1).

The pre-trained model has learnt to recognise visual attributes that are important to a wide range of classes, giving it an effective starting point for new assignments.

Fig. 1 Approach of transfer learning

The information is transferred by utilising the quantities of the previously trained model and just training the additional layers which have been included to the model for the fresh assignment.

3 Methodology

3.1 Dataset Description

In this research study, there has been utilisation of the open-source chest X-ray pneumonia database readily accessible on Kaggle, which consists of 5856 chest X-ray (JPEG) images. The images present in the said dataset have resolutions fluctuating from 640 × 640 to 1024 × 1024.

In the dataset, there are a total of 1583 images which are subjected to normal cases, whereas 4273 images are subjected to pneumonia cases.

The dataset is divided into an appropriate number of training, validation, and testing datasets. The entire dataset is then distributed in ratios of 70, 15, and 15% for the training, validation, and testing datasets, respectively.

Table 1 depicts the dissemination of the data during the training, validating, and testing stages of the suggested model. In our proposed model, 0 denotes normal instances and 1 denotes pneumonia instances. Figure 2 depicts some of the dataset's X-ray image samples.

3.2 Dataset Pre-processing

The procedure of preparing and altering the unprocessed information to an appropriate format for assessment is known as data preparation. This stage is a critical phase in data analysis since it determines the degree of reliability and accuracy of the final outcomes. Multiple steps are involved in the procedure, including data cleansing, combining data, data modification, and data compression.

For example, image input could be scaled to correspond with the dimension of an image neural network. Since, it's apparent that the dataset is severely unbalanced (Fig. 3.). We have about three times the typical number of pneumonia patients here. When it pertains to medical data, this is a fairly typical occurrence. The data will

Table 1 Dissemination of the dataset

Type	Train	Validation	Test
Normal	2981	643	649
Pneumonia	1118	235	230
Total	4099	878	879
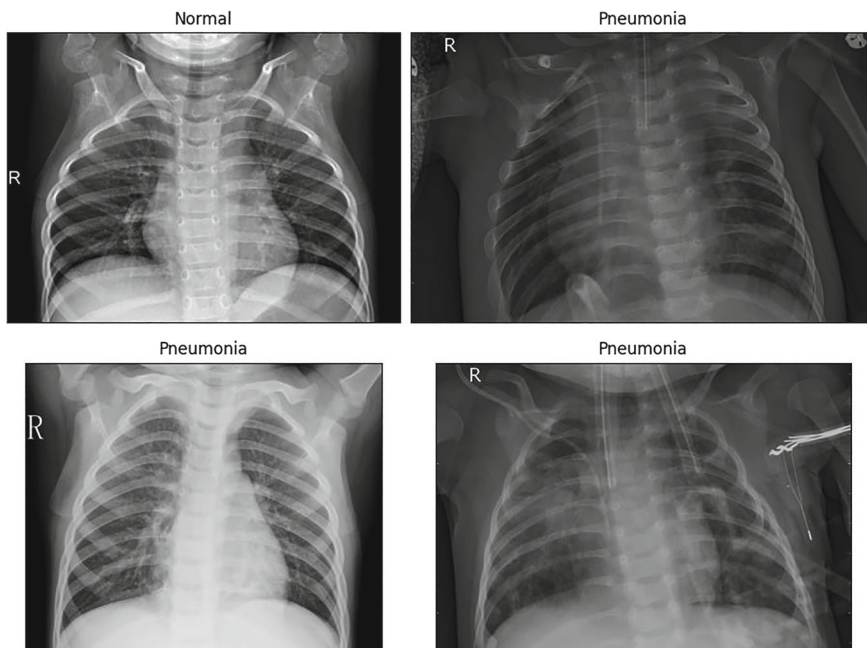
Fig. 2 Samples from training dataset illustrating normal and pneumonia cases

always be skewed. Either there will be an excess of normal instances or an excess of illness cases.

Data Augmentation

As formerly indicated, CNNs carry out significantly with enormous datasets. The functioning database, however in contrast, is not that vast. Several batches of tensor image data using real-life dataset can be developed that allows the image data preprocessing and transformation to become easier and efficient while training of the proposed model.

The goal of data augmentation is to boost both the scope and variety of the training dataset by generating new instances through different procedures. It improves the effectiveness of the model by subjecting it to a broader range of variances resulting in it being more resilient to differences in the input data.

For this research study, image augmentation was performed by rotation of images around by an angle ranging from 0 to 180 degrees, that essentially spins the pixel of the image window and occupies the region of the image when there was previously no image pixel. Images in the training dataset were rotated by an angle of 0.3, some of the images were shifted at random vertically and horizontally by 25% of the height and width respectively, shearing of some of the images randomly by 20%, flipping images at random horizontally and vertically, zooming images at random by 40%,
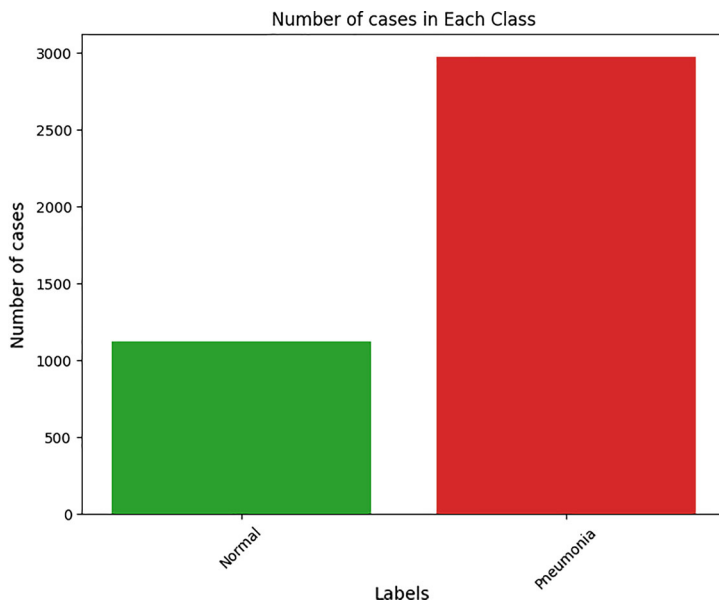
Fig. 3 Total number of cases belonging to the two classes in the training dataset

and fill mode was selected as the nearest. The augmented data is generated randomly from the training dataset, which is illustrated in the following Fig. 4.

3.3 Model Approach

ResNet50V2

A CNN (Convolutional Neural Network) that has been pre-trained is a representation of a neural network that has been developed using an extensive set of data to recognise distinctive characteristics and patterns in images. The network is then trained on an enormous amount of images and its labels, and the weights and biases learnt by the network are then retained as a pre-trained model. Vikash et al. exploited and worked on the notion of transfer learning in a deep learning structure which was beneficial in the identification of pneumonia using pre- trained Image-Net networks [26] and their respective compositions. A basic overview of the said pre-trained architecture ResNet50V2 is provided below:

- Its architecture, which has 50 layers, enables the creation of extremely deep networks while eliminating issues like disappearing gradients. $224 \times 224 \times 3$ is the size of input image.
- The first layer is a convolutional layer with $64\ 7 \times 7$ filters and a stride of 2, which decreases the input size by 50%.
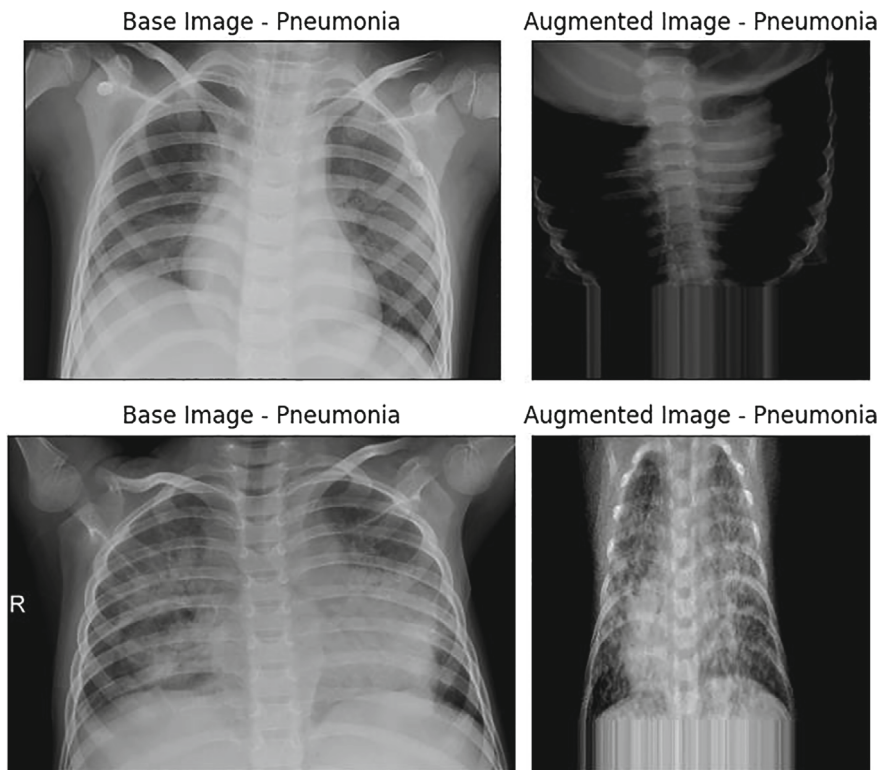
Fig. 4 Augmented images from training dataset

- A batch normalisation layer is inserted after each convolutional layer to normalise the activations and accelerate training.
- In order to further minimise the input data, a max pooling layer with a pool size of 3×3 and a stride of 2 is included.
- The residual blocks are the fundamental building components of ResNet50V2. Each residual block has numerous convolutional layers accompanied by a skip connection that adds the initial input to the convolutional layers' output. This aids the algorithm overcome the vanishing gradient problem and allows it to learn richer interpretations.
- At the network's end, a global average pooling layer is added to create a singular vector by combining the attributes maps.

Fine-Tuned Approach

For our proposed model, the quantity of training data needed to obtain high performance on the new job was reduced using *fine-tuning technique*, which enabled the transmission of information learnt by a model from one domain to another related area. The practice of further developing an algorithmic model that has already been

trained on an additional task or dataset that is connected to the initial objective is known as fine-tuning a model.

In the proposed model, three full connected dense layers were added after the average pooling layer. A tensor has been flattened into a one-dimensional vector using the flatten() method. Following flattening the model in the fully linked layer, dense layer 1 with 512 units and ReLU activation function was implemented. Afterward, a dropout layer with a dropout size of 0.3 was applied. subsequently, a dense layer 2 with 256 units and the activation function ReLU was added. After the dense layer 2, additional dropout layer utilising a dropout size of 0.3 was added, followed by a dense layer 3 containing 2 units with the softmax activation function (Fig. 5).

4 Experimental Parameterization and Performance Assessment Metrics

This section consists of the experimental setup, including the optimizer, deep learning tuning parameters, and performance measures used to determine the efficacy of the model.

4.1 Experimental Setup

The experiments were conducted employing the programming language Python and the subsequent empirical parameters such as the following: We used 70 and 15% of the images for training and testing, correspondingly, for data segmentation. We made it certain that the images selected for testing are not utilised during training. All the images in the dataset were scaled to 256×256 pixels in order for training the deep transfer learning models. These train environments are as follows: epoch size is set to 50, categorical cross-entropy is chosen as the loss function, As the optimisation tool, Adam is utilised, with a base learning rate set to 0.001, and batch size set to 32 for all the dataset (train/val/test). Also, in the optimisation section metrics such as accuracy, recall, specificity, precision, and AUC value has been chosen for performance assessment of all the models. Furthermore, all the models are trained separately. Moreover, rather than the 1000 classes used in ImageNet, a final dense layer is modified in single models to produce two classes indicating normal and pneumonia.

Adam Optimizer

Adam (Adaptive Moment Estimation) is a deep learning optimisation method that is extensively utilised for updating the model's parameters throughout training. It also provides faster convergence and is fairly resilient to hyperparameter selection. It retains an exponentially diminishing aggregate of squared slopes and historical
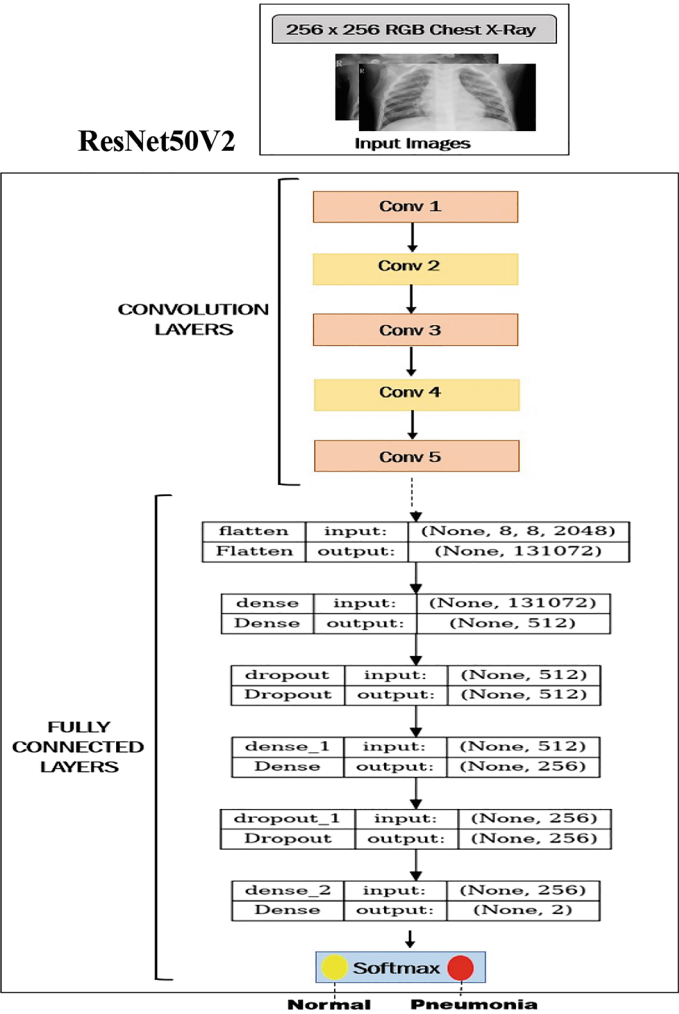
Fig. 5 Overview of the architecture of our proposed CNN model

slopes of the parameters which is then employed to modify the variables in order to tailor to the loss function's structure.

By keeping the average movement of the gradient and the subsequent phases of the gradient, it integrates the benefits of momentum and RMSprop, 2 additional optimisation techniques. As a result, the model's convergence occurs more quickly, and its generalisation capabilities are enhanced.

Categorical Cross-Entropy

In machine learning, categorical cross-entropy is a frequently used loss function, employed for both binary and multiclass classification problems. The degree to which

the expected probability distribution differs from the actual probability distribution of the intended class labels is measured. The categorical cross-entropy loss function is given as follows:

$$categorical_{loss} = -\left(y_{true} \times \log\left(y_{predictions}\right)\right)$$

where y_{true} serves the true class label (0 or 1) and $y_{predictions}$ denotes the expected probability that it belongs to the positive class (i.e., the class denoted by label 1).

Early Stopping

Early stopping is a machine learning strategy intended to reduce over-fitting and enhance a model's generalisation effectiveness. In the course of the model's training, early stopping is implemented which monitors the validation dataset performance and it essentially stops the training process when the efficiency of the validation dataset starts degrading. In the proposed model, Patience is taken to be 10 which denotes the number of epochs or iterations that are needed until terminating the training procedure when efficiency on the validation set no longer improves. Verbose is chosen to be 1 which will generate less information, reducing complexity and making the training procedure less noisy, and restore_best_weights has been set to "True" in order to retain the model's weights to their best documented state during the training process. This implies that the weights at the end of the epoch where the model has achieved its best performance will be preserved instead of the weights at the end of training.

Loss Learning Rate Scheduler

An example of a learning rate scheduler in Keras is the LossLearningRateScheduler, which modifies the learning rate in accordance with the loss function's output. The learning rate increases if the loss function continues to improve, decreases when it reaches a plateau, or both. When the learning rate is too elevated the model may exceed the minima, which may be avoided by using this scheduler.

The training and testing processes are carried out on an NVIDIA GPU T100 with 24 Go RAM. The parameters used for training the proposed model and the other deep learning models with which a comparison has been made are demonstrated in Table 2.

Table 2 Experimentation parameters for model training

Parameters	Values
Initialised weights	ImageNet
Input image size	256×256
Model output	Softmax probability
Total number of epochs	50

4.2 Performance Assessment Metrics

Metrics for performance assessment are used to assess a model's performance in different deep learning and machine learning models.

Accuracy

Accuracy is a measure in machine learning that quantifies the percentage of accurate predictions produced by a model on a particular set of data. Accuracy is described as the ratio of accurate predictions to total predictions produced by the model. Mathematically, accuracy is defined as:

$$accuracy = \frac{nTP + nTN}{nTP + nTN + nFP + nFN} \times 100$$

Accuracy is a popular measure in machine learning, particularly in binary classification situations in which the aim is to determine whether an instance corresponds to one of two categories.

Recall

Recall is a measure in machine learning that assesses the model's capacity to recognise each pertinent case of certain classes in a collection of data. The proportion of true positives (TP) to the total of true positives and false negatives (FN) is known as recall. Mathematically, recall is defined as:

$$recall = \frac{nTP}{nTP + nFN} \times 100$$

Recall is often referred to as sensitivity or the true positive rate (TPR). It is an effective measure for binary classification issues in which the aim is to establish whether a case belongs to one of two classes. A high recall score implies that the model performs well at detecting all instances of the positive label.

Specificity

Specificity is a performance metric in binary classification that assesses a model's capacity to accurately recognise negative cases, commonly known as True Negative Rate (TNR). It is defined as the proportion of correct negative predictions to total negative cases in the dataset. Mathematically, specificity is defined as:

$$specificity = \frac{nTN}{nTN + nFP} \times 100$$

Specificity is an essential statistic, particularly if the negative class is more interesting or relevant, as in medical diagnostics, where false negatives might have catastrophic implications. A model that has greater specificity is more likely to properly detect negative cases, resulting in fewer false negatives.

Precision

Precision is a measure in machine learning that assesses a model's capacity to produce accurately predicted outcomes for any particular class. Precision is defined as the proportion of true positives (TP) to the total of true positives and false positives (FP). Mathematically, precision is defined as:

$$precision = \frac{nTP}{nTP + nFP} \times 100$$

Positive predictive value (PPV) is another term for precision. It serves as an effective measure for binary classification issues in which the aim is to establish whether or not an instance belongs to one of two classes. A higher precision score implies that the model is effective at producing positive predictions for the particular class and is less prone to producing false positives.

F1 Score

The F1 score (f1) is a machine learning measure that incorporates recall and precision into a single number, offering an equitable evaluation of the efficacy of a model. The f1 score is a harmonic average of precision and recall, with a value of 1 indicating flawless precision and recall. Mathematically, f1 score is defined as:

$$f1 = 2 \times \frac{recall \times precision}{recall + precision}$$

The f1 score serves a purpose in binary classification issues with asymmetrical distributions of categories, for instance, fraud detection, spam classification, or medical evaluation problems, when suitable precision and recall for both categories are required. The f1 score uses the harmonic mean, which gives more significance to the lesser of the two values, implying that a model must have high recall and precision in order to score highly.

The terms "positive case" and "negative case" are used to describe the pneumonia and normal, respectively. As a result, nTP and nTN stand for the accurately predicted normal and pneumonia images, respectively, whereas nFP and nFN stand for the incorrectly predicted normal and pneumonia instances, respectively.

ROC-AUC (Area Under the Curve) Score

AUC score is an assessment measure for evaluating a binary classification model's competence to differentiate between categories that are positive and negative. The Receiver Operating Characteristic (ROC) curve's area beneath the curve is used to compute the area under the curve (AUC) measurement. The effectiveness of a binary classification model at different criteria for categorization is shown visually by the ROC curve. For different barrier values, it fundamentally contrasts the true positive rate (TPR or recall) and the false positive rate (FPR or specificity). The AUC score can vary from 0 to 1, with 0 representing poor performance and 1 representing
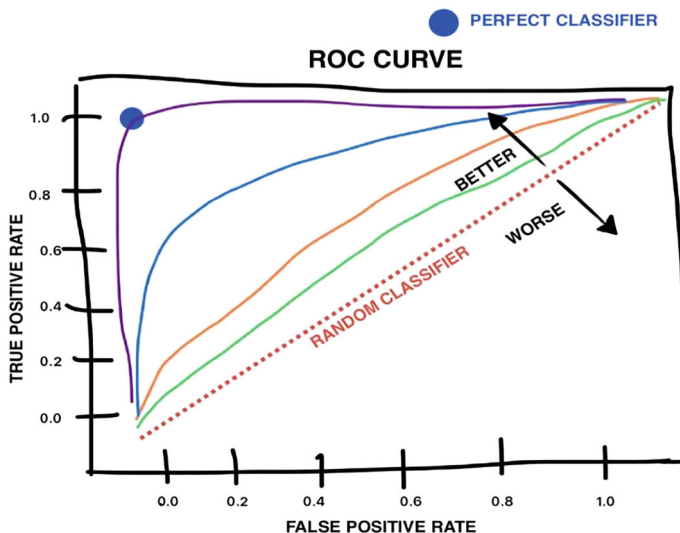
Fig. 6 Interpretation of ROC curve

ideal performance. To evaluate the AUC value, it takes the actual test labels and the predictions made on the test dataset as arguments (Fig. 6).

5 Evaluation of Performance Metrics, Comparative Study and GradCAM Visualisation

This section provides the results of our proposed model, and a comparison has been made with some deep learning algorithms on the basis of the classification report, confusion matrix, loss curve, and ROC-AUC curve. Also, there is a gradCAM visualisation of random chest x-ray images from the test dataset that illustrates the original image, a heatmap, and a superimposed image.

5.1 Discussion

In this section of the study, we will be discussing about several performance assessment metrics in determining the efficiency of the proposed model and a comparison has been made with other DL algorithms as a means of demonstrating the dominance of the proposed model.

For a comparative study, we have made use of the other deep learning models namely, VGG19, MobileNetV2, and DenseNet121.

VGG19: VGG19 is a 19-layer convolutional neural network architecture developed by the Visual Geometry Group (VGG). It includes convolutional layers, pooling layers, and fully connected layers. The network's initial layers are in charge of obtaining low-level information like corners and edges, whereas the deeper layers identify higher-level features like object components and object categories. The characteristics retrieved by the convolutional layers are used by the fully linked layers [27] at the network's conclusion to create predictions regarding the input image.

It features a complex design with about 140 million distinct variables, making it ideal for the recognition of images applications [28]. Pre-training is the process of training a neural network using an enormous database, such as ImageNet [26], followed by utilising the learnt characteristics to initialise the network for an intended application. This can increase the network's efficiency while also reducing training time for the assignment at issue.

MobileNetV2: MobileNet_V2 [29] is an enhanced rendition of MobileNet_V1. It is a convolutional neural network. It contains just 54 several layers and accepts an image size of 224 × 224. MobileNetV2's structure is built on the concept of component-separated convolutional layers, which divide the convolution procedure between a depth-wise convolution and a point-wise convolution. This assists in minimising the amount of connectivity parameters and enhances network functionality on mobile devices that have restricted computing resources.

The architecture of the network also contains numerous inversion residual blocks, which are intended to boost the network's depiction capability whilst maintaining the processing expenses minimal. These blocks provide a skip connection between each block's input and output, allowing the gradient to travel directly through the component without being reduced.

DenseNet121: DenseNet121 is a 2016 convolutional neural network (CNN) structure that is a member of the DenseNet family of neural networks, known for being notable for their densely linked blocks. The input to each layer in DenseNet121 is the combination of all the characteristics mappings from the levels before it. This enables the system to save data from previous levels and minimizes the issue of vanishing gradients [27, 28]. It also leads to an increasingly effective network in terms of variable utilization, which permits deeper structures.

DenseNet121 comprises 121 layers in its entirety, comprising four dense blocks (collections of densely linked convolutional layers) and three transition layers (used to lower the spatial dimensions of the characteristic mapping). The dense blocks enable the reuse of features, which enhances the network's precision. The use of batch normalization and ReLU activation following each convolutional layer is a further vital component of DenseNet121 [22]. This assists in stabilizing the training process and accelerating convergence.

Tables 3, 4, 5 and 6 provide the results of the two classes Normal (0) and Pneumonia (1) in the test dataset in the form of a classification report.

Classification Report

In machine learning, a classification report is for analysing the performance of a classification model. It essentially summarises several different performance measures

Table 3 Proposed model's precision, recall, and f1 score on the basis of classification report

Proposed model	Precision	Recall	f1 score
Normal (0)	0.93	0.96	0.94
Pneumonia (1)	0.98	0.97	0.98

Table 4 VGG19 model's precision, recall, and f1 score on the basis of classification report

VGG19	Precision	Recall	f1 score
Normal (0)	0.84	0.95	0.90
Pneumonia (1)	0.98	0.94	0.96

Table 5 MobileNetV2 model's precision, recall, and f1 score on the basis of classification report

MobileNetV2	Precision	Recall	f1 score
Normal (0)	0.87	0.93	0.90
Pneumonia (1)	0.97	0.94	0.96

Table 6 DenseNet121 model's precision, recall, and f1 score on the basis of classification report

DenseNet121	Precision	Recall	f1 score
Normal (0)	0.91	0.90	0.91
Pneumonia (1)	0.94	0.95	0.94

for each class in the dataset, which comprises of accuracy, recall, precision, f1 score and support (total number of samples in each class).

The summary of the report described the extent to which the classification model has been performed for each class in the test dataset. It helped in determining the model's advantages and disadvantages and in reaching judgements regarding how to enhance its efficiency. From the above classification report, on analysing the values for every metrics, it could be seen that the proposed model performed much better and hence emerging as a dependable model.

Confusion Matrix

When testing an algorithm for classification against a test dataset with known true values, a confusion matrix may be used to assess how well it performs. The predictions about the true positive (TP), true negative (TN), false positive (FP), and false negative (FN) of the model are given by the tabular representation of a confusion matrix. A confusion matrix in a binary classification task generally consists of four distinct components:

True positive (TP): The total number of occurrences in which an algorithm adequately predicts a positive outcome.

True negative (TN): The total number of occurrences in which an algorithm adequately predicts a negative outcome.

False positive (FP): The total number of occurrences in which an algorithm wrongfully predicts a positive outcome.

False negative (FN): The total number of occurrences in which an algorithm wrongfully predicts a negative outcome.

Figures 7, 8, 9 and 10 provide the results of the two classes Normal (0) and Pneumonia (1) in the test dataset in the form of a confusion matrix by providing the TP, TN, FP, and FN values for the proposed model and the other models.

From the above confusion matrix, we can conclude that for our proposed model using the ResNet50V2 algorithm, the model was able to correctly identify 236 normal cases and 614 pneumonia cases, whereas the model incorrectly identified a total of 29 images (Fig. 7). The confusion matrix components for every respective model

Fig. 7 Proposed model
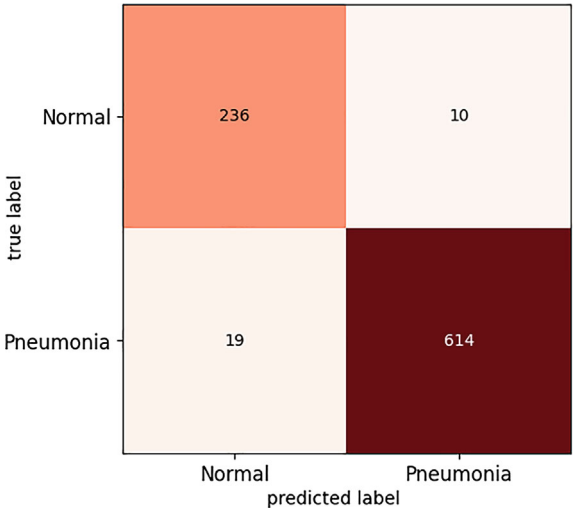
Fig. 8 VGG19 model
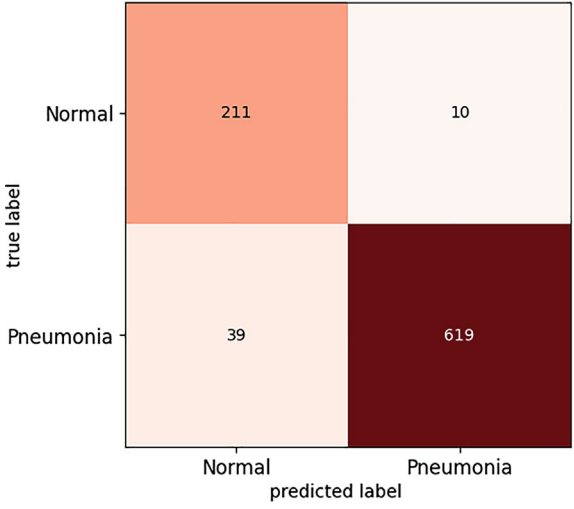
Fig. 9 MobileNetV2 model
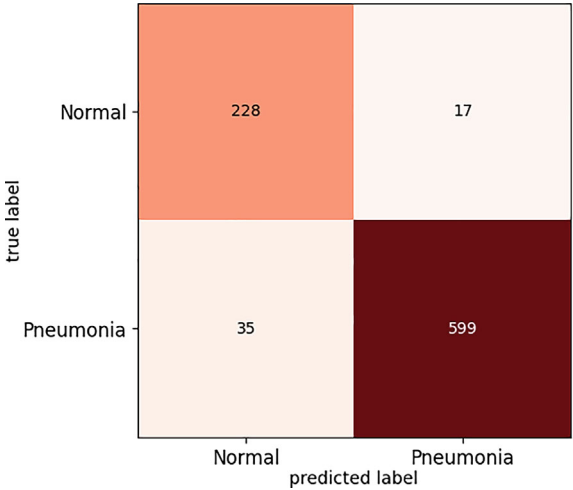
Fig. 10 DenseNet121
model
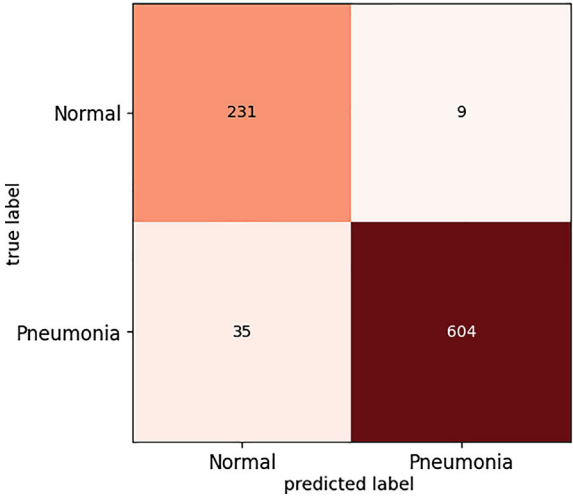
were utilised in the evaluation of performance assessment measures like accuracy, precision, recall, specificity, and f1 score.

5.2 Numerical Analysis

For a making a comparison between our suggested model and the other deep learning models, in terms of the performance metrics used in order to make conclusions about

the effectiveness of the proposed model using the architecture of pre-trained model ResNet50V2.

Results

In this section, the numerical analysis has been done on the basis of the loss curve, and AUC score curve at each epoch. From the graphs, we can infer that during the training process, the validation dataset performed effectively since it was able to learn all the features.

Loss Curve

A training and validation loss curve is a plot of the model's loss during training on the training and validation samples. The number of training epochs or iterations is shown by the x-axis, while the loss measure is represented by the y-axis. From Fig. 11 we can infer that the training and validation loss curves initially fluctuate, whereas as the training process progresses, both the training and loss curves rarely overlap and are close enough to indicate that the model has learnt to capture the pattern in the new data well enough (Figs. 12, 13 and 14).

ROC–AUC *Curve*

The basis for adopting AUC score as a performance metric is that when working with an unbalanced dataset, incorporating the area under the Receiver Operating Characteristic curve (ROC-AUC) as a performance assessment measure might be more insightful than accuracy alone. The AUC score goes from 0 to 1, with a high AUC value indicating that the model is proficient at differentiating between positive
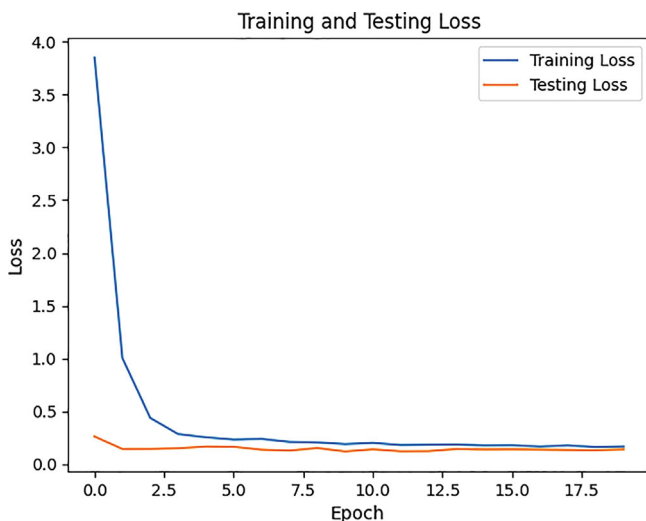
Fig. 11 Proposed model
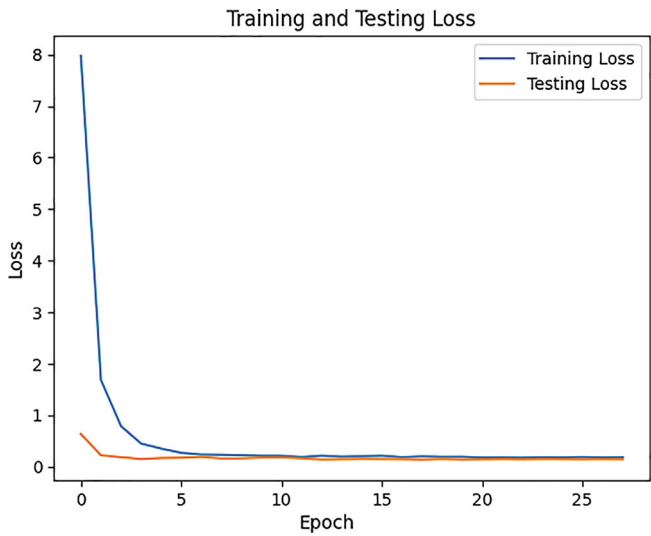
Fig. 12 VGG19 model
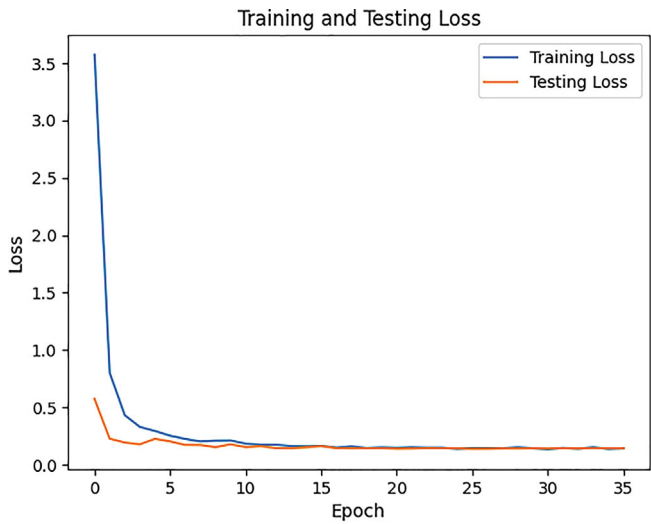
Fig. 13 MobileNetV2 model

and negative instances, whilst accuracy solely monitors the fraction of correctly categorised samples, which can be confusing when the set of data is unbalanced.

On evaluating the predictions on the test dataset, we get the following results. An AUC (Area Under the ROC Curve) score of **0.9919** for both normal and pneumonia classes indicates that the model can accurately identify between positive and negative
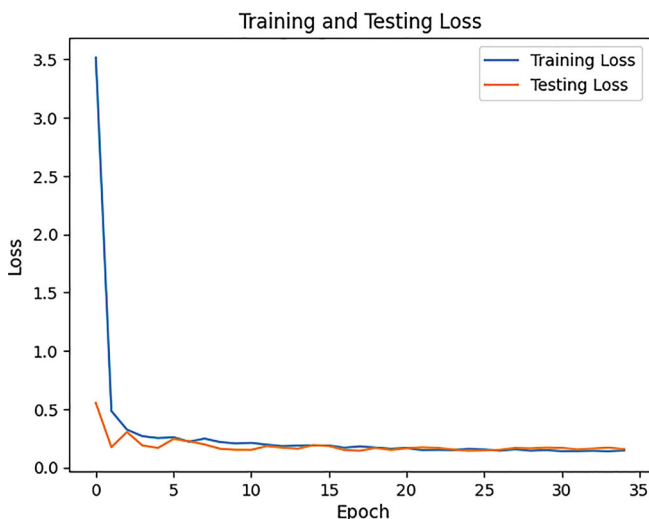
Fig. 14 DenseNet121 model

data, which is a strong indicator of its effectiveness (in Fig. 15). The proposed model performs well since the curve is concave up and closer to the plot's top left corner, indicating a superior model for binary classification (Figs. 16, 17 and 18).

The numerical data in Tables 7, 8, 9 and 10 show the results achieved by using the components of a confusion matrix on the test dataset for each respective model.

From the above tables, we can draw conclusions that the proposed model gave performing results in comparison to the other models. To obtain a more thorough understanding of the model's performance, we also calculated the f1 score, which measures the model's ability to predict true positive samples while minimising false positives and false negatives. The model's f1 score of 0.9769 indicates that it is performing effectively and provides a good proportion of precision and recall.

5.3 GradCAM Visualisation

For understanding and visualising deep neural networks by finding the areas of an input image that are crucial for an appropriate classification conclusion, a method called GradCAM (Gradient-weighted Class Activation Mapping) is used. A method called gradient class activation map (Grad-CAM) is utilised in CNNs to produce category-specific heatmaps. A trained CNN framework was used to build this class-specific heatmap from a particular input image [30, 31].
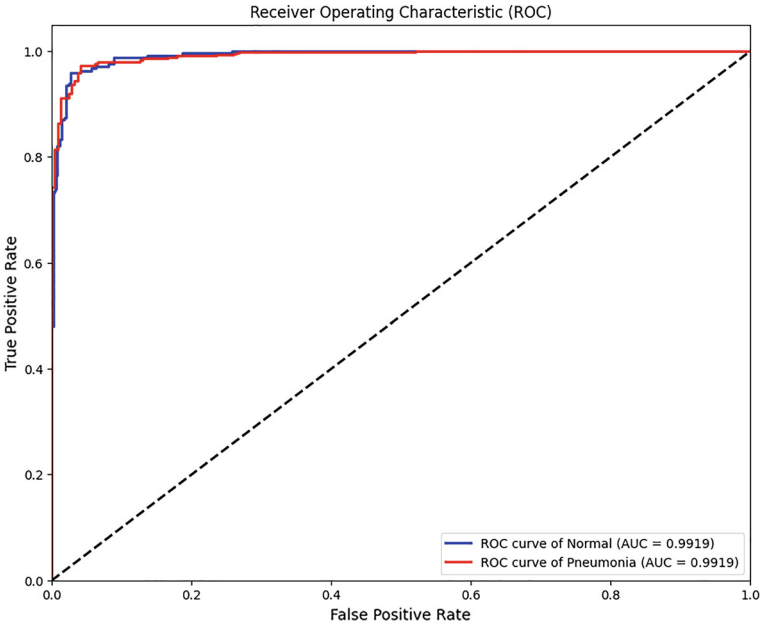
Fig. 15 Proposed model
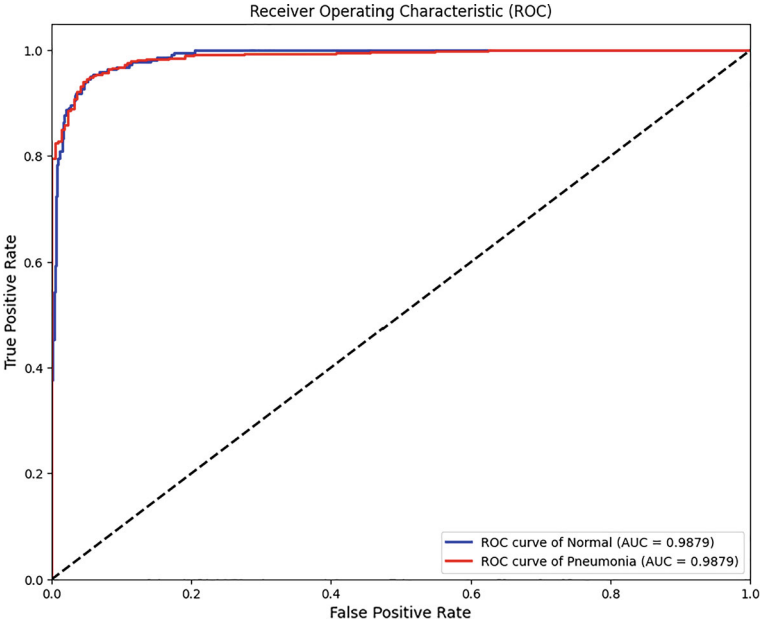
Fig. 16 VGG19 model
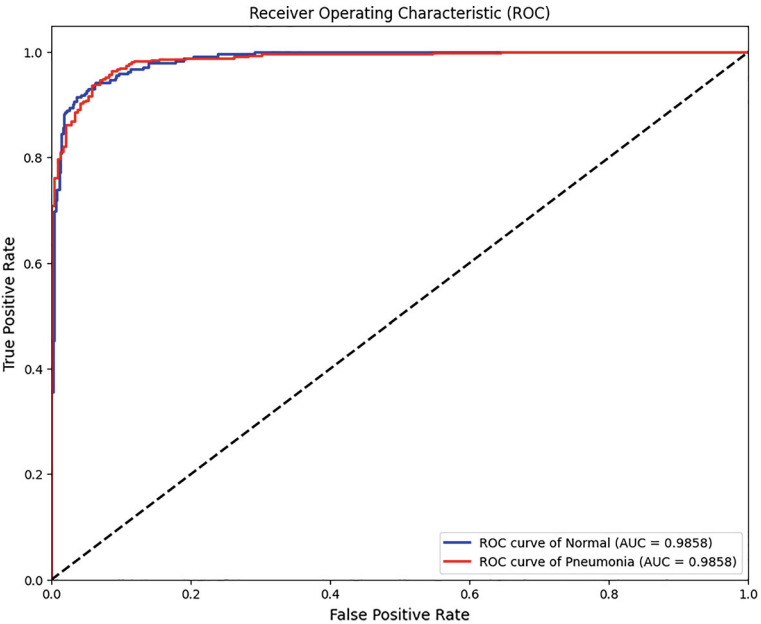
Fig. 17 MobileNetV2 model
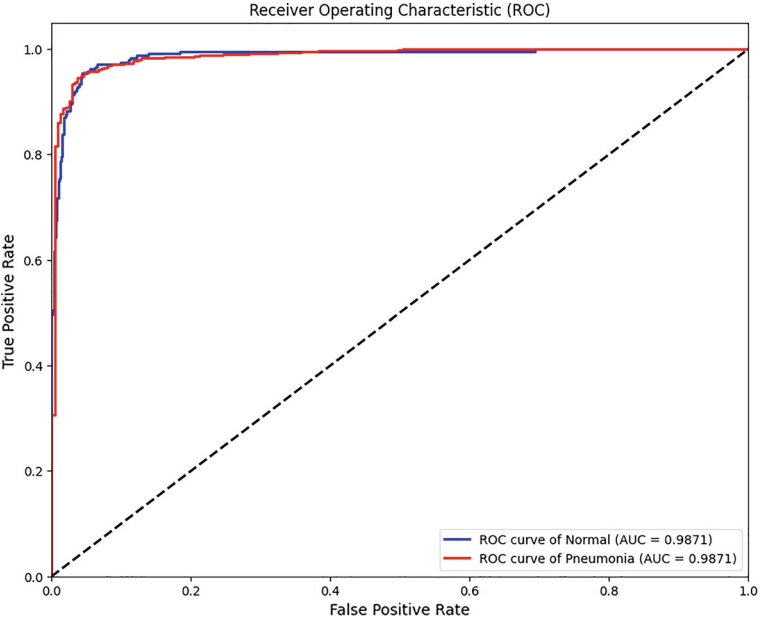
Fig. 18 DenseNet121 model

Table 7 Proposed model's performance metrics

Performance measures	Accuracy (%)	Recall (%)	Precision (%)	Specificity (%)	f1 score
Proposed model	96.70	96.99	98.39	95.93	0.9769

Table 8 VGG19 model's performance metrics

Performance measures	Accuracy (%)	Recall (%)	Precision (%)	Specificity (%)	f1 score
VGG19 model	94.42	94.07	98.41	95.47	0.9619

Table 9 MobileNetV2 model's performance metrics

Performance measures	Accuracy (%)	Recall (%)	Precision (%)	Specificity (%)	f1 score
MobileNetV2 model	94.08	94.47	97.24	93.06	0.9584

Table 10 DenseNet121 model's performance metrics

Performance measures	Accuracy (%)	Recall (%)	Precision (%)	Specificity (%)	f1 score
DenseNet121 model	94.99	94.52	98.53	88.89	0.9648

Approach

For every class z, we first evaluate the gradient of the score for the class z, qz (prior to the softmax) with respect to the attribute mappings Ck of a convolutional layer. This allows us to derive the class biased localisation map of breadth x and height y for any class z. The neuron significance weights ck for the target class are obtained by global average-pooling these gradients that flow back.

$$\alpha_k^z = \overbrace{\frac{1}{W} \sum_i \sum_j}^{\text{Global average pooling}} \underbrace{\frac{\partial q^z}{\partial C_{ij}^k}}_{\text{Gradients via backups}}$$

We execute a weighted amalgamation of activation maps after computing ck for the desired class z, followed by ReLU. The following formula results in final class discriminative map.

$$L_{Grad-CAM}^z = \text{ReLU} \left(\underbrace{\sum_k \alpha_k^z C^k}_{\text{linear combination}} \right)$$

To determine the pneumonia detection full disclosure, the Grad-CAM method is implemented. For the visualisation of input images, the input images are preprocessed, and the predictions are decoded using the appropriate command in order to extract the features. Furthermore, the last layer of the model is removed because it concentrates on the rich spatial representations learnt by the convolutional layers rather than the degradation of spatial knowledge that happens when transforming attributes into classification possibilities.

This makes it possible to analyse the selection procedure of the machine learning model at a finer scale and can assist in determining which elements of the image being processed are deemed most crucial for the task of classifying. Since the layers that are fully linked in a deep neural network frequently do not include any spatial details about an input image, GradCAM employs the layer prior to those layers. On the contrary, they transform the preceding convolutional layers' output attributes into classification likelihood, which is then applied to estimation. For our model, the last convolution layer is "conv5_block3_out".

With regard to the feature maps of the model's last convolutional layer, the Grad-CAM method calculates the gradients of the expected class outcome. Once these gradients have been combined, a heatmap highlighting the crucial areas of the input image that led to the estimated class is produced. The results are displayed as follows:

The regions of the provided x-ray image that the model concentrates on during the procedure of detection and classification have been highlighted by this approach, indicating that the feature maps created in the final convolution layer involve the spatial information necessary to effectively preserve the visual pattern. This visual pattern aids in differentiating the courses that have been allocated. The layers and recovered characteristics of the trained model are used to apply the Grad-CAM approach.

The first column of the above figure (Fig. 19) illustrates the original test dataset images, the second column depicts the heatmap visualisation of the original image; and the third column shows the GradCAM depiction, which is overlayed on the original image using the same dimensions of the input image. The most crucial areas are shown in the heatmap's brightest colours (Yellow), which is then superimposed onto the original input images, which has been illustrated by the colour Red in the superimposed image. The areas of the input image that the model utilised to create predictions are visually represented in this way.
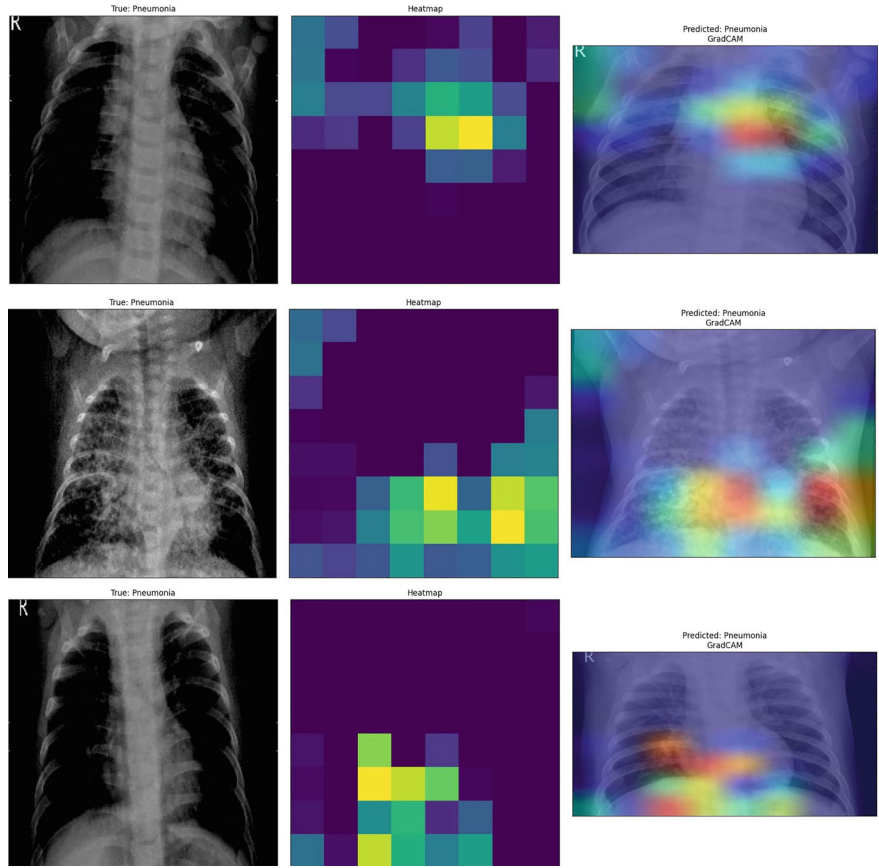
Fig. 19 Grad-CAM visualisation of test dataset images

5.4 Comparative Analysis

In this section, there is a comparison of training and testing accuracy and loss of the proposed model and other deep learning models in order to determine how the suggested model often outperforms other DL algorithms (Fig. 20).

The model is doing extremely well on the test set, which is the unseen data, as opposed to the training dataset, with a testing accuracy of 96.70% and a training accuracy of 93.71%. The model's generalisation ability to fresh data that it was not exposed to during training is gauged by the model's testing accuracy. Consequently, a high testing accuracy shows that the model has made good progress in generalisation and is capable of making reliable assumptions about fresh data. The model's outcome on the training data is measured by the training loss, and its outcome on an untested batch of observations that it hasn't seen during training is measured by the testing loss. The test loss of 0.11976 and training loss of 0.16436 suggest that the model is
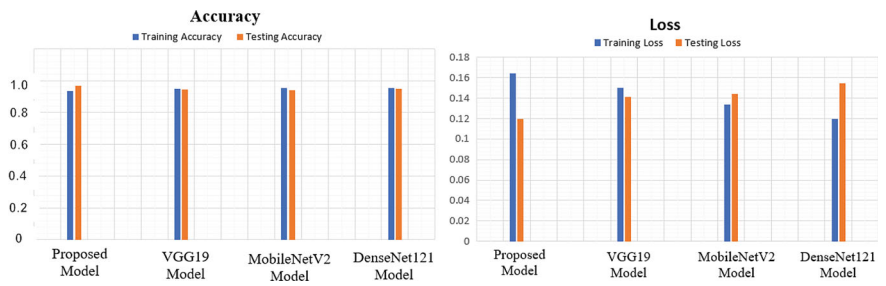
Fig. 20 Comparison of accuracy and loss among all algorithms respectively

performing well on both the training and testing datasets. The fact that the difference between testing loss and training loss is significantly large depicting that the model does not fit the training data too closely and generalises effectively to new unseen information points.

Also, in this section, a comparison is made between the other deep learning pre-trained models and the proposed model based on the performance assessment metrics used. Table 11 provides information about the proposed model and other pre-trained models' performance in distinguishing between the two classes.

We analysed these pre-trained models based on the values of accuracy, recall, specificity, f1- score and AUC score shown in Table 11. The suggested model worked well, with a classification accuracy of 96.70%, where VGG19 and MobileNetV2 followed DenseNet121 in order of accuracy, with 94.99% for DenseNet121, 94.42% for VGG19, and 94.08% for MobileNetV2. The suggested model outperforms existing models with an improved AUC value of 0.9919 for both the classes (Normal and Pneumonia). The suggested model has done exceptionally better than other models in terms of specificity as well.

Table 11 Comparison of performance metrics

Performance measures	Proposed model	VGG-19	MobileNetV2	DenseNet121
Accuracy	96.70%	94.42%	94.08%	94.99%
Recall	96.99%	94.07%	94.47%	94.52%
Precision	98.39%	98.41%	97.24%	98.53%
Specificity	95.93%	95.47%	93.06%	88.89%
F1 score	0.9769	0.9619	0.9584	0.9648
AUC score	0.9919	0.9879	0.9858	0.9871

6   Conclusion

A deep learning-based model has been developed in this work to categorise chest X-ray images into two groups: pneumonia and normal class. The ResNet50V2 network's design serves as the foundation for the proposed model, where we have fine-tuned the model by adding full linked layers and several other DL tuning hyperparameters like dropout ratio. This study was inspired by the expanding use of x-ray scan imaging techniques and CAD in the identification of medical disorders. Using pre-trained weights from the ImageNet dataset, transfer learning is being utilised to train, verify, and test this model across the dataset of chest x-ray jpeg images.

The research's diagnostic accuracy has been compared to state-of-the-art models. It has undergone a proper statistical evaluation in terms of performance, accuracy, recall, specificity, AUC, F1 score, and other properties. According to the results, the suggested transfer learning model operates better than cutting-edge techniques for automatically identifying radiographic illnesses. The recommended method is capable of differentiating between the two states. The suggested technique has an accuracy (96.70%), recall (96.99%), specificity (95.93%), F1 score (0.9769), and AUC (0.9919), and it can distinguish between the 2 states (pneumonia or not).

7   Future Scope

For deep learning to work successfully and avoid overfitting, a large amount of data is required. Medical imaging data on alarming deficits with low incidence are difficult to get in regular practice. Classifying pneumonia sometimes involves additional duties including identifying additional lung conditions or anomalies. To increase accuracy and efficiency, multi-task learning may be used to integrate several tasks into a single model. Also, we can include other diseases which could be diagnosed used chest x-rays.

The effectiveness of the suggested model can be increased by employing model emulation techniques, refining the model by layer addition, and other regularisation approaches. By combining the capabilities of two separate networks in a way, we can more accurately diagnose pneumonia from chest X-ray pictures. Ensemble two different neural network models together and using the K-fold technique and observe the performance of the models. On the available datasets, the current models yielded promising results, nevertheless, they still need to be tested in real life situations. Real-world data, such as clinical data or data obtained from multiple imaging modalities, can be utilised to validate the model's conclusions.

References

1. Orbann, C., Sattenspiel, L., Miller, E., Dimka, J.: Defining epidemics in computer simulation models: how do definitions influence conclusions? Epidemics **19**, 24–32 (2017)
2. Pneumonia. https://data.unicef.org/topic/child-health/pneumonia/. Last accessed 08 Nov 2022
3. Aydogdu, M., Ozyilmaz, E., Aksoy, H., Gursel, G., Ekim, N.: Mortality prediction in community-acquired pneumonia requiring mechanical ventilation; values of pneumonia and intensive care unit severity scores. Tuberk Toraks **58**, 25–34 (2010)
4. Chaudhuri, S., Chatterjee, S., Katz, N., Nelson, M., Goldbaum, M.: Detection of blood vessels in retinal images using two-dimensional matched filters. IEEE Trans. Med. Imaging **8**, 263–269 (1989)
5. Chowdhury, M.E.H., Alzoubi, K., Khandakar, A., Khallifa, R., Abouhasera, R., Koubaa, S., Ahmed, R., Hasan, A.: Wearable real-time heart attack detection and warning system to reduce road accidents. Sensors **19**, 2780 (2019)
6. Dele Davies, H., Wang, E.E.-L., Manson, D., Babyn, P.S., Shuckett, B.: Reliability of the chest radiograph in the diagnosis of lower respiratory infections in young children. Pediatr. Infect. Dis. J. **15**, 600–604 (1996)
7. Hopstaken, R., Witbraad, T., Van Engelshoven, J., Dinant, G.: Inter-observer variation in the interpretation of chest radiographs for pneumonia in community-acquired lower respiratory tract infections. Clin Radiol **59**, 743–752 (2004)
8. Neuman, M.I., Lee, E.Y., Bixby, S., DiPerna, S., Hellinger, J., Markowitz, R., Servaes, S., Monuteaux, M.C., Shah, S.: Variability in the interpretation of chest radiographs for the diagnosis of pneumonia in children. J. Hosp. Med. **7**, 294–298 (2011)
9. Palla, T.G.; Tayeb, S. Intelligent Mirai Malware Detection for IoT Nodes, vol. *10*, pp. 1241. *Electronics* (2021).
10. Chowdhury, M.E.H., Khandakar, A., Alzoubi, K., Mansoor, S., Tahir, A.M., Reaz, M.B.I., Al-Emadi, N.: Real-time smart-digital stethoscope system for heart diseases monitoring. Sensors **19**, 2781 (2019)
11. Tahir, A.M., Chowdhury, M.E.H., Khandakar, A., Al-Hamouz, S., Abdalla, M., Awadallah, S., Reaz, M.B.I., Al-Emadi, N.: A systematic approach to the design and characterization of a smart insole for detecting vertical ground reaction force (vGRF) in gait analysis. Sensors **20**, 957 (2020)
12. LeCun, Y., Bengio, Y., Hinton, G.: Deep learning. Nature **521**(7553), 436 (2015)
13. Krizhevsky, A., Sutskever, I., Hinton, G.E.: Pdf ImageNet classification with deep convolutional neural networks Commun. ACM **60**, 84–90 (2017)
14. Kallianos, K., Mongan, J., Antani, S., Henry, T., Taylor, A., Abuya, J., Kohli, M.: How far have we come? Artificial intelligence for chest radiograph interpretation. Clin. Radiol. (**74**, 338–345 (2019)
15. Saeed, M.M., Al Aghbari, Z., Alsharidah, M.: Big data clustering techniques based on spark: a literature review. PeerJ Comput. Sci. **6**, 321 (2020)
16. Taghanaki, S.A., Das, A., Hamarneh, G.: Vulnerability analysis of chest X-ray image classification against adversarial attacks. In: Understanding and Interpreting Machine Learning in Medical Image Computing Applications, pp. 87–94. Springer, Cham (2018)
17. Krizhevsky, A., Sutskever, I., Hinton, G.E.: Imagenet classification with deep convolutional neural networks. In: Advances in Neural Information Processing Systems, pp. 1097–1105. (2012)
18. Donahue, J., Jia, Y., Vinyals, O., Hoffman, J., Zhang, N., Tzeng, E., Darrell, T.: DeCAF: a deep convolutional activation feature for generic visual recognition. In: Proceedings of the 31st International Conference on Machine Learning, vol. 32, pp. 647–655 (2014)
19. Ouhda, M., El Asnaoui, K., Ouanan, M., Aksasse, B.: Contentbased image retrieval using convolutional neural networks. In: First International Conference on Real Time Intelligent Systems, pp 463–476. Springer, Cham (2017)

20. Elasnaoui, K., Chawki, Y., Radeva, P., Idri, A.: Automated methods for detection and classification pneumonia based on X-ray images using deep learning. arXiv preprint arXiv:2003.14363 (2020)
21. Albawi, S., Mohammed, T. A., Al-Azawi, S.: Understanding of a convolutional neural network. In: Proceedings of the 2017 International Conference on Engineering and Technology (ICET), Antalya, Turkey, pp. 1–6 (2017)
22. Goyal, M., Goyal, R., Lall, B.: Learning activation functions: a new paradigm of understanding neural networks. arXiv:1906.09529. arXiv (2019)
23. Chouhan, V., Singh, S.K., Khamparia, A., Gupta, N., Tiwari, P., Moreira, C., Damasevicius, R., De Albuquerque, V.H.C.: A novel transfer learning based approach for pneumonia detection in chest X-ray images. Appl. Sci. **10**, 559 (2020)
24. Deng, J., Dong, W., Socher, R., Li, L.-J., Li, K., Fei-Fei, L.: Imagenet: a large-scale hierarchical image database. In: Proceedings of the 2009 IEEE Conference on Computer Vision and Pattern Recognition, Miami, FL, USA, pp. 248–255 (2009)
25. Yang, H., Mei, S., Song, K., Tao, B., Yin, Z.: Transfer-learning-based online mura defect classification. IEEE Trans. Semicond. Manuf. **31**, 116–123 (2017)
26. Gershgorn, D.: The data that transformed AI research—and possibly the world. https://qz.com/1034972/the-data-that-changed-the-direction-of-ai-research-and-possibly-the-world/ (2017). Last accessed 23 Nov 2019
27. ResNet, AlexNet, VGGNet, Inception: Understanding Various Architectures of Convolutional Networks. https://cv-tricks.com/cnn/understand-resnet- alexnet-vgg-inception/ (2022). Last accessed 23 Jan 2019
28. LeCun, Y., Kavukcuoglu, K., Farabet, C.: Convolutional networks and applications in vision. In: Proceedings of the 2010 IEEE International Symposium on Circuits and Systems, Paris, France, pp. 253–256 (2010)
29. Sandler, M., Howard, A., Zhu, M., Zhmoginov, A., Chen, L.-C.: MobileNetV2: inverted residuals and linear bottlenecks. In: Proceeding of the IEEE Conference on Computer Vision And Pattern Recognition (CVPR), Salt Lake City, UT, pp. 4510–4520 (2018)
30. Selvaraju, R.R., Cogswell, M., Das, A., Vedantam, R., Parikh, D., Batra, D.: Grad-CAM: visual explanations from deep networks via gradient-based localization. In: Proceedings of the 2017 IEEE International Conference on Computer Vision (ICCV), Venice, Italy, pp. 618–626 (2017)
31. Villuendas-Rey, Y., et al.: A transfer learning method for pneumonia classification and visualization. In MDPI, Mexico (2020)

Precision Agriculture Using IoT Sensors

Yashwardhan, Aakriti Kumari, Yatharth Negi, and Sudeep Varshney

Abstract Advancement in IOT technology over years has led to emergence of many new concepts, smart agriculture is one of them. Smart agriculture systems include technologies such as IOT and wireless networks to reduce human intervention by monitoring environmental conditions and then take appropriate action based on user input. In India agriculture sector contributes more than 20% to GDP and above 70% population is involved in farming (Naresh and Munaswamy in Int. J. Recent. Technol. Eng. 7:98–102, 2019 [6]). To achieve the target of a 5 trillion-dollar economy, it is important to resolve the issues in farming. Modernization of traditional farming techniques can be a solution to this. Quality and quantity of agricultural yield can be improved by a smart agriculture system. This project aims at making a model of a smart agriculture system highlighting features like irrigation that is intelligently controlled and makes decisions based on precise real-time field data. It also includes features of monitoring soil condition, animal intrusion monitoring, weather management, pest control, etc. All of these actions will be controlled by any remote smart device or internet-connected computer, and they will be carried out by integrating ESP32 with Wi-Fi, actuators, and sensors.

Keywords Precision agriculture · UV light · IOT · WSN

1 Introduction

Agriculture in the Indian economic system is one of the foremost occupations which is done by the rural people on a very large scale as it provides them job opportunities which can help them with earning basic necessities and to cope up with the society. This agricultural sector helps in generating food, fiber, various types of spices, and other products asked by the sophisticated society out there. Agriculture is the basic source of income for approximately 60% of India's population and is the largest

Yashwardhan · A. Kumari · Y. Negi · S. Varshney (✉)
Sharda School of Engineering and Technology, Sharda University, Greater Noida, India
e-mail: sudeep.varshney@sharda.ac.in

source of livelihoods among all the sectors present. Climatic changes will have a notable impact on the agricultural sector as nowadays the automobile industry, pharmaceutical industries, and various others are contributing to air pollution as well as water pollution by generating harmful pollutants and gases into the atmosphere such as CFCs, carbon dioxide, sulfur dioxide and releasing harmful toxic substances into the water bodies which in turn makes it difficult for irrigation of crops and reduces their productivity. Groundwater irrigation and rain-fed agriculture are some of the traditional concepts which are used to produce efficient crops which may use water content in a sustainable way. Our system is designed to use water more efficiently. In the earlier system the planter would manually go to the fields to make the water inflow, but now the system automatically does that efficiently. In India, the main source of employment is in the confederated sectors of agriculture. With 82 percent of growers being small and marginal, 70% of its pastoral houses still rely solely on husbandry for their survival. India is the world's largest producer of pulses, with production reaching about (25% of total worldwide output), consumption about (27% of total global consumption), and importer (14%) of pulses [1]. The rising global water extremity: In addition to managing failure and conflict between water druggies, the available freshwater is further defiled by the mortal and beast population and the pollution situations have increased at an intimidating rate. If this pattern continues, food product usage will be confined, affecting mortal productivity and, as a result, the entire ecosystem in the future. The population has increased dramatically, and it has done so faster than the rate of increase in food production. This is the primary and most serious source of the problem (see Table 1).

Every crop requires different amounts of water for the proper growth which also depends on various climatic zones. For example, a typical grass crop requires roughly 6.5 mm of water per day in a semi-arid region with a mean temperature of 20 °C. A sub-humid climate with a mean temperature of 30 °C necessitates about 7.5 mm of water per day for the same grass crop [2].

A major contribution to the growth of any nation, especially developing countries, is accounted for by its agricultural sector. The low volume of crops and fruits is a result of the traditional methods of husbandry, which many farmers still use. However, it is observed that the advent of robotization has made the yields better. It is therefore believed that ultramodern wisdom and technological application in the agrarian sector will improve crop yield. But there are also many other factors that affect productivity, such as pest attacks, animal intrusion, and excessive use of pesticides. This, to an

Table 1 Average daily water need of standard grass during irrigation season

Climatic zone	Mean daily temperature		
	Low (less than 15 °C)	Medium (15–25 °C)	High (more than 25 °C)
Desert/arid	4–6	7–8	9–10
Semi-arid	4–5	6–7	8–9
Sub-humid	3–4	5–6	7–8
Humid	1–2	3–4	5–6

extent, can be controlled by scattering germicides, applying sticky traps, or using ultrasonic pest repellers. It is also important to prevent attacks of wild animals and insects when the crop grows. To cater to all these issues, it is imperative to develop an intertwined system that works on all factors that affect productivity growth through all the stages, like cultivation, harvesting, and storage. This paper examines a useful system to capture near real-time field data and control field operations. It aims at making husbandry "smart" through application of robots and IoT technologies. The paper features sensors, which are interconnected with each other to provide real-time field data and to perform tasks like humidity and temperature sensing, moisture sensing, etc. Additionally, it includes aspects of smart irrigation with smart control, which would be grounded on real-time field data. Lastly, wild animal intrusions is detected using motion sensors which may destroy the crops. Any remote smart device or computer will be used to control all of these procedures. Further actions will be carried out by integrating Esp32 with Wi-Fi, actuators, and sensors.

2   Literature Review

In [4], the author presents a smart system using IoT which includes various sensors like moisture and temperature sensor, humidity sensor and rain detection sensor for measuring various soil parameters. Smartphones with blynk are used as an interface. NodeMCU acts as the brain of the system and on the basis of fixed threshold moisture content it decides whether to water the crop or not.

In [3], the authors used temperature, humidity, motion, and moisture sensors in which these sensors sense the real-time data and based on that data action is taken according to a threshold value which has been set already. It uses an android application as an interface which requires continuous internet connectivity. Also the irrigation system is of both type manually and as well as automated.

In [5], the authors present a real-time monitoring model of soil parameters such as temperature, moisture, and Ph. This system also has the feature of crop disease detection using image analysis. Alerts will be sent through SMS. The whole system is solar powered.

In [6], the authors used AVR microcontroller atmega, ZigBee module, temperature sensor, moisture sensor, humidity sensor, Obstacle sensor, Raspberry pi, Raspbian operating system, Sinaprog, AVR studio version 4, and camera. The system is divided into three different nodes. Node1 is a GPS-based mobile robot that will carry out functions such as Keeping vigilance, Bird and animal scaring, Weeding, and Spraying within the field boundary. Node2 is a warehouse which consists of temperature, humidity and motion sensor, water pump and room heater cooling fan interfaced with microcontroller. Node3 is smart irrigation which consists of a moisture sensor and according to the data which is processed by the microcontroller, the water pump is turned ON/OFF.

In [7], the author's purpose is a smart system which can be used in greenhouse and temperature dependent plants. This system has CC3200 as its main block which

consists of an integrated microcontroller, network processor, and Wi-Fi unit on the same die. TMP007 temperature sensor and HDC1010 moisture sensor along with MT9D111 camera sensor is also integrated with CC3200. The captured current image is sent to farmers using GPRS.

In [8], the authors proposed a system for precision agriculture which interfaces soil moisture, HR 202 humidity, LM35 temperature, and water level sensor. The proposed system is based on WSN system architecture. ARM processor is the microcontroller that serves as the system's brain. When the water level sensor and soil moisture sensor sense the value which is less than the set threshold value then the motor will turn on automatically and if the moisture level increases beyond the set threshold value pump will be turned off. Recorded data and current state of motor is displayed through the LED screen as well as through any smartphone.

In [9], the authors proposed android-based mobile application as a recommendation system that will provide information regarding weather updates based on farmer's location, new farming tools and technology, proper information about crops, fertilizers, daily market prices, and news/loan informational updates. Android SDK tool is used for the implementation. This app supports multiple languages.

In [10], the authors mainly focused on locust problem and temperature and humidity forecasting. They have used temperature sensor, humidity sensor, soil moisture sensor, water pump, speaker, UV light, Node MCU, and Raspberry pi. They use both web applications as well as Android applications. Machine learning algorithms such as linear regression and logistic regression are used to predict temperature and humidity from data. Because locusts are sensitive to noise, the "raspberry pi″ sends a command to" a speaker to make sounds in order to eliminate them.

In [11], a Mobile robot is proposed by authors which consist of a transmitter section and monitoring section. Raspberry Pi 2 Model B acts as a microcontroller having various sensors including humidity sensor, pH sensor, Thermo hygro sensor, CO_2 sensor, Soil moisture sensor, Obstacle sensor. Camera is also mounted on a robot which is interfaced with Raspberry pi 2 Model B to monitor the live events at the field. Robot performs tasks like sensing the soil parameters, spraying pesticides, making strange noises when encountering some obstacles and switching on the electric motor whenever there is shortage of moisture content in the crop fields. The monitoring section consists of an Android smartphone, ZigBee receiver, and a Laptop with application language.

In [12], the authors use NodeMCU chip, humidity, temperature sensor, soil moisture sensor, Arduino microcontroller. Blynk is used as an interface for Android and iOS and ThinkSpeak is used to visualize, analyze, and store the data which they get from sensors. When the temperature, humidity, and soil sensor sense the data which is less than threshold value then the pump will automatically ON.

3 System Design and Analysis

Proposed Model

The proposed model of "Precision Agriculture Using IoT Sensors" combines several IoT sensors to enable efficient and data-driven farming practices. The model incorporates the following sensors:

1. **DHT11**: For better crop yield it is important to check all soil parameters. DHT11 sensor is used for temperature and humidity sensing. It outputs both temperature and humidity as serial data.DHT11 sensors can be purchased as sensors or modules. The only difference between sensors and modules is that modules have internal filter capacitors and pull-up resistors, and sensors must use them externally if needed. It has an operating voltage between 3.5 and 5.5 V and accuracy of -1% to $+1\%$ (see Fig. 1).
2. **HC-SR04**: In our proposed system, HC-SR04 sensor detects the animal intrusion in the field. The transmitter releases a specially designed 8-pulse pattern. If pulses are reflected back it indicates the presence of obstruction. The distance of obstruction is calculated by multiplying the speed of sound (340 m/s) and the time taken by Echo pin to get the reflected pulse (see Fig. 2).
3. **Soil Moisture Sensor**: A soil moisture sensor is a tool that measures the soil's present moisture content as well as its ability to store water. In order to measure the water content, a fork-shaped analytic device with two exposed conductors is placed into the soil or wherever the water content is to be calculated (see Fig. 3).
4. **ESP32**: We have used more powerful microcontroller than Arduino, i.e., ESP32. The Arduino falls short in many areas despite its great assets. Arduino has clock speed of around 16 MHz, whereas ESP32 has up to 240 MHz. It has 520 KB

Fig. 1 DHT11 (temperature and humidity sensor)
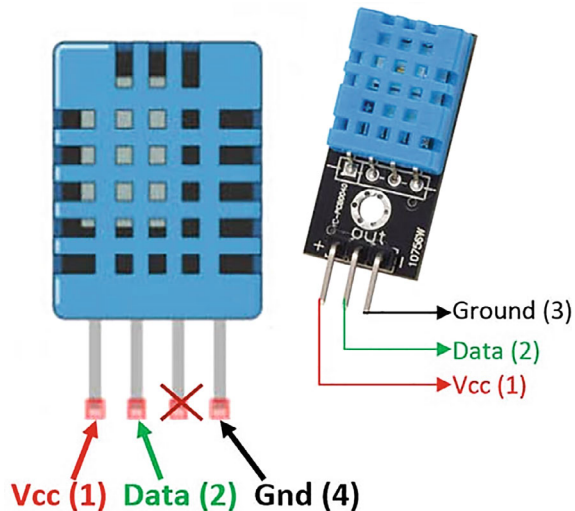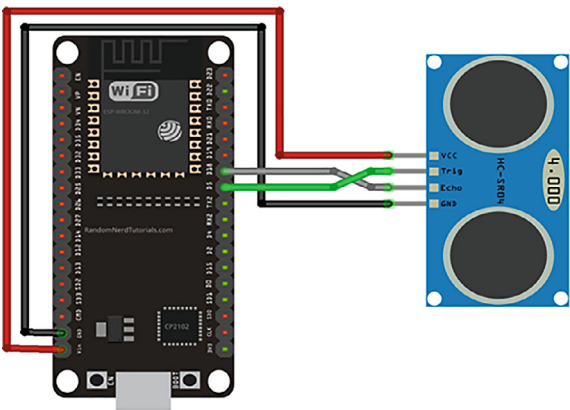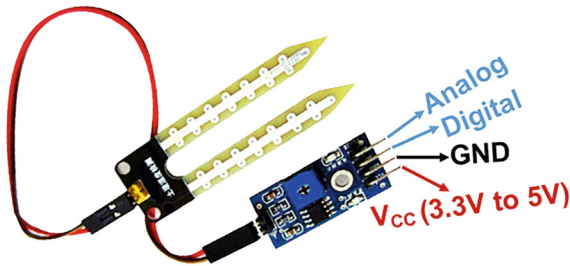
SRAM, 448 KB ROM, and 16 KB RTC SRAM. It also supports 802.11 b/g/n
Wi-Fi connections at speeds up to 150 Mbps (see Fig. 4).

5. **UV Light**: Usage of pesticides in traditional agricultural practices can often lead
   to some of the major human diseases such as Alzheimer and asthma. There-
   fore, usage of UV light can reduce the usage of pesticides and can help in high
   productivity of crops without any major drawback (see Fig. 5).
6. **CAPACITOR**—Capacitors are devices used to store electrical charge in elec-
   trical circuits. Capacitors work on the principle that bringing a grounded
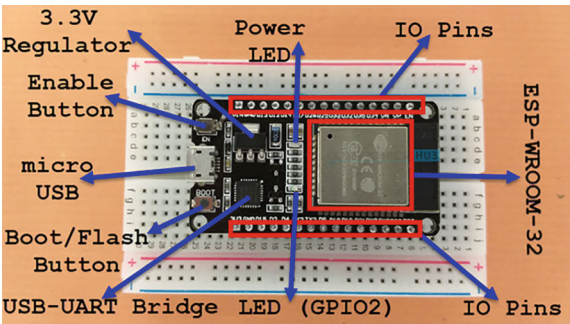
Fig. 5 UV LEDs
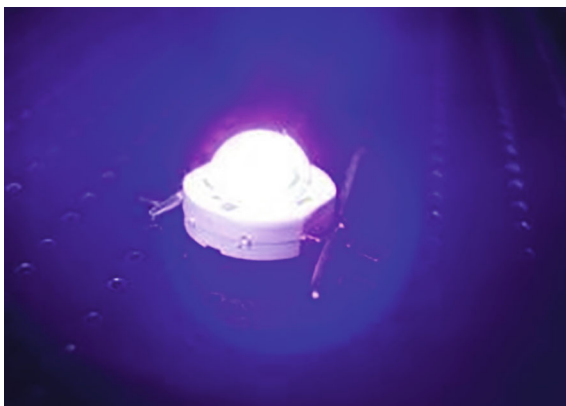
Fig. 6 Capacitor 12 V 1000 UF

conductor closer together significantly increases the capacitance of the conductor. So a capacitor has two plates spaced apart with equal and opposite charges (see Fig. 6).

7. **IC LM7805—**A 5 V voltage regulator known as the IC 7805 restricts the output voltage to 5 V throughout a range of input voltages. It provides the circuit with an additional layer of security and functions as a great component against input voltage fluctuations. It is affordable, easily accessible, and widely utilized (see Fig. 7).

By integrating these IoT sensors into a comprehensive system, farmers can gather real-time data on environmental conditions, plant health, and soil moisture. This data can then be analyzed and utilized to implement precision farming techniques, including targeted irrigation, nutrient management, and pest control. The model aims to enhance resource utilization, increase crop yields, and promote sustainable agricultural practices.

It is important to note that the selection of specific sensors may vary based on the requirements of the farming system, crop types, and environmental factors. The mentioned sensors (DHT11, HC-SR04, UV lights, ESP32, and moisture sensor)

Fig. 7 IC LM7805
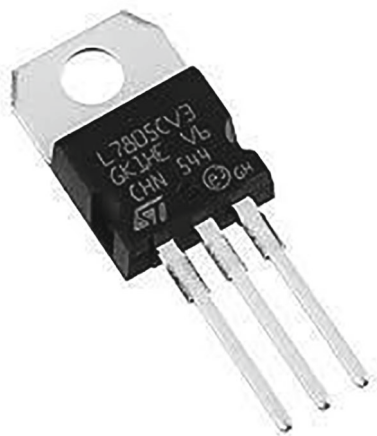
represent a sample configuration for a Precision Agriculture system using IoT sensors.

4   Working

The system is implemented on the basis of the ESP32 IOT module, which works on 3.3–5 V. The IC7805 is a voltage converter that is used to convert 12–5 V. The AC power supply is directly passed to the step-down transformer, which is connected to a rectifier circuit of 4 PN junction diodes that is used to convert the alternating current to direct current. Furthermore, the 470 uF capacitor is further connected to the terminals for smoothing the voltage (see Fig. 8).

The 5 V activates the ESP32 and all the other sensors connected to it. It is an IOT module that is used to communicate with routers and make local web applications. Sensors are connected to digital and analogue pins and continuously transmit data. ESP32 creates a local page which can be accessed by every device that is connected to the router. We have created the web page, which is designed in HTML, CSS, Bootstrap, and JavaScript, for client-side interaction such as input of a value and interaction with buttons. The system has 2 modes for irrigation: automatic and manual. In automatic mode, the farmer has to set maximum and minimum boundaries of moisture from the table provided on the webpage for various crops. As the values are set, JSON sends a parcel to ESP32 and the command gets encoded, and the pump works automatically based on those values and the current moisture level sensed by the moisture sensor. The application also has a weather forecasting system which will update regarding the weather forecast based on geographical location of farm field. Continuous temperature and humidity of soil is sensed by implementing the two-in-one sensor (DHT11), and the real-time data will be sent again using the JSON parcel from ESP32 to the server application, which will show the current
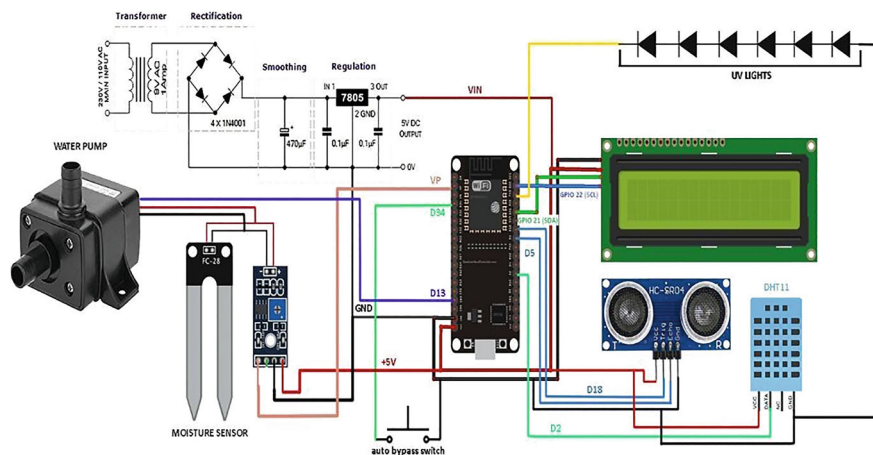
Fig. 8 Circuit diagram of proposed system

temperature and humidity of the surrounding area as these two parameter plays an important role in crop growth. We also have the drastic feature of animal interference detection, where ultrasonic sensors working on sonar technology detect the presence of animals using variations in distance; this activity can also be accessed from the dashboard. We have used UV lights, which work as an alternative of pesticide, so that less pesticide should be used and more organic procedures can be followed. This can also be controlled using a dashboard by the farmer themselves.

UV Light

As a complement or alternative to pesticides, UV light offers farmers new options for disease control in plants. Ultraviolet (UV) light has been found to have pesticidal properties and can effectively control pests and pathogens in agricultural settings. Farmers face economic and environmental challenges as pathogens become resistant to traditional fungicides. For microorganisms such bacteria, viruses, protozoa, fungus, and algae, UV-C radiation is the most powerful germicidal agent [9, 10]. The highest level of germicidal activity is produced by UV-C radiation with a wavelength between 250 and 260 nm, while the maximum effect is produced by UV-C radiation with a wavelength of 253.7 nm. Research trials conducted have shown it to be effective in killing powdery mildew and downy mildew. This could be useful for both conventional and organic farmers.

Weather Forecasting

Everything in the atmosphere interacts to create different weather conditions and phenomena. In this system, we are developing an user interface through which we can get information regarding the weather at a particular location which in turn will help the user by sowing crops or to maintain moisture level beforehand. This can be done through weather API (Application Programming Interfaces) which allows you to

connect large databases of weather forecasts and various other information. Weather is just the sum of all these interactions. Temperature, air pressure, wind (speed and direction), relative humidity, precipitation, visibility, cloud type and extent, sunshine duration, etc., are the conditions that determine the weather of a particular location.

Animal Intrusion Detection

The invasion of animals into living areas is increasing day by day, affecting human life and property, causing conflicts between humans and animals, but according to the laws of nature, all living things on this earth must be protected. Agriculture is the backbone of the economy, but animal encroachment on agricultural lands causes enormous crop losses. Elephants and other animals often attack the agricultural field adversely affecting farmers in many ways, including looting crops, damaging grain bins, damaging water supplies, homes and other property, and injuring or killing people. Indian farmers face serious threats from pests, natural disasters and animal damage, leading to lower yields. Because human and animal safety are equally important. Therefore, animal intrusion detection systems are required in agricultural areas. The ultrasonic distance module HC-SR04 allows non-contact measurement from 2 to 400 cm, with a distance accuracy of 3 mm. This module contains an ultrasonic transmitter, receiver, and control circuitry. The transmitter releases a specially designed 8-pulse pattern. If pulses are reflected back it indicates the presence of obstruction. Immediately, the APR board will turn on. A sound is played to distract the animal. The call will be sent to your dashboard.

Fertilizer Recommendation

Old traditional methods are no longer suitable for deteriorating soil and weather conditions. In fact, they adversely affect the soil. Unfortunately, even farmer experience is not yet sufficient to assess the impact of climatic conditions and soil on yield. Why? Because his NRT data on the ground is very low, if not zero. So we developed a recommendation system for farmers to help them make informed decisions. Depending on the crop selected, the best pesticides will be suggested based on growth and crop type.

Field Monitoring

The real-time data that is received from the sensors connected can be shown to the user through the user interface. In that the user will be notified regarding the moisture of soil, temperature, encroachments through various sensors connected to the system, and the farmer can even set the limit for the water to sprinkle for a particular crop in order to yield high productivity. If the level of water falls below the set limit, the motor starts automatically, and if the water level rises up to set limit, the motor stops. Soil management can also be done by determining soil characteristics such as moisture content, soil humidity, and temperature. IoT sensors make it simple to calculate these parameters.

Fig. 9 Proposed system

5 Result

As shown in Fig. 9, the experimental setup for the smart agriculture system in which the various sensors such as motion sensor, soil moisture sensor (HC-SR04), humidity sensor, and temperature sensor (DHT11) are connected to the microcontroller board (ESP32). The sensors will be fetching near real-time data from the environment and sending it to the controller. The result shows that if the moisture content is greater than the threshold value that is being set up by the user for the effective productivity of a particular crop then the water pump will automatically turn OFF and vice versa. And the trespassing of animals that may harm crop fields will be detected by motion sensors that will notify the user by an alert.

In Fig. 10, the webpage has been developed which will be interfaced with the system in which the necessary information regarding the moisture content, temperature, fertilizers suggestion for the crops has been mentioned, by this the user will get a fair idea about setting up of threshold value. This interface will be used to turn ON/OFF the UV light from a remote location. It will also provide us with the weather forecast feature in which the user gets to know about the humidity, temperature, and prediction of rainfall beforehand so that crops will not get damaged by climatic conditions.

6 Conclusion and Future Scope

The above work aims to infuse technology to the field of agriculture (that has already been performed since ages through old traditional methods). The referred project is focusing on modifying our old traditional methods to ease out the process of agriculture. As a result it has been observed that using this method the field of agriculture needs less manpower, more yield, less time-consuming; it will also definitely reduce the percentage of crops being wasted due to undesired amount of water or fertilizers applied to it. The sensor provided will automatically control the amount of water to

Fig. 10 Designed web application
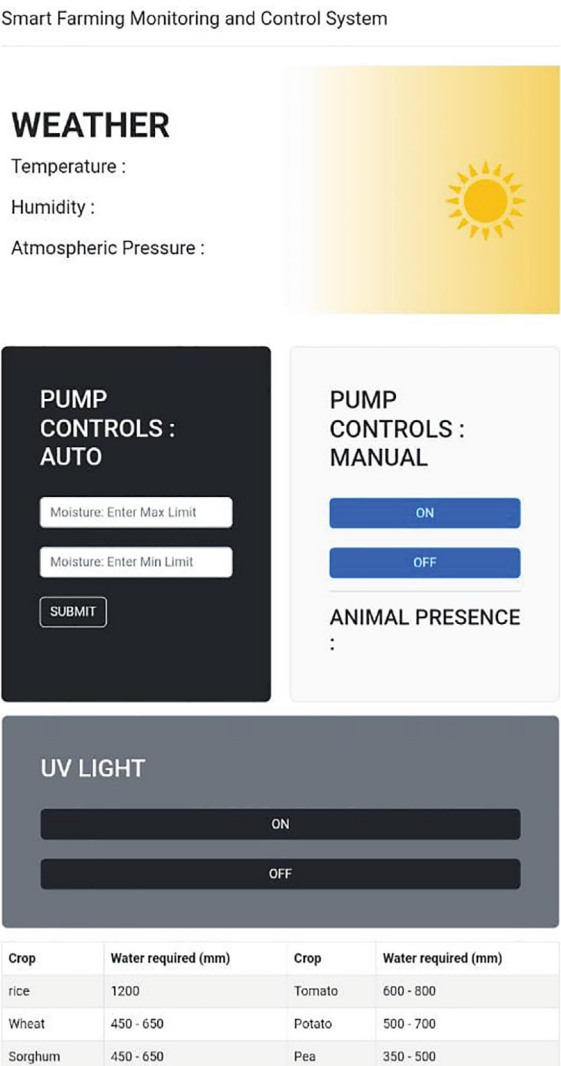
be provided to the field for respective crops. The various data collected are automatically sensed by the sensor installed which therefore brings the requirements of the crops into the knowledge of the farmer exactly at the time when required and thus keeping the crops much healthy and controlling wastage of crops. This prototype is flexible enough to modify itself according to the need at the specific moment.

As we have already said, in this work we have proposed a prototype, hence immense further modifications can be continued in future, if any sort of further work is to be performed. The proposed modifications can be further enhanced by introducing cameras and by using machine learning algorithms which may further

help in "image based plant diseases detection". Any disease in the crops can be diagnosed at a very initial or primary stage itself and prevented hence reducing crop wastage. The user face can be enhanced by adding regional languages to make it convenient for farmers who know only their regional languages.

References

1. https://www.fao.org/india/fao-in-india/india-at-a-glance/en/
2. https://www.fao.org/3/s2022e/s2022e02.htm
3. Sushanth, G., Sujatha, S.: IOT based smart agriculture system. In: 2018 International Conference on Wireless Communications, Signal Processing and Networking (WiSPNET), pp. 1–4. IEEE (Mar. 2018)
4. Abhiram, M.S.D., Kuppili, J., Manga, N.A.: Smart farming system using IoT for efficient crop growth. In: 2020 IEEE International Students' Conference on Electrical, Electronics and Computer Science (SCEECS), pp. 1–4. IEEE (Feb. 2020)
5. Patil, K.A., Kale, N.R.: A model for smart agriculture using IoT. In: 2016 International Conference on Global Trends in Signal Processing, Information Computing and Communication (ICGTSPICC), pp. 543–545. IEEE (Dec. 2016)
6. Naresh, M., Munaswamy, P.: Smart agriculture system using IOT technology. Int. J. Recent. Technol. Eng. **7**(5), 98–102 (2019)
7. Abirami, G., Helan, R.R.H., Geetha, P., Thamizharasi, M.: Smart Agriculture System
8. Sinha, B.B., Dhanalakshmi, R.: Recent advancements and challenges of Internet of Things in smart agriculture: a survey. Futur. Gener. Comput. Syst. **126**, 169–184 (2022)
9. Bintsis, T., Litopoulou-Tzanetaki, E., Robinson, R.K.: Existing and potential applications of ultraviolet light in the food industry–a critical review. J. Sci. Food Agric. **80**(6), 637–645 (2000)
10. Shin, J.Y., Kim, S.J., Kim, D.K., Kang, D.H.: Fundamental characteristics of deep-UV light-emitting diodes and their application to control foodborne pathogens. Appl. Environ. Microbiol. **82**(1), 2–10 (2016)
11. Boursianis, A.D., Papadopoulou, M.S., Diamantoulakis, P., Liopa-Tsakalidi, A., Barouchas, P., Salahas, G., Goudos, S.K.: Internet of things (IoT) and agricultural unmanned aerial vehicles (UAVs) in smart farming: a comprehensive review. Internet Things **18**, 100187 (2022)
12. Salim, S.A., Amin, M.R., Rahman, M.S., Arafat, M.Y., Khan, R.: An IoT-based smart agriculture system with locust prevention and data prediction. In: 2021 8th International Conference on Information Technology, Computer and Electrical Engineering (ICITACEE), pp. 201–206. IEEE (Sep. 2021)

On the Analysis of a Very Severe Cyclonic Storm Nilofar Over the Arabian Sea: A Numerical Weather Prediction Model Study

Nitin Lohan (ID)**, Gaurav Tiwari** (ID)**, Sushil Kumar** (ID)**, and Ashish Routray** (ID)

Abstract Through numerical simulation, an attempt is made to study the dynamics and spatial characteristics involved during the very severe cyclonic storm (VSCS) Nilofar over the Arabian Sea (ARB). For this purpose, numerical experiments are carried out using the Weather Research and Forecasting (WRF) model with two-way nested domains at 27 km (outer) and 9 km (inner) horizontal resolution. The NCEP-NCAR Final analyses (FNL) data at $1° \times 1°$ grid resolution is used in the WRF as initial and boundary conditions. The parameters simulated by the model, specifically mean sea level pressure (MSLP), 10 m surface wind and rainfall, are found close to the available India Meteorological Department (IMD) and other observations. In this study, we have also tried to determine what atmospheric and oceanic conditions compelled this very severe cyclonic storm to dissipate before making landfall. The study found that distraction of latent heat circulation in the lower troposphere due to negative sea surface temperature (SST) anomaly, increasing winds shear, atmospheric stability and decreasing water–vapour mixing ratio mainly in the middle and upper troposphere were the factors responsible for tropical cyclone (TC) Nilofar's dissipation before the landfall. Overall, the present case study shows that the model has performed reasonably well over the ARB and addressed the dynamics and characteristics of the VSCS Nilofar to a great extent.

Keywords Tropical cyclones · WRF model · Rainfall · Sea surface temperature

N. Lohan · S. Kumar (✉)
Department of Applied Mathematics, SoVSAS, Gautam Buddha University, Greater Noida, Uttar Pradesh, India
e-mail: sushil12@gmail.com

G. Tiwari
Department of Earth and Environmental Sciences, Indian Institute of Science Education and Research Bhopal, Bhopal, India

A. Routray
National Centre for Medium Range Weather Forecasting (NCMRWF), Ministry of Earth Sciences, Noida, Uttar Pradesh, India

157

1 Introduction

The northeastern region of the Arabian Sea (ARB) is prone to heavy rainfall and strong winds allied to tropical cyclones (TCs). Despite not higher frequency of TCs, the coastal states of India, Pakistan and Oman suffer damages, including loss of human lives and livestock, destruction of property, and agricultural and industrial production caused by cyclone-induced strong winds and heavy rainfall irrespective of whether cyclones make landfall or not. Usually, when the central pressure falls by 5–6 hPa from the surroundings of a low-pressure system under favourable conditions and the wind speed is as high as 63 km/h, tropical cyclonic storms form over the North Indian Ocean (NIO) [11]. According to WMO technical report 2008, about 7% of global TCs are generated over the NIO, including the Bay of Bengal (BoB) and ARB [10]. Also, compared to pre-monsoon season, the post-monsoon tropical storms are highly devastating, causing loss of life and damage to property when they cross the coastal region of India, Pakistan and Oman. Therefore, a practically precise forecast of the TCs has extreme importance to avoid or reduce the loss of life and damage to property. In the field of weather prediction, high-resolution numerical weather prediction (NWP) models have been vital for a decade or so. Initial conditions, boundary conditions and physics parameters used in the mesoscale NWP models highly influent the prediction of tropical cyclones [1]. Conditional Instability of the Second Kind (convective available potential energy) supports the development of TCs indicated by cyclonic inflow in the lower tropospheric boundary layer [7]. The NWP model performances are affected by grid sizes and the geographical region of interest; hence the best set of physical parameters for any region may not be suitable for some other region. Different parameterization schemes can give different results for different model resolutions as their physics and dynamics differ. Hence, the horizontal and vertical resolutions are also essential factors under consideration. Figure 1 shows the tracks of cyclonic activities over the ARB in October 1985–2014 (Source: India Meteorological Department, i.e., IMD). Enough cyclones didn't reach/ cross the coastline and followed a typical northeasterly northwestward trajectory but impacted well on the nearby land.

It is a challenge to understand better the TCs' genesis, development and associated characteristics. Riehl [12] and Kleinschmidt [8] introduced the concept that heat transfer from the ocean is the primary energy source for a TC formation. Emanuel [3] described a mature TC as a steady and axisymmetric flow whose energy cycle works like an ideal Carnot engine. Some dynamical and thermo-dynamical conditions favour cyclogenesis [4]. When warm air starts to spiral from the outer region toward the storm centre, its pressure drops and entropy increases; during this, kinetic energy dissipation in the atmospheric boundary layer and enthalpy transfer from the sea surface occurs. In the lower troposphere near the eyewall, a mature TC associates the strongest wind and wind magnitude generally decreases with increased height and radius. These radiuses of maximum winds tend to contract when a TC intensifies [14, 15]. Willoughby et al. [16] explained an axisymmetric framework investigates
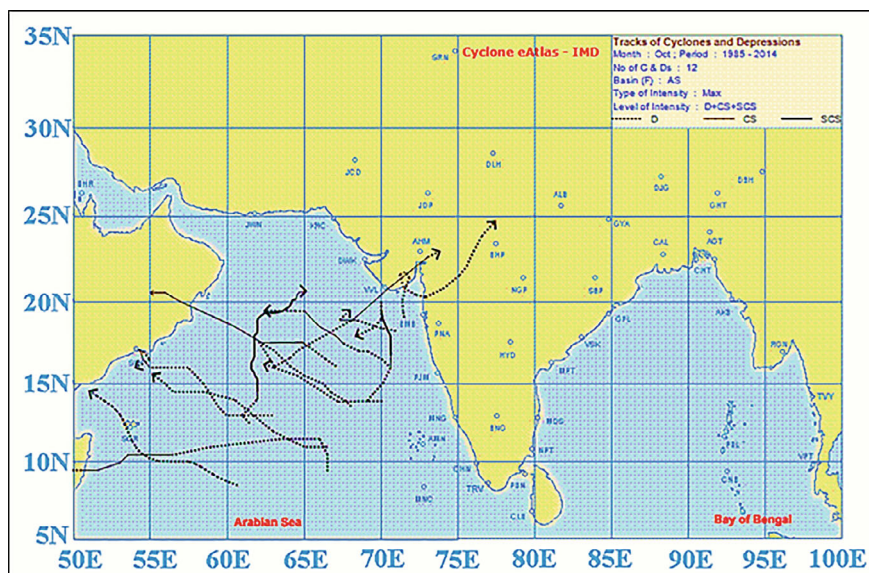
Fig. 1 All cyclone tracks over the ARB from 1985 to 2014 taken from the India Meteorological Department

many TC features and a TC strengthened by asymmetric deep convection elements [13].

1.1 Description of Very Severe Cyclonic Storm Nilofar

A very Severe Cyclonic Storm, 'Nilofar', was engendered from a low-pressure area over the Arabian Sea on 21st October 2014. It intensified into deep depression at 08:30 h IST of 26th October, near lat. 14.0°N and lon. 62.0°E and into a cyclonic storm (CS) at 11:30 h IST on 26th October over the same region. Then TC Nilofar travelled almost northwards and further intensified into a Severe Cyclonic Storm (SCS) at 02:30 h IST on 27th October and into a VSCS at about 11:30 h IST of the same day. After further movement, TC Nilofar intensified into Severe Cyclonic Storm in the early morning of 27th October and around noon of the same day, it became a VSCS. Nilofar weakened into a SCS on 29th October and into a low-pressure area on 30th October 2014 (IMD Report: Nilofar).

Section 2 provides a brief description of the methodology used in this study. The methodology describes the overview of data used, experimental domain configuration and numerical experiment. In Sect. 3, the results are shown and discussed, while the conclusions are given in Sect. 4.

2 Methodology and Numerical Experiment

In this study, a fully compressible non-hydrostatic Advanced Research WRF model has been used, which is developed by National Center for Atmospheric Research (NCAR). The WRF model (version 3.8) is configured over the Arabian Sea. D-01 (parent domain) covers a larger region comprised of 163×157 grids with 27 km horizontal resolution, whereas the D-02 (nested domain) with 346×346 grids and three times increased horizontal resolution covering the ARB and its environments with 56 model vertical levels with third order Runge–Kutta time integration scheme and Arakawa C-grid horizontal grid pattern. The model's initial conditions and boundary conditions are obtained from NCEP-NCAR FiNaL analyses (FNL) data. The lateral boundary conditions are updated in an interval of 6 h with varying Real-Time Global Sea Surface Temperature (SST) throughout the model integration. The land surface boundary conditions are taken from United State Geological Survey with a horizontal grid spacing of 10 min (D-01) and 5 min (D-02). The model has some prognostic variables, including potential temperature, geo-potential, surface pressure, perturbation quantities, three-dimensional wind, turbulent kinetic energy and scalars like cloud water & water vapour mixing ratio, etc. The planetary boundary layer physics used in the present study is the Mellor-Yamada-Janjic scheme [6] with Betts-Miller-Yamada cumulus convection [6], WRF single-moment 6-class microphysics scheme [5], Rapid Radiation Transfer Model (RRTM) for long-wave radiation [2, 9] scheme for shortwave radiation. The model is integrated for 144 h from 00 UTC on 26th October 2014 to 00 UTC on 1st November 2014. WRF Model configuration details are given in Table 1.

3 Results and Discussion

3.1 10 m Surface Wind and Mean Sea Level Pressure (MSLP) Simulation of the Nilofar

Figure 2 shows a time series of maximum sustained windspeed (MSW) at 10 m height against the MSLP, starting from 00 UTC on 26th October to 06 UTC on 31st October 2014. It showed a high correlation between these two parameters with a very high negative correlation coefficient value, i.e., -0.909 means that as MSLP decreases, the corresponding value of 10 m wind will increase. 10 m wind attains its maximum value when MSLP is minimal. Regarding the IMD tropical cyclone intensity scale, the model simulation indicates that TC Nilofar was a very severe cyclonic storm.

Table 1 WRF model configuration details

WRF Model configuration details over Arabian Sea	
Dynamics	Non-hydrostatic
Horizontal grid resolution	D01: 27 km D02: 9 km
Map projection	Mercator
Initial & Lateral boundary condition	NCEP/NCAR GFS forecast RTG_SST_HR data
Horizontal grid system	Arakawa C-grid
Integration time step	90 s
Topography	USGS
Vertical Coordinates	Terrain-following hydrostatic pressure Vertical coordinate with 56 vertical levels
Micro physics	WSM 6-class scheme
Cumulus scheme	Betts-Miller-Yamada scheme
Land surface option	Unified Noah land surface model
Radiation scheme	RRTM for longwave Dudhia for shortwave
Planetary boundary layer physics	Mellor-Yamada-Janjic scheme
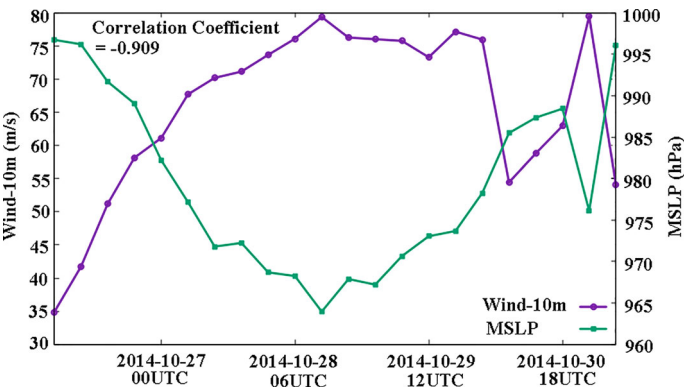
Fig. 2 Simulated MSW at 10 m height (m/s) and MSLP (hPa) valid for cyclone Nilofar

3.2 Analysis of Rainfall Pattern and Intensity

Observed simulated cyclone-induced rainfall for four days, 28th October (first column), 29th October (second column), 30th October (third column) and 31st October 2014 (fourth column) is shown in Fig. 3. The model simulated rainfall is given in the first row (Fig. 3a–d) while Tropical Rainfall Measurement Mission

(TRMM) observation and thermal infrared satellite imagery with 12.0-μm wavelength (TIR2 INSAT-3D) are given in the second (Fig. 3e–h) and third rows (Fig. 3i–l), respectively. The TIR2 imagery has a 4 km spatial resolution with 10 quantization bits structure and provides lower-troposphere moisture information.

The maximum rainfall estimation from the model and observation reaches a value above 640 mm/day and agrees with the maximum in both. On 28th October, the pattern shifted northwestward, and the eastern and southeastern coast of Oman were fed by 5–10 mm/day rainfall which the model and observations clearly show. The whole pattern (system) travelled in the east-NW direction for the next two days. On 30th October, the northwestern coast of Gujarat in India had some extent of rainfall. Here, TRMM observation shows a comparatively high number against model output. On 31st October at 03 UTC, the TC Nilofar dissipated over the ARB. The western coast of India experienced enough rainfall on the same day, according to model output and TRMM observation. Model and TIR2 satellite imagery show a well-matched rainfall pattern that started from Gujarat and goes far inside the country in the north-eastward direction. On this day, a larger area is fed by 80–160 mm/
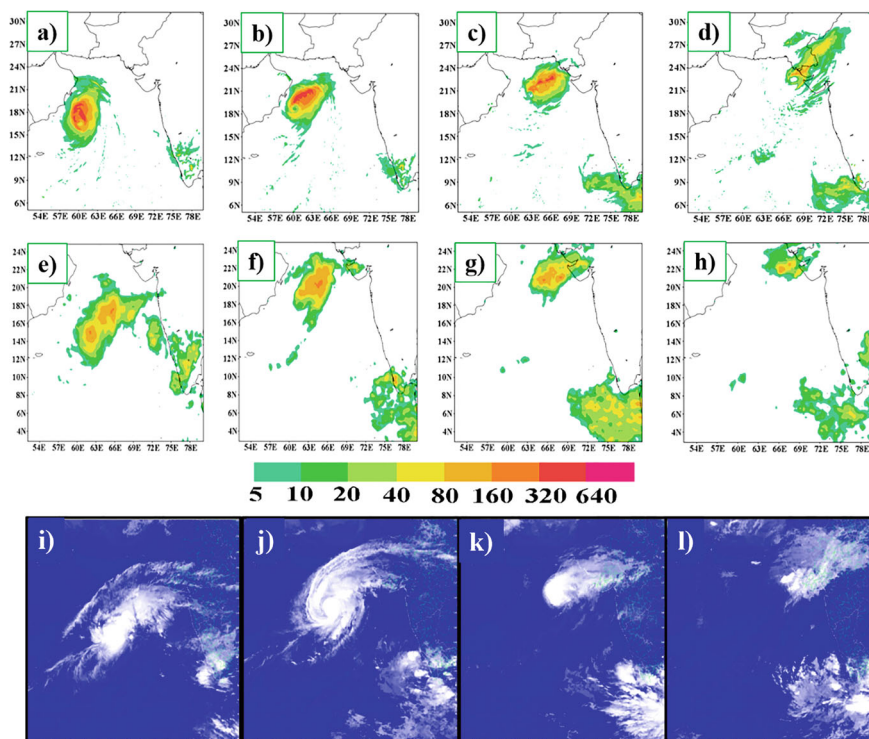
Fig. 3 **a–d** is the rainfall plots valid from 28th October to 31st October 2014, respectively. Upper panel is showing model outputs, middle panel is showing TRMM observation and bottom panel is showing TIR2 satellite imagery, respectively

Fig. 4 Model simulated
maximum reflectivity (dBz)
valid for 06 UTC 30th
October 2014
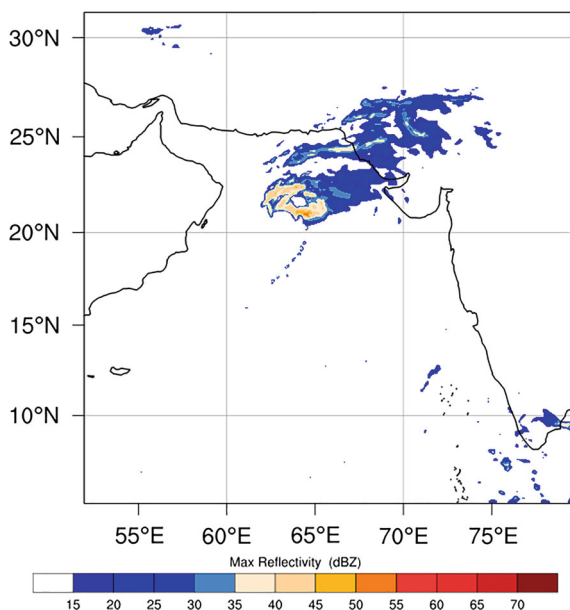
day amount of rainfall and up to 640 mm/day at some places. Here the model is
over-estimated by TRMM observations.

The model simulated maximum reflectivity (dBz) for D-02 at 00 UTC of 30th
October is given in Fig. 4. Larger the value (45–70 dBz) in the eyewall over the ARB
and lesser values (15–30 dBz) near/over the Indian coast supporting the explanation of
rainfall distribution on the same day. Simulation of TC Nilofar shows a well-captured
comma cloud organisation around the cyclonic eye.

Figure 5 shows the model simulated relative humidity (RH) on 30th October at
1000, 850, 500 and 250 hPa, respectively. More than 60–80% of relative humidity
at the middle and upper troposphere is attributed significantly to the spiral bands of
precipitation.

3.3 Climatology of SST Over the ARB and Factors Responsible for Dissipation of TC Nilofar Before the Landfall

The mean SST time series from 1985 to 2014 for 26th to 31st October is given
in Fig. 6a–f using ERA-Interim daily SST data. Time series support the sufficient
warming of ocean water required for tropical cyclone genesis because SST must
be 26.5 °C or more, and warm surface water must be 40–45 m deep. Figure 7a–f
shows the model SST anomaly for 26th to 31st October 2014, respectively. On 26th
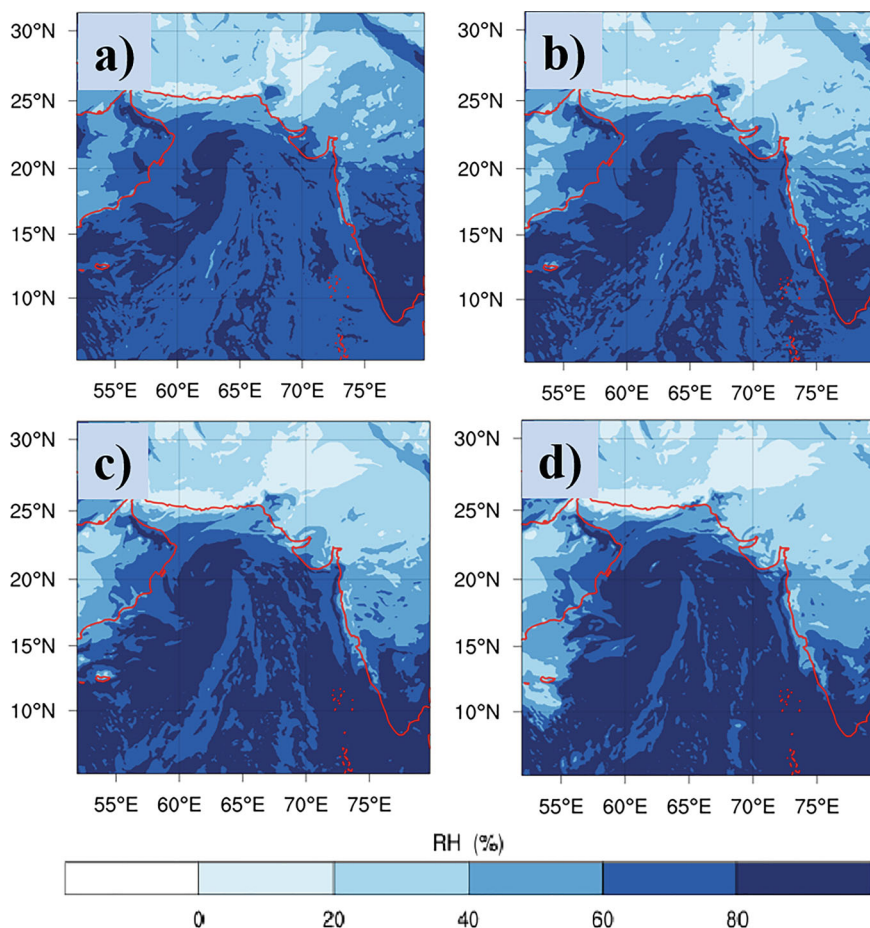
Fig. 5 Model simulated relative humidity valid for 30th October 2014 at 1000 hPa, 850 hPa, 500 hPa and 250 hPa, respectively

October, positive SST anomaly ranges from 0.2 to 0.6 °C in the cyclonic region. This extent further moved along with the cyclone's movement for the next two days. A large region over the mid-ARB consists of negative SST anomaly followed by 29th October. Negative SST anomaly can distract the circulation of latent heat in the lower troposphere. This change in daily SST anomaly may be one of the factors responsible for the decrease in TC intensity, for its movement toward the Gujarat coast after 29th October and thus for its dissipation before making landfall.

Figure 8a–c shows vertical profile of model simulated zonal wind (m/s) at eyewall for 29th, 30th and 31st October 2014, respectively. Figure 8d–f represents the same but for vertical wind (m/s). A replica for water–vapour mixing ratio (QVAPOR; unit: kg/kg) is given in Fig. 8g–i. Negative and positive values in the figures are indicating the change in the direction. In the case of tropical cyclones, typically a wind shear
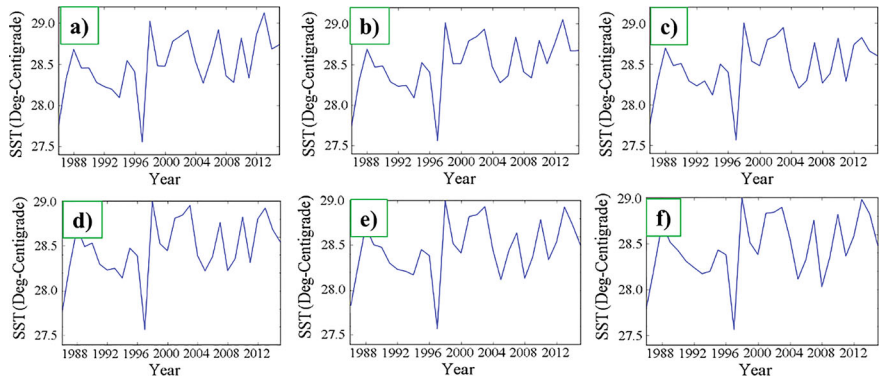
Fig. 6 SST climatology over the ARB for the period 1985–2014 valid for 26th–31st October, respectively
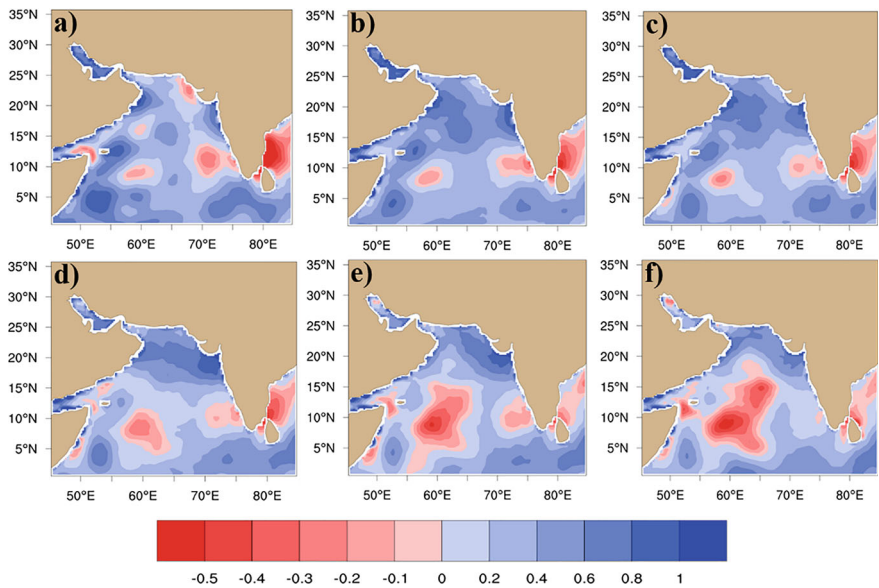
Fig. 7 Simulated SST (°C) anomaly over the ARB for the year 2014 valid for 26th–31st October, respectively

of 10 m/s responses from intensification to dissipate. In Fig. 8, first two columns in upper and middle panels are showing a monotonic increasing zonal wind shear comparatively. Atmospheric stability is increasing by the time which is governing from high to higher wind shear in the case of Fig. 8c and f. In Fig. 8g, QVAPOR has a continuous decreasing trend in the lower and middle troposphere but it is almost zero in the upper troposphere. Same pattern is followed by Fig. 8h and i, QVAPOR in middle and upper troposphere, both, is zero.
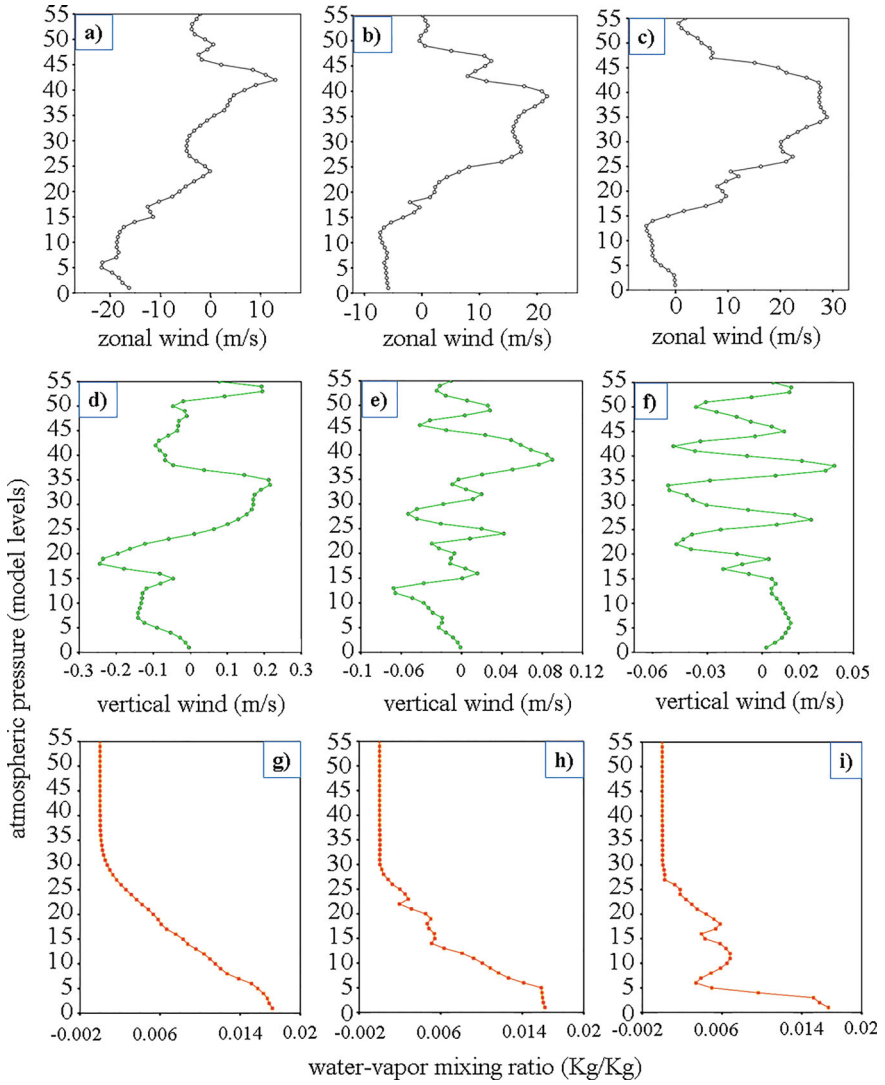
Fig. 8 a–c Vertical profile of zonal wind (m/s) valid for 29th–31st October 2014, respectively; **d–f** is showing vertical profile of vertical wind (m/s) valid for 29th–31st October 2014, respectively; **g–i** is showing vertical profile of water–vapour mixing ratio (kg/kg) valid for 29th–31st October 2014, respectively

The first and second rows in Fig. 9 show the model simulated maximum convective available potential energy (CAPE) during the life period of TC Nilofar at 00 UTC on 29th and 30th October 2014, respectively. Cyclone Nilofar extracted heat from the ARB through sensible and latent heat fluxes. Some factors like cold sea surface temperature and dry air in the vicinity of the cyclone can limit the intensification of
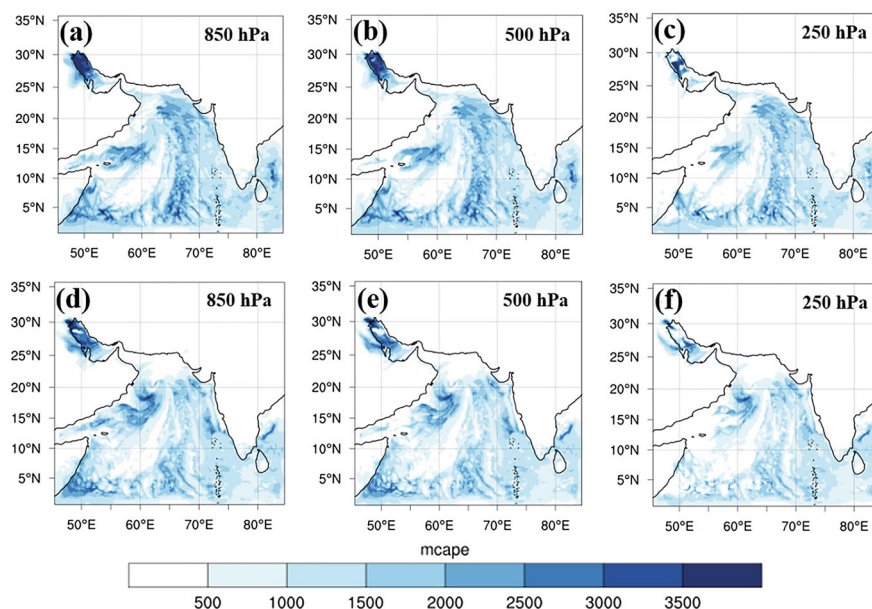
Fig. 9 Maximum CAPE (J/kg) over the ARB on 29th and 30th October 2014

tropical cyclones. Dry air limits the ascending motion because it is less buoyant than moist air at the same given temperature, and it also decreases the net condensation and latent heat release. It is clear from Fig. 9 that when we move from the lower to the upper troposphere, there is a continuous decrease in the amount of CAPE value. Since CAPE is related to maximum potential vertical velocity within an updraft and larger values of CAPE indicate the intensification of TC, there is a significant decrease in the CAPE values from 29 to 30th October. From Fig. 8h, QVAPOR continuously decreases up to 282 hPa (almost), which is zero in the vertical column above it. At the same time, CAPE is less than 1000 (J/kg) near the eye wall. This fact supports the intensity reduction of TC Nilofar on this day.

Hence, by these analyses, we may reach a point where increasing wind shear, atmospheric stability, decreasing QVAPOR mainly in the middle and upper troposphere, and weak CAPE are the other factors responsible for TC Nilofar's dissipation before landfall.

4   Conclusions

WRF model has been used to carry out simulations of non-land falling very severe cyclonic storm Nilofar which formed over the ARB in October 2014. The parameters simulated by the model, specifically; mean sea level pressure (MSLP), 10 m surface

wind and rainfall, are found close to the available observations. The purpose of this study was to explore the non-land falling cyclone, which also may be as vulnerable as a landfalling cyclone becomes because the coastal regions of India, Oman and Pakistan suffer in terms of the damage, including loss of human lives and livestock, destruction of property, agricultural, and industrial production caused by cyclone induced strong winds and heavy rainfall respective to storms not make landfall or not. Also, we opened a few aspects that may be responsible for dissipating the cyclone before reaching the land. Sea surface temperature, wind shear, atmospheric stability and water-vapour mixing ratios are favourable parameters that play a significant role in this direction. Overall, the present case study shows that the model has performed reasonably well over the ARB and addressed the dynamics and characteristics of the VSCS Nilofar to a great extent.

References

1. Chandrasekar, R., Balaji, C.: Sensitivity of tropical cyclone Jal simulations to physics parameters. J. Earth Syst. Sci. **121**, 923–946 (2012)
2. Dudhia, J.: Numerical study of convection observed during winter monsoon experiment using a mesoscale two-dimensional model. J. Atmos. Sci. **46**, 3077–3107 (1989)
3. Emanuel, K.A.: An air-sea interaction theory for tropical cyclones. Part I. J. Atmos. Sci. **42**, 1062–1071 (1986)
4. Gray, W.M.: Tropical Cyclone Genesis. Department of Atmospheric Science Paper, 234, Colorado State University, Fort Collins, CO, 121 pp. (1975)
5. Hong, S.-Y., Lim, J.-O.J.: The WRF single–moment 6–class microphysics scheme (WSM6). J. Korean Meteor. Soc. **42**, 129–151 (2006)
6. Janjic, Z.I.: The step-mountain eta coordinate model: further developments of the convection, viscous sublayer, and turbulence closure schemes. Mon. Wea. Rev. **122**, 927–945 (1994)
7. Kanase, K.D., Salvekar, P.S.: Study of weak intensity cyclones over bay of Bengal using WRF model. Atmos. Clim. Sci. **4**, 534–548 (2014)
8. Kleinschmidt, E., Jr.: Gundlagen einer theorie des tropischen zyklonen. Arch. Meteorol. Geophys. Bioklimatol. Ser. A **4**, 53–72 (1951)
9. Mlawer, E.J., Taubman, S.J., Brown, P.D., Iacono, M.J., Clough, S.A.: Radiative transfer for inhomogeneous atmosphere: RRTM, a validated correlated-k model for the longwave. J. Geophys. Res. **102**(D14), 16663–16682 (1997)
10. Osuri, K.K., Mohanty, U.C., Routray, A., Kulkarni, M.A., Mohapatra, M.: Customization of WRF-ARW model with physical parameterization schemes for the simulation of tropical cyclones over North Indian Ocean, Nat Hazards. https://doi.org/10.1007/s11069-011-9862-0
11. Panda, J., Giri, R.K.: A comprehensive study of surface and upper air characteristics over two stations on the west coast of India during the occurrence of a cyclonic storm. Nat. Hazards **64**, 1055–1078 (2012)
12. Riehl, H.: A model for hurricane formation. J. Appl. Phys. **21**, 917–925 (1950)
13. Riehl, H., Malkus, J.S.: Some aspects of Hurricane Daisy, 1958. Tellus **13**, 181–213 (1961)
14. Shapiro, L.J., Willoughby, H.E.: The response of balanced hurricanes to local sources of heat and momentum. J. Atmos. Sci. **39**, 378–394 (1982)

15. Willoughby, H.E.: Temporal changes of the primary circulation in tropical cyclones. J. Atmos. Sci. **47**, 242–264 (1990)
16. Willoughby, H.E., Jin, H.-L., Lord, S.J., Piotrowicz, J.M.: Hurricane structure and evolution as simulated by an axisymmetric, nonhydrostatic numerical model. J. Atmos. Sci. **41**, 1169–1186 (1984)

Crypto-Encoding Communication with Graph Theory

Pariksha Gupta [ID]**, Sangeeta Gupta** [ID]**, and Sweta Srivastav** [ID]

Abstract The science of converting plain text into encrypted text and encrypted text into plain text is known as cryptography. This strategy has been utilized by militaries and diplomats ever since antiquity. In this paper, we are interested in inventing encryption and decryption algorithms to encrypt and decrypt plain text with the use of graph theory techniques. Throughout the paper, we will use the Sun-let graph and Pan graph to encrypt and decrypt our data.

Keywords Sun-let graph · Pan graph · Cryptography · Encryption · Decryption

1 Introduction

Graph theory plays a very important role in different fields like networking, computer science, electronics, robotics, etc. The concept of graph theory can be used with cryptography in the encryption and decryption of secret messages. Since antiquity, communication has relied on secret messages for diplomats and militaries. This paper aims to bridge the gap between graph theory and cryptography. Amudha et al. [1] discussed the application of graph theory in their paper by taking the graphs like Euler graph and Hamiltonian graph. Nandhini et al. [2] presented an approach to graph theory in cryptography. Also, they discussed the connection between graph theory and cryptography by using the concept of a spanning tree to encrypt the message. Baizhu et al. [3] introduced different types of algorithms to secure communication with the help of graphs like corona graphs, bipartite graphs, and star graphs. Abduljaleel et al.

P. Gupta (✉) · S. Gupta · S. Srivastav
Department of Mathematics, Sharda School Basic Sciences and Research, Sharda University,
Greater Noida, India
e-mail: parikshagupta0@gmail.com

S. Gupta
e-mail: sangeeta.gupta@sharda.ac.in

S. Srivastav
e-mail: sweta.srivastav@sharda.ac.in

[4] proposed an algorithm using graph theory which depends on the audio files as a basis for exploiting a set of keys for encoding color images. The concept of cycle graph, complete graph, and minimum spanning tree has been used to develop the complex cipher by Etaiwi [5].

This paper explores the concepts of graph theory with cryptography and generates the encryption and decryption algorithm with the help of the Sun-let graph and Pan-graph. For basic definitions and terminologies of graph theory, we follow Harary [6].

Definition 1 The *m-Pan graph* is obtained by connecting a cycle graph C_m to a singleton graph K_1 with a bridge.

Definition 2 The sun-let graph is the graph attained by attaching pendant edges to a *m*-cycle graph. It is denoted as S_n.

Definition 3 Cryptography is the science of transforming a secret message into an encrypted form by using codes so that only the concerned person can interpret it.

Definition 4 Encryption is the process of transforming a plain text message into a cipher text.

Definition 5 Decryption is the process of conversion of cipher text into plain text.

2   Results

2.1   Secret Communication with Sun-Let Graph and Pan-Graph

Throughout the paper, we will consider the following table as Standard Table to check the values (see Table 1).

To initiate the encryption algorithm, initially we incorporate the ASCII index. Let the length of the text be *m*. We first represent each letter of the message by the ASCII code values (see Table 2).

Table 1 Numerical representation of the alphabet

A	B	C	D	E	F	G	H	I	J
0	1	2	3	4	5	6	7	8	9
K	L	M	N	O	P	Q	R	S	T
10	11	12	13	14	15	16	17	18	19
U	V	W	X	Y	Z				
20	21	22	23	24	25				

Table 2 ASCII value representation of alphabets

A	B	C	D	E	F	G	H	I	J
65	66	67	68	69	70	71	72	73	74
K	L	M	N	O	P	Q	R	S	T
75	76	77	78	79	80	81	82	83	84
U	V	W	X	Y	Z				
85	86	87	88	89	90				

Apply the following cipher to the arrived numerical values: (*Numerical value* + *m*) (mod 26).

Case 1—If *m* is even then follow the next few steps:

Step 1—Let $\{v_1, v_2, v_3, \ldots\ldots\ldots, v_n, v'_{n+1}, v'_{n+2}, \ldots\ldots\ldots, v'_m\}$ be the variables assigned to the values.

Step 2—Assuming $\{v_1, v_2, v_3, \ldots\ldots\ldots, v_n, v'_{n+1}, v'_{n+2}, \ldots\ldots\ldots, v'_m\}$ as the vertices of the graph. Draw the Sun-let graph taking $\{v_1, v_2, v_3, \ldots\ldots\ldots, v_n\}$ as the vertices of the cycle and $\{v'_{n+1}, v'_{n+2}, \ldots\ldots\ldots, v'_m\}$ as the spokes of the cycle.

Step 3—Convert the graph into an adjacency matrix and mark it as the Key value.

Step 4—Add $\{v_1, v_2, v_3, \ldots\ldots\ldots, v_n, v'_{n+1}, v'_{n+2}, \ldots\ldots\ldots, v'_m\}$ to the 1st, 2nd,………, mth column respectively excluding diagonal elements.

Step 5—Apply the following cipher to the diagonal elements: $2v_m$ (mod *m*), ∀*m*.

Step 6—Arrange all the elements of the matrix and the key–value matrix row-wise in a list separately. If any number in the list is less than 15 then convert it into an alphabet from the standard table.

Step 7—To encrypt the space between the words, put any special character and follow the above steps to encrypt all the words.

Step 8—Send the above list of matrices along with the key-value matrix and key operation to the receiver.

Case 2—If *m* is odd then follow the next few steps:

Step 1—Assign the variables to the values.

Step 2—Assuming $\{v_1, v_2, v_3, \ldots\ldots\ldots, v_m\}$ as the vertices of the graph. Draw a $(m-1)$-Pan graph by first making the vertices of the cycle and then the singleton graph.

Step 3—Convert the graph into an adjacency matrix and mark it as a key value.

Step 4—Add $\{v_1, v_2, v_3, \ldots\ldots\ldots, v_m\}$ to the 1st, 2nd,………, mth column respectively excluding diagonal elements.

Step 5—Apply the following cipher to the diagonal elements: $2v_m$ (mod m), $\forall m$.

Step 6—Arrange all the elements of the matrix and the key–value matrix row-wise in a list separately. If any number in the list is less than 15 then convert it into an alphabet. (For example: Putting A $\leftrightarrow$ 0, B $\leftrightarrow$ 1, and so on.)

Step 7—To encrypt the space between the words, put any special character and follow the above steps to encrypt all the words.

Step 8—Send the above list of matrices along with the key-value matrix list and key operation to the receiver.

Algorithm for decryption:

To initiate the decryption algorithm, follow the next few steps –

Step 1—Check the code for any special character and any alphabets. If a special character exists, then it will be considered as space between the words, and if any alphabets are present then convert them into numbers from the standard table.

Step 2—Arrange the codes in the form of m x m matrix row-wise. If m is the number of elements in the code then the $\sqrt{m}$ will be the number of rows and columns.

Step 3—Subtract the Key value matrix from the matrix obtained.

Step 4—Make the diagonal elements zero.

Step 5—Extract the common column element from each column except zero.

Step 6—Apply the following operation: $v_n + 4$ (mod 26) and check each value from the standard table.

Step 7—Hence, the original text appeared.

OBSERVATION 1: For a sentence, the same key operation will be followed for all the words.

OBSERVATION 2: If the length of the word is less than or equal to 3, then we can use either a cycle graph or a Path graph. The key operation will remain the same when the length is three for the Cycle graph or Path graph.

OBSERVATION 3: While counting the number of letters in a sentence, we will disregard the spaces between them.

OBSERVATION 4: We will draw a different graph for each word present in the sentence.

To verify the above encryption and decryption algorithm, we will refer to the following examples:

Examples 1 *Let us assume that we have to transfer a message i.e., 'GRATITUDE' then the first step is to convert the alphabet into numerical values using the ASCII index values. Here, m = 9 (odd), so we will refer to Case 2 to encrypt this message.*

G	R	A	T	I	T	U	D	E
71	82	65	84	73	84	85	68	69

On applying the following cipher: (*Numerical value* + *m*) (mod 26), we will get the following numerical values of the text –

G	R	A	T	I	T	U	D	E
2	13	22	15	4	15	16	25	0

Assign the variable $\{v_1, v_2, v_3, \ldots\ldots\ldots, v_m\}$ to the values.

2	13	22	15	4	15	16	25	0
v_1	v_2	v_3	v_4	v_5	v_6	v_7	v_8	v_9

Assuming $\{v_1, v_2, v_3, \ldots\ldots\ldots, v_m\}$ as the vertices of the graphs and draw the (*m* − 1) *Pan graph* (see Fig. 1).

Converting the above graph into an adjacency matrix. Let A be that matrix –

$$A = \begin{bmatrix} 0\ 1\ 0 & 0\ 0\ 0 & 0\ 1\ 0 \\ 1\ 0\ 1 & 0\ 0\ 0 & 0\ 0\ 0 \\ 0\ 1\ 0 & 1\ 0\ 0 & 0\ 0\ 0 \\ 0\ 0\ 1 & 0\ 1\ 0 & 0\ 0\ 0 \\ 0\ 0\ 0 & 1\ 0\ 1 & 0\ 0\ 0 \\ 0\ 0\ 0 & 0\ 1\ 0 & 1\ 0\ 0 \\ 0\ 0\ 0 & 0\ 0\ 1 & 0\ 1\ 0 \\ 1\ 0\ 0 & 0\ 0\ 0 & 1\ 0\ 1 \\ 0\ 0\ 0 & 0\ 0\ 0 & 0\ 1\ 0 \end{bmatrix}$$

Fig. 1 8—Pan graph
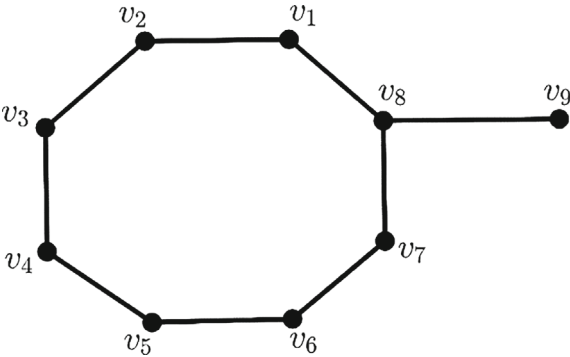
Take the copy of the A matrix as A'. Assuming A as the key–value matrix and keeping it for future use. Add the value of $\{v_1, v_2, v_3, \ldots\ldots\ldots, v_9\}$ to each matrix column of matrix A' respectively except for the diagonal elements.

$$B = \begin{bmatrix} 0 & 14 & 22 & 15 & 4 & 15 & 16 & 26 & 0 \\ 3 & 0 & 23 & 15 & 4 & 15 & 16 & 25 & 0 \\ 2 & 14 & 0 & 16 & 4 & 15 & 16 & 25 & 0 \\ 2 & 13 & 23 & 0 & 5 & 15 & 16 & 25 & 0 \\ 2 & 13 & 22 & 15 & 0 & 16 & 16 & 25 & 0 \\ 2 & 13 & 22 & 15 & 5 & 0 & 17 & 25 & 0 \\ 2 & 13 & 22 & 15 & 4 & 16 & 0 & 26 & 0 \\ 3 & 13 & 22 & 15 & 4 & 15 & 17 & 0 & 1 \\ 2 & 13 & 22 & 15 & 4 & 15 & 16 & 26 & 0 \end{bmatrix}$$

For diagonal elements, apply the cipher $2v_m \pmod{m}$, $\forall m$, and we will get the following matrix –

$$A' = \begin{bmatrix} 0 & 14 & 22 & 15 & 4 & 15 & 16 & 26 & 0 \\ 3 & 4 & 23 & 15 & 4 & 15 & 16 & 25 & 0 \\ 2 & 14 & 8 & 16 & 4 & 15 & 16 & 25 & 0 \\ 2 & 13 & 23 & 8 & 5 & 15 & 16 & 25 & 0 \\ 2 & 13 & 22 & 15 & 3 & 16 & 16 & 25 & 0 \\ 2 & 13 & 22 & 15 & 5 & 3 & 17 & 25 & 0 \\ 2 & 13 & 22 & 15 & 4 & 16 & 5 & 26 & 0 \\ 3 & 13 & 22 & 15 & 4 & 15 & 17 & 8 & 1 \\ 2 & 13 & 22 & 15 & 4 & 15 & 16 & 26 & 5 \end{bmatrix}$$

Convert the elements of the above matrix row-wise into a form of a list as below –

[0 14 22 15 4 15 16 26 0 3 4 23 15 4 15 16 25 0 2 14 8 16 4 15 16 25 0 2 13 23 8 5 15 16 25 0 2 13 22 15 3 16 16 25 0 2 13 22 15 5 3 17 25 0 2 13 22 15 4 16 5 26 0 3 13 22 15 4 15 17 8 1 2 13 22 15 4 15 16 26 5]

In the above code, replace the numbers which are less than 15 with an alphabet from the standard table. Now, send these lists along with the key operation to the receiver.

[A O 22 15 E 15 16 26 A D E 23 15 E 15 16 25 A C O I 16 E 15 16 25 A C N 23 I F 15 16 25 A C N 22 15 D 16 16 25 A C N 22 15 F D 17 25 A C N 22 15 E 16 F 26 A D N 22 15 E 15 17 I B C N 22 15 E 15 16 26 F]

[0 1 0 0 0 0 0 1 0 1 0 1 0 0 0 0 0 0 1 0 1 0 0 0 0 0 0 1 0 1 0 0 0 0 0 0 1 0 1 0 0 0 0 0 0 1 0 1 0 0 0 0 0 1 0 1 0 0 0 0 0 0 1 0 1 0 1 0 0 0 0 1 0 1 0 0 0 0 0 0 1 0]

Key operation $= v_n + 4 \pmod{26}$

Decryption: The encrypted message is given below. To decrypt it, we will follow the above-mentioned steps.

[A O 22 15 E 15 16 26 A D E 23 15 E 15 16 25 A C O I 16 E 15 16 25 A C N 23 I F 15 16 25 A C N 22 15 D 16 16 25 A C N 22 15 F D 17 25 A C N 22 15 E 16 F 26 A D N 22 15 E 15 17 I B C N 22 15 E 15 16 26 F]

[0 1 0 0 0 0 0 1 0 1 0 1 0 0 0 0 0 0 0 1 0 1 0 0 0 0 0 0 0 1 0 1 0 0 0 0 0 0 0 1 0 1 0 0 0 0 0 0 0 1 0 1 0 0 0 0 0 0 0 1 0 1 0 1 0 0 0 0 0 1 0 1 0 0 0 0 0 0 0 1 0]

Key operation $= v_n + 4 \pmod{26}$

There is no special character present in the code. Convert the alphabet into its numerical value from the standard table as shown below.

[0 14 22 15 4 15 16 26 0 3 4 23 15 4 15 16 25 0 2 14 8 16 4 15 16 25 0 2 13 23 8 5 15 16 25 0 2 13 22 15 3 16 16 25 0 2 13 22 15 5 3 17 25 0 2 13 22 15 4 16 5 26 0 3 13 22 15 4 15 17 8 1 2 13 22 15 4 15 16 26 5]

The total number of values present in the list is 81. So, it will be a 9×9 matrix.

$$A' = \begin{bmatrix} 0 & 14 & 22 & 15 & 4 & 15 & 16 & 26 & 0 \\ 3 & 4 & 23 & 15 & 4 & 15 & 16 & 25 & 0 \\ 2 & 14 & 8 & 16 & 4 & 15 & 16 & 25 & 0 \\ 2 & 13 & 23 & 8 & 5 & 15 & 16 & 25 & 0 \\ 2 & 13 & 22 & 15 & 3 & 16 & 16 & 25 & 0 \\ 2 & 13 & 22 & 15 & 5 & 3 & 17 & 25 & 0 \\ 2 & 13 & 22 & 15 & 4 & 16 & 5 & 26 & 0 \\ 3 & 13 & 22 & 15 & 4 & 15 & 17 & 8 & 1 \\ 2 & 13 & 22 & 15 & 4 & 15 & 16 & 26 & 5 \end{bmatrix}$$

Now subtract the key-value matrix from it and make the diagonal elements 'zero' by any operation as shown below –

$$A' - A = \begin{bmatrix} 0 & 14 & 22 & 15 & 4 & 15 & 16 & 26 & 0 \\ 3 & 0 & 23 & 15 & 4 & 15 & 16 & 25 & 0 \\ 2 & 14 & 0 & 16 & 4 & 15 & 16 & 25 & 0 \\ 2 & 13 & 23 & 0 & 5 & 15 & 16 & 25 & 0 \\ 2 & 13 & 22 & 15 & 0 & 16 & 16 & 25 & 0 \\ 2 & 13 & 22 & 15 & 5 & 0 & 17 & 25 & 0 \\ 2 & 13 & 22 & 15 & 4 & 16 & 0 & 26 & 0 \\ 3 & 13 & 22 & 15 & 4 & 15 & 17 & 0 & 1 \\ 2 & 13 & 22 & 15 & 4 & 15 & 16 & 26 & 0 \end{bmatrix} - \begin{bmatrix} 0 & 1 & 0 & 0 & 0 & 0 & 0 & 1 & 0 \\ 1 & 0 & 1 & 0 & 0 & 0 & 0 & 0 & 0 \\ 0 & 1 & 0 & 1 & 0 & 0 & 0 & 0 & 0 \\ 0 & 0 & 1 & 0 & 1 & 0 & 0 & 0 & 0 \\ 0 & 0 & 0 & 1 & 0 & 1 & 0 & 0 & 0 \\ 0 & 0 & 0 & 0 & 1 & 0 & 1 & 0 & 0 \\ 0 & 0 & 0 & 0 & 0 & 1 & 0 & 1 & 0 \\ 1 & 0 & 0 & 0 & 0 & 0 & 1 & 0 & 1 \\ 0 & 0 & 0 & 0 & 0 & 0 & 0 & 1 & 0 \end{bmatrix}$$

$$= \begin{bmatrix} 0 & 13 & 22 & 15 & 4 & 15 & 16 & 25 & 0 \\ 2 & 0 & 22 & 15 & 4 & 15 & 16 & 25 & 0 \\ 2 & 13 & 0 & 15 & 4 & 15 & 16 & 25 & 0 \\ 2 & 13 & 22 & 0 & 4 & 15 & 16 & 25 & 0 \\ 2 & 13 & 22 & 15 & 0 & 15 & 16 & 25 & 0 \\ 2 & 13 & 22 & 15 & 4 & 0 & 16 & 25 & 0 \\ 2 & 13 & 22 & 15 & 4 & 15 & 0 & 25 & 0 \\ 2 & 13 & 22 & 15 & 4 & 15 & 16 & 0 & 0 \\ 2 & 13 & 22 & 15 & 4 & 15 & 16 & 25 & 0 \end{bmatrix}$$

Now, extract the common numbers from each column. The numbers are:

[2 13 22 15 4 15 16 25 0]

Apply the key operation: $v_n + 4 \pmod{26}$ and check the value from the standard table. Hence, the original message appeared as:

G R A T I T U D E

Example 2 *Suppose we want to communicate the message '**HEALTH IS WEALTH**' then the first step is to note down the ASCII index for each letter. Here, $m = 14$ (even) so we will refer to Case 1 to encrypt this message.*

H	E	A	L	T	H	I
72	69	65	76	84	72	73
S	W	E	A	L	T	H
83	87	69	65	76	84	72

On applying the following cipher: (*Numerical value* $+ m$) (mod 26), we will get the following numerical values of the text –

H	E	A	L	T	H	I
8	5	1	12	20	8	9
S	W	E	A	L	T	H
19	23	5	1	12	20	8

Assign the variable $\{v_1, v_2, v_3, \ldots \ldots, v_m\}$ to the values.

8	5	1	12	20	8
v_1	v_2	v_3	v_4	v_5	v_6

9	19
v_1	v_2

23	5	1	12	20	8
v_1	v_2	v_3	v_4	v_5	v_6

Assuming $\{v_1, v_2, v_3, \ldots\ldots\ldots, v_n, v'_{n+1}, v'_{n+2}, \ldots\ldots\ldots, v'_m\}$ as the vertices of the graph. Draw the Sun-let graph for each word by taking $\{v_1, v_2, v_3, \ldots\ldots\ldots, v_n\}$ as the vertices of the cycle and $\{v'_{n+1}, v'_{n+2}, \ldots\ldots\ldots, v'_m\}$ the spokes of the cycle. For the second word 'IS' we can choose a path graph (see Fig. 2).

Converting all three graphs into an adjacency matrix and saving them as a key value matrix for later use.

$$
A = \begin{bmatrix} 0 & 1 & 1 & 1 & 0 & 0 \\ 1 & 0 & 1 & 0 & 1 & 0 \\ 1 & 1 & 0 & 0 & 0 & 1 \\ 1 & 0 & 0 & 0 & 0 & 0 \\ 0 & 1 & 0 & 0 & 0 & 0 \\ 0 & 0 & 1 & 0 & 0 & 0 \end{bmatrix} B = \begin{bmatrix} 0 & 1 \\ 1 & 0 \end{bmatrix} C = \begin{bmatrix} 0 & 1 & 1 & 1 & 0 & 0 \\ 1 & 0 & 1 & 0 & 1 & 0 \\ 1 & 1 & 0 & 0 & 0 & 1 \\ 1 & 0 & 0 & 0 & 0 & 0 \\ 0 & 1 & 0 & 0 & 0 & 0 \\ 0 & 0 & 1 & 0 & 0 & 0 \end{bmatrix}
$$
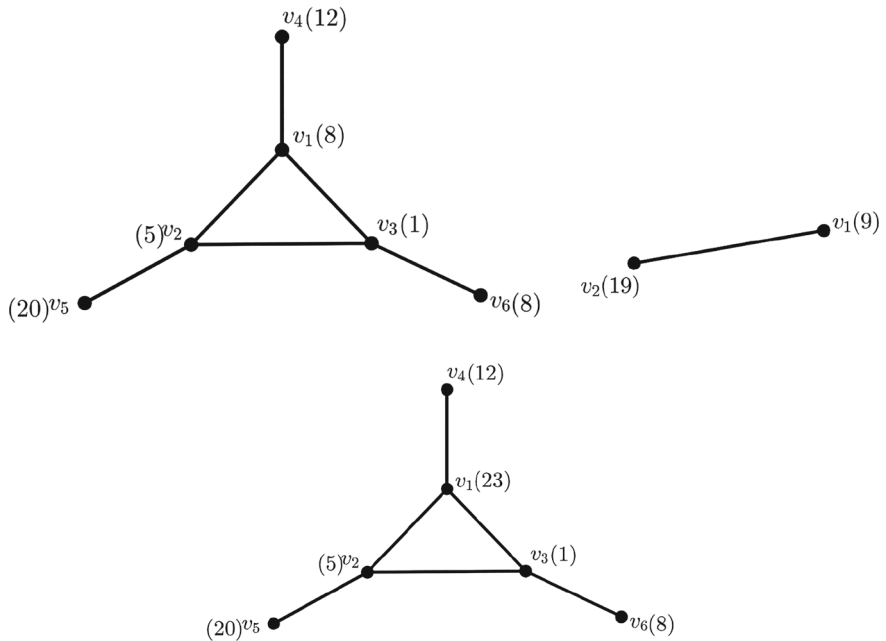
Fig. 2 Representation in sun-let graph

Take a copy of each matrix and add $\{v_1, v_2, v_3, \ldots\ldots, v_n, v'_{n+1}, v'_{n+2}, \ldots\ldots, v'_m\}$ to each column except diagonal elements. For diagonal elements, apply the following cipher: $2v_m \pmod{m}, \forall m$

$$A' = \begin{bmatrix} 2 & 6 & 2 & 13 & 20 & 8 \\ 9 & 10 & 2 & 12 & 21 & 8 \\ 9 & 6 & 2 & 12 & 20 & 9 \\ 9 & 5 & 1 & 10 & 20 & 8 \\ 8 & 6 & 1 & 12 & 12 & 8 \\ 8 & 5 & 2 & 12 & 20 & 2 \end{bmatrix} B' = \begin{bmatrix} 10 & 20 \\ 10 & 10 \end{bmatrix}$$

$$C' = \begin{bmatrix} 4 & 6 & 2 & 13 & 20 & 8 \\ 24 & 10 & 2 & 12 & 21 & 8 \\ 24 & 6 & 2 & 12 & 20 & 9 \\ 24 & 5 & 1 & 10 & 20 & 8 \\ 23 & 6 & 1 & 12 & 12 & 8 \\ 23 & 5 & 2 & 12 & 20 & 2 \end{bmatrix}$$

Convert the elements of the above matrices row-wise into the form of a list as below –

[2 6 2 13 20 8 9 10 2 12 21 8 9 6 2 12 20 9 9 5 1 10 20 8 8 6 1 12 12 8 8 5 2 12 20 2 $ 10 20 10 10 @ 4 6 2 13 20 8 24 10 2 12 21 8 24 6 2 12 20 9 24 5 1 10 20 8 23 6 1 12 12 8 23 5 2 12 20 2]

In the above code, replace the numbers which are less than 15 with an alphabet from the standard table. Now, send these lists along with the key operation to the receiver.

[C G C N 20 I J K C M 21 I J G C M 20 J J F B K 20 I I G B M M I I F C M 20 C $ K 20 K K @ E G C N 20 I 24 K C M 21 I 24 G C M 20 J 24 F B K 20 I 23 G B M M I 23 F C M 20 C]

[0 1 1 1 0 0 1 0 1 0 1 0 1 1 0 0 0 1 1 0 0 0 0 0 0 1 0 0 0 0 0 0 1 0 0 0 @ 0 1 1 0 & 0 1 1 1 0 0 1 0 1 0 1 0 1 1 0 0 0 1 1 0 0 0 0 0 0 1 0 0 0 0 0 0 1 0 0 0]

Key operation $= v_n - 1 \pmod{26}$

Decryption: The encrypted message is given below. To decrypt it, we will follow the above-mentioned steps.

[C G C N 20 I J K C M 21 I J G C M 20 J J F B K 20 I I G B M M I I F C M 20 C $ K 20 K K @ E G C N 20 I 24 K C M 21 I 24 G C M 20 J 24 F B K 20 I 23 G B M M I 23 F C M 20 C]

[0 1 1 1 0 0 1 0 1 0 1 0 1 1 0 0 0 1 1 0 0 0 0 0 0 1 0 0 0 0 0 0 1 0 0 0 @ 0 1 1 0 & 0 1 1 1 0 0 1 0 1 0 1 0 1 1 0 0 0 1 1 0 0 0 0 0 0 1 0 0 0 0 0 0 1 0 0 0]

There are special characters in the list indicating the space between the words. Considering the space in mind, segregate both lists–

[C G C N 20 I J K C M 21 I J G C M 20 J J F B K 20 I I G B M M I I F C M 20 C]

[0 1 1 1 0 0 1 0 1 0 1 0 1 1 0 0 0 1 1 0 0 0 0 0 0 1 0 0 0 0 0 0 1 0 0 0]

[K 20 K K]

[0 1 1 0]

[E G C N 20 I 24 K C M 21 I 24 G C M 20 J 24 F B K 20 I 23 G B M M I 23 F C M 20 C]

[0 1 1 1 0 0 1 0 1 0 1 0 1 1 0 0 0 1 1 0 0 0 0 0 0 1 0 0 0 0 0 0 1 0 0 0]

Convert the alphabet into its numerical value from the standard table as shown below.

[2 6 2 13 20 8 9 10 2 12 21 8 9 6 2 12 20 9 9 5 1 10 20 8 8 6 1 12 12 8 8 5 2 12 20 2]

[10 20 10 10]

[4 6 2 13 20 8 24 10 2 12 21 8 24 6 2 12 20 9 24 5 1 10 20 8 23 6 1 12 12 8 23 5 2 12 20 2]

Convert the above matrices in the form of $m \times m$.

Now subtract the key-value matrix from it as shown below –

$$A' - A = \begin{bmatrix} 2 & 6 & 2 & 13 & 20 & 8 \\ 9 & 10 & 2 & 12 & 21 & 8 \\ 9 & 6 & 2 & 12 & 20 & 9 \\ 9 & 5 & 1 & 10 & 20 & 8 \\ 8 & 6 & 1 & 12 & 12 & 8 \\ 8 & 5 & 2 & 12 & 20 & 2 \end{bmatrix} - \begin{bmatrix} 0 & 1 & 1 & 1 & 0 & 0 \\ 1 & 0 & 1 & 0 & 1 & 0 \\ 1 & 1 & 0 & 0 & 0 & 1 \\ 1 & 0 & 0 & 0 & 0 & 0 \\ 0 & 1 & 0 & 0 & 0 & 0 \\ 0 & 0 & 1 & 0 & 0 & 0 \end{bmatrix} = \begin{bmatrix} 2 & 5 & 1 & 12 & 20 & 8 \\ 8 & 10 & 1 & 12 & 20 & 8 \\ 8 & 5 & 2 & 12 & 20 & 8 \\ 8 & 5 & 1 & 10 & 20 & 8 \\ 8 & 5 & 1 & 12 & 12 & 8 \\ 8 & 5 & 1 & 12 & 20 & 2 \end{bmatrix}$$

$$B' - B = \begin{bmatrix} 10 & 20 \\ 10 & 10 \end{bmatrix} - \begin{bmatrix} 0 & 1 \\ 1 & 0 \end{bmatrix} = \begin{bmatrix} 10 & 19 \\ 9 & 10 \end{bmatrix}$$

$$C' - C = \begin{bmatrix} 4 & 6 & 2 & 13 & 20 & 8 \\ 24 & 10 & 2 & 12 & 21 & 8 \\ 24 & 6 & 2 & 12 & 20 & 9 \\ 24 & 5 & 1 & 10 & 20 & 8 \\ 23 & 6 & 1 & 12 & 12 & 8 \\ 23 & 5 & 2 & 12 & 20 & 2 \end{bmatrix} - \begin{bmatrix} 0 & 1 & 1 & 1 & 0 & 0 \\ 1 & 0 & 1 & 0 & 1 & 0 \\ 1 & 1 & 0 & 0 & 0 & 1 \\ 1 & 0 & 0 & 0 & 0 & 0 \\ 0 & 1 & 0 & 0 & 0 & 0 \\ 0 & 0 & 1 & 0 & 0 & 0 \end{bmatrix} = \begin{bmatrix} 4 & 5 & 1 & 12 & 20 & 8 \\ 23 & 10 & 1 & 12 & 20 & 8 \\ 23 & 5 & 2 & 12 & 20 & 8 \\ 23 & 5 & 1 & 10 & 20 & 8 \\ 23 & 5 & 1 & 12 & 12 & 8 \\ 23 & 5 & 1 & 12 & 20 & 2 \end{bmatrix}$$

Make the diagonal elements 'zero' by any operation –

$$\begin{bmatrix} 0 & 5 & 1 & 12 & 20 & 8 \\ 8 & 0 & 1 & 12 & 20 & 8 \\ 8 & 5 & 0 & 12 & 20 & 8 \\ 8 & 5 & 1 & 0 & 20 & 8 \\ 8 & 5 & 1 & 12 & 0 & 8 \\ 8 & 5 & 1 & 12 & 20 & 0 \end{bmatrix} \begin{bmatrix} 0 & 19 \\ 9 & 0 \end{bmatrix} \begin{bmatrix} 0 & 5 & 1 & 12 & 20 & 8 \\ 23 & 0 & 1 & 12 & 20 & 8 \\ 23 & 5 & 0 & 12 & 20 & 8 \\ 23 & 5 & 1 & 0 & 20 & 8 \\ 23 & 5 & 1 & 12 & 0 & 8 \\ 23 & 5 & 1 & 12 & 20 & 0 \end{bmatrix}$$

Now, extract the common numbers from each column except zero. The numbers are:

[8 5 1 12 20 8]

[9 19]

[23 5 1 12 20 8]

Apply the key operation: $v_n - 1 \pmod{26}$ and check the value from the standard table.

HEALTH IS WEALTH

Hence, the original message appeared.

3   Conclusion

In this paper, we have investigated the encryption and decryption algorithm with the help of graph theory. Sun-let graph and pan graph have been used to encrypt the communication. Securing communication is widely used by diplomats and militaries since ancient times. Also, in today's world where securing data is the most important task, this can be helpful. In addition, one can use other families of the graph in encryption and decryption by applying other operations on graphs. Securing data with graph theory in a programming language like Python and MATLAB is an open problem.

References

1. Amudha, P., Sagayaraj, A.C., Sheela, A.S.: An application of graph theory in cryptography. Int. J. Pure Appl. Math. **119**(13), 375–383 (2018)
2. Nandhini, R., Maheswari, V., Balaji, V.: A graph theory approach on cryptography. J. Comput. Math. **2**(1), 97–104 (2018)
3. Ni, B., Qazi, R., Rehman, S.U., Farid, G.: Some graph-based encryption schemes. J. Math. (2021)

4. Abduljaleel, I.Q., Abdul-Ghani, S.A., Naji, H.Z.: An image of encryption algorithm using graph theory and speech signal key generation. In: Journal of Physics: Conference Series, vol. 1804, no. 1, p. 012005. IOP Publishing (2021)
5. Al Etaiwi, W.M.: Encryption algorithm using graph theory. J. Sci. Res. Rep. **3**(19), 2519–2527 (2014)
6. Gallian, J.A.: A dynamic survey of graph labeling. Electron. J. Comb. **1**(Dynamic Surveys), DS6 (2018)

Cybersecurity Incidents in Relation to Fraudulent SIM Card Registration in Malawi

Mangani D. Kazembe, Sudeep Varshney, and Keshav Gupta

Abstract One of the frequently used secure way of carrying out transactions on the cyberspace is the use of SMS OTP which is used in financial transaction verifications, a site registrant's mobile number availability, and in social media. SMS OTP has been the most preferred service than email OTP by many users. The cyberspace is a global borderless environment where people of bad intentions can exploit weakness in one geographical location and use them on the cyberspace which inevitably affect other geographical locations. Of recent, there have been reports of cybersecurity issues targeting users which include; malicious emails, malicious websites, child pornography and others. Pursuing these services has led to mobile numbers whose registered national identities has pointed to non-existent owners or data not available in the national database. Statistics from investigating agencies indicate that there is a strong correlation coefficient between the cybersecurity incidents and mobile numbers whose national identification does not exist. This paper presents correlation analysis of these cybersecurity incidents and demonstrates how they relate to the number of the national identities that do not exist, with special focus on Malawi. Specifically, the correlation analysis uses the numerical data collected between 2016 and 2021.

Keywords Correlation · One-time password · Mobile network operator

M. D. Kazembe (✉)
Department of Computer Science and Engineering, Sharda University, Greater Noida, Uttar Pradesh, India
e-mail: daudi.kazembe@yahoo.com

S. Varshney
School of Engineering and Technology (SET), Department of Computer Science and Engineering | Coordinator NIRF, Sharda University, Greater Noida, Uttar Pradesh, India

K. Gupta
School of Engineering and Technology (SET), Department of Computer Science and Engineering, Sharda University, Greater Noida, Uttar Pradesh, India

1   Introduction

Malawi has about 10 million live SIM cards which is about 52% of the total population [1]. These are divided among four MNO of Airtel Malawi, TNM, Access Communication, and MTL [2]. As of February 2022, Malawi had about 4 million internet users [3].

Internet provides a seamless and borderless interaction of users in the virtual environment called cyberspace. These users live in geographical locations controlled by governments [4]. Users may take advantage of weaknesses in some locations and cause cyberspace incidents that may affect other users in any location [5]. Some countries effect mandatory SIM registration as part of efforts to control cyberspace-related incidents [6].

Over the past years, there have been media reports in Malawi about cyberspace incidents like mobile fraud, online fraud, business email compromise (fake email), and others [7]. Each of these incidents has a mobile number that is used to register for a transaction and receive an OTP for verification and authentication [8]. An email address would be created to look like a genuine business email address; like j0hn@ example.com for john@example.com. Then the receiver without observing, proceeds to do the transactions based on communication from such an email [9]. There some websites which are created just to engage in online fraud, stealing users' private information, etc. [10]. In the case of Malawi, pursuit of such incidents has ended up in mobile numbers registered in Malawi's MNOs. Cybersecurity involves putting in place measures aimed at protecting computer systems and users. These could be physical, logical, technical, and non-technical. These measures are coupled with regulations, policies, and procedures enforced in geographical authorities contributing to the overall security of the cyberspace [11]. Of interest in these measures are access control, verification, and authentication.

a. *Objective of the study*

Rendering cyberspace a water-tight security without considering how authentication [12] of centralized national identity cards used in SIM card registration [13] may leave out loopholes in cybersecurity. A few weaknesses in a security system such as cybersecurity can lead to major issues on a system, especially that the cyberspace spans the globe.

This paper discusses SIM card registration with focus on Malawi using the national identity card and how it relates to cyberspace issues that were noted during data collection. This gap has not been discussed in the Literature Review section by fellow researchers.

b. *Motivation*

Media reports have always indicated that there are incidents of mobile fraud where it was assumed that the problem could be due to regulations and how they are being applied. Looking at the issues that they were involving technology, it was appropriate

to make a research, use appropriate methods to determine the cause of the problem, and analyze it and see if the problem would be solved using technological techniques.

c. *Organization*

This papers covers some notable research works done related to SIM card registration in Malawi and other countries. This is covered in Literature Review section. The literature review explains objectives of the research works and the gaps that they were trying to cover. It also shows how the literature has left some areas which have led to the problem covered in this paper. The methodology section presents the techniques used to collect data that was used in this paper. The collection methods include quantitative and qualitative. Of great importance is the quantitative data collection which paved way establishing relationship between numerical datasets.

2   Literature Review

This presents some of the research works that have been done by scholars and researchers.

Most of them had done their works focusing on Malawi, while others among them did their work focusing on other geographical locations while having impact on the same research area. They include SIM card registration policy, while some focused on laws and regulations that govern SIM card regulation. Some literature covers types of SIM card registration and makes some recommendations and implications of each case.

Furthermore, some have covered application of algorithms in ensuring cybersecurity in relation to SIM card registration. What is conspicuously missing is the relationship between cybersecurity and SIM card registration. A number of research works has been done covering use of SMS OTP and email OTP. SMS OTP has been recommended as the more secure way; however, this literature leaves out the research that covers strict SIM card registration which is the secure basis for authenticated SMS OTP in most cyberspace transactions. Such transactions could be monetary or not, but still require secure authentication in as far as OTP is concerned.

Other research works are focusing on suggesting the use of special features for authentication have also been considered in this paper. As a case in point is the use of QR code scanning in authenticating a document such as a national identity. This has been taken on board due to its applicability and that the sampled area, Malawi, has a national identity which has that kind of feature and can be used in SIM card registration where the national identity can be authenticated before being used in SIM card registration.

And the last and not least research works are those that demonstrate the existence of online fraud whose basis is the SMS OTP that use malicious mobile numbers only registered to be used in bad motives. Just like malware, this is also a threat to cybersecurity.

The research papers in this section are not an exhaust study of relevant material. However, they have been picked for their most related works to the geographical location under study, Malawi, and their relevant material which is believed to have some applicability to the study covered in this paper. The gap that has been left by the following review is largely creating a good environment to social engineering which is a threat to authentication in cybersecurity (see Table 1).

3   Methodology

First, the research identified participants in data collection. These included mobile communication and internet users, government agencies in regulation and law enforcement. Random sampling was applied in mobile and internet users as in university colleges in which random student and lecturers were interviewed, common markets where sellers and customers were interviewed, and other random people along the streets of Malawi. This data collection was qualitative which focused much on how the users of mobile communication and internet viewed the services. Then of interest were the figures that were collected from government law enforcement agencies. They was a recorded reflection of what the sampled people had talked about. Among the cybersecurity incidents that were recorded by the government agencies, Table 2 shows the complete summary of the data collected from 2016 to 2021.

From the dataset collected from the law enforcement agency, there was another quantitative data that showed availability of national identity that corresponds to a mobile number used in opening the account that was involved in the transaction. Table 3 shows this type of data summed up for the period from 2016 to 2021.

Looking at these arrays of data from cybersecurity incidents and national identity availability, the Pearson Correlation coefficient (below) was used to determine whether there was a relationship between the datasets.

The purpose of using the correlation analysis was to determine the cause of the cybersecurity incidents.

a. *Correlation function*

This is the Pearson Correlation equation whose application assisted to determine the strength of the relationship of the independent and dependent variables.

The stronger the relationship the more it displayed the cause of the cybersecurity incidents. Taking the number of cybersecurity incidents as dependent variables and availability of national identity behind a SIM card as independent variable.

4   Results

The totals in Table 2 were calculated with totals in Table 3 using Pearson correlation and the results were obtained.

Table 1 Some notable and relevant research papers considered in this literature review

Author and name of paper	Method	Results	Objectives	Limitations and future works
Makoza [14]	Qualitative method	Lesson in SIM card registration policies. And Policy transfers	To find the means through which SIM card registration policy may be transferred in countries without the policy	The inability to gather views from stakeholders for the SIM card registration. Future research will investigate policy transfer involving stakeholders
Makanda et al. [15]	Need assessment and requirements analysis	Existence of cybersecurity laws Institutions for cybersecurity	To find out if there is a major study done on the cybersecurity position of Malawi	No enough expert staff in cybersecurity institutions. Use of unregistered SIM cards
Makoza [6]	Qualitative methodology	Study demonstrated the need to address the use of mobile phones in committing crimes and therefore to implement mandatory SIM card registration	To present policy transfer in the context of a developing country	The lesson drawing in Malawi on SIM card registration was limited to experiences of the Government officials without proper formal transfer of information from other contexts
Gelb et al. [16]	System analysis (Myanmar, Malawi and Cambodia)	Know Your Customer (KYC) process requirements	To distinguish between different types of documentation and different financial market segments according to their Know Your Customer requirements	Some users had more than one SIM cards

Table 1 (continued)

Author and name of paper	Method	Results	Objectives	Limitations and future works
El Ayeb et al. [17]	Fraud detection algorithm	None	To propose to address the problem of mobile money fraud by studying different community detection approaches	Data visualization, search and analysis, etc.
Haque et al. [18]	Feature analysis covering authenticity, integrity, non-repudiation, and availability	Description of proposed method	To propose a method on document verification intending to provide authenticity, integrity, availability, and non-repudiation	None
Wanja [19]	Object oriented analysis and design	Verification platform for the users to activate their SIM modules after purchasing them from MNOs. Activating the SIM would be done after a user has been issued with a signed public key by a certificate Authority Some SIM cards were purchased from unauthorized sellers	To design, develop and test a prototype used by the mobile network operators and the users for self-registration of SIM cards	Unauthorized sellers sometimes sold double allocated numbers which resulted in a lot of strange and unwanted calls. Some personal information was given out to unauthorized people
Karhadkar et al. [20]	Project implementation of Encrypted QR code concept	Description of proposed project	To implement a system to verify personal identity before they book a flight at entry gate	None

Table 1 (continued)

Author and name of paper	Method	Results	Objectives	Limitations and future works
Muñoz [21]	Mixed research methodology (Qualitative and Quantitative)	Most of smartphone users had QR code readers on their devices	To introduce a new avenue for innovation and improvement in electoral system by using hybrid Quick Response (QR) Code Technology	The research was done during COVID-19 restrictions and therefore results did not represent the citizenry well
Donatus et al. [22]	Qualitative method	Solution to solve a gap that is addressed by empirical studies from both academia and the industry for a problem that researchers feel should be a none issue in the twenty-first century	To provide a solution to solve a gap that is addressed by empirical studies from both academia and industry for a problem that researchers feel should be a none issue in the twenty-first century	Not mentioned

Table 2 Cybersecurity incidents from 2016 to 2021 in Malawi [7]

Incident	2016	2017	2018	2019	2020	2021	Total
Malicious emails	28	58	16	50	36	43	231
Malicious websites	3	6	9	2	2	6	28
Mobile fraud (sms)	175	121	187	181	88	199	951
Defamatory content	107	202	132	220	168	139	968
Child pornography	161	110	175	176	150	144	916
Online fraud	1	5	5	2	3	5	21
Introduction of malware	2	2	1	1	2	2	10
Disabling computer systems	2	2	2	1	3	3	13
Violent content	9	8	12	9	3	11	52
Disseminating false news about COVID-19	0	0	0	0	69	51	120
Mobile fraud (transactions)	113	93	124	109	82	89	610

Table 3 Status of national identity used in mobile numbers in the cyber incidents [7]

Incident	ID Found	ID not Found
Malicious emails	1	230
Malicious websites	1	27
Mobile fraud (sms)	9	942
Defamatory content	126	842
Child pornography	433	483
Online fraud	0	21
Introduction of malware	0	10
Disabling computer systems	0	13
Violent content	11	41
Disseminating false news about COVID-19	72	48
Mobile fraud (transactions)	187	423
Total	840	3080

The cybersecurity incidents, according to the source [7], were reported by persons who were victims within Malawi, and some were reported from other countries where it was discovered by agents that they were initiated using a mobile number operated in Malawi. The incidents reported within Malawi included Mobile Fraud both transaction and SMS.

a. **Numerical Data from the source file**

The data in Fig. 1 is a summarized copy of Tables 2 and 3 with the three labeled columns showing the variables provided in the mentioned tables.

$$r = \sqrt{\frac{\Sigma(x_i - \overline{x})(y_i - \overline{y})}{\left(\Sigma(x - \overline{x})^2 \Sigma(y - \overline{y})^2\right)}} \qquad (1)$$

b. **Application of the equation in Python**

The following Python code was used to implement the Pearson Correlation formula. It run a comma separated values function on a data file named ***data.csv***.

c. **Correlation Values**

After running the code in Listing 1, the following displays the numerical values that represents the strengths of the relationships between variables.

d. **Visualization of Correlation Values**

The data values in Fig. 2 is visualized in Fig. 3. The visualization is made against a color scale on the right side of the figure where the color on top corresponds to the strongest value of 1 and the color on bottom corresponds to the weakest value of 0.4

Listing 1 Python code implementing Pearson correlation

```
1  #importing necessary libraries
2  import pandas as pd
3  import seaborn as sb
4
5  df = pd.read_csv ('data.csv')
6  #display numerical data from data.csv
7  print (df.to_string())
8
9  pcorr = df.corr(method='pearson')
10
11 #correlation values
12 print(pcorr)
13
14 #correlation visualization
15 sb.heatmap(pcorr,
16          xticklabels=pcorr.columns,
17          yticklabels=pcorr.columns,
18          cmap='RdBu_r',
19          annot=True,
20          linewidth=0.5)
```

Fig. 1 Correlation values for variables

Fig. 2 Correlation Values for variables

Fig. 3 Visualization of correlation values for variables

5 Discussion

The results shown in the preceding section show that there are different relationships between variable that were collected during data collection. Figure 2 shows numerical values of 1 which is a self-relationship and obviously has the highest value of strength. The next highest strength is between mobile numbers associated with non-existent national identity and cybersecurity issues which is 0.95. The lowest strength is the numerical value between mobile numbers associated with existent national identity and cybersecurity issues which is 0.63.

On the aforesaid relationships, of interest is the one with the highest strength, 0.95.

This relationship portrays that if all mobile numbers are registered using national identity that are existent in the national database, there could be fewer cybersecurity issues. This can be seen in the strengths of the relationships.

6 Conclusion and Future Scope

Security measures are designed after a corresponding vulnerability has been discovered. Every security measure counts [23]. It's not easy to explore all security vulnerabilities in a system. This paper has assisted in establishing the possible source of the cybersecurity incidents that possibly affects users from other geographical location. From this analysis, it is concluded that the SIM cards registered using fraudulent national identity cards were used to cause cybersecurity incidents as shown in Tables 2 and 3.

It is also concluded that if there could be strict SIM card registration using live authentication, it would be possible to trace the sources and therefore reduce the

vulnerabilities and consequently improve cybersecurity in relation to threats that emanate from social engineering of the sort discussed in this paper.

References

1. worlddata: worlddata (2020). https://www.worlddata.info/africa/malawi/telecommunication.php. Accessed 13 Sep. 2022
2. BusinessMalawi: Businessmalawi. Nubian bantu ltd. BusinessMalawi https://www.businessmalawi.com/list-of-malawi-mobile-service-providers/. 13 Sep. 2022
3. datareportal: Datareportal. kepios. datareportal (2022). https://datareportal.com/reports/digital-2022-malawi. 13 Sep. 2022
4. Rights, C.: Citizenship rights in Africa. Citizenship rights in Africa. Citizenship Rights (2017). https://citizenshiprightsafrica.org/public-statement-mass-registration-of-malawian-citizens-for-national-identity-cards/. Accessed 4 Sep 2022
5. Foundation, E.F.: A borderless internet, with borderless laws? Stanford university. Electronic Frontier Foundation (2019). https://www.eff.org/event/borderless-internet-borderless-laws. Accessed 13 Sep. 2022
6. Makoza, F.: Learning from abroad on sim card registration policy: the case of Malawi. In: Handbook of Research on Technology Integration in the Global World, pp. 389–406. IGI Global (2019)
7. Tolani, C.: Malawi police website. Malawi police. Chiso Tolani (2021). https://www.police.gov.mw/index.php/about-us/branches/criminal-investigations/cybercrime_reports. Accessed 13 Sep 2022
8. Iskandar, K.: 2fa SMSs: influence of cybersecurity behavior & OTP message content on security. B.S. thesis, University of Twente (2022)
9. F. B. of Investigations: Scams and safety. United States government. Federal Bureau of Investigations (2022). https://www.fbi.gov/scams-and-safety/common-scams-and-crimes/business-email-compromise. Accessed 14 Sep. 2022
10. Chhabra, S., Gupta, V., Kumar, A., Anand, A.: Online fraud detection. EPRA Int. J. Res. Dev. (IJRD) **7**(4), 162–166 (2022)
11. Srinivas, J., Das, A.K., Kumar, N.: Government regulations in cyber security: framework, standards and recommendations. Futur. Gener. Comput. Syst. **92**, 178–188 (2019)
12. Matthews, K.: What to know about user authentication and cyber security topics cybersecurity (2020). https://www.information-age.com/what-to-know-about-user-authentication-cyber-security-123487818/
13. Fathiyana, R.Z., Hidayat, F., Rahardjo, B.: An integration of national identity towards single identity number with blockchain (2020)
14. Makoza, F.: An exploratory study on policy transfer for sim card registration in Malawi. Int. J. Technol. Diffus. (IJTD) **6**(1), 33–45 (2015)
15. Makanda, K., Vallent, T.F., Kim, H.: Remarks on national cyber security for under developed and developing countries: focused on Malawi. Am. J. Eng. Res. (AJER) **6**(7), 257–260 (2017)
16. Gelb, A., Castrillon, D., et al.: Identifying and verifying customers: when are KYC requirements likely to become constraints on financial inclusion? Center for Global Development, Technical report (2019)
17. El Ayeb, S., Hemery, B., Jeanne, F., Cherrier, E.: Community detection for mobile money fraud detection. In: 2020 Seventh International Conference on Social Networks Analysis, Management and Security (SNAMS), pp. 1–6. IEEE (2020)
18. Haque, M.M., Adnan, M.N., Kabir, M.A., Rashid, M.R.A., Yasin, A.S.M., Pervez, M.S.: An innovative approach of verification mechanism for both electronic and printed documents. Int. J. Adv. Comput. Sci. Appl. **11**(8) (2020)

19. Wanja, G.M.: A prototype to identify fraudulent sim card registration using public key infrastructure verification approach. Ph.D. dissertation, Strathmore University (2021)
20. Karhadkar, V., Tomar, A., Bhor, S., Chirayil, D.: Ticket verification and passenger authentication using encrypted QR code for airport verification system (2021)
21. Muñoz, M.A.V.: Towards a secured I-election system in the Philippines: the development of hybrid QR code technology for sustainable election system to increase voter turnout (2022)
22. Donatus, A., Silvance, A., Joshua, A.: An integrated mobile identity authentication model. Int. Res. J. Innov. Eng. Technol. **6**(1), 68 (2022)
23. Kotkova, D., Sternova, T., Kalvach, Z., Kotek, L.: The Process to Plan Security Measures for Cultural Events, pp. 1–6 (2021)

On Signed Product Cordial Labeling of Pan-Related Graphs

Sarang Sadawarte and **Sweta Srivastav**

Abstract In this article, we investigate the signed product cordial behavior of m-pan graph. The path joining two copies and path union of r copies of m-pan graph are shown to be signed product cordial under certain conditions.

1 Introduction

Graph labeling is widely studied and researched area in the field of graph theory. The labeling of graph is a function that carries set of vertices or edges to non-negative integers. Gallian [1] surveyed on various types of graph labeling which provides enlightened review on this area. The concept of cordial labeling was first coined in 1958 by Cahit [2]. The notion of product cordial labeling was introduced by Sundaram et al. [4]. Signed cordiality named as S-Cordiality was first introduced by Harary. The concept of signed product cordial labeling was introduced by Babujee [3]. Sadawarte S. and Srivastav S. proved many results on m-pan graphs (when $m = 3, 4$) [5]. Throughout the paper, graph W is finite, simple and undirected.

S. Sadawarte (✉) · S. Srivastav
Department of Mathematics, Sharda School Basic Sciences and Research, Sharda University, Greater Noida, India
e-mail: sarangsadawarte@gmail.com

S. Srivastav
e-mail: sweta.srivastav@sharda.ac.in

2   Terminology and Notation

Definition 1 A $(0 - 1)$ labeling of graph W with induced edge labeling $\eta^*(st)$: $E(W)$ $\to \{0, 1\}$ and stated as $\eta^*(st) = \eta(s)\eta(t)$, $e = st$ is known as product cordial labeling if

(a) $|t_\eta (0) - t_\eta (1)| \leq 1$

(b) $|e_\eta (0) - e_\eta (1)| \leq 1$. A graph W which preserves product cordiality known as

a product cordial graph.

Definition 2 Let $W = (V, E)$ be a graph and let $\eta * (st)$: $V(W) \to \{-1, 1\}$ is vertex labeling of W. Consider the induced mapping $\eta * (st)$: $E(W) \to \{-1, 1\}$ and derived as $\eta * (e) = \eta(s). \eta(t)$ (where $e = st$ and $s, t \in V$ is called signed product labeling if following criteria satisfies

(a) $|t_\eta (-1) - t_\eta (1)| \leq 1$

(b) $|e_\eta (-1) - e_\eta (1)| \leq 1$. We represent, $t_\eta (-1)$ as the numbers of vertices labeled

with -1, $e_\eta (1)$ as the numbers of vertices labeled with 1 and $e_\eta (-1)$ 1denote corresponding numbers of edges labeled with -1, $e_\eta (1)$ denote corresponding numbers of edges labeled with 1. A graph W which preserves signed product cordiality known as a signed product cordial graph.

Definition 3 The m-pan graph oriented with joining a cycle graph C_m to a pendent node.

Definition 4 A chord of an m-pan graph is an edge which joins two non-adjacent vertices $C_m.$

3   Results

Theorem 1 *The m-pan graphs are signed product cordial.*

Proof. Let $t_1, t_2, ..., t_m$ be consecutive vertices of m-pan graph. Fix a pendent vertex. Fix a pendent vertex $\eta(t) = 1$. Define a vertex labeling mapping η: $V(W) \to \{-1, 1\}$ as given below:
For $r \equiv 0, 1 \pmod 4$

$$\eta(t_h) = \begin{cases} -1; h = 1, 2 \pmod 4 \\ 1; h = 0, 3 \pmod 4 \end{cases}$$

Table 1 Signed product cordial pattern for edges of m-pan graph

Observations of r	Labeling of edges
$r \equiv 0 \pmod 4$	$e_\eta(-1) = e_\eta(1) + 1$
$r \equiv 1 \pmod 4$	$e_\eta(-1) = e_\eta(1)$
$r \equiv 3 \pmod 4$	$e_\eta(-1) = e_\eta(1)$

For $r \equiv 3 \pmod 4$

$$\eta(t_h) = \begin{cases} -1; h = 2, 3 \pmod 4 \\ 1; h = 0, 1 \pmod 4 \end{cases}$$

Table 1 elaborates labeling pattern of edges. Clearly, the condition of signed product cordiality $|e_\eta(-1) - e_\eta(1)| \leq 1$ is satisfied. Hence, the resultant graph W is signed product cordial.

Example 1 The signed product cordial labeling of resultant graph W under condition $r \equiv 1 \pmod 4$ is constructed with Fig. 1.

Theorem 2 *The m-pan graphs with one chord are signed product cordial.*

Proof. Let $t_1, t_2, ..., t_m$ be consecutive vertices of m-pan graph. Fix a pendent vertex $\eta(t) = 1$ and join an edge $e = v_2 v_n$. Define a vertex labeling mapping $\eta: V(W) \rightarrow \{-1, 1\}$ as given below:
For $r \equiv 0 \pmod 4$

$$\eta(t_h) = \begin{cases} -1; h = 0, 3 \pmod 4 \\ 1; h = 1, 2 \pmod 4 \end{cases}$$

Fig. 1 5-pan graph
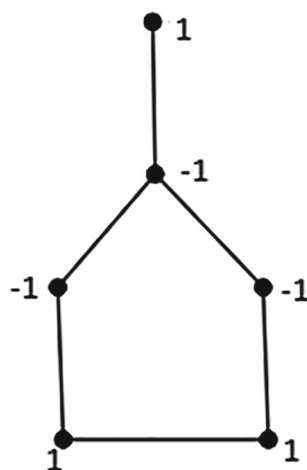
For $r \equiv 1(\text{mod } 4)$

$$\eta(t_h) = \begin{cases} -1; h = 1, 2(\text{mod } 4) \\ 1; h = 0, 3(\text{mod } 4) \end{cases}$$

For $r \equiv 3(\text{mod } 4)$

$$\eta(t_h) = \begin{cases} -1; h = 2, 3(\text{mod } 4) \\ 1; h = 0, 1(\text{mod } 4) \end{cases}$$

Table 2 elaborates labeling pattern of edges. Clearly, the condition of signed product cordiality $|e_\eta(-1) - e_\eta(1)| \leq 1$ is satisfied. Hence, the resultant graph W is signed product cordial.

Example 2 The signed product cordial labeling of the resultant graph W under certain condition $r \equiv 0(\text{mod } 4)$ is elaborated by Fig. 2.

We constructed the graph $W = \{2\text{-m pan:Pr}\}$ with merging two same copies of m-pan graph with indefinite path length. We introduced $W = \{r\text{-m pan:Pr}\}$ as path union of r same copies of m-pan graph.

Theorem 3 *The graph* $W = \{2\text{-m pan:}P_r\}$ *is signed product cordial.*

Table 2 Signed product cordial pattern for edges of m-pan graphs with one chord

Observations of r	Labeling of edges
$r \equiv 0(\text{mod } 4)$	$e_\eta(-1) = e_\eta(1)$
$r \equiv 1(\text{mod } 4)$	$e_\eta(-1) + 1 = e_\eta(1)$
$r \equiv 3(\text{mod } 4)$	$e_\eta(-1) + 1 = e_\eta(1)$

Fig. 2 5-pan graph with a chord
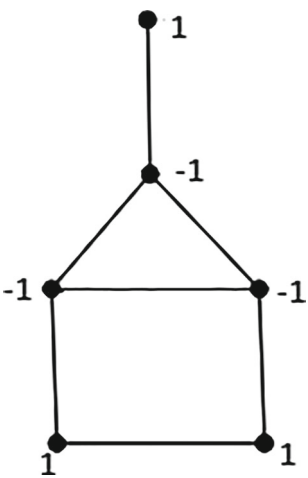
Proof. Let us denote first and second copies of m-pan as t_1, t_2, ... t_m and s_1, s_2... s_m, respectively. Let vertices 1st, 2nd and rth of path P_r be represented by x_1, x_2, ..., x_r which carries condition as first vertex $x_1 = t_1$ and rth vertex, $x_r = s_1$.

Consider a mapping $\eta: V(W) \to \{-1, 1\}$ as given below:

When $m \equiv 0, 1, 3 \pmod 4$, we observe some cases.

Case I For $r \equiv 0 \pmod 4$, $m \equiv 0 \pmod 4$

$$\eta(t_h) = \eta(s_h) = \eta(x_h) = \begin{cases} -1; \ h = 1, 2 \pmod 4 \\ 1; \ h = 0, 3 \pmod 4 \end{cases}$$

Case II For $r \equiv 1 \pmod 4$, $m \equiv 0 \pmod 4$

$$\eta(t_h) = \eta(x_h) = \begin{cases} -1; h = 0, 3 \pmod 4 \\ 1; h = 1, 2 \pmod 4 \end{cases}$$

$$\eta(s_h) = \begin{cases} -1; h = 1, 2 \pmod 4 \\ 1; h = 0, 3 \pmod 4 \end{cases}$$

Case III For $r \equiv 2, 3 \pmod 4$, $m \equiv 0 \pmod 4$

$$\eta(t_h) = \eta(s_h) = \begin{cases} -1; h = 1, 2 \pmod 4 \\ 1; h = 0, 3 \pmod 4 \end{cases}$$

$$\eta(x_h) = \begin{cases} -1; h = 2, 3 \pmod 4 \\ 1; h = 0, 1 \pmod 4 \end{cases}$$

Case IV For $r \equiv 0 \pmod 4$, $m \equiv 1 \pmod 4$

$$\eta(s_h) = \eta(x_h) = \begin{cases} -1; h = 1, 2 \pmod 4 \\ 1; h = 0, 3 \pmod 4 \end{cases}$$

$$\eta(t_h) = \begin{cases} -1; h = 0, 3 \pmod 4 \\ 1; h = 1, 2 \pmod 4 \end{cases}$$

Case V For $r \equiv 1, 2 \pmod 4$, $m \equiv 1 \pmod 4$

$$\eta(t_h) = \eta(s_h) = \begin{cases} -1; h = 0, 3 \pmod 4 \\ 1; h = 1, 2 \pmod 4 \end{cases}$$

$$\eta(x_h) = \begin{cases} -1; h = 1, 2 \pmod 4 \\ 1; h = 0, 3 \pmod 4 \end{cases}$$

Case VI For $r \equiv 3 \pmod 4$, $m \equiv 1 \pmod 4$

$$\eta(s_h) = f(x_h) = \begin{cases} -1; & h = 1, 2 \pmod 4 \\ 1; & h = 0, 3 \pmod 4 \end{cases}$$

$$\eta(t_h) = \begin{cases} -1; & h = 0, 3 \pmod 4 \\ 1; & h = 1, 2 \pmod 4 \end{cases}$$

Case VII For $r \equiv 0 \pmod 4$, $m \equiv 3 \pmod 4$

$$\eta(t_h) = \begin{cases} -1; & h = 0, 1 \pmod 4 \\ 1; & h = 2, 3 \pmod 4 \end{cases}$$

$$\eta(s_h) = \begin{cases} -1; & h = 2, 3 \pmod 4 \\ 1; & h = 0, 1 \pmod 4 \end{cases}$$

$$\eta(x_h) = \begin{cases} -1; & h = 1, 2 \pmod 4 \\ 1; & h = 0, 3 \pmod 4 \end{cases}$$

Case VIII For $r \equiv 1, 2 \pmod 4$, $m \equiv 3 \pmod 4$

$$\eta(t_h) = \eta(s_h) = \begin{cases} -1; & h = 0, 1 \pmod 4 \\ 1; & h = 2, 3 \pmod 4 \end{cases}$$

$$\eta(x_h) = \begin{cases} -1; & h = 1, 2 \pmod 4 \\ 1; & h = 0, 3 \pmod 4 \end{cases}$$

Case IX For $r \equiv 3 \pmod 4$, $m \equiv 3 \pmod 4$

$$\eta(t_h) = \begin{cases} -1; & h = 2, 3 \pmod 4 \\ 1; & h = 0, 1 \pmod 4 \end{cases}$$

$$\eta(s_h) = \begin{cases} -1; & h = 0, 1 \pmod 4 \\ 1; & h = 2, 3 \pmod 4 \end{cases}$$

$$\eta(x_h) = \begin{cases} -1; & h = 2, 3 \pmod 4 \\ 1; & h = 0, 1 \pmod 4 \end{cases}$$

The corresponding observed cases of m with labeling pattern of edges resulted in Table 3. Therefore, conditions $|v_\eta(-1) - v_\eta(1)| \le 1$ and $|e_\eta(-1) - e_\eta(1)| \le 1$ are preserved and verified.

Example 3 The graph $W = \{2\text{–}5 \, pan\text{:}P_5\}$ is signed product cordial shown in Fig. 3.

Theorem 4 *The graph $W = \{r\text{-}m \, pan\text{:}P_r\}$ preserves signed product cordial labeling.*

Table 3 Signed product cordial pattern for vertices and edges of $W = \{2\text{-m pan:}P_r\}$

Cases for r, m	Vertices pattern	Edges pattern
$r \equiv 0(\mathrm{mod}\ 4)$, $m \equiv 0, 1, 3(\mathrm{mod}\ 4)$	$v_\eta(-1) = v_\eta(1)$	$e_\eta(-1) + 1 = e_\eta(1)$
$r \equiv 1(\mathrm{mod}\ 4)$, $m \equiv 0, 3(\mathrm{mod}\ 4)$	$v_\eta(-1) = v_\eta(1) + 1$	$e_\eta(-1) = e_\eta(1)$
$r \equiv 1(\mathrm{mod}\ 4)$, $m \equiv 1(\mathrm{mod}\ 4)$	$v_\eta(-1) = v_\eta(1)$	$e_\eta(-1) = e_\eta(1)$
$r \equiv 2(\mathrm{mod}\ 4)$, $m \equiv 0, 1, 3(\mathrm{mod}\ 4)$	$v_\eta(-1) = v_\eta(1)$	$e_\eta(-1) = e_\eta(1) + 1$
$r \equiv 3(\mathrm{mod}\ 4)$, $m \equiv 0, 1, 3(\mathrm{mod}\ 4)$	$v_\eta(-1) = v_\eta(1) + 1$	$e_\eta(-1) = e_\eta(1)$
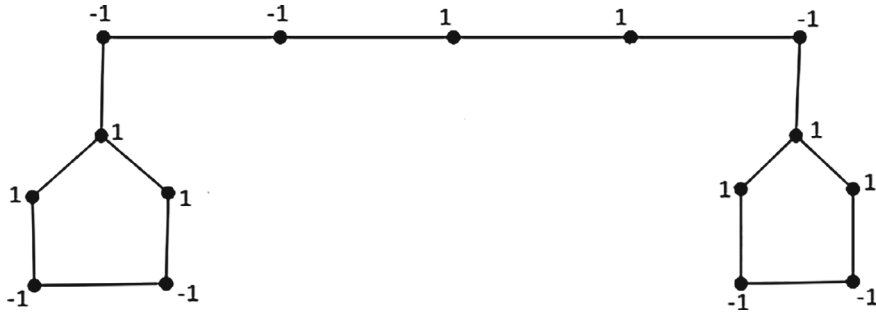
Fig. 3 2–5-pan graph

Proof. Consider the vertices of 1st, 2nd, ..., rth copy graph as $t_{p1}, t_{p2}, ..., t_{pr}$. Let x_1, $x_2, ..., x_r$ be the vertices of path P_r with condition $x_1 = t_{p1}$, $x_2 = t_{p2}, ..., x_r = t_{pr}$. State a vertex function $\eta: V(W) \to \{-1, 1\}$ with following.

For $m \equiv 0, 1, 3(\mathrm{mod}\ 4)$, we examine some cases given below:

Case I For $r \equiv 0(\mathrm{mod}\ 4)$, $m \equiv 0\ (\mathrm{mod}\ 4)$

$$\eta(t_{hg}) = \eta(t_{hg-2}) = \eta(t_{hg-3}) = \begin{cases} -1; h = 1, 2(\mathrm{mod}\ 4) \\ 1; h = 0, 3(\mathrm{mod}\ 4) \end{cases}$$

Case II For $r \equiv 1(\mathrm{mod}\ 4)$, $m \equiv 0\ (\mathrm{mod}\ 4)$

$$\eta(t_{hg}) = \eta(t_{hg-1}) = \eta(t_{hg-2}) = \begin{cases} -1; h = 1, 2(\mathrm{mod}\ 4) \\ 1; h = 0, 3(\mathrm{mod}\ 4) \end{cases}$$

Case III For $r \equiv 2(\mathrm{mod}\ 4)$, $m \equiv 0\ (\mathrm{mod}\ 4)$

$$\eta(t_{hg}) = \eta(t_{hg-1}) = \eta(t_{hg-2}) = \begin{cases} -1; h = 1, 2(\mathrm{mod}\ 4) \\ 1; h = 0, 3(\mathrm{mod}\ 4) \end{cases}$$

Case IV For $r \equiv 3(\mathrm{mod}\ 4)$, $m \equiv 0\ (\mathrm{mod}\ 4)$

$$\eta\left(t_{hg}\right) = \eta\left(t_{hg-2}\right) = \eta\left(t_{hg-3}\right) = \begin{cases} -1; h = 1, 2(\text{mod } 4) \\ 1; h = 0, 3(\text{mod } 4) \end{cases}$$

Case V For $r \equiv 0(\text{mod } 4)$, $m \equiv 1 \ (\text{mod } 4)$

$$\eta\left(t_{hg}\right) = \begin{cases} -1; h = 1, 2(\text{mod } 4) \\ 1; h = 0, 3(\text{mod } 4) \end{cases}$$

$$\eta\left(t_{hg-2}\right) = \eta\left(t_{hg-3}\right) = \begin{cases} -1; \ h = 0, 3(\text{mod } 4) \\ 1; \ h = 1, 2(\text{mod } 4) \end{cases}$$

Case VI For $r \equiv 1(\text{mod } 4)$, $m \equiv 1 \ (\text{mod } 4)$

$$\eta\left(t_{hg}\right) = \begin{cases} -1; \ h = 1, 2(\text{mod } 4) \\ 1; \ h = 0, 3(\text{mod } 4) \end{cases}$$

$$\eta\left(t_{hg-1}\right) = \eta\left(t_{hg-2}\right) = \begin{cases} -1; h = 0, 3(\text{mod } 4) \\ 1; h = 1, 2(\text{mod } 4) \end{cases}$$

Case VII For $r \equiv 2, 3(\text{mod } 4)$, $m \equiv 1(\text{mod } 4)$

$$\eta\left(t_{hg}\right) = \begin{cases} -1; h = 0, 3(\text{mod } 4) \\ 1; h = 1, 2(\text{mod } 4) \end{cases}$$

$$\eta\left(t_{hg-2}\right) = \eta\left(t_{hg-3}\right) = \begin{cases} -1; h = 1, 2(\text{mod } 4) \\ 1; h = 0, 3(\text{mod } 4) \end{cases}$$

Case VIII For $r \equiv 0(\text{mod } 4)$, $m \equiv 3 \ (\text{mod } 4)$

$$\eta\left(t_{hg}\right) = \begin{cases} -1; h = 2, 3(\text{mod } 4) \\ 1; h = 0, 1(\text{mod } 4) \end{cases}$$

$$\eta\left(t_{hg-2}\right) = \eta\left(t_{hg-3}\right) = \begin{cases} -1; h = 0, 1(\text{mod } 4) \\ 1; h = 2, 3(\text{mod } 4) \end{cases}$$

Case IX For $r \equiv 1(\text{mod } 4)$, $m \equiv 3 \ (\text{mod } 4)$

$$\eta\left(t_{hg}\right) = \begin{cases} -1; h = 0, 1(\text{mod } 4) \\ 1; h = 2, 3(\text{mod } 4) \end{cases}$$

$$\eta\left(t_{hg-1}\right) = \eta\left(t_{hg-2}\right) = \begin{cases} -1; h = 2, 3(\text{mod } 4) \\ 1; h = 0, 1(\text{mod } 4) \end{cases}$$

Case X For $r \equiv 2 (\bmod\ 4)$, $m \equiv 3\ (\bmod\ 4)$

$$\eta(t_{hg}) = \begin{cases} -1; h = 0,\ 1 (\bmod\ 4) \\ 1; h = 2,\ 3 (\bmod\ 4) \end{cases}$$

$$\eta(t_{hg-2}) = \eta(t_{hg-3}) = \begin{cases} -1; h = 2,\ 3 (\bmod\ 4) \\ 1; h = 0,\ 1 (\bmod\ 4) \end{cases}$$

Case XI For $r \equiv 3 (\bmod\ 4)$, $m \equiv 3 (\bmod\ 4)$

$$\eta(t_{hg}) = \begin{cases} -1; h = 0,\ 1 (\bmod\ 4) \\ 1; h = 2,\ 3 (\bmod\ 4) \end{cases}$$

$$\eta(t_{hg-2}) = \eta(t_{hg-3}) = \begin{cases} -1;\ h = 2,\ 3 (\bmod\ 4) \\ 1;\ h = 0,\ 1 (\bmod\ 4) \end{cases}$$

The corresponding observed cases of m with labeling pattern of edges resulted in Table 4. Therefore, condition $|e_\eta(-1) - e_\eta(1)| \leq 1$ is preserved and verified.

Example The graph $W = \{5\text{–}5\ \text{pan}:P_5\}$ is signed product cordial shown in Fig. 4.

Table 4 Signed product cordial pattern for edges and vertices of $\{r\text{-}m\ pan:P_r\}$

Cases for r, m	Vertices pattern	Edges pattern
$r \equiv 0 (\bmod\ 4)$, $m \equiv 0, 1, 3 (\bmod)$	$v_\eta(-1) = v_\eta(1)$	$e_\eta(-1) + 1 = e_\eta(1)$
$r \equiv 1\ (\bmod\ 4)$, $m \equiv 0\ (\bmod\ 4)$	$v_\eta(-1) + 1 = v_\eta(1)$	$e_\eta(-1) = e_\eta(1) + 1$
$r \equiv 1 (\bmod\ 4)$, $m \equiv 1, 3 (\bmod\ 4)$	$v_\eta(-1) = v_\eta(1)$	$e_\eta(-1) = e_\eta(1)$
$r \equiv 2\ (\bmod\ 4)$, $m \equiv 0, 1, 3 (\bmod\ 4)$	$v_\eta(-1) = v_\eta(1)$	$e_\eta(-1) = e_\eta(1) + 1$
$r \equiv 3\ (\bmod\ 4)$, $m \equiv 0 (\bmod\ 4)$	$v_\eta(-1) = v_\eta(1) + 1$	$e_\eta(-1) = e_\eta(1)$
$r \equiv 3 (\bmod\ 4)$, $m \equiv 1, 3 (\bmod\ 4)$	$v_\eta(-1) = v_\eta(1)$	$e_\eta(-1) = e_\eta(1)$
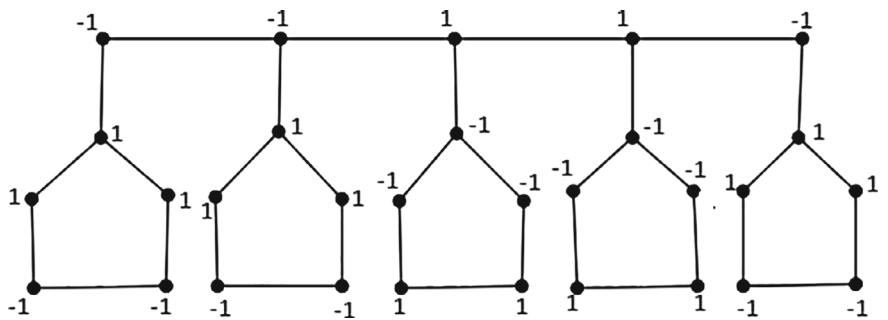
Fig. 4 5–5-pan graph

4　Conclusion

In this paper, we emphasized path joining two copies m-pan graph and path union of r copies of m-pan graph is signed product cordial. To elaborate several families of graph which satisfies corresponding results is an open problem for the further research.

References

1. Gallian, J.A.: A dynamic survey of graph labelling. Electron. J. Comb. DS6 (2016)
2. Cahit, I.: Cordial graphs: a Weaker version of graceful and harmonious graphs. Ars Comb. **23**, 201–207 (1887)
3. Babujee, J.B., Loganathan, S.: On signed cordial labelling. Sci. Res. J. Appl. Math. **2**, 1525–1530 (2011)
4. Sundaram, M., Ponraj, R., Somasundram, S.: Total product cordial labeling of graphs, bulletin of pure and applied sciences. Section E. Math. Stat. **25**, 199–203, (2006)
5. Sadawarte, S., Srivastav, S.: Signed product cordial labeling of some pan graphs. Mater. Todays: Proc. **57**, Part 5, 2307–2310 (2022)

Supply Chain Analysis and Prediction Using Machine Learning

Gauri Gupta, Nitendra Kumar, Padmesh Tripathi, Priyanka Agarwal, and Iftikhar Haider

Abstract Supply chain is a network of entire of the organizations, individuals, activities, technologies, and resources intricated in the formation and sale of a product. Thus, supply chain involves a huge amount of data. In ever-changing and today's complex world, finding the relevant and appropriate data supplanted by the too much data that is available for the supply chain, is a big concern. Various methods have been proposed to analyze the supply chain. The present chapter deals with the analysis of complex supply chain data using machine learning. The goal was to gain customer insights from the dataset available on Kaggle. The data was preprocessed by eliminating null values and irrelevant features. Then classification and regression models, such as logistic regression, Gaussian Naïve Bayes, support vector machine (SVM), K-nearest neighbor (KNN), random forest, and decision trees, were utilized. These models helped in classification of late deliveries and fraudulent transactions, as well as in prediction of sales and order quantities. RFM analysis has been employed to segment customers based on recency, frequency, and monetary values. The data was visualized through graphs, comparing metrics like total sales and average price. Also, the chapter features a website displaying data preprocessing, feature plots, and classifier graphs.

G. Gupta
Better Parker Real Estate Brokers LLC, Dubai, UAE

N. Kumar (✉) · P. Agarwal
Amity Business School, Amity University, Noida, UP, India
e-mail: nkshukla.kumar4@gmail.com

P. Agarwal
e-mail: pagarwal5@amity.edu

P. Tripathi
Department of Applied Sciences, Delhi Technical Campus, Greater Noida, India

I. Haider
Department of Mathematics and IT, Center for Preparatory Studies, Sultan Qaboos University, Muscat, Oman
e-mail: haider@squ.edu.om

1   Introduction

In today's modern era, each and every field of study demands emerging techniques.
The same demands the supply chain analysis. A number of new techniques have been
employed to analyze supply chain. ML is one of them which has wide applications
in different fields.

1.1   Supply Chain

A supply chain is a structure which consists of different units, which augment value
from the primary resource sources to the final products. During this, information on
production, market, etc., are being exchanged [1]. These different units are the indi-
viduals, resources, organizations, technologies, and activities in which are engaged
in production and sale of the product (see Fig. 1).

In a supply chain incorporates everything starting from the supply of raw materials
from the supplier to the industrialists who produce the product through to its final
delivery to the customer.

In the ever-evolving landscape of today's global economy, the dynamics of supply
chain management are experiencing profound transformations. In order to thrive and
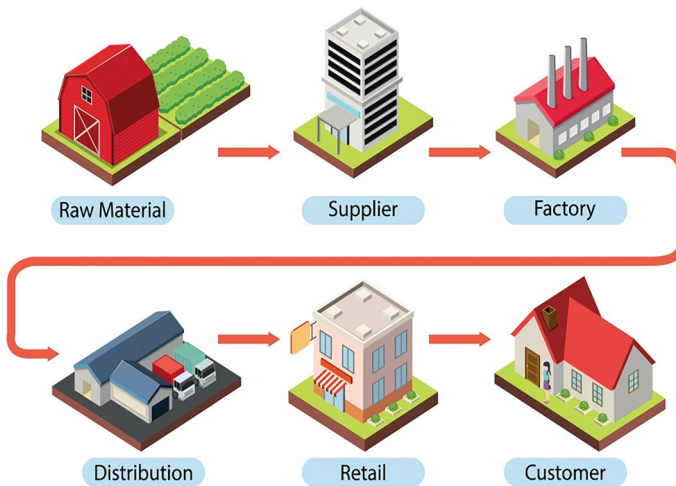
Fig. 1 Diagram of supply chain. (*Source* www.freepik.com)

remain competitive, enterprises must continuously adapt their strategies to align with market fluctuations. The efficient and cost-effective flow of information, capital, logistics, and human resources has become the lifeblood of modern businesses, dictating their economic success. Access to accurate information throughout the supply chain, from order inception to product delivery, has ushered in a new era of improved quality and enhanced production capacity for enterprises [2].

The supply chain represents a comprehensive process encompassing various stages, from raw material procurement and warehousing to production, inventory management, outbound logistics, transportation, and distribution. A mature and efficient supply chain information management system is essential for on-demand traceability, process visualization, and automation. Therefore, the precise collection and swift dissemination of information at each stage are critical components of achieving operational excellence [3].

Several supply chain models are available to be used. These models focus mainly on two parameters, namely efficiency and effectiveness. These models attempt blend of both in different approaches to achieve the desired goal. These models depend on the requirement of business with their constraints and goals.

Figure 2 shows the commonly used supply chain models:

Continuous Flow Model: This model is best suitable for those industries which are mature enough in their field of expertize. The term continuous flow reflects it.

Agile Model: This model is best suitable for the industries which have irregular demand and cannot be sure about the orders that are made.

Fast Chain Model: This model is best suitable for the industries which are involved in the products having short lifecycles like the items which deteriorate fast, fashion items, etc.
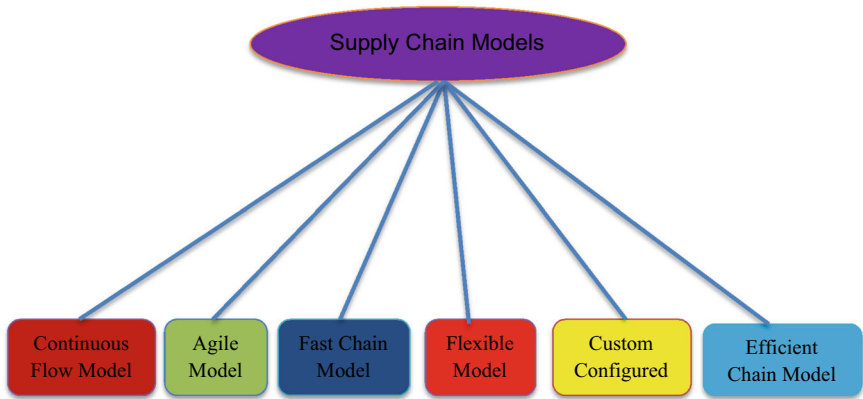
Fig. 2 Different supply chain models

Flexible Model: This model is best suitable for the industries which have stable level of demand and in peak time a predictable demand.

Custom Configured Model: This model is best suitable for the industries which concentrate on customizing. Such industries use custom configured model.

Efficient Chain Model: This model is best suitable for the industries which are playing in extremely competitive market where pricing has major role.

1.2 Machine Learning

Arthur Samuels, an employee of IBM, coined the word machine learning (ML) in 1959. One of the most versatile characters of ML is that without any programming, it empowers computers proficient in learning, i.e., computers learn without using programming. ML brands computers to have learning ability like humans. It comes under the study area of artificial intelligence [4, 5]. Figure 3 reflects connection between three powerful techniques. ML is a powerful emerging tool which has been employed in numerous fields of engineering, science, medical, and management.

As ML is a data-driven technology, increment in data improves performance of ML. In general, two processes learning and testing are involved in working environment of ML systems. Preprocessing of data is one of the most vital steps in ML. This pre-processing consists of three parts [6]:

(i) Data cleaning: removal of unwanted, uneven, or missing parts and data denoising is implemented [7, 8].
(ii) Data integration: integration of data is performed if more than one data sources are available.
(iii) Data transformation: data transformation contains tasks like discretization, normalization, etc.

Depending on learning type, ML is classified into three categories:

Fig. 3 ML as sub-field of AI
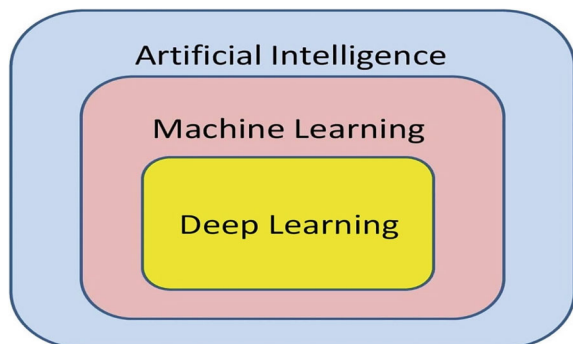
  (i) Supervised learning: In supervised learning, data with input and output is used. Regression, classification, and active learning come in this category.
 (ii) Unsupervised learning: In unsupervised category, data with only inputs is used. Clustering and grouping come in this category.
(iii) Reinforcement learning: In reinforcement learning, no input or output of data is concerned. Dynamic programming is high choice of application here.

Machine Learning (ML) offers a powerful toolset for analyzing and predicting supply chain performance. This paper delves into the application of ML in "Supply Chain Analysis and Prediction," driven by the goals of operational efficiency, demand forecasting, risk mitigation, customer satisfaction, sustainability, and competitiveness. The objective of this research is to explore the utility of ML in supply chain analysis and prediction, evaluating algorithm effectiveness for insights, demand forecasting, inventory optimization, and risk mitigation. Additionally, we aim to identify the challenges and opportunities presented by ML in supply chain management and provide best practice recommendations to enhance operational efficiency, reduce costs, boost customer satisfaction, and promote sustainable practices within supply chains [9].

1.3   Challenges in Supply Chain Analysis and Prediction

Multi-tier and global supply chains have become the norm, involving a complex network of suppliers, manufacturers, distributors, and retailers spanning the globe. Analyzing and forecasting the dynamics within such intricate networks pose significant challenges. Geopolitical events, trade regulations, and cultural variations can have profound impacts on supply chain operations, introducing layers of complexity to the analysis and prediction process.

Real-time data and responsiveness are paramount for supply chain accuracy, yet achieving this can be challenging due to data delays, gaps, or inaccessibility across various supply chain stages. Real-time analysis requires robust data integration, timely data feeds, and efficient processing capabilities. The ability to adapt quickly to changing conditions and adjust predictions based on new data is vital for optimal supply chain performance [10].

Systemic risk is another challenging issue in supply chain. Interconnected and Global supply chains are ever more showing the systemic risks, whereas individual letdowns proliferate across sectors, firms and borders. Systemic risks have appeared from the choices of individual firms, for example buffer reduction and outsourcing and now can't be controlled [11].

Addressing these challenges necessitates a blend of domain expertise, data engineering skills, advanced ML models, and close collaboration between data scientists and supply chain experts. A deep understanding of supply chain intricacies is essential for the successful implementation of ML solutions. Supply chains comprise

interconnected elements such as Marketing, Procurement, Warehouse Management, and Transportation, making it crucial to consider the holistic picture.

Our dataset offers a wealth of features, unveiling customer and market patterns. Supply chain analytics encompass descriptive, predictive, and prescriptive analyses, helping uncover risks, validate data, and assist in mitigating disruptions. Supply chain analysis enables precise decision-making, resulting in improved yearly margins, cost reduction, risk management, and future readiness. It aids in identifying less productive items and understanding post-order customer requirements.

Advanced analytics also facilitate the detection of connections and the issuance of low-cost, sustainable risk alerts. Moreover, the integration of ML into supply chain management provides opportunities to optimize operations through data-driven decision-making. By harnessing the power of ML algorithms, businesses can enhance demand forecasting accuracy, optimize inventory levels, and improve supply chain efficiency [5].

This paper sets the stage for a comprehensive exploration of Machine Learning's application in supply chain analysis and prediction. It addresses the inherent challenges and outlines the path toward operational excellence in supply chain management through the integration of cutting-edge technology and domain expertise. This research seeks to empower enterprises to navigate the complexities of the modern supply chain landscape, enabling them to thrive in the global marketplace. By embracing ML and data-driven strategies, businesses can position themselves for sustained success in the ever-changing world of supply chain management.

2   Literature Review

Supply chain management is unequivocally pivotal in ensuring the triumphant operation of an expansive array of industries. The incessant advancements in machine learning have ushered in a new era, where the integration of these technologies has the potential to revolutionize supply chain analysis and prediction. This sweeping literature review embarks on a comprehensive expedition, traversing the annals of prior research endeavors that have illuminated the multifaceted role of machine learning in this domain. It provides a profound insight into the methodologies, algorithms, and a multitude of empirical case studies that epitomize the evolution of this field [12].

Machine Learning Techniques for Supply Chain Analysis:

Regression Models: A paradigm shift has been catalyzed by introducing demand prediction anchored in support vector regression (SVR). Their groundbreaking approach consistently outperformed conventional methods, with SVR significantly augmenting demand accuracy. This monumental advancement heralded a transformative era in inventory management and operational efficiency [13].

Classification Models: In [14], for the Adoption of classification models to identify and assess risks within supply chains was ingeniously advocated. By harnessing the formidable synergy of random forests and decision trees, their innovative approach enabled real-time risk classification, arming organizations with the foresight to proactively devise and deploy mitigation strategies.

Ensemble Learning: Building upon the foundation laid in [14, 15] delved into the realm of ensemble learning. They proposed a novel approach that fused multiple machine learning models, including decision trees, random forests, and gradient boosting, to fortify supply chain risk prediction. Their results showcased a remarkable leap in predictive accuracy and robustness [16].

Demand Forecasting using Machine Learning:

Time Series Analysis: [17] embarked on a pioneering endeavor by harnessing long short-term memory (LSTM) networks for demand prediction. The results were nothing short of awe-inspiring. LSTM's unparalleled ability to decipher intricate time patterns led to demand forecasts of unprecedented precision. This precision, in turn, translated into a substantial reduction in inventory-related expenditures.

Neural Networks: In [18], authors charted a trailblazing course by introducing a deep learning architecture that harnessed convolutional neural networks (CNN) for demand prediction. The complexity of high-dimensional demand data posed no challenge to the prodigious capabilities of CNN. The outcome was a substantial elevation in forecast accuracy, with implications extending far beyond inventory management [19].

Risk Assessment and Mitigation Using Machine Learning:

Risk Identification: [20] embarked on a mission to identify and prioritize supply chain risks using machine learning methods such as decision trees and random forests. Their pioneering work facilitated the dynamic prioritization of risks, enabling organizations to swiftly focus their resources on mitigating the most critical risks.

Real-time Risk Monitoring: In [21] pushed the boundaries by introducing real-time risk monitoring through machine learning. Their groundbreaking approach relied on autoencoders and one-class SVMs to detect anomalies in real time. This invaluable capability empowered organizations to take proactive measures and execute risk mitigation strategies with unparalleled swiftness [22].

The Expansive Horizon of Machine Learning in Supply Chain Management:

This exhaustive literature review serves as a testament to the immense potential that machine learning harbors within the realm of supply chain analysis and prediction. Its application not only refines and amplifies decision-making processes but also ushers in a new era of inventory optimization and more effective risk assessment. As we cast our gaze toward the future, it becomes increasingly apparent that research endeavors must be dedicated to surmounting challenges and seamlessly integrating machine learning with emerging technologies.

For it is this fusion that promises to endow organizations with the competitive edge needed to navigate the intricate and dynamic landscape of efficient supply chain management effectively. The trailblazing papers discussed in this review merely scratch the surface, beckoning researchers to delve deeper into the boundless realm of possibilities that machine learning offers [23].

3 Methodology

The aim of this methodology is to provide a systematic and structured approach to address the research objectives and investigate the application of machine learning models in analyzing and predicting supply chain dynamics [24].

3.1 Description of Dataset

The research used an extensive supply chain dataset from Data Co Global, tailored for machine learning. This dataset includes crucial supply chain data: provisioning, production, sales, and commercial distribution. Notably, it connects structured and unstructured data, allowing insights extraction [25] (see Fig. 4).

3.2 Data Visualization

In data visualization the various parameters of the dataset are studied and it is visualized by using matplotlib library in python.

Europe market has the maximum sales and Africa maker has lowest sales as compared to all other regions as shown in Fig. 5.

People from western European region have ordered the most and the central Asian region people have ordered least as shown in Fig. 6.

Fig. 4 A basic supply chain
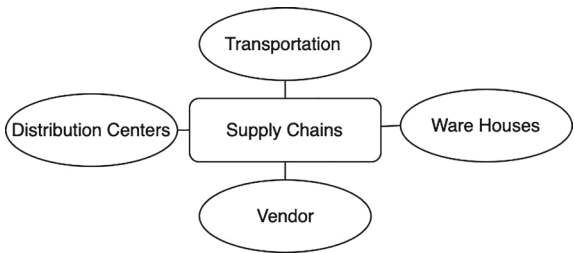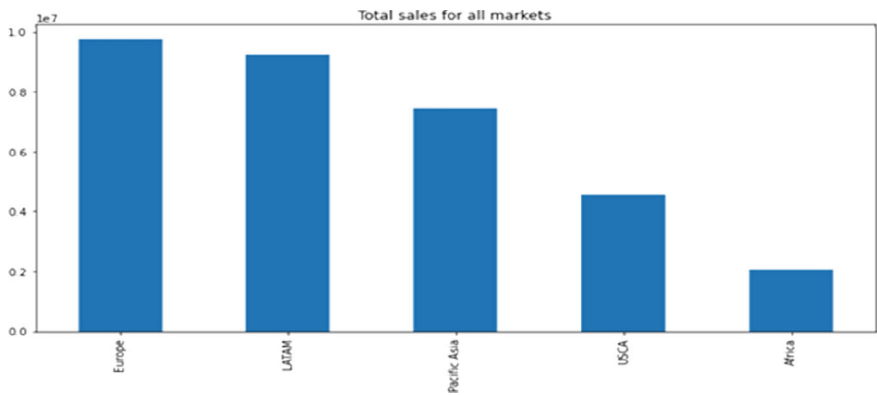
Fig. 5 Total sales for all markets
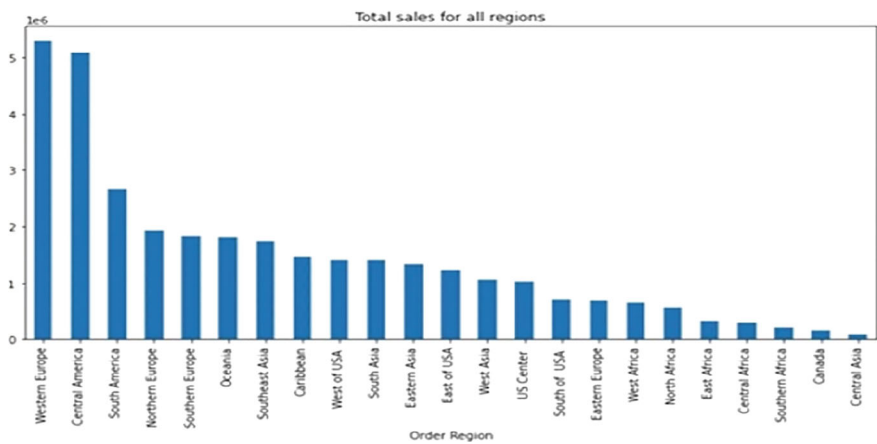
Fig. 6 Total sales for all regions

3.2.1 Finding the Relationship Between Prices and Sales of Product

Figure 7 explains that the product price and sales per customer have linear relationship with each other.

3.2.2 Finding the Product Having the Highest Demand

Fishing Products and Cleats are higher in demand and CDs and Toys seem to have very low demand than other products as shown in Fig. 8.

Fig. 7 Sales versus Price plot
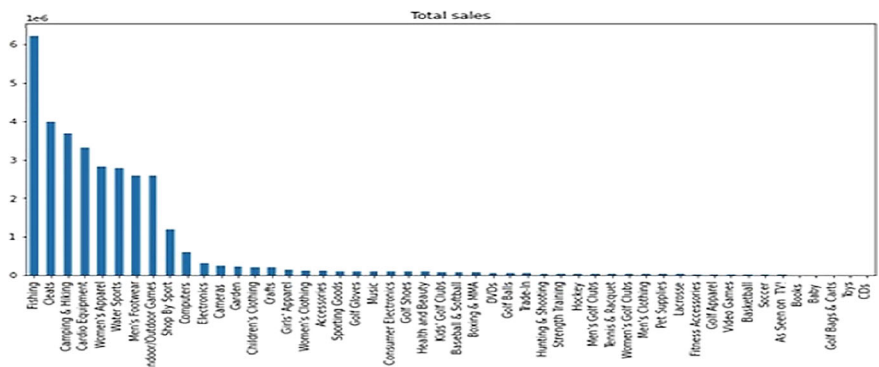
Fig. 8 Product with highest demand

3.2.3 Analyses of Sales Based on Suitable Time Stamps

Conclusions from Fig. 9

a. The greatest number of orders came in October followed by November which can be seen in the graph of order of month and order for all other months are almost consistent.
b. Highest numbers of orders are placed by customers in 2017.
c. Saturday recorded the highest number of average sales Wednesday with the least.
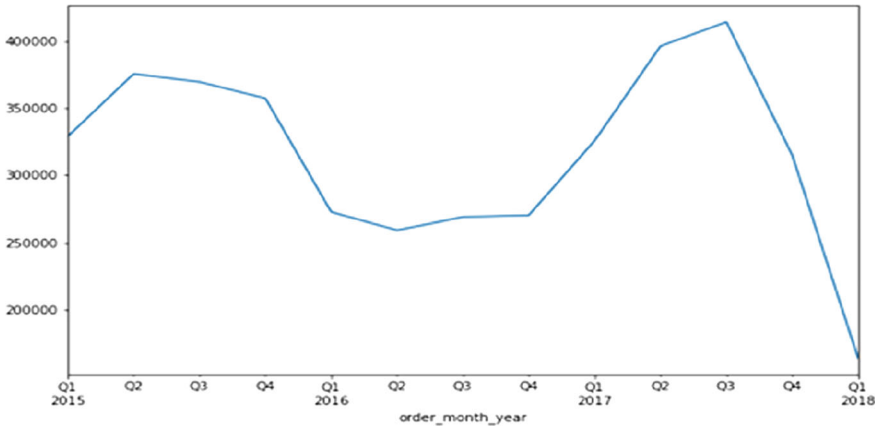
Fig. 9 Sales versus price plot based on timestamps

3.3 Data Preprocessing

Prior to data preprocessing, understanding machine learning parameters and the prediction objective is crucial. We opted for classification and regression algorithms, focusing on two main challenges: late delivery and fraudulent transactions, which are common in supply chain operations [26].

Late Delivery: Delivering products to customers on time without late delivery is another important aspect for a supply chain company because customers will not be satisfied if products are not delivered on time. What category of products are being delivered late the most?

Fraudulent transactions have been a huge problem ever since the beginning of globalization. The ambivalent confusion always exists while making a transaction online. We try to predict the chances of a transaction being fraudulent or not. Cleats, Men's footwear, women apparel, indoor/Outdoor games, fishing are the top 5 products having probability of late deliveries (see Fig. 10).

Customer segmentation: Understanding customer needs and targeting specific clusters of customers based on their need is one way for a supply chain company to increase the number of customers and to gain more profits.

Since, purchase history of customers is already available in the dataset, it can use RFM analysis for customer segmentation. Even though there are so many different methods for customer segmentation, RFM analysis is being used because it utilizes numerical values to show customer recency, frequency, and monetary values and the output results are easy to interpret as shown in Table 1.

The table above is the result of conducting an RFM analysis on customer data. RFM analysis is a technique used in marketing and customer relationship management to segment customers based on their transaction history. RFM stands for
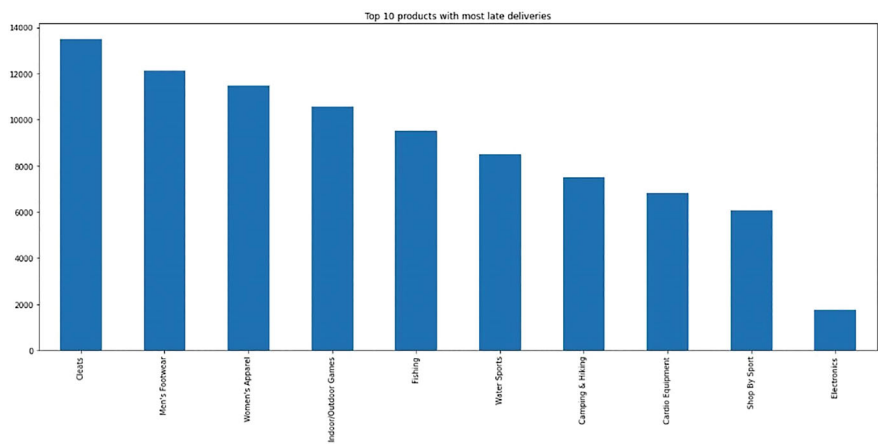
Fig. 10 Products with late delivery

Table 1 RFM values for the date set

Customer ID	R-values	F-values	M-values
1	792	1	2362.250061
2	136	10	2842.700073
3	229	18	6143.760057
4	380	14	4370.629991
5	457	7	2993.629991

recency, frequency, and monetary values, and each of these metrics is calculated for individual customers to gain insights into their purchasing behavior and preferences. Here's a detailed description of each column in the table:

Customer ID: This column represents a unique identifier for each customer, allowing you to associate the RFM values with specific individuals or entities.

R-Values (Recency): The "R" in RFM stands for Recency, which measures how recently a customer has made a purchase. To calculate the R-Values, you typically determine the number of days since the customer's last purchase. Customers who have lower R-Values are considered more recent buyers, while those with higher R-Values are less recent.

F-Values (Frequency): The "F" in RFM represents Frequency, which indicates how often a customer makes purchases. Typically, you count the number of transactions a customer has made over a specific period.

Customers with higher F-Values are considered more frequent buyers, while those with lower values make fewer purchases.

M-Values (Monetary Value): The "M" in RFM stands for Monetary Value, which quantifies the total amount of money a customer has spent on purchases.

Customers with higher M-Values are considered higher-value customers, indicating that they have spent more money.

RFM analysis is often used for customer segmentation, where customers are grouped into segments based on combinations of these three metrics. For example, "Champions" might represent customers with low R-Values, high F-Values, and high M-Values, signifying recent, frequent, and high-value customers. The specific criteria for segmentation can vary depending on business goals and the characteristics of the customer base.

Using the RFM Values pre-processing was done to add them into another column using NumPy and were categorized for a range of predefined values as shown in Table 2.

The table above is the result of conducting an RFM (Recency, Frequency, and Monetary) analysis on customer data, followed by segmentation based on the RFM scores. RFM analysis is a technique used in marketing and customer relationship management to segment customers based on their transaction history. Here's a detailed description of each column in the table:

Order: This column represents the order or rank of the customer based on their RFM scores. It could be used to priorities or rank customers based on their RFM attributes.

Customer ID: This is a unique identifier for each customer.

R_Value (Recency): The "R" in RFM stands for Recency, which measures how recently a customer has made a purchase. The R-values represents the recency score assigned to each customer. In this table:

R_Value of 4, indicating that they are not very recent buyers.

R_Value of 2, suggesting they are relatively recent buyers.

R_Value of 3, indicating a moderate level of recency.

F_Value (Frequency): The "F" in RFM represents Frequency, which indicates how often a customer makes purchases. The F_Value represents the frequency score assigned to each customer. In this table:

F_Value of 4, indicating they make infrequent purchases.

Table 2 Customer Segmentation

Order Customer ID	R_ Value	F_ Value	M_ Value	R_ Score	F_ Score	M_ Score	RFM_ Score	RFM_ Total Score	Customer segmentation
1	792	1	2362.25	4	4	3	443	11	Champions
2	136	10	2842.70	2	2	2	222	6	Can't lose
3	229	18	6143.76	3	1	1	311	5	At risk
4	380	14	4370.62	4	2	2	422	8	Promising
5	457	7	2993.79	4	3	2	432	9	Recents

F_Value of 2, suggesting they make frequent purchases.

F_Value of 1, indicating a low frequency of purchases.

F_Value of 3, indicating a moderate frequency of purchases.

M_Value (Monetary Value): The "M" in RFM stands for Monetary Value, which quantifies the total amount of money a customer has spent on purchases. The M_ Value represents the monetary score assigned to each customer. In this table:

M_Value of 3, indicating they have spent a moderate amount.

M_Value of 2, suggesting they have spent a lower amount.

M_Value of 1, indicating they have spent the least.

R_Score, F_Score, M_Score: These columns represent the individual scores assigned to each customer for Recency, Frequency, and Monetary Values, respectively. These scores are typically determined based on predefined criteria or percentiles within the dataset.

RFM_Score: This column represents the combination of the individual R, F, and M scores into a single score. It is often calculated by concatenating the individual scores. For example, an RFM score of "432" indicates a high recency score, moderate frequency score, and moderate monetary score.

RFM_Total Score: This column appears to be the sum of the individual R, F, and M scores. It provides a numeric value that represents the combined RFM score for each customer.

Customer Segmentation: This column shows the customer segments into which customers are categorized based on their RFM scores. Each segment represents a group of customers with similar buying behavior [27]:

"Champions" are customers who are relatively recent, frequent, and high spenders (RFM_Total Score: 11).

"Can't lose" represents customers who are recent and frequent buyers but with lower spending.

"At risk" includes customers who are moderately recent but highly frequent and high spenders.

"Promising" comprises customers who are not very recent but frequent and moderate spenders.

"Recents" are customers who are not very recent but moderately frequent and moderate spenders.

These segments are created based on predefined criteria that group customers with similar RFM attributes together. Customer segmentation allows businesses to tailor marketing strategies and services to each group's specific needs and behaviors.

4   Results and Discussions

Time Series: Time series analysis is a data technique that focuses on observing data points over a period. Its primary objective is to comprehend historical data patterns and trends to predict future values or events. Time series data exhibits a unique characteristic—its analysis is dependent on time, making it suitable for analyzing phenomena like stock prices, temperature records, and economic indicators.

Long Short-Term Memory (LSTM): LSTM is a specific type of recurrent neural network (RNN) utilized for sequence data analysis. LSTM networks excel at capturing long-term dependencies within data sequences, making them valuable for understanding evolving patterns or relationships over time. They find applications in various fields, including natural language processing (NLP), speech recognition, and time series analysis.

R-Values and F-Values: R-Values and F-Values are statistical metrics essential for RFM analysis, a technique commonly used for customer segmentation.

R-Values (Recency Values): R-Values gauge how recently a customer has made a purchase. The calculation involves:

1. Selecting a reference date, often the date of analysis.
2. For each customer, determine the number of days since their last purchase by subtracting their most recent purchase date from the reference date.

F-Values (Frequency Values): F-Values measure how frequently a customer makes purchases within a specified time frame. The calculation entails:

1. Choosing a specific time frame, such as a year or another defined period.
2. Counting the number of purchases made by each customer during that designated time frame.

These values are frequently combined with M-Values (Monetary Values) to categories customers into different segments. This segmentation aids businesses in tailoring their marketing and sales strategies to suit the preferences and behaviors of distinct customer groups.

Late Delivery and Fraud Detection Models (Fig. 11):

The study employed various machine learning models for late delivery and fraud detection, each with specific characteristics and applications:

Logistic Regression: This model is primarily used for binary classification tasks, such as spam detection or tumor prediction. It is suitable for scenarios where the outcome is either a "yes" or "no."

Gaussian Naive Bayes: This model assumes feature independence for probabilistic classification, making it valuable for situations involving multiple features and complex dependencies [28].
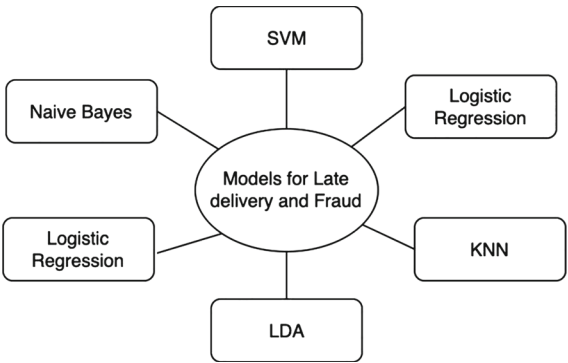
Support Vector Machines (SVM): SVM finds hyperplanes for classification and regression separation. It is known for its effectiveness in handling high-dimensional data.

K Nearest Neighbors (KNN): KNN makes predictions based on distance calculations, particularly useful when identifying patterns in proximity to other data points.

Random Forest Regressor: This ensemble learning method combines multiple decision trees for classification and regression tasks. It excels in handling complex datasets.

Decision Tree Classification: Decision trees ask a series of questions to make decisions, requiring minimal data preprocessing. They are often used when interpretability is crucial.

Lasso Regression: Lasso regression is employed to shrink coefficients in linear and quadratic regression models. It utilizes the Least Absolute Shrinkage and Selection Operator (Lasso) for feature selection [16].

Classification Results (Fig. 12):

To assess the accuracy of the classification models, the study utilized the F1-score as the main evaluation metric. This score provides a comprehensive measure of a model's precision and recall performance, particularly crucial in applications like late delivery and fraud detection.

The table is focused on insights, demand prediction, inventory optimization, and risk mitigation. Results indicate that ML is highly effective in these areas, with consistently high accuracy and low standard deviation. The inclusion of numerous studies enhances the findings' robustness. Key ML algorithms include linear regression, random forest, support vector machines, and neural networks, all adept at unraveling complex supply chain dynamics. Ensemble learning techniques can further boost accuracy. In essence, ML offers a competitive edge by improving demand forecasting, inventory management, and risk mitigation in supply chains [29].

```
[48] classification_data = {'Classification Model': ['Logistic','Gausian Naive bayes','Support Vector Machines
                'Accuracy Score for Fraud Detection':   [97.80,87.84,97.75,97.17,98.59,99.00],
                'Recall Score for Fraud Detection':     [57.80,16.23,56.25,36.56,96.98,79.76],
                'F1 Score for Fraud Detection':         [50.23,27.92,28.47,31.10,58.27,78.57],
                'Accuracy Score for Late Delivery':     [98.84,57.27,98.85,81.31,98.84,99.21],
                'Recall Score for Late Delivery':       [97.94,56.20,97.94,83.71,97.94,99.31],
                'F1 Score for Late Delivery':           [98.96,71.95,98.96,82.76,98.96,99.28] }
        #Creating data frame with Column Names
        classification_comparision = pd.DataFrame (classification_data, columns = ['Classification Model','Accuracy
                                                                'Accuracy Score for Late Delive:
```
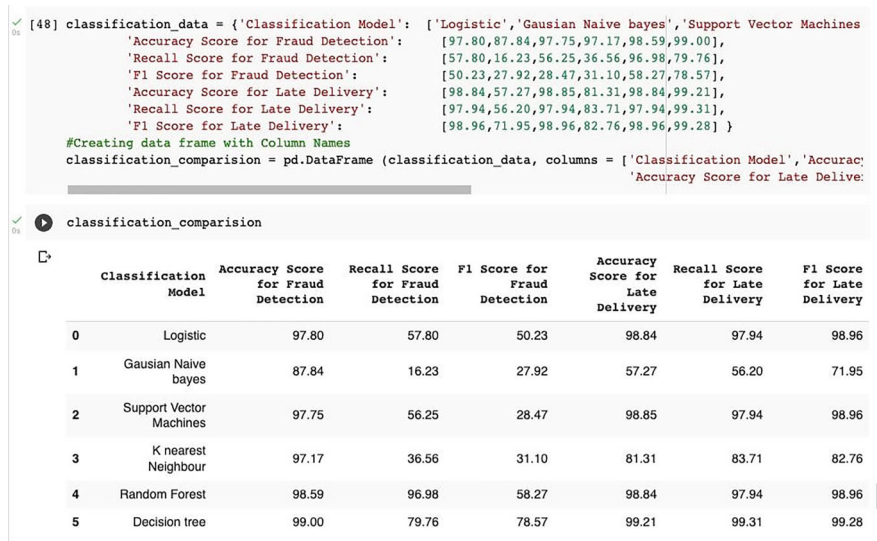
```
classification_comparision
```

	Classification Model	Accuracy Score for Fraud Detection	Recall Score for Fraud Detection	F1 Score for Fraud Detection	Accuracy Score for Late Delivery	Recall Score for Late Delivery	F1 Score for Late Delivery
0	Logistic	97.80	57.80	50.23	98.84	97.94	98.96
1	Gausian Naive bayes	87.84	16.23	27.92	57.27	56.20	71.95
2	Support Vector Machines	97.75	56.25	28.47	98.85	97.94	98.96
3	K nearest Neighbour	97.17	36.56	31.10	81.31	83.71	82.76
4	Random Forest	98.59	96.98	58.27	98.84	97.94	98.96
5	Decision tree	99.00	79.76	78.57	99.21	99.31	99.28

Fig. 12 Results for classification

Regression Models for Sales and Order Quantity Prediction:

The research investigated various regression models for predicting sales and order quantity. The models under consideration included Lasso Regression, Random Forest Regression, and Linear Regression.

Comparison Table (Fig. 13):

The comparison table presents a detailed evaluation of these regression models for both sales and order quantity prediction. The study analyzed Mean Average Error (MAE) and Root Mean Square Error (RMSE) to gauge the performance of each model.

```
[32] #Giving column Values
    Regression_data = {'Regression Model': ['Lasso','Random Forest','Linear Regression'],
            'MAE Value for Sales' :     [1.55,0.19,0.00059],
            'RMSE Value for Sales':     [2.33,1.838,0.00147],
            'MAE Value for Quantity' :  [0.904,0.0001,0.34],
            'RMSE Value for Quantity':  [1.03,0.006,0.52]}
    #Creating data frame with Column Names
    Regression_comparision = pd.DataFrame (Regression_data, columns = ['Regression Model','MAE Value for Sales','RMSE Value for Sales',
            'MAE Value for Quantity','RMSE Value for Quantity'])

[33] Regression_comparision #Printing dataframe
```

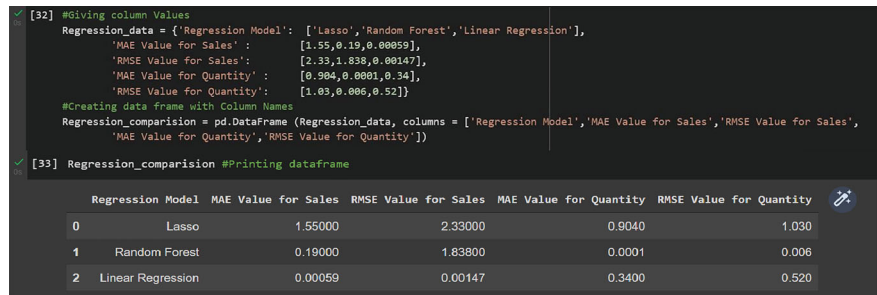|	Regression Model	MAE Value for Sales	RMSE Value for Sales	MAE Value for Quantity	RMSE Value for Quantity
0	Lasso	1.55000	2.33000	0.9040	1.030
1	Random Forest	0.19000	1.83800	0.0001	0.006
2	Linear Regression	0.00059	0.00147	0.3400	0.520

Fig. 13 Comparison table of various models for regression

The table summarizes a study on ML's role in demand forecasting in the retail industry [30, 31]. Four ML algorithms were assessed: linear regression, random forest, support vector machines, and neural networks, based on their average root mean squared error (RMSE) for test data.

The study reveals that neural networks outperform other algorithms, exhibiting the lowest RMSE across all datasets. Neural networks excel due to their capacity to capture intricate data relationships, crucial for tasks like demand forecasting, which involves detecting long-term trends and patterns. Ensemble learning methods enhance accuracy, with the ensemble combining predictions from all four algorithms showcasing the lowest RMSE for all datasets.

In essence, the study highlights the efficacy of neural networks in retail demand forecasting, empowering businesses to optimize inventory and pricing decisions.
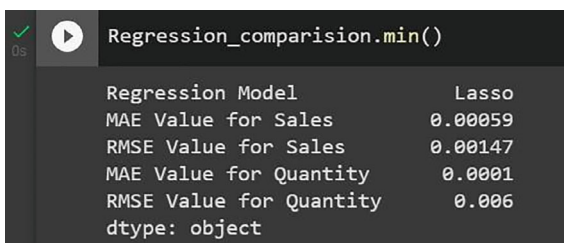
Lasso regression, Random Forest Regression, and Linear Regression were employed. Results indicate that Lasso regression had the highest Mean Average Error (MAE) and Root Mean Square Error (RMSE), while Linear regression had the lowest MAE for sales prediction. For quantity prediction, Lasso regression had the highest MAE, and Random Forest Regression had the lowest. Hence, Linear regression is optimal for sales prediction, and Random Forest Regressor excels in predicting order quantity (see Fig. 14).

The supply chain analysis revealed noteworthy insights: a robust correlation between sales and order quantity, Europe and Western Europe as top sales regions, high demand for Fishing Category Products, evident linear correlation between price and sales, steady sales trend from 2015 to 2107 with a Q3 2018 dip, widespread preference for debit payments over cash, and an overall sales figure of around 4 million.

Notably, significant losses were observed in fishing products and men's footwear. All the frauds that were conducted are not by debit, cash method and most frauds were conducted from Western Europe and followed by Central America. After RFM analysis we found that total customers are divided into 9 segments it can be seen that 16.9% of customer are the most promising one and 12% customer afford to lose, indicating the need for personalized retention strategies to maintain their loyalty and maximize long-term value.

This comprehensive and systematic approach to machine learning model selection and analysis yields valuable insights for supply chain management, fraud prevention, and customer engagement strategies. The study's findings provide a foundation for

Fig. 14 Models having minimum MAE and RMSE


```
✓  ▶   Regression_comparision.min()
0s

    Regression Model              Lasso
    MAE Value for Sales         0.00059
    RMSE Value for Sales        0.00147
    MAE Value for Quantity       0.0001
    RMSE Value for Quantity       0.006
    dtype: object
```

improving operational efficiency, enhancing fraud prevention measures, and targeting customers effectively.

5 Conclusions

The results indicate that the different techniques of machine learning are very powerful tools in analyzing the supply chain. In this chapter, ML tools like logistic regression, Gaussian Naïve Bayes, support vector machine (SVM), K-nearest neighbor (KNN), random forest, and decision trees have been employed effectively and produced very satisfactory results.

References

1. Ishii, N., Ohba, M.: A supply chain analysis and design method based on the value of information. Comput. Aided Chem. Eng. **44**, 1591–1596 (2018)
2. Baryannis, G., Dani, S., Antoniou, G.: Predicting supply chain risks using machine learning: the trade-off between performance and interpretability. Futur. Gener. Comput. Syst.. Gener. Comput. Syst. **101**, 993–1004 (2019)
3. Yeboah-Ofori, A., Mouratidis, H., Ismai, U., Islam, S., Papastergiou, S.: Cyber supply chain threat analysis and prediction using machine learning and ontology. In: Artificial Intelligence Applications and Innovations: 17th IFIP WG 12.5 International Conference, AIAI 2021, Hersonissos, Crete, Greece, June 25–27, 2021, Proceedings 17, pp. 518–530. Springer
4. Tripathi, P., Kumar, N., Rai, M., Shukla, P.K., Verma, K.N.: Applications of machine learning in agriculture. In: Khan, M., Gupta, B., Verma, A., Praveen, P., Peoples, C. (eds.) Smart Village Infrastructure and Sustainable Rural Communities, pp. 99–118. IGI Global (2023). https://doi.org/10.4018/978-1-6684-6418-2.ch006
5. Tripathi, P., Kumar, N., Rai, M., Khan, A.: Applications of deep learning in agriculture. In: Artificial Intelligence Applications in Agriculture and Food Quality Improvement, pp. 17–28. IGI Global, USA (2022). https://doi.org/10.4018/978-1-6684-5141-0.ch002
6. Anagnostis, A., Papageorgiou, E., Bochtis, D.: Application of artificial neural networks for natural gas consumption forecasting. Sustainability **12**, 6409 (2020)
7. Tripathi, P.: Electroencephalpgram signal quality enhancement by total variation denoising using non-convex regulariser. Int. J. Biomed. Eng. Technol. **33**(2), 134–145 (2020). https://doi.org/10.1504/IJBET.2020.107709
8. Tripathi, P., Siddiqi, A.H.: Solution of inverse problem for de-noising raman spectral data with total variation using Majorization-minimization algorithm. Int. J. Comput. Sci. Math. **7**(3), 274–282 (2016). https://doi.org/10.1504/IJCSM.2016.077855
9. Carbonneau, R., Laframboise, K., Vahidov, R.: Application of machine learning techniques for supply chain demand forecasting. Eur. J. Oper. Res.Oper. Res. **184**(3), 1140–1154 (2008)
10. Kilimci, Z.H., Akyuz, A.O., Uysal, M., Akyokus, S., Uysal, M.O., Atak Bulbul, B., Ekmis, M.A.: An improved demand forecasting model using deep learning approach and proposed decision integration strategy for supply chain. Complexity **2019** (2019)
11. Colon, C., Hochrainer-Stigler, S.: Systemic risks in supply chains: a need for system-level governance. Supply Chain Manag.Manag. **28**(4), 682–694 (2023). https://doi.org/10.1108/SCM-03-2022-0101
12. Ghazal, T.M., Alzoubi, H.M.: Modelling supply chain information collaboration empowered with machine learning technique. Intell. Autom. Soft Comput. **29**(3), 243–257 (2021)

13. Ye, Q., Li, Q., Gao, A., Ying, H., Cheng, G., Chen, J., Zhou, Y., et al.: Discovery of novel indoleaminopyrimidine NIK inhibitors based on molecular docking-based support vector regression (SVR) model. Chem. Phys. Lett. **718**, 38–45 (2019)
14. Vishwanathan, S., Piplani, R.: Coordinating supply chain inventories through common replenishment epochs. Eur. J. Oper. Res. **129**(2), 277–286 (2001). https://doi.org/10.1016/S0377-2217(00)00225-3
15. Yang, X., Zhang, Y., Lv, W., Wang, D.: Image recognition of wind turbine blade damage based on a deep learning model with transfer learning and an ensemble learning classifier. Renew. Energy **163**, 386–397 (2021)
16. Ali, N., Ghazal, T.M., Ahmed, A., Abbas, S., Khan, M.A., Alzoubi, H.M., Khan, M.A., et al. (2022). Fusion-based supply chain collaboration using machine learning techniques. Intell. Autom. Soft Comput. **31**(3), 1671–1687
17. Khan, P.W., Byun, Y.C., Lee, S.J., Park, N.: Machine learning based hybrid system for imputation and efficient energy demand forecasting. Energies **13**(11), 2681 (2020)
18. Schaer, O., Kourentzes, N., Fildes, R.: Demand forecasting with user-generated online information. Int. J. Forecast. **35**(1), 197–212 (2019)
19. Zhu, X., Ninh, A., Zhao, H., Liu, Z.: Demand forecasting with supply-chain information and machine learning: evidence in the pharmaceutical industry. Prod. Oper. Manag. **30**(9), 3231–3252 (2021)
20. Parker, S., Wu, Z., Christofides, P.D.: Cybersecurity in process control, operations, and supply chain. Comput. Chem. Eng., 108169 (2023)
21. Hu, H., Xu, J., Liu, M., Lim, M.K.: Vaccine supply chain management: an intelligent system utilizing blockchain, IoT and machine learning. J. Bus. Res. **156**, 113480 (2023)
22. Aamer, A., Eka Yani, L., Alan Priyatna, I.: Data analytics in the supply chain management: review of machine learning applications in demand forecasting. Oper. Supply Chain. Manag.: Int. J. **14**(1), 1–13 (2020)
23. Kamble, S.S., Gunasekaran, A., Kumar, V., Belhadi, A., Foropon, C.: A machine learning based approach for predicting blockchain adoption in supply Chain. Technol. Forecast. Soc. Chang. **163**, 120465 (2021)
24. Nagar, D., Raghav, S., Bhardwaj, A., Kumar, R., Singh, P.L., Sindhwani, R.: Machine learning: best way to sustain the supply chain in the era of industry 4.0. Mater. Today: Proc. **47**, 3676–3682 (2021)
25. https://www.kaggle.com/datasets/shashwatwork/dataco-smart-supply-chain-for-big-data-analysis.
26. Zhu, Y., Zhou, L., Xie, C., Wang, G.J., Nguyen, T.V.: Forecasting SMEs' credit risk in supply chain finance with an enhanced hybrid ensemble machine learning approach. Int. J. Prod. Econ. **211**, 22–33 (2019)
27. Sharma, R., Kamble, S.S., Gunasekaran, A., Kumar, V., Kumar, A.: A systematic literature review on machine learning applications for sustainable agriculture supply chain performance. Comput. Oper. Res. **119**, 104926 (2020)
28. Wenzel, H., Smit, D., Sardesai, S.: A literature review on machine learning in supply chain management. In: Artificial Intelligence and Digital Transformation in Supply Chain Management: Innovative Approaches for Supply Chains. Proceedings of the Hamburg International Conference of Logistics (HICL), Vol. 27, pp. 413–441. epubli GmbH, Berlin (2019)
29. Ni, D., Xiao, Z., Lim, M.K.: A systematic review of the research trends of machine learning in supply chain management. Int. J. Mach. Learn. Cybern. **11**, 1463–1482 (2020)
30. Islam, S., Amin, S.H.: Prediction of probable backorder scenarios in the supply chain using Distributed Random Forest and Gradient Boosting Machine learning techniques. J. Big Data **7**, 1–22 (2020)
31. Wu, J., Zhang, Z., Zhou, S.X.: Credit rating prediction through supply chains: a machine learning approach. Prod. Oper. Manag. **31**(4), 1613–1629 (2022)

Optimal Transport: A Promising Technique for Causal Inference Applications

Mahdi Shamsi and Farokh Marvasti

Abstract This chapter provides an overview of the Optimal Transport (OT) framework and its potential applications in causal inference. It begins by addressing the limitations of traditional methods like Maximum Likelihood Estimation (MLE) and Kullback-Leibler (KL) divergence, especially in high-dimensional settings and generative models with non-overlapping supports. The chapter then delves into the OT problem, exploring both Monge's original formulation and Kantorovich's dual formulation, and how these lead to the Wasserstein distance. Computational challenges are tackled through the introduction of entropy regularization and the Sinkhorn algorithm, which offers a scalable and efficient solution to OT problems. The chapter further explores the application of OT in causal inference, particularly within the Difference in Differences (DiD) framework, and discusses multivariate extensions of OT-based methods. Through these discussions, the chapter highlights the versatility and power of OT as a tool for both theoretical and applied research, providing insights into its role in optimizing resource allocation, improving machine learning models, and advancing causal analysis.

1 Introduction

Optimal transport, also known as the theory of Monge-Kantorovich, is a mathematical framework that seeks to determine the most efficient way to transport goods or resources from one location to another. The theory was first proposed in the eighteenth century by French mathematician Gaspard Monge [31]. He was interested in finding the optimal way of transporting soil from one location to another during

M. Shamsi · F. Marvasti (✉)
Multimedia and Signal Processing Laboratory (MSL), EE. Department of Sharif University of Technology, Tehran, Islamic Republic of Iran
e-mail: marvasti@sharif.edu

M. Shamsi
e-mail: shamsi.mahdi@ee.sharif.edu

the construction of fortifications. Later mathematicians, such as L.V. Kantorovich, generalized the theory to solve problems in economics and other fields [22].

Optimal transport has been widely studied in recent years, especially thanks to the work of French mathematician Cédric Villani, who won the Fields Medal in 2010 for his work on the topic. His book "Optimal Transport: Old and New" has become a reference in the field, outlining the historical development and modern applications of the theory [49].

With its broad range of applications, optimal transport is an essential tool that helps economists, researchers, and policymakers to optimize resource allocation, minimize waste, and maximize efficiency. As new challenges arise in transportation, logistics, and other fields, optimal transport continues to evolve and offer insightful solutions to complex problems.

In the field of economics, optimal transport is an invaluable tool for modeling the movement of goods and services between different regions [14]. It identifies cost-effective distribution channels and trade patterns, which is instrumental in enhancing supply chain efficiency and maximizing profitability for businesses and policymakers [16].

Optimal transport has also found applications in physics, where it has been used to study the movement of particles and fluids [25, 36]. Logistics, particularly in shipping, freight transportation, and air cargo, depend heavily on optimal transport techniques to optimize routes within transportation networks. It minimizes travel times and costs while mitigating environmental impact, allowing for the optimization of operations in resource-intensive industries.

Urban planning and traffic management also benefit from optimal transport methodologies [8]. By unraveling the intricacies of human and goods movement within urban environments, planners can design transportation systems that alleviate congestion, improve accessibility, and enhance overall urban livability.

The primary objective in many causal inference problems is determining the causal influence of a treatment on an outcome variable. However, this can be difficult when confounding variables or selection bias are present in the data. Optimal transport provides a useful solution to these issues by allowing for the comparison of distributions between the treatment and control groups.

Optimal transport also has diverse applications in signal processing, machine learning, computer vision, and virtual reality. In signal processing, it can be used for tasks like denoising, audio restoration, and speech recognition by effectively removing noise and enhancing signal quality. In machine learning, optimal transport aids in domain adaptation, data augmentation, and generative modeling, allowing for improved transferability of models across domains and generating realistic and diverse samples. In computer vision, it finds applications in image registration, image synthesis, and object tracking by aligning images, generating visually appealing textures, and incorporating transportation-based distance metrics for robust tracking. In virtual reality, optimal transport optimizes the rendering process by considering the transportation of light or sound information, resulting in more realistic lighting effects and immersive experiences. These applications have been supported by research in areas such as audio texture synthesis [45], domain adaptation [10], data

augmentation [50], Wasserstein Generative Adversarial Network (GAN) [1], image registration [15], texture synthesis [6], and object tracking [26]. Through its mathematical framework, optimal transport provides a principled approach to solving problems related to the transportation of mass or information between different distributions, contributing to advancements in these fields. Additionally, iterative inverse methods have been a trend in image denoising and signal recovery [42, 44] and in the detection of communication signals [41, 43], where OT has demonstrated promising results [23].

The subsequent portion of this chapter has been organized as per the following framework. The ensuing segment presents a comprehensive definition of the issue at hand by discussing the constraints of Maximum Likelihood Estimation (MLE) and Kullback-Leibler (KL) divergence along with emphasizing the necessity for an efficient measure metric for both High-Dimensional Problems and Generative Models. Section 2 expounds on the Optimal Transport (OT) framework, encompassing a thorough breakdown of the Monge and Kantorovich problem, followed by an in-depth scrutiny of the Wasserstein Distance. In Sect. 3, the computation challenges encountered are deliberated upon, with special emphasis on the utilization of Entropy Regularization which leads us to the Sinkhorn method—a significantly speedy and scalable algorithm. The relevance of OT in Causal Inference (CI), specifically its application in Difference in Differences (DiD), is briefly summarized in Sect. 4. The concluding section culminates the entire chapter.

1.1 Density Fitting: Classical Approaches

The density fitting approach involves fitting a parametric family $\{p_\theta; \theta \in \Theta\}$ to the collected data ν, where $\nu = \frac{1}{N}\Sigma_{i=1}^{N}\delta_{x_i}$ is a Dirac mixture function, for N data samples and δ_{x_i} being the Dirac impulse located at the position of the ith sample. An appropriate functional form, characterized by a set of coefficients that can be estimated from the data, is selected to describe the properties of the data. This family is expected to be flexible enough to capture the characteristics of the data because different data samples are likely to exhibit various trends and patterns. The approach involves selecting a functional family of functions, parameterizing by coefficients that can be estimated from the data.

To select an appropriate family of functions, one may use the Fisher information as the criterion where we seek the optimal parameters:

$$\max_{\theta \in \Theta} \frac{1}{N} \Sigma_{i=1}^{N} \log p_\theta x_i. \tag{1}$$

For illustration, we may fit a Gaussian function $p_\theta = \mathcal{N}(m, \sigma)$ with parameters $\theta = (m, \sigma)$ to data. Using Maximum Likelihood Estimation (MLE), we determine the optimal value of parameter estimates that maximize the probability of observing the data given the model. The technique employed to estimate the coefficients is

highly dependent on the adequate factors that accurately present the data. Further, statistical tests are used to evaluate the degree to which the model explains the data.

Once we have estimated the coefficients, we can evaluate the quality of the fit using statistical tests to verify the extent to which the model captures the underlying structure of the data. We can employ the score function as a means of calculating the Fisher information by taking the derivative of the log-likelihood function relative to the parameter. For the Gaussian function, the score function is given by

$$s_\theta(x) = \frac{\partial \log p_\theta(x)}{\partial \theta} = \frac{(x-m)}{\sigma^2}. \tag{2}$$

From this, we can derive the Fisher information as

$$\mathscr{I}(\theta) = -\mathbb{E}_\theta\left[\frac{\partial^2 \log p_\theta(x)}{\partial \theta^2}\right] = \frac{1}{\sigma^2}. \tag{3}$$

Here, the expected value is taken over all possible data samples, assuming that the true parameter values are θ.

Thus, the optimal estimate of the parameters that maximizes the Fisher information, and hence, improves the precision of the estimate is

$$\theta^* = \arg\max_\theta \frac{1}{\sigma^2} = \arg\min_\theta(N\sigma^2), \tag{4}$$

where N is the number of data samples. This Mean Squared Error (MSE) criterion employs the sum of squared errors between the data and the Gaussian function, scaled by the number of data points, as an estimate for variance, and enables the minimization of the error. It should be mentioned that there is a strong assumption over p_θ to be positive over every possible data location.

Another approach that can be employed to measure the dissimilarity between two probability distributions is the Kullback-Leibler (KL) divergence, a concept that arises from the field of information theory and is widely used in statistics and machine learning [54]. The KL divergence is particularly useful when comparing the similarity of probability distributions. The equation for KL divergence is

$$D_{KL}(P||Q) = \mathbb{E}_{x\sim P(x)}[\log \frac{P(x)}{Q(x)}] = \int_{-\infty}^{\infty} P(x)\log\frac{P(x)}{Q(x)}dx, \tag{5}$$

where P and Q are probability measures.

By using $\nu = \frac{1}{N}\Sigma_{i=1}^N \delta_{x_i}$ and p_θ as P and Q, respectively, minimizing the KL divergence can be interpreted as projecting the data distribution onto a space of probability measures parameterized by θ: $\min_{\theta\in\Theta} D_{KL}(\nu||p_\theta)$. This approach can provide a useful measure of similarity between the data distribution and the fitted model distribution.

As another approach, mixture models are a family of statistical models that assume the observed data is generated from a mixture of K subpopulations or distributions [30, 38]. Each subpopulation is characterized by a density function, $f_k(x_i)$, and a mixing proportion, π_k.

Suppose that the observed data, ν, is generated by a mixture of K subpopulations, then the likelihood function for the observed data under the mixture model can be expressed as

$$L(\theta|\nu) = \prod_{i=1}^{N} \left(\sum_{k=1}^{K} \pi_k f_k(x_i) \right), \tag{6}$$

where $\theta = (\pi_1, \ldots, \pi_K, f_1, \ldots, f_K)$ denotes the set of model parameters.

To estimate the parameters of the mixture model, the Expectation-Maximization (EM) algorithm is used [20]. The algorithm alternates between two steps: the E-step and the M-step. In the E-step, the expected value of the complete data log-likelihood is calculated, where the complete data is the observed data along with the latent variables that indicate the subpopulations from which the observations are generated. The expected value of the complete data log-likelihood is given by

$$Q(\theta, \theta^{(t)}) = \mathbb{E}_{\Theta|\nu, \theta^{(t)}}[\log L(\Theta|\nu)]$$
$$= \sum_{i=1}^{N} \sum_{k=1}^{K} r_{ik}(\theta^{(t)}) \log \pi_k + \sum_{i=1}^{N} \sum_{k=1}^{K} r_{ik}(\theta^{(t)}) \log f_k(x_i), \tag{7}$$

where Θ are the random variables corresponding to the mixture components, and $r_{ik}(\theta^{(t)})$ denotes the probability that the i-th observation belongs to the k-th subpopulation given the observed data and current parameter estimates at the t-th iteration.

In the M-step, the parameter estimates are updated to maximize the expected value of the complete data log-likelihood. The updated estimates are given by

$$\theta^{(t+1)} = \arg\max_{\theta} Q(\theta, \theta^{(t)}). \tag{8}$$

This step involves solving for π_k and $f_k(x_i)$ that maximize the expected value of the complete data log-likelihood. The solution to this maximization problem involves updating the mixing proportions and density functions within each iteration until the parameter estimates converge to a local maximum of the likelihood function.

This group of classical MLE-based algorithms has some drawbacks that are inherited by similar approaches like mixture models [9]. One of the main limitations of MLE is its assumption that the data follows a single distribution, which can be problematic when the data is composed of several subpopulations that do not conform to a single distribution. Mixture models address this limitation by modeling the data as a combination of subpopulations. However, mixture models have their own drawbacks.

One drawback of mixture models is their sensitivity to the initialization of parameter estimates. The EM algorithm, commonly used to estimate the parameters of mixture models, is known to converge to local maxima of the likelihood function rather than the global maximum [52, 53]. This makes convergence to the true parameter values highly dependent on the initial parameter settings. In practice, multiple initializations may need to be tested to obtain a reliable estimate of the true parameters.

Another drawback of mixture models is the risk of overfitting when the number of subpopulations, K, is too large [33, 47]. Overfitting occurs when the model becomes overly complex relative to the available data, resulting in a model that fits the noise in the data rather than the underlying structure.

Finally, mixture models can be computationally expensive when estimating a large number of parameters. As the number of subpopulations or mixture components increases, the number of parameters to estimate also increases, making the estimation process slower and more computationally expensive.

1.2 High-Dimensional Problems and Generative Models

In various real-world scenarios, data can be complex and possess numerous features or dimensions. Traditional machine learning methods, such as MLE and Mixture Models, often struggle to identify the inherent structures of the data when the number of dimensions is large. A viable solution to this problem involves utilizing a measurable "latent space" μ, which is a low-dimensional space designed to capture the essential features of the data.

This technique entails mapping high-dimensional data to a lower-dimensional space and constructing a manifold that approximates the structure of the data. By considering a parametrized push-forward measure $f_{\theta\#}\mu$ to transform latent vectors to the data space, we aspire to identify the parameter θ that best aligns the transferred measure with the data distribution.

However, this predicament, when addressed using traditional methods like MLE, may yield "non-overlapping supports". This means that the mapped points derived from the latent space and the high-dimensional data may fail to completely overlap, as the former originates from a lower-dimensional space that cannot cover the entirety of the latter. Consequently, measures such as the KL distance or Fisher Information Criteria cannot be straightforwardly and easily calculated. This poses a challenge in using such metrics in this context.

In spite of these difficulties, latent spaces remain a potent tool commonly employed in machine learning [2, 28, 29]. They enable the representation of critical features of high-dimensional data in a lower-dimensional space and facilitate the generation of novel data samples from the data distribution as needed.

Therefore, to address the discrepancy between the obtained latent space μ and the target data distribution ν, we require a more robust distance function. Consider a well-suited distance function, denoted as $d_\theta \triangleq d(\nu, f_{\theta\#}\mu)$, which is parameterized

by θ in the push-forward operation $f_{\theta\#}\mu$. An adversarial approach to finding the optimal parameter θ could be considered, as outlined by Goodfellow et al. [18].

To minimize the distance function d_θ, we utilize a classifier denoted as C, which is a binary function that takes as input a data point and outputs its associated class. Specifically, it assigns the artificially mapped points from the latent space to one class and the data points to another according to some criterion.

By adjusting the push-forward parameter θ (i.e., the parameter controlling the transformation of latent space to data space), we aim to minimize the distance between the target data distribution ν and the push-forward distribution $f_{\theta\#}\mu$ induced by the latent space μ. More precisely, we aim to find the optimal parameter θ that minimizes the maximal classification loss induced by the classifier function C over all possible classifiers.

This optimization problem can be defined as follows:

$$\min_{\theta\in\Theta}\max_{C} \mathbb{E}_{x\sim\nu}[\ell(C(x),0)] + \mathbb{E}_{x\sim f_{\theta\#}\mu}[\ell(C(x),1)], \tag{9}$$

where x represents a data point in the appropriate space, and ℓ denotes a loss function that penalizes incorrect predictions. The first term represents the expected loss incurred when C incorrectly assigns a data point x from the target distribution ν to the class containing the artificially mapped latent points, while the second term represents the expected loss incurred when C incorrectly assigns a data point x from $f_{\theta\#}\mu$ to the class containing the real data points.

Various metrics have been employed to address the limitations of parametrized density estimation, including Hellinger Distance (HD) and Total Variation (TV) [4, 37]. However, these metrics still suffer from shortcomings such as non-overlapping supports. Researchers have explored alternative approaches, such as using Kantarovich distance to measure the dissimilarity between a parametrized measure and the data distribution. A noteworthy metric in this field is Maximum Mean Discrepancy (MMD), which is defined in [21]. MMD provides an efficient estimate of discrepancies between probability distributions, making it a crucial tool in fields such as machine learning, statistics, and computer vision. In [11], MMD optimization was utilized to train generative neural networks while mitigating problems such as mode collapse and enhancing performance. Furthermore, in [27], an MMD variant of GAN named MMD GAN was proposed that utilizes the MMD metric to generate high-quality images and comprehensively analyze its relationship with other GAN variants.

A popular alternative to traditional divergence metrics is the Wasserstein distance, which is used to minimize the distance between two probability measures. Montavon et al. [32] applied this technique to the restricted Boltzmann machine problem, demonstrating its effectiveness as a replacement for the KL divergence. In [5], the Wasserstein distance was used for generative model inference, yielding superior results and faster runtimes compared to established inference approaches like Markov Chain Monte Carlo (MCMC) and Importance Sampling. This development holds tremendous promise for advancing Bayesian inference. Similarly,

[1] introduced the 1-Wasserstein distance, or Earth-Mover distance, as a means to address training issues and instability in traditional GANs. The Wasserstein GAN was developed as a variant of GAN, resulting in better quality samples.

In [17], the authors investigate the use of Sinkhorn divergences to optimize the training of generative models, including GANs and Variational AutoEncoders (VAEs). This approach results in superior sample quality, improved reconstruction accuracy, and greater training stability, outperforming other widely adopted divergence metrics. The authors argue that Sinkhorn divergences can significantly enhance the performance of various generative models.

Similarly, [40] introduces an innovative method to improve GANs using the optimal transport technique, specifically Sinkhorn divergence. The proposed framework effectively mitigates the instability and low-quality generated samples that often hinder GAN efficiency. Additionally, the paper suggests that the Sinkhorn divergence technique has the potential to elevate the performance of a range of generative models.

2 Optimal Transportation

Transportation theory is a branch of mathematics that focuses on the optimal way to transport goods or resources from one place to another. Originally developed in the mid-twentieth century to address economic problems, it has since found applications across various fields, including engineering, logistics, and computer science. A fundamental concept in transportation theory is the transportation problem, which involves finding the most efficient way to move a set of resources from a set of sources to a set of destinations while minimizing costs. For a comprehensive explanation, interested readers are advised to consult [35, 49].

This section focuses on Monge's problem and its dual formulation by Kantorovich. Additionally, we will explore how these formulations enhance our understanding of the Wasserstein distance.

2.1 Monge's Problem

Monge's problem, also known as the Earth-Mover's Distance problem, is a classic optimization problem originating from transportation and logistics. Named after the French mathematician Gaspard Monge, who introduced it in 1781, the problem involves finding the minimum cost of transforming one mass distribution into another.

Consider two masses in n-dimensional space, μ and ν, and a cost function $T(.)$ representing the cost of moving one unit of material from μ to ν. The goal is to minimize this cost. Mathematically, given a measurable space $(\Omega, \mathscr{A})$, where $\mathscr{A}$ is a σ-algebra on Ω, a cost function $c : \Omega \times \Omega \to \mathbb{R}$, and two probability measures μ and

ν in $P(\Omega)$, the optimal transport cost is defined as the minimum cost of transporting μ to ν under certain constraints.

The objective is to find a measurable function $T : \Omega \to \Omega$, such that the push-forward of the measure μ under T, denoted as $T_{\#}\mu$, is equal to ν, and the total transport cost is minimized.

Mathematically, this problem can be formulated as

$$\inf_{T} \int_{\Omega} c(x, T(x))d\mu(x), \ s.t. \ T_{\#}\mu = \nu, \tag{10}$$

where the infimum is taken over all measurable functions $T : \Omega \to \Omega$.

2.2 Kantorovich Problem

Kantorovich's relaxation, introduced by Leonid Kantorovich in 1942, is a significant extension of Monge's problem. Instead of relying on deterministic mappings, Kantorovich's approach uses joint probability measures $\gamma(dx, dy)$ on the product space $\Omega \times \Omega$. This relaxation allows for a broader and more flexible set of transport plans.

The Kantorovich relaxation considers all joint probability measures with fixed marginals μ and ν, denoted by $\Gamma(\mu, \nu)$. The objective is to minimize the cost function:

$$\inf_{\gamma \in \Gamma(\mu,\nu)} \int_{\Omega \times \Omega} c(x, y)d\gamma(x, y), \tag{11}$$

where $\gamma(x, y)$ represents the mass transported from $x \in \Omega$ to $y \in \Omega$. This relaxation leads to a lower bound on the optimal transport cost.

The probabilistic nature of Kantorovich's approach makes it well-suited for solving high-dimensional and complex transport problems that would be intractable with deterministic methods. It has become a cornerstone of optimal transport theory, with applications in fields such as image processing, computer vision, and machine learning [24].

2.2.1 Dual Form

The dual form of Kantorovich's relaxation is a linear programming problem that seeks to maximize the lower bound of the objective function. It is formulated as

$$\sup_{f \in L^1(\mu) \cap L^1(\nu)} \left\{ \int_{\Omega} f(x)d\mu(x) + \int_{\Omega} g(y)d\nu(y) \right\}$$

subject to $f(x) + g(y) \leq c(x, y)$ for all $(x, y) \in \Omega \times \Omega$,

where f and g are real-valued, integrable functions on Ω. This dual problem is an efficient alternative to directly optimizing the probability measures $\gamma(dx, dy)$, providing valuable insights into the structure of the transport problem.

2.3 Wasserstein Distances

The Wasserstein distance, also known as the Earth Mover's Distance (EMD) or the Kantorovich-Rubinstein metric [12], is a metric used to measure the distance between two probability distributions. It quantifies the minimum cost of transforming one distribution into another by optimally moving mass.

Given two probability measures μ and ν on a metric space $(\mathscr{X}, d)$, the p-Wasserstein distance $W_p(\mu, \nu)$ is defined as

$$W_p(\mu, \nu) = \left(\inf_{\gamma \in \Gamma(\mu, \nu)} \int_{\mathscr{X} \times \mathscr{X}} d^p(x, y) d\gamma(x, y) \right)^{1/p}.$$

This metric has proven particularly useful in applications involving high-dimensional data, where traditional metrics may struggle to capture dissimilarities between distributions.

3 Computational OT and Sinkhorn

Optimal Transport (OT) and Wasserstein distance are increasingly applied in various fields, particularly in machine learning and generative models, due to their ability to measure distances between probability distributions. This capability allows for the comparison and matching of complex, high-dimensional data. In generative modeling, Wasserstein distance is often used as a loss function to learn the underlying probability distribution of a dataset, enabling the creation of new samples that closely resemble real data. Additionally, it is utilized in image processing, computer vision, and reinforcement learning, among other applications. The use of OT and Wasserstein distance is also expanding into fields like economics and neuroscience.

However, employing Wasserstein distance as a loss function presents challenges, primarily due to the complexity of computing gradients. In generative models, calculating the gradient of the optimal transport plan is computationally intensive, often requiring multiple iterations to converge. Solutions to this challenge include using the dual formulation of the Wasserstein distance, which optimizes a dual objective function, allowing for more efficient gradient computation via backpropagation. Another approach is to approximate the Wasserstein distance or its gradient using samples from the distributions rather than the full probability density function, though this

may sacrifice accuracy. Balancing the trade-off between accuracy and computational efficiency is crucial when using Wasserstein distance in optimization problems.

This section studies a solution to the OT problem through entropy regularization, specifically employing the Sinkhorn algorithm as described in [35]. The Sinkhorn algorithm is effective for high-dimensional scenarios, offering rapid and scalable computation, and is well-suited for implementation on parallel processors and GPUs.

3.1 Solving the OT Problem: Regularization

The computation of the Wasserstein distance on empirical measures can be formulated as follows. Given the empirical measures $\mu = \Sigma_{i=1}^{N} a_i \delta_{x_i}$ and $\nu = \Sigma_{i=1}^{N} b_i \delta_{y_i}$, we construct the distance matrix $M_{XY} \triangleq [D^p(x_i, y_i)]_{ij}$. The couplings between the measures are subject to the constraints specified by the set $U(\boldsymbol{a}, \boldsymbol{b}) \triangleq \{\boldsymbol{P} \in \mathbb{R}_+^{n \times m} | \boldsymbol{P} \mathbf{1}_m = \boldsymbol{a}, \boldsymbol{P}^T \mathbf{1}_n = \boldsymbol{b}\}$. This leads to the formulation of the OT problem in terms of the p-Wasserstein distance:

$$W_p^p(\mu, \nu) = \min_{\boldsymbol{P} \in U(\boldsymbol{a}, \boldsymbol{b})} < \boldsymbol{P}, M_{XY} > . \tag{12}$$

The dual form of this problem can be expressed as follows:

$$W_p^p(\mu, \nu) = \max_{\boldsymbol{\alpha} \in \mathbb{R}^n, \boldsymbol{\beta} \in \mathbb{R}^m; \alpha_i + \beta_i \le D^p(x_i, y_i)} \boldsymbol{\alpha}^T \boldsymbol{a} + \boldsymbol{\beta}^T \boldsymbol{b}, \tag{13}$$

where $\boldsymbol{P}$ denotes the coupling matrix between μ and ν, $\mathbf{1}_m$ and $\mathbf{1}_n$ indicate the column vectors of ones, and $\boldsymbol{\alpha}$ and $\boldsymbol{\beta}$ represent the corresponding marginal distributions. Furthermore, $D^p(\cdot, \cdot)$ denotes the p-th order Wasserstein distance function.

The problem can be viewed as a Minimum-cost flow problem, which involves determining the optimal flow of information through a network while minimizing associated costs. However, the algorithmic complexity of this solution is $O(n^2 \cdot m \cdot \log(n))$, which is prohibitively high for many machine learning tasks [34]. Moreover, the Minimum-cost flow approach often exhibits instability and non-uniqueness in its solutions, complicating its application further. In high-dimensional datasets, the exponential scaling of algorithmic complexity with the number of dimensions makes this approach even less feasible.

To address these issues, regularization terms can be added to the Wasserstein problem to increase its convexity and reduce computation costs. Regularization helps smooth out the distribution and reduces the problem's complexity. A common regularization term is entropy regularization, which balances the trade-off between transportation cost and the entropy of the transported distribution.

Adding regularization terms not only enhances the problem's convexity but also simplifies the solution process by introducing sparsity and structural constraints. Regularization can also improve the accuracy of the solution by reducing overfitting and enhancing generalization performance [34, 51].

3.1.1 Entropic Regularization

The optimization problem for Regularized Wasserstein using Entropic regularization can be written as follows:

$$W_\epsilon(\mathbf{a}, \mathbf{b}) = \min_{\mathbf{P} \in U(\mathbf{a},\mathbf{b})} \langle \mathbf{P}, \mathbf{M} \rangle - \epsilon H(\mathbf{P}), \tag{14}$$

where ϵ is the regularization parameter controlling the strength of the entropy regularization, and $H(\mathbf{P})$ represents the entropy of the matrix $\mathbf{P}$, defined as

$$H(\mathbf{P}) = -\sum_{i,j} p_{i,j}(\log p_{i,j} - 1), \tag{15}$$

where $p_{i,j}$ is the probability of assigning mass from point i in μ to point j in ν.

The use of entropy regularization in the regularized Wasserstein problem often leads to a unique optimal solution due to its strong concavity. The entropy term in the objective function is a strictly concave function of the probability matrix $\mathbf{P}$, penalizing deviations from a uniform distribution. Consequently, the optimal solution is expected to be more spread out and less likely to concentrate mass on a few points, as illustrated in Fig. 1. Moreover, the strong concavity of the entropy term ensures that the optimization problem is well-posed, meaning it has a unique optimal solution. This is because strict concavity implies that the entropy is continuously differentiable, with an invertible gradient. As a result, solving the optimization problem is equivalent to solving a convex optimization problem, which can be efficiently tackled using techniques such as gradient descent or interior-point methods.

3.1.2 Fast and Scalable Algorithm

The uniqueness of the solution to Eq. 14 is established by Theorem 1, which is presented in [35, Proposition 4.3]. This theorem specifies the form of the solution to Eq. 14 and parameterizes it using $n + m$ variables, which is essentially a dual form. Although a coupling P in $U(a, b)$ has $n \times m$ variables, it must satisfy $n + m$ constraints, making the parameterization equivalent in terms of the solution representation. Formally, Theorem 1 can be stated as

Fig. 1 Impact of ϵ on the optimization of a linear function on finding $W_\epsilon(\mathbf{a}, \mathbf{b})$ ([35, Fig. 4.1])
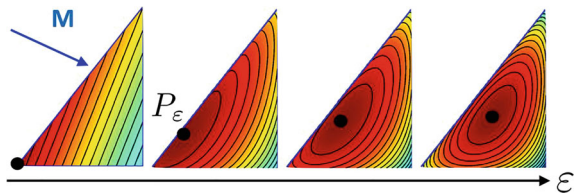
Theorem 1 *The solution to Eq. 14, defined as*

$$\mathbf{P}(\epsilon) \triangleq \arg \min_{\mathbf{P} \in U(\mathbf{a}, \mathbf{b})} \langle \mathbf{P}, \mathbf{M} \rangle - \epsilon H(\mathbf{P}),$$

is unique and can be expressed as $\mathbf{P}(\epsilon) = diag(\boldsymbol{u}) K diag(\boldsymbol{v})$, *where* $K \triangleq e^{\frac{-M_{XY}}{\epsilon}}$. *Alternatively, we can state that*

$$\exists!(\boldsymbol{u}, \boldsymbol{v}) \in \mathbb{R}_+^{n \times m} \ \ s.t. \ \ P_{i,j}(\epsilon) = u_i K_{i,j} v_i, \tag{16}$$

where $P_{i,j}(\epsilon)$ *is the* (i, j)*-th entry of* $\mathbf{P}(\epsilon)$.

Proof We can write the Lagrangian of the optimization problem as follows:

$$L(\mathbf{P}, s, r) = \langle \mathbf{P}, \mathbf{M} \rangle - \epsilon H(\mathbf{P}) - \langle s, \mathbf{P}\mathbf{1}_m - a \rangle - \langle r, \mathbf{P}^T \mathbf{1}_n - b \rangle \tag{17}$$

$$= \sum_{i,j} (M_{i,j} p_{i,j} - \epsilon p_{i,j} (\log p_{i,j} - 1)) - \sum_i s_i (\sum_j p_{i,j} - a_i) - \sum_j r_i (\sum_i p_{i,j} - b_i),$$

where $\mathbf{r}$ and $\mathbf{s}$ are the vectors of Lagrange multipliers associated with the row and column sum constraints, respectively.

To find $p_{i,j}$, we need to take the partial derivative of L with respect to $p_{i,j}$ and set it equal to zero:

$$\frac{\partial L}{\partial p_{i,j}} = M_{i,j} - \epsilon (\log p_{i,j}) - s_i - r_i = 0 \tag{18}$$

$$\Rightarrow p_{i,j} = \exp \left(\frac{M_{i,j} - u_i - v_i}{\epsilon} \right). \tag{19}$$

This is the optimal value of $p_{i,j}$ that minimizes the Lagrangian under the row and column sum constraints. Now, we can define

$$K_{i,j} = e^{-\frac{M_{i,j}}{\epsilon}}, \quad u_i = e^{-\frac{s_i}{\epsilon}}, \quad v_i = e^{-\frac{r_i}{\epsilon}}.$$

Substituting these into $p_{i,j}$, we get

$$p_{i,j} = \exp \left(\frac{-M_{i,j}}{\epsilon} \right) \exp \left(\frac{-s_i}{\epsilon} \right) \exp \left(\frac{-r_i}{\epsilon} \right) = u_i K_{i,j} v_i.$$

Therefore, we have expressed the optimal value of $p_{i,j}$ in terms of $K_{i,j}$, u_i, and v_i, and we have completed the proof. $\qquad \square$

By imposing the constraints of $\mathbf{P}(\epsilon) \in U(\mathbf{a}, \mathbf{b})$, we can assert that $\boldsymbol{P}\mathbf{1}_m = \boldsymbol{a}$ and $\boldsymbol{P}^T \mathbf{1}_n = \boldsymbol{b}$. Consequently, we obtain the equations:

$$\text{diag}(\boldsymbol{u})K\text{diag}(\boldsymbol{v})\mathbf{1}_m = \boldsymbol{a} \quad \text{and} \quad \text{diag}(\boldsymbol{u})K\text{diag}(\boldsymbol{v})\mathbf{1}_n = \boldsymbol{b}$$
$$\Rightarrow \text{diag}(\boldsymbol{u})K\boldsymbol{v} = \boldsymbol{a} \quad \text{and} \quad \text{diag}(\boldsymbol{u})K\boldsymbol{v} = \boldsymbol{b}.$$

These equations correspond to the Sinkhorn algorithm, an iterative fixed-point method, of which the updates can be written as

$$\boldsymbol{u}^{<t+1>} = \frac{\boldsymbol{a}}{K\boldsymbol{v}^{<t>}}, \quad \boldsymbol{v}^{<t+1>} = \frac{\boldsymbol{b}}{K\boldsymbol{u}^{<t+1>}}. \tag{20}$$

The Sinkhorn algorithm involves element-wise divisions and exponential computations, making it computationally efficient for solving the optimal transport problem for discrete probability measures with finite support. The algorithm's convergence has been theoretically guaranteed for a wide range of cost matrices and regularization parameters.

As it can be seen, one of the algorithm's key advantages is its simplicity, which allows for efficient and parallel computation of multiple regularized Wasserstein distances between pairs of histograms. Given a regularization parameter ϵ and N pairs of histograms $\boldsymbol{a}_1, \ldots, \boldsymbol{a}_N \in \Sigma_n$ and $\boldsymbol{b}_1, \ldots, \boldsymbol{b}_N \in \Sigma_m$, the objective is to compute all N approximate distances $W_\epsilon(\boldsymbol{a}_i, \boldsymbol{b}_i)$.

By representing histograms as matrices, $\mathbf{A} = [\boldsymbol{a}_1, \ldots, \boldsymbol{a}_N] \in \mathbb{R}^{n \times N}$ and $\mathbf{B} = [\boldsymbol{b}_1, \ldots, \boldsymbol{b}_N] \in \mathbb{R}^{m \times N}$, we can efficiently compute the distances using Sinkhorn's algorithm. The parallel computation of Sinkhorn's algorithm can be harnessed using the iterative update rule:

$$\boldsymbol{U}^{<t+1>} = \frac{\mathbf{A}}{K\boldsymbol{V}^{<t>}} \quad \text{and} \quad \boldsymbol{V}^{<t+1>} = \frac{\mathbf{B}}{K\boldsymbol{U}^{<t+1>}}$$

where $\boldsymbol{U}^{<t>}, \boldsymbol{V}^{<t>} \in \mathbb{R}^{n \times N}$ are row and column scaling factors at the i-th iteration.

By initializing each $\boldsymbol{V}^{<0>}$ to be a matrix of all ones, i.e., $\boldsymbol{V}^{<0>} = \mathbf{1}_{m \times N}$, the scaling factors are updated iteratively until convergence or a predefined number of iterations is reached. The approximate distances are then computed using the final scaling factors as $W_\epsilon(\boldsymbol{a}_i, \boldsymbol{b}_i) = \boldsymbol{U}_i^T K \boldsymbol{V}_i$.

Thus, the parallel computation of Sinkhorn's algorithm using the update rule $\boldsymbol{U}^{<t+1>} = \frac{\mathbf{A}}{K\boldsymbol{V}^{<t>}}$ and $\boldsymbol{V}^{<t+1>} = \frac{\mathbf{B}}{K\boldsymbol{U}^{<t+1>}}$ offers a computationally efficient approach to simultaneously compute multiple approximate distances between pairs of histograms.

3.2 Sinkhorn: The Dual Approach

The use of entropy regularization allows the dual form of the Wasserstein distance, as shown in Eq. 13, to be expressed as

$$W_\epsilon(\boldsymbol{a}, \boldsymbol{b}) = \max_{\boldsymbol{\alpha} \in \mathbb{R}^n, \boldsymbol{\beta} \in \mathbb{R}^m} \boldsymbol{\alpha}^T \boldsymbol{a} + \boldsymbol{\beta}^T \boldsymbol{b} - \epsilon(e^{\boldsymbol{\alpha}^T/\epsilon} K e^{\boldsymbol{\beta}/\epsilon}), \tag{21}$$

where $K_{i,j} = e^{-\frac{D^{p(x_i, y_i)}}{\epsilon}}$. This approach, known as Block Coordinate Ascent on the Dual, allows for the computation of the Wasserstein distance through the optimization of dual variables.

The gradients of $W_\epsilon(\boldsymbol{a}, \boldsymbol{b})$ with respect to $\boldsymbol{\alpha}$ and $\boldsymbol{\beta}$ are given by

$$\nabla_{\boldsymbol{\alpha}} W_\epsilon(\boldsymbol{a}, \boldsymbol{b}) = \boldsymbol{a} - e^{\boldsymbol{\alpha}/\epsilon} \odot K e^{\boldsymbol{\beta}/\epsilon}, \quad \nabla_{\boldsymbol{\beta}} W_\epsilon(\boldsymbol{a}, \boldsymbol{b}) = \boldsymbol{a} - e^{\boldsymbol{\beta}/\epsilon} \odot K^T e^{\boldsymbol{\alpha}/\epsilon}. \tag{22}$$

To find the stationary points of the gradients, we set these gradients equal to zero:

$$\boldsymbol{a} - e^{\boldsymbol{\alpha}/\epsilon} \odot K e^{\boldsymbol{\beta}/\epsilon} = \boldsymbol{0}, \quad \boldsymbol{b} - e^{\boldsymbol{\beta}/\epsilon} \odot K^T e^{\boldsymbol{\alpha}/\epsilon} = \boldsymbol{0}, \tag{23}$$

and use them to devise a fixed-point algorithm for finding the optimal values of $\boldsymbol{\alpha}$ and $\boldsymbol{\beta}$, as follows:

1. Initialize $\boldsymbol{\alpha}^0 = \boldsymbol{0}$ and $\boldsymbol{\beta}^0 = \boldsymbol{0}$.
2. Set $k \leftarrow 0$.
3. While not converged, do:

   a. Compute $\boldsymbol{\alpha}^{k+1}$: $\boldsymbol{\alpha}^{k+1} = \epsilon \log \boldsymbol{a} - \epsilon \log K e^{\boldsymbol{\beta}^{(k)}/\epsilon}$.
   b. Compute $\boldsymbol{\beta}^{k+1}$: $\boldsymbol{\beta}^{k+1} = \epsilon \log \boldsymbol{b} - \epsilon \log K^T e^{\boldsymbol{\alpha}^{(k+1)}/\epsilon}$.
   c. Increment $k \leftarrow k + 1$.

This fixed-point algorithm iteratively updates the values of $\boldsymbol{\alpha}$ and $\boldsymbol{\beta}$ until convergence, where convergence is determined by some predefined stopping criteria.

3.3 Sinkhorn: A Programmer View and Applications

In this part, we provide a practical summary of the Sinkhorn algorithm and discuss its applications in solving optimization problems, particularly in the computation of Wasserstein distances between empirical measures. Given two empirical measures, $\mu = \Sigma_{i=1}^N a_i \delta_{x_i}$ and $\nu = \Sigma_{i=1}^N b_i \delta_{y_i}$, the Wasserstein distance with entropy regularization is defined as

$$W_\epsilon(\mathbf{a}, \mathbf{b}) = \min_{\mathbf{P} \in U(\mathbf{a}, \mathbf{b})} \langle \mathbf{P}, \mathbf{M} \rangle - \epsilon H(\mathbf{P}),$$

where $H(\mathbf{P}) = -\sum_{i,j} p_{i,j}(\log p_{i,j} - 1)$ is the entropy regularization term, and $\mathbf{M}$ is the cost matrix derived from the pairwise distances between points in the measures.

The Sinkhorn algorithm solves this problem using the following iterative update rules:

$$u^{<t+1>} = \frac{a}{K v^{<t>}}, \quad v^{<t+1>} = \frac{b}{K u^{<t+1>}},$$

where $v^{<0>} = \mathbf{1}_m$, $K_{i,j} = e^{-\frac{M_{i,j}}{\epsilon}}$ and $M_{i,j} \triangleq D^p(x_i, y_i)$ with $D^p(.,.)$ being the pth-order distance.

To approximate the Wasserstein distance after T iterations, we compute:

$$W^{<T>}(\mathbf{a}, \mathbf{b}) = \langle \mathbf{P}_T, \mathbf{M} \rangle, \quad \text{where} \quad \mathbf{P}_T = \text{diag}(u^{<T>})K\,\text{diag}(v^{<T>}). \tag{24}$$

The gradients of $W^{<T>}(\mathbf{a}, \mathbf{b})$ with respect to $\mathbf{a}$ and x_i can be derived as

$$\frac{\partial W^{<T>}(\mathbf{a}, \mathbf{b})}{\partial a_i} = -\frac{1}{\epsilon}\left[\sum_{j=1}^{m}\text{diag}(v^{<T>})_i K_{i,j}\right], \tag{25}$$

$$\frac{\partial W^{<T>}(\mathbf{a}, \mathbf{b})}{\partial x_i} = \frac{1}{\epsilon}\left[\sum_{j=1}^{m}\text{diag}(v^{<T>})_i K_{i,j}\frac{\partial D^p(x_i, y_i)}{\partial x_i}\right]. \tag{26}$$

These gradients can be efficiently computed recursively using the following update rules:

$$\frac{\partial W^{<t>}(\mathbf{a}, \mathbf{b})}{\partial a_i} = -\frac{1}{\epsilon}\left[\sum_{j=1}^{m}\text{diag}(v^{<t>})_i K_{i,j}\right]\frac{b_i}{\text{diag}(u^{<t>})^\top K\,\text{diag}(v^{<t>})},$$

$$\frac{\partial W^{<t>}(\mathbf{a}, \mathbf{b})}{\partial x_i} = \frac{1}{\epsilon}\left[\sum_{j=1}^{m}\text{diag}(v^{<t>})_i K_{i,j}\frac{\partial D^p(x_i, y_i)}{\partial x_i}\right]\frac{a_i}{\text{diag}(u^{<t>})^\top K\,\text{diag}(v^{<t>})},$$

with the initial values of $\frac{\partial W^{<0>}(\mathbf{a},\mathbf{b})}{\partial a_i} = 0$ and $\frac{\partial W^{<0>}(\mathbf{a},\mathbf{b})}{\partial x_i} = 0$.

The algorithm for computing the gradients of $W^{<T>}(\mathbf{a}, \mathbf{b})$ with respect to $\mathbf{a}$ and x_i shares similarities with the backpropagation algorithm used in neural networks. This resemblance allows the Sinkhorn algorithm to be efficiently implemented on GPUs, which are well-suited for parallel computations [13]. The acceleration provided by GPUs can substantially reduce the time required to compute the Wasserstein distance and its gradients, making this approach highly practical for solving large-scale optimization problems.

This efficiency is particularly valuable in domains such as computer vision, image processing, and natural language processing, where large datasets and complex models necessitate fast and reliable computational methods.

4 OT in Causal Inference

Optimal transport (OT) is a powerful tool for estimating causal effects in various counterfactual scenarios, where different interventions are assumed to result in different outcomes. By leveraging OT, researchers can compare the probability distributions of an outcome variable under different interventions to estimate causal effects.

For instance, in a study evaluating a new drug's efficacy in treating a particular disease, OT can be used to estimate the probability distributions of the disease's progression in both treatment and control groups. This allows for an assessment of the causal impact of the drug. Moreover, OT can facilitate the exploration of counterfactual scenarios, such as estimating the probability distribution of the disease if an alternative treatment or dosage had been administered.

In this section, we address a significant challenge in causal inference (CI), specifically the Difference in Differences (DiD) method, as discussed by [46].

4.1 Difference in Differences

The Difference in Differences (DiD) method is widely used in econometrics and social sciences to estimate the impact of an intervention by comparing the changes in outcomes between a treatment group and a control group over time. Specifically, it compares the outcome change in the treatment group before and after the intervention to the outcome change in the control group over the same period [19].

For example, consider a government policy aimed at reducing smoking rates, implemented in some regions (treatment group) but not others (control group). To measure the policy's effect, one would compare the change in smoking rates between the two groups before and after the policy's implementation. A significant difference in these changes can be attributed to the policy.

DiD relies on careful selection of treatment and control groups and assumes no other factors influence the outcome besides the intervention. This method is prevalent in policy evaluation, health economics, and labor economics [48].

4.2 DiD Model

The DiD model is expressed as

$$Y_{it} = \alpha + \beta T_i + \gamma (Post_t \times T_i) + \delta X_{it} + \epsilon_{it}, \tag{27}$$

where:

- Y_{it} is the outcome variable for individual i at time t,
- T_i is a treatment indicator (1 if individual i receives the treatment, 0 otherwise),
- $Post_t$ is a post-treatment indicator (1 if time t is after the treatment, 0 otherwise),
- X_{it} is a vector of control variables,
- α is the intercept,
- β is the average treatment effect (ATE),
- γ is the difference-in-differences (DiD) estimator,
- δ is a vector of coefficients for the control variables,
- ϵ_{it} is the error term.

Figure 2 visualizes the DiD model, where $Y_{11,N}$ represents the counterfactual outcome of Y_{11} in the absence of treatment. The goal is to estimate the average treatment effect (d_1) by analyzing the treated and control units. A key assumption is the Parallel Trends Assumption, which posits that, in the absence of treatment, the treatment and control groups would have followed similar trends. This assumption is crucial for valid DiD analysis, as it helps eliminate confounding factors and isolate the treatment effect [3]:

$$\mathbb{E}\{Y_{11} - Y_{11,N}\} = (\mathbb{E}\{Y_{11}\} - \mathbb{E}\{Y_{10}\}) - (\mathbb{E}\{Y_{01}\} - \mathbb{E}\{Y_{00}\}).$$

While classical DiD focuses on aggregate outcomes, it may not capture individual heterogeneity-where different individuals may respond differently to the same treatment due to factors like genetics, age, or health status. Ignoring this variability can lead to biased estimates and an incomplete understanding of the treatment's impact. To address this, [3] introduced the Changes in Changes (CiC) estimator:

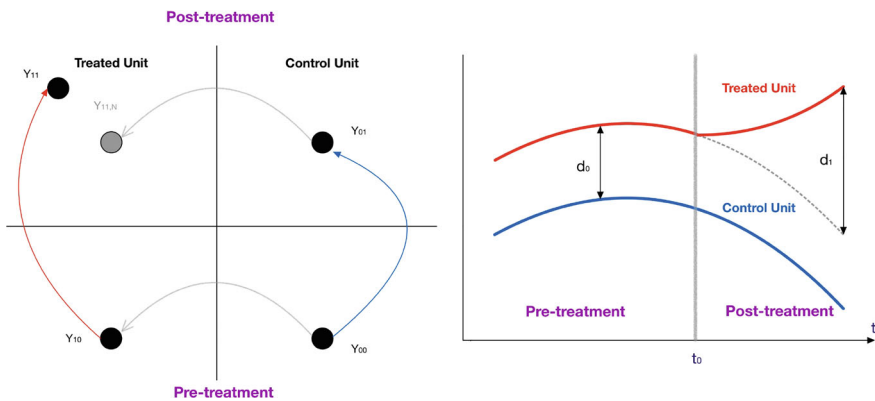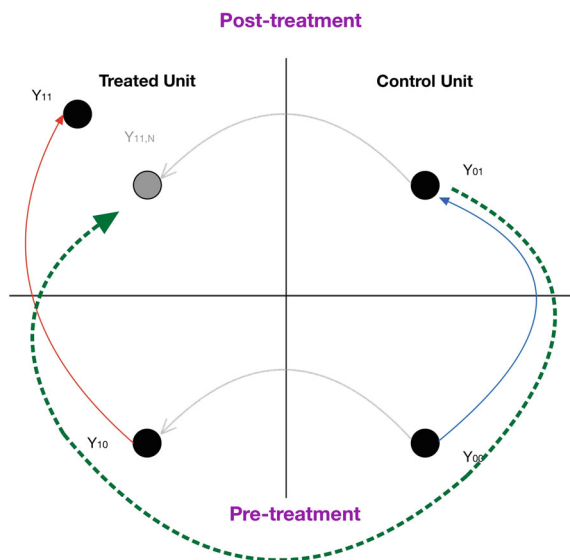$$F_{Y_{11,N}}(y) = F_{Y_{10}}\left(F_{Y_{00}}^{-1}(F_{Y_{01}}(y))\right). \tag{28}$$

Fig. 2 Treatment effect in the DiD model

Fig. 3 Estimation path in the CiC estimator

Incorporating individual heterogeneity, as in the CiC method, allows for a more comprehensive analysis of the treatment's true effect, providing insights into subpopulations that may benefit differently from the intervention. As demonstrated in Fig. 3, the CiC method estimates the path from the post-treatment outcome of the control unit to the counterfactual post-treatment outcome of the treated unit by examining their observed distributions in the pre-treatment state. This extends the DiD approach beyond the average point of view to incorporate a broader perspective that considers each case and condition by analyzing probability distributions. In essence, classical univariate OT has been utilized as a result of this DiD extension.

4.3 Multivariate CiC

As discussed by [46], the current version of the CiC estimator is limited to univariate outcomes due to its reliance on quantile function definitions. This limitation is particularly problematic in scenarios with multivariate outcomes, such as in digital marketing or gene knockdown experiments, where correlations between variables are crucial.

To address these limitations, [46] propose a multivariate extension of the CiC estimator using optimal transport theory. This approach leverages OT maps to generalize the "parallel trends" assumption to multivariate settings via co-monotonicity.

4.3.1 Multivariate Model

This subsection provides a technical overview of the canonical model underlying the classical difference-in-differences and changes-in-changes estimators, as illustrated in Fig. 4. The model is centered around a stochastic process Y_t, $t = 0, 1$ that operates in two time periods: before the intervention ($t = 0$) and after the intervention ($t = 1$). The outcome of interest, modeled as a stochastic process, has a distribution at each time point denoted by μ_t. For simplicity, Y_t is assumed to be a scalar, though the broader aim of this paper is to extend the model to multidimensional cases. Thus, Y_t is considered a latent variable $U_t \in \mathbb{R}$, which may vary over time while its distribution ν remains constant. This latent variable U_t encapsulates unobserved intrinsic characteristics of the unit under study, such as genetic or educational background.

The stochastic process (Y_t) evolves differently depending on whether the unit is in the control group or the treatment group. In the control group, the process experiences only a natural drift that accounts for time-dependent variations unrelated to the intervention. In the treatment group, however, the process is influenced by both the natural drift and the treatment effects. The main goal is to disentangle these two effects. The following items describe models for each of these processes:

- The Natural Drift Model:
  To model of the natural drift of a stochastic process $\{Y_t\}_t$ from the pre-intervention period ($t = 0$) to the post-intervention period ($t = 1$) without any treatment, two
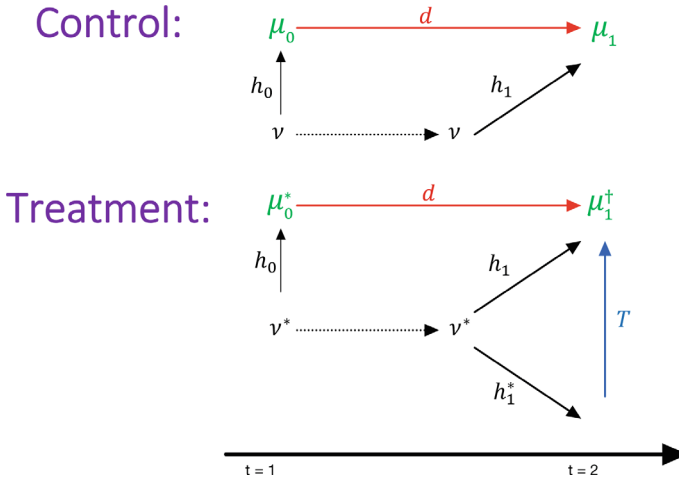

Fig. 4 This image shows a set of maps that exist within the realm of measures. The use of an arrow indicates the implementation of a pushforward map, as seen in the case of $\mu_1 = d_\# \mu_0$. A broken arrow represents a pushforward map that preserves the original measure. Included in these maps are the natural drift map, denoted by d, and the map used to convert actual outcomes to hypothetical ones, labeled T. The data collected for analysis comes from four distinct measures, which are color-coded in *green* ([46, Fig. 1])

production functions, h_t, are postulated, such that $Y_t = h_t(U_t)$. We assume that the distribution μ_t of Y_t is the pushforward of ν by h_t resulting in $\mu_t = (h_t)_{\#}\nu$. If h_0 is invertible, we get $\nu = (h_0^{-1})_{\#}\mu_0$, which allows us to write $\mu_1 = (h_1 \circ h_0^{-1})_{\#}\mu_0 =:$ $\mathsf{d}_{\#}\mu_0$, where $\mathsf{d} = h_1 \circ h_0^{-1}$ is the natural drift map.

Identifying the natural drift map when working with uncoupled data, where independent copies of Y_0 and Y_1 are observed, is challenging. A common approach is to impose additional assumptions on the function d and estimate it using multi-variable regression with coupled observations. For example, d can be identified if it is monotonic with a known direction of monotonicity. Other methods include assuming that copulas between distributions remain the same or that the pointwise differences between corresponding cumulative distribution functions are equal. However, the optimal transport approach offers a more general method for extending the parallel trends assumption to multivariate settings, requiring only that h_0 and h_1 be co-monotone, meaning they move roughly in the same direction.

- The Treatment Model:

Estimating the treatment effect can be complicated by differences in the distribution of units in the treatment group compared to the control group. To address this, the model assumes latent variables $U_0^{\star}$ and $U_1^{\star}$ with a shared time-invariant distribution $\nu^{\star}$, which may differ from ν. The outcome after treatment is denoted by $Y_1^{\star} = h_1^{\star}(U_1^{\star})$, where $h_1^{\star}$ is an unknown production function. The "fundamental problem of causal inference" arises because the counterfactual outcome $Y_1^{\dagger} = h_1(U_1^{\star})$ is unobserved, making the treatment effect difficult to estimate.

To overcome this challenge, the potential outcomes framework is used to estimate the counterfactual $Y_1^{\dagger}$. By estimating the natural drift map d using control group data, the distribution $\mu_1^{\dagger}$ of $Y_1^{\dagger}$ can be estimated. Linear treatment effects, such as the Average Treatment Effect on the Treated (ATT), can then be estimated using this distribution. Nonlinear effects, like the Quantile Treatment Effect (QTE), can be estimated under the assumption that the production function $h_1^{\star}$ is increasing. Brenier's theorem from optimal transport is used to obtain the unique monotone map that produces the QTE. However, in practice, the production function $h_1^{\star}$ is often not monotonically increasing, making the model potentially unidentifiable without further assumptions. The theory of optimal transport is used as a promising framework for extending this model to higher dimensions.

4.4 Estimator

This section interprets the CiC estimator using optimal transport theory, extending its application to multivariate settings. The identifiability of the causal model presented earlier relies on the uniqueness of the increasing map d and potentially the map T for estimating nonlinear treatment effects. This uniqueness is supported by Brenier's theorem [7], a key result in optimal transport theory. Brenier's theorem ensures that among all maps T such that $Q = T_{\#}P$ for given probability measures P and Q defined

on $\mathbb{R}^d$, where P is absolutely continuous with respect to the Lebesgue measure, the unique Brenier map is the gradient of a convex function. Additionally, the optimal transport problem has a unique solution $\bar{\gamma}$ such that $(X, Y) \sim \bar{\gamma}$ if and only if $X \sim P$ and $Y = \bar{T}(X)$ almost surely. For $d = 1$, non-decreasing maps correspond to gradients of convex functions. Thus, the map d is identifiable if it is increasing, which is guaranteed when the production functions h_0 and h_1 are monotone or co-monotonic.

Building on this idea, extending the DiD framework and CiC estimator to higher-dimensional contexts is straightforward. In multivariate settings, monotonicity is generalized through the production functions h_0, h_1, and potentially $h_1^\star$, followed by identifying an appropriate estimator consistent with the model using optimal transport theory. In higher dimensions, cyclic monotonicity is used, where a map $T : \mathbb{R}^d \to \mathbb{R}^d$ is cyclically monotone if

$$\sum_{i=1}^m \|u_i - T(u_{i+1})\|^2 \le \sum_{i=1}^m \|u_i - T(u_i)\|^2,$$

holds for any cycle $u_1, \ldots, u_m$, with $u_{m+1} = u_1$, in the domain. The concept of cyclic co-monotonicity extends the co-monotone assumption in the one-dimensional case, defined by

$$\langle u_1 - u_2, T(u_1) - T(u_2) \rangle \ge 0, \tag{29}$$

which drives identifiability. Therefore, two production functions h_0 and h_1 are cyclically co-monotone if

$$\sum_{i=1}^m \langle h_0(u_i), h_1(u_{i+1}) - h_1(u_i) \rangle \ge 0, \tag{30}$$

for any cycle $u_1, \ldots, u_m, u_{m+1} = u_1$ in their domain. This implies that the map $\mathsf{d} = h_1 \circ h_0^{-1}$ is cyclically monotone, which is unique and identifies the Brenier map $\mu_1 = \mathsf{d}_\# \mu_0$. Although cyclic co-monotonicity provides a technical solution, it lacks interpretability, making it important to find assumptions that ensure identifiability based solely on the co-monotonicity condition.

4.4.1   Multivariate Estimator

For the purpose of achieving identification of the natural generalization of the CiC estimator via optimal transport, they leverage existing literature on truthfulness in mechanism design. Particularly, a theorem on cyclic monotonicity and monotonicity is used:

Theorem 2 ([39]) *If K and F are convex and finite subsets of $\mathbb{R}^d$ respectively, a function $T : K \to F$ is cyclically monotone if and only if it is monotone.*

While the two conditions are typically distinct, they become equivalent when the map is restricted to a finite set of values. This assumption limits the model to situations where the post-intervention distribution μ_1 has a finite support. Although the size of the support can be arbitrarily large, this assumption is effectively irrelevant and can be explained by numerical precision. For small support sizes, it may even act as a statistical regularizer and benefit the estimation process.

Based on the previous subsection and Fig. 4, it is possible to establish a new causal model that facilitates the identification of the counterfactual distribution. The model assumes that the observed data is derived from four distributions defined on $\mathbb{R}^d$, namely $\mu_0, \mu_1, \mu_0^\star$, and $\mu_1^\star$. Additionally, the model assumes the existence of production functions h_0, h_1, and $h_1^\star$, along with latent distributions ν and $\nu^\star$ also defined on $\mathbb{R}^d$. Specifically, $\mu_0, \mu_1, \mu_0^\star$, and $\mu_1^\star$ are given by $(h_0)_{\#}\nu, (h_1)_{\#}\nu, (h_0)_{\#}\nu^\star$, and $(h_1^\star)_{\#}\nu^\star$, respectively. Ultimately, the model aims to estimate the counterfactual distribution $\mu_1^\dagger = (h_1)_{\#}\nu^\star$.

Consider the following five assumptions in the context of the Multivariate CiC estimator:

- The measures μ_0 and $\mu_0^\star$ must be supported on a convex set K_0 and $K_0^\star$, respectively, and be absolutely continuous with respect to the Lebesgue measure.
- The measures μ_1 and $\mu_1^\dagger$ should be supported on finite sets F_1 and $F_1^\dagger$, respectively.
- h_0 and h_1 must be co-monotone, and $h_1 \circ h_0^{-1}$ must be a well-defined function.
- h_0 and $h_1^\star$ should be co-monotone, and $h_1^\star \circ h_0^{-1}$ should also be a well-defined function.
- $\mu_1^\star$ should be sustained on a convex set $K_1^\star$.

The main theorem of the Multivariate CiC estimator can now be stated professionally:

Theorem 3 ([46, Theorem 2]) *By first three assumtions, a unique map* $\mathsf{d} : K_0^\star \to F_1^\dagger$ *exists such that* $\mu_1^\dagger = \mathsf{d}_{\#}\mu_0^\star$. *This map is identified as the Brenier map from* μ_0 *to* μ_1. *Moreover, if last two assumptions also hold, a unique map* $\mathsf{T} : K_1^\star \to F_1^\dagger$ *such that* $\mu_1^\dagger = \mathsf{T}_{\#}\mu_1^\star$ *exists. This map is identified as the Brenier map from* $\mu_1^\star$ *to* $\mu_1^\dagger = \mathsf{d}_{\#}\mu_0^\star$.

4.5 Simulation: Multivariate OT-CiC Estimator

The study underscores the efficacy of the proposed approach in estimating joint counterfactual distributions through the use of synthetic data. Specifically, the results demonstrate the inadequacy of the CiC estimator's tensorization in capturing the dependence structure. On the other hand, the use of an optimal transport-based methodology successfully recovers the authentic counterfactual marginals of the linear production functions in $\mathbb{R}^2$.

The experiment was conducted by considering $n = 3000$ units in $\mathbb{R}^2$ for each treatment arm. Samples of latent variables were drawn from the distribution ν at two time points ($t = 0, 1$) to mimic natural drift, while draws from $\nu^\star$ were kept fixed

for counterfactual validation purposes. For controls, the first coordinate of ν is distributed according to $\mathsf{Beta}(3, 2)$ and the second coordinate according to $\mathsf{Beta}(2, 3)$; for treatments, the first coordinate of $\nu^{\star}$ is distributed according to $\mathsf{Beta}(2, 3)$ and the second coordinate according to $\mathsf{Beta}(3, 2)$. A set of production functions was considered, namely $h_0(u) = \begin{bmatrix} 1 & \alpha \\ \alpha & 1 \end{bmatrix} u$ and $h_1(u) = \begin{bmatrix} 1 & -\alpha \\ -\alpha & 1 \end{bmatrix} u$, and it was showed that these linear production functions are co-monotone but not element-wise monotone as required by the CiC estimator. n independent samples from each of the distributions μ_0, μ_1 and $\mu_0^{\star}$ were generated, as well as samples from the true counterfactual distribution $\mu_1^{\dagger}$ for validation purposes. To estimate the transport map d, an optimal plan was first computed using observed data and rounded it to an optimal transport map. This map is only defined on the data from μ_0. To predict counterfactuals treatment on data from $\mu_0^{\star}$, nearest neighbor interpolation was employed, which performed sufficiently well due to the fact that the Beta distribution is supported on [0, 1] for all parameter choices, ensuring that μ_0 and $\mu_0^{\star}$ have identical support in this example. In particular, the results showed that the OT based estimator remained close to the true counterfactual distribution while the naive tensorization of CiC may depart significantly.

The presented results showcase the effectiveness of the kernel density estimator (KDE) in determining the counterfactual joint distribution, as evidenced in Fig. 5, along with the recovered marginals depicted in Fig. 6. It is observed that CiC recovers a joint distribution with the correct shape, albeit oriented in an incorrect direction within the $\mathbb{R}^2$ framework. The authors also conducted empirical CDF (eCDF) computations for their 3000 genuine counterfactual observations, as well as the counterfactuals generated by the two methods, across a uniform mesh consisting of 10,000 points. Figure 7 provides a visual representation of the almost perfect eCDF recovery via OT. The results indicate that OT has an order of magnitude smaller Mean Absolute Difference (MAD) over each mesh point, with a smaller standard deviation, further highlighting its superiority over other methods.
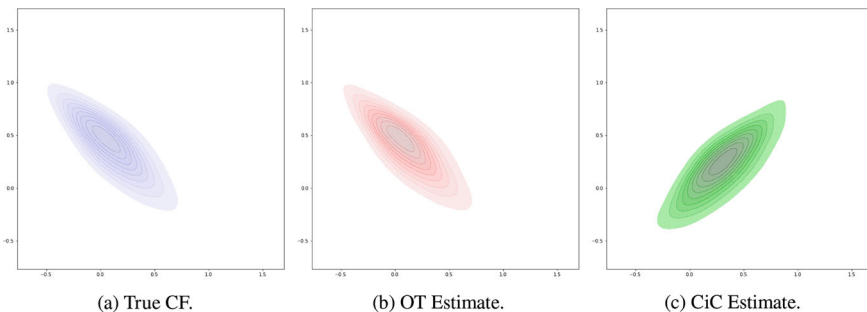

(a) True CF.   (b) OT Estimate.   (c) CiC Estimate.

Fig. 5 The distribution of counterfactual outcomes for the treated is presented through KDE plots, where the first covariate is represented on the horizontal axis and the second on the vertical axis. The KDE bandwidth is set at 0.5 ([46, Fig. 3])
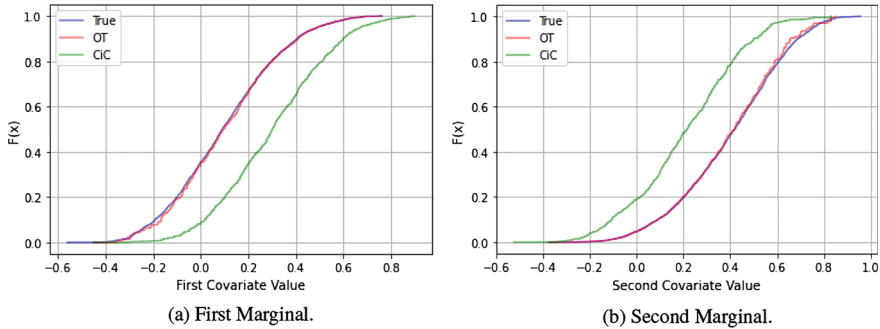
(a) First Marginal. (b) Second Marginal.

Fig. 6 The recuperation of counterfactual marginals through employment of OT and CiC ([46, Fig. 2])
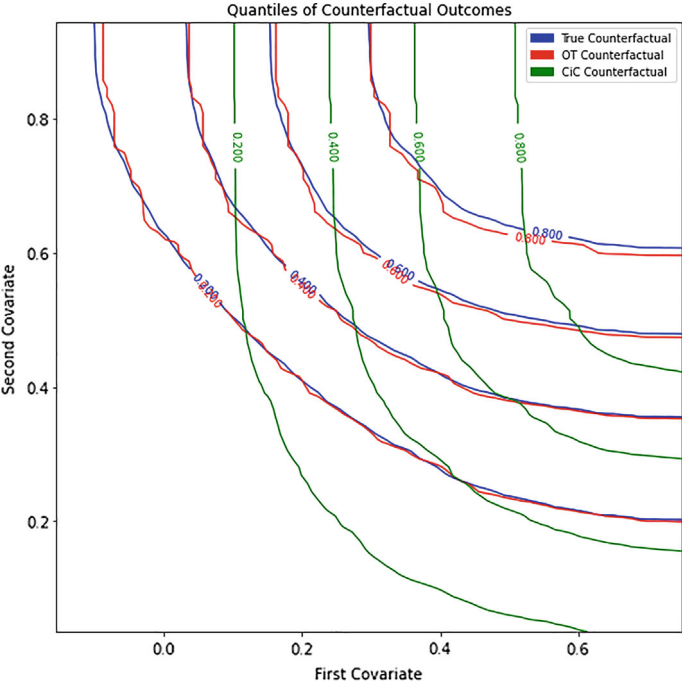

Fig. 7 The quantiles of the eCDF have been calculated over a uniformly spaced grid consisting of 10,000 points ([46, Fig. 7, arxiv])

5 Conclusion

In conclusion, this chapter provided an in-depth exploration of the optimal transport problem and its significant potential in causal inference. We began by identifying the shortcomings of traditional methods, such as Maximum Likelihood Estimation

(MLE) and Kullback-Leibler (KL) divergence, particularly in scenarios involving non-overlapping supports and high-dimensional mappings in generative models. We then traced the development of the optimal transport problem, from Monge's initial formulation to Kantorovich's dual approach, emphasizing its connection to the Wasserstein distance. The chapter also covered the practical implementation of optimal transport using the Sinkhorn algorithm, highlighting its efficiency and scalability for large-scale applications. Finally, we explored the application of optimal transport in causal inference, with a focus on the Difference in Differences (DiD) method and its extension to the Multivariate Changes in Changes algorithm, demonstrating the versatility and power of optimal transport in addressing complex causal inference challenges.

References

1. Arjovsky, M., Chintala, S., Bottou, L.: Wasserstein generative adversarial networks. In: International Conference on Machine Learning, pp. 214–223. PMLR (2017)
2. Arvanitidis, G., Hansen, L.K., Hauberg, S.: Latent Space Oddity: on the Curvature of Deep Generative Models (2017). arXiv:1710.11379
3. Athey, S., Imbens, G.W.: Identification and inference in nonlinear difference-in-differences models. Econometrica **74**(2), 431–497 (2006)
4. Beran, R.: Minimum hellinger distance estimates for parametric models. The Annals of Statistics, pp. 445–463 (1977)
5. Bernton, E., Jacob, P.E., Gerber, M., Robert, C.P.: Inference in generative models using the wasserstein distance **1**(8), 9 (2017). arXiv:1701.05146
6. Bonneel, N., Rabin, J., Peyré, G., Pfister, H.: Sliced and radon wasserstein barycenters of measures. J. Math. Imaging Vis. **51**, 22–45 (2015)
7. Brenier, Y.: Polar factorization and monotone rearrangement of vector-valued functions. Commun. Pure Appl. Math. **44**(4), 375–417 (1991)
8. Carlier, G., Jimenez, C., Santambrogio, F.: Optimal transportation with traffic congestion and wardrop equilibria. SIAM J. Control Optim. **47**(3), 1330–1350 (2008)
9. Chen, J.: Consistency of the MLE under mixture models. Stat. Sci. **32**(1), 47–63 (2017)
10. Courty, N., Flamary, R., Tuia, D.: Domain adaptation with regularized optimal transport. In: Machine Learning and Knowledge Discovery in Databases: European Conference, ECML PKDD 2014, Nancy, France, 15–19 Sept. 2014. Proceedings, Part I 14, pp. 274–289. Springer (2014)
11. Dziugaite, G.K., Roy, D.M., Ghahramani, Z.: Training generative neural networks via maximum mean discrepancy optimization (2015). arXiv:1505.03906
12. Edwards, D.A.: On the kantorovich-rubinstein theorem. Expositiones Mathematicae **29**(4), 387–398 (2011)
13. Eisenberger, M., Toker, A., Leal-Taixé, L., Bernard, F., Cremers, D.: A unified framework for implicit sinkhorn differentiation. In: Proceedings of the IEEE/CVF Conference on Computer Vision and Pattern Recognition, pp. 509–518 (2022)
14. Fajgelbaum, P.D., Schaal, E.: Optimal transport networks in spatial equilibrium. Econometrica **88**(4), 1411–1452 (2020)
15. Feydy, J., Séjourné, T., Vialard, F.X., Amari, S.i., Trouvé, A., Peyré, G.: Interpolating between optimal transport and mmd using sinkhorn divergences. In: The 22nd International Conference on Artificial Intelligence and Statistics, pp. 2681–2690. PMLR (2019)
16. Galichon, A.: A survey of some recent applications of optimal transport methods to econometrics. Econ. J. **20**(2), C1–C11 (2017)

17. Genevay, A., Peyré, G., Cuturi, M.: Learning generative models with sinkhorn divergences. In: International Conference on Artificial Intelligence and Statistics, pp. 1608–1617. PMLR (2018)

18. Goodfellow, I., Pouget-Abadie, J., Mirza, M., Xu, B., Warde-Farley, D., Ozair, S., Courville, A., Bengio, Y.: Generative adversarial nets. Adv. Neural Inf. Process. Syst. **27** (2014)

19. Goodman-Bacon, A.: Difference-in-differences with variation in treatment timing. J. Econ. **225**(2), 254–277 (2021)

20. Govaert, G., Nadif, M.: An EM algorithm for the block mixture model. IEEE Trans. Pattern Anal. Mach. Intell. **27**(4), 643–647 (2005)

21. Gretton, A., Borgwardt, K., Rasch, M., Schölkopf, B., Smola, A.: A kernel method for the two-sample-problem. Adv. Neural Inf. Process. Syst. **19** (2006)

22. Kantorovich, L.V.: On the translocation of masses. In: Dokl. Akad. Nauk. USSR (NS), vol. 37, pp. 199–201 (1942)

23. Karlsson, J., Ringh, A.: Generalized sinkhorn iterations for regularizing inverse problems using optimal mass transport. SIAM J. Imaging Sci. **10**(4), 1935–1962 (2017)

24. Kolouri, S., Park, S.R., Thorpe, M., Slepcev, D., Rohde, G.K.: Optimal mass transport: signal processing and machine-learning applications. IEEE Signal Process. Mag. **34**(4), 43–59 (2017)

25. Komiske, P.T., Metodiev, E.M., Thaler, J.: The hidden geometry of particle collisions. J. High Energy Phys. **2020**(7), 1–53 (2020)

26. Lee, J., Bertrand, N.P., Rozell, C.J.: Unbalanced optimal transport regularization for imaging problems. IEEE Trans. Comput. Imaging **6**, 1219–1232 (2020)

27. Li, C.L., Chang, W.C., Cheng, Y., Yang, Y., Póczos, B.: Mmd gan: towards deeper understanding of moment matching network. Adv. Neural Inf. Process. Syst. **30** (2017)

28. Li, Z., Tao, R., Wang, J., Li, F., Niu, H., Yue, M., Li, B.: Interpreting the latent space of gans via measuring decoupling. IEEE Trans. Artif. Intell. **2**(1), 58–70 (2021)

29. Liu, Y., Jun, E., Li, Q., Heer, J.: Latent space cartography: visual analysis of vector space embeddings. In: Computer Graphics Forum, vol. 38, pp. 67–78. Wiley Online Library (2019)

30. McLachlan, G.J., Lee, S.X., Rathnayake, S.I.: Finite mixture models. Annu. Rev. Stat. Appl. **6**(1), 355–378 (2019)

31. Monge, G.: Mémoire sur la théorie des déblais et des remblais. Mem. Math. Phys. Acad. Royale Sci. 666–704 (1781)

32. Montavon, G., Müller, K.R., Cuturi, M.: Wasserstein training of restricted boltzmann machines. Adv. Neural Inf. Process. Syst. **29** (2016)

33. Nasserinejad, K., van Rosmalen, J., de Kort, W., Lesaffre, E.: Comparison of criteria for choosing the number of classes in bayesian finite mixture models. PloS One **12**(1), e0168838 (2017)

34. Orlin, J.B.: A polynomial time primal network simplex algorithm for minimum cost flows. Math. Program. **78**, 109–129 (1997)

35. Peyré, G., Cuturi, M., et al.: Computational optimal transport: With applications to data science. Found. Trends® Mach. Learn. **11**(5–6), 355–607 (2019)

36. Pollard, C., Windischhofer, P.: Transport away your problems: calibrating stochastic simulations with optimal transport. Nucl. Instrum. Methods Phys. Res. Sect. A: Accel., Spectrometers Detect. Assoc. Equip. **1027**, 166119 (2022)

37. Pollard, D.: Total variation distance between measures. Asymptopia (chap. 3) (2005)

38. Reynolds, D.A. et al.: Gaussian mixture models. Encycl. Biom. **741**(659-663) (2009)

39. Saks, M., Yu, L.: Weak monotonicity suffices for truthfulness on convex domains. In: Proceedings of the 6th ACM conference on Electronic commerce, pp. 286–293 (2005)

40. Salimans, T., Zhang, H., Radford, A., Metaxas, D.: Improving gans using optimal transport (2018). arXiv:1803.05573

41. Shamsi, M.: Non-orthogonal time-frequency space modulation (2023). arXiv:2309.10889

42. Shamsi, M., Ghandi, M., Marvasti, F.: A nonlinear acceleration method for iterative algorithms. Signal Process. **168**, 107346 (2020)

43. Shamsi, M., Marvasti, F.: Enhancing the sefdm performance in high-doppler channels (2023). arXiv:2309.11774

44. Shamsi, M., Marvasti, F.: Acceleration algorithms for iterative methods. In: Sampling, Approximation, and Signal Analysis: Harmonic Analysis in the Spirit of J. Rowland Higgins, pp. 521–552. Springer (2024)
45. Tartavel, G., Peyré, G., Gousseau, Y.: Wasserstein loss for image synthesis and restoration. SIAM J. Imaging Sci. **9**(4), 1726–1755 (2016)
46. Torous, W., Gunsilius, F., Rigollet, P.: An optimal transport approach to causal inference (2021). arXiv:2108.05858
47. Van Havre, Z., White, N., Rousseau, J., Mengersen, K.: Overfitting bayesian mixture models with an unknown number of components. PloS one **10**(7), e0131739 (2015)
48. Villa, J.M.: DIFF: dimplifying the estimation of difference-in-differences treatment effects. Stata J. **16**(1), 52–71 (2016)
49. Villani, C. et al.: Optimal Transport: Old and New, vol. 338. Springer (2009)
50. Waheed, A., Goyal, M., Gupta, D., Khanna, A., Al-Turjman, F., Pinheiro, P.R.: Covidgan: data augmentation using auxiliary classifier GAN for improved covid-19 detection. IEEE Access **8**, 91916–91923 (2020)
51. Wilson, A.G.: The use of entropy maximising models, in the theory of trip distribution, mode split and route split. J. Transp. Econ. Policy 108–126 (1969)
52. Wu, C., Yang, C., Zhao, H., Zhu, J.: On the convergence of the EM algorithm: a data-adaptive analysis (2016). arXiv:1611.00519
53. Wu, C.J.: On the convergence properties of the EM algorithm. Ann. Stat. 95–103 (1983)
54. Zhang, Y., Pan, J., Li, L.K., Liu, W., Chen, Z., Liu, X., Wang, J.: On the properties of kullback-leibler divergence between multivariate gaussian distributions. Adv. Neural Inf. Process. Syst. **36** (2024)

Analysis of a Queueing Model with Catastrophe and First Exceptional Service

Rachna Khurana, Manju Sharma, Shikha Singh, and Archana Singh

Abstract In this paper, we have developed a multiple vacation queuing model which is subject to catastrophe. Catastrophe makes the queue instantly empty and system evolves afresh. An exceptional service is provided to the first customer of each busy period and at the end of each busy period server goes on vacation, while in operation server is also subject to breakdown. This type of systems has numerous applications such as manufacturing processes, computer communication networks and service sectors. The generating function technique is used to derive some important performance measures.

Keywords First exceptional service · Catastrophe · Multiple server vacations · Service breakdown and repair

1 Introduction

Queues with catastrophes are very common in computer networks, where all the files get corrupted due to virus attack and no further task is possible to be taken for service until the problem is resolved. Some time is needed to repair the whole system and first service after repair takes some extra time to accomplish the task. Apart from computer communication networks, this catastrophic situation is also seen in various other real life systems which may be modeled as queues. A sudden road block due to any natural calamity in hilly areas brings traffic to a standstill position and all

R. Khurana (✉)
Department of Mathematics, Sharda School of Basic Sciences and Research, Sharda University Agra, Agra, India
e-mail: rachnaakshaj@gmail.com

M. Sharma
Departmnet of Mathematics, R.B.S. College, Agra, India

S. Singh · A. Singh
Department of Computer Application, Anand Engineering College, Agra, India
e-mail: rachnaakshaj@gmail.com

the vehicles are forced to take u-turn. Biological systems can also be modeled as catastrophic queues in which virus and bacteria bring catastrophe to the immune system. So, catastrophic queues are important to be studied in order to know and improve the performance of the system concerned. A good amount of work in this area has been done by many authors.

Welch [17] introduced the concept of first exceptional customer service of each busy period in M/G/1 queueing system. Using different service distribution functions he obtained queue size, waiting time and waiting-plus-service time. Boucherie et al. [5] studied the effect of negative customer in M/G/1 queue. Li et al. [9] devised recursive method for determining stationary probability of queue length in the M/M/1 queueing model, which is characterized by exceptional service. Baba [3] applied supplementary variable technique for analyzing M/G/1 queue in which first N customers get exceptional service. Gray et al. [8] obtained queue length distribution and mean queue length for a multiple vacation queue model which is subject to break down. Krishna et al. [14] presented transient solution for M/M/1 queue model with the possibility of catastrophes. Kumar et al. [15] analyzed catastrophes and server failures of M/M/1 queue and derived steady-state probabilities. Jain et al. [11] studied M/M/1/N queueing system which experience variable catastrophes. They obtained time dependent as well as steady solutions. Ghimire et al. [7] used generating function technique to find the measures of performance of multiple vacations and breakdowns M/M/1 queues with heterogeneous arrival and departure. Ayyappan et al. [2] deduced probability generating functions for the multiple vacation $M^{[X]}$/G/1 queue with restricted admissibility, breakdowns, and repairs. Begum et al. [4] considered M^x/G/1 queue model where disaster occurs at the time of main server is active. Substitute slow server is replaced at the time main server fails and sent for repair process. Khurana et al. [12, 13] studied extensively M/M/1 multiple vacations, breakdown and repair queue model with first exceptional service then followed by N exceptional service. Deepa et al. [6] found steady-state probabilities of M/M/1/N queueing model with two types of server vacations and working breakdowns using computable matrix technique. Using matrix geometric technique, Indra et al. [10] presented analysis of Geo/Geo/1 model with catastrophes. Shanmugasundaram et al. [16] derived stationary probabilities under steady state of M/G/1 feedback queue. Alshreef [1] presented the solution of a chemical queueing model with catastrophes and server repair and failure.

In this paper, our effort is to study M/M/1queue model which characterizes by catastrophes, multiple vacations, server breakdown, and repair. These types of models have a wide range of applications in real world.

2 Model Description

In this queueing model, we have considered a first exceptional service system with catastrophe which results removal of all the customers from the system. The server may get breakdowns while serving the customers. After repair process, service is

started from the interrupted customer. At the end of each busy period, the server goes on vacation. Exceptional service is provided to every first customer of busy period. The customer arrives in the system with different rates during active service, vacation, and breakdown. The times to break down, repair times, and length of vacation follow exponential distributions.

2.1 Notations and Steady-State Probabilities

λ: Arrival rate at the time of active service

λ_0: Arrival rate at the time of vacations

λ_1: Arrival rate at the time of breakdowns

μ_1: First customer service rate of a busy period

μ_2: Second or following customer service rate of a busy period

v: Server vacation rate

b: Server breakdown rate

r: Server repair rate

α: Catastrophe rate.

$$\rho_0 = \frac{\lambda_0}{\lambda_0 + \alpha + v}$$

$$\lambda_0, \lambda > 0, \lambda_1 \geq 0$$

$$\mu_1, \mu_2, b, , v, r, \alpha > 0$$

Following are the steady-state probabilities of the model.

$P_{o,i}$: The probability that there are i customer in the system and the server has gone on vacation. $i \geq 0$.

$P_{1,i,1}$: The probability that there are i customer in the system at the time of active service and first customer is being served of the busy period. $i \geq 1$.

$P_{1,i,2}$: The probability that there are i customer in the system at the time of active service and second or following customer is being served of the busy period. $i \geq 1$.

$P_{2,i,1}$: The probability of i customer in the system at the time of repair process and the first customer is being served of the busy period. $i \geq 1$.

$P_{2,i,1}$: The probability of i customer in the system at the time of repair process and the second or following customer is being served is of the busy period. $i \geq 1$.

2.2 Normalization Condition

Observing the states of the system, normalization condition is

$$\sum_{i=0}^{\infty} P_{0,i} + \sum_{i=1}^{\infty} (P_{1,i,1} + P_{1,i,2} + P_{2,i,1} + P_{2,i,1}) = 1$$

2.3 Generating Function for the Model

In order to apply generating function technique, we define in this section following partial generating functions:

$$F_0(z) = \sum_{i=0}^{\infty} P_{0,i} z^i,$$

$$F_{1,1}(z) = \sum_{i=1}^{\infty} P_{1,i,1} z^i,$$

$$F_{1,2}(z) = \sum_{i=1}^{\infty} P_{1,i,2} z^i,$$

$$F_{2,1}(z) = \sum_{i=1}^{\infty} P_{2,i,1} z^i,$$

$$F_{2,2}(z) = \sum_{i=1}^{\infty} P_{2,i,2} z^i,$$

Defining the generating function to find queue length distribution:

$$F(z) = F_0(z) + F_{1,1}(z) + F_{1,2}(z) + F_{2,1}(z) + F_{2,2}(z)$$

3 Analysis of Mean Queue Length

Following are the steady-state equations of the proposed model for the subsequent analysis:

$$(\lambda_0 + \alpha)P_{0,0} = \mu_1 P_{1,1,1} + \mu_2 P_{1,1,2} \tag{1}$$

$$(\lambda_0 + \alpha + \nu)P_{0,i} = \lambda_0 P_{0,i-1}, \ i \geq 1 \tag{2}$$

$$(\lambda + \mu_1 + b + \alpha)P_{1,1,1} = \nu P_{0,1} + r P_{2,1,1}, \tag{3}$$

$$(\lambda + \mu_2 + b + \alpha)P_{1,1,2} = \mu_1 P_{1,2,1} + \mu_2 P_{1,2,2} + r P_{2,1,2}, \tag{4}$$

$$(\lambda + \mu_1 + b + \alpha)P_{1,i,1} = \lambda P_{1,i-1,1} + \nu P_{0,i} + r P_{2,i,1}, \ i \geq 2 \tag{5}$$

$$(\lambda + \mu_2 + b + \alpha)P_{1,i,2} = \lambda P_{1,i-1,2} + \mu_1 P_{1,i+1,1} + \mu_2 P_{1,i+1,2} + r P_{2,i,2}, \ i \geq 2 \tag{6}$$

$$(\lambda_1 + r + \alpha)P_{2,1,1} = b P_{1,1,1} \tag{7}$$

$$(\lambda_1 + r + \alpha)P_{2,1,2} = b P_{1,1,2} \tag{8}$$

$$(\lambda_1 + r + \alpha)P_{2,i,1} = \lambda_1 P_{2,i-1,1} + b P_{1,i,1} \ i \geq 2 \tag{9}$$

$$(\lambda_1 + r + \alpha)P_{2,i,2} = \lambda_1 P_{2,i-1,2} + b P_{1,i,2} \ i \geq 2 \tag{10}$$

(i) **The Generating Function**

Now, utilizing the generating function method, we obtain from Eq. (2)

$$F_0(z) = \sum_{i=0}^{\infty} P_{0,i} z^i = \frac{P_{0,0}}{1 - \rho_0 z}, \tag{11}$$

We obtain from Eqs. (3) and (5)

$$(\lambda + \mu_1 + b + \alpha - \lambda z)F_{1,1}(z) = \nu[F_0(z) - P_{0,0}] + r F_{2,1}(z) \tag{12}$$

Equations (4) and (6) give us

$$(\lambda + \mu_2 + b + \alpha - \lambda z)F_{1,2}(z) = \frac{\mu_1}{z}F_{1,1}(z) + \frac{\mu_2}{z}F_{1,2}(z)$$
$$+ rF_{2,2}(z) - \{(\lambda_0 + \alpha)P_{0,0} - \alpha\} \qquad (13)$$

From Eqs. (7) and (10), we get

$$F_{2,1}(z) = \frac{b}{\lambda_1 + r + \alpha - \lambda_1 z}F_{1,1}(z) \qquad (14)$$

From Eqs. (8) and (10), we get

$$F_{2,2}(z) = \frac{b}{\lambda_1 + r + \alpha - \lambda_1 z}F_{1,2}(z) \qquad (15)$$

Utilizing Eqs. (14) in (12)

$$(\lambda + \mu_1 + b + \alpha - \lambda z)F_{1,1}(z) = \nu\left[F_0(z) - P_{0,0}\right] + \frac{rb}{\lambda_1 + r + \alpha - \lambda_1 z}F_{1,1}(z)$$

$$\left(\lambda + \mu_1 + b + \alpha - \lambda z - \frac{rb}{\lambda_1 + r + \alpha - \lambda_1 z}\right)F_{1,1}(z) = \nu\left(\frac{1}{1 - \rho_0 z} - 1\right)P_{0,0}$$

$$F_{1,1}(z) = \frac{\nu P_{0,0}\rho_0 z}{A(1 - \rho_0 z)} \qquad (16)$$

Similarly, using (15) in (13)

$$\begin{pmatrix} \lambda + \mu_2 + b + \alpha - \lambda z \\ -\frac{\mu_2}{z} - \frac{rb}{\lambda_1 + r + \alpha - \lambda_1 z} \end{pmatrix}F_{1,2}(z) = \frac{\mu_1}{z}\frac{\nu P_{0,0}\rho_0 z}{A(1 - \rho_0 z)}$$
$$- \{(\lambda_0 + \alpha)P_{0,0} - \alpha\}$$

$$\left(\lambda + \mu_2 + b + \alpha - \lambda z - \frac{\mu_2}{z} - \frac{rb}{\lambda_1 + r + \alpha - \lambda_1 z}\right)F_{1,2}(z) = \frac{\mu_1}{z}\frac{\nu P_{0,0}\rho_0 z}{A(1 - \rho_0 z)} - \{(\lambda_0 + \alpha)P_{0,0} - \alpha\}$$

$$F_{1,2}(z) = \frac{1}{B}\left[\frac{\mu_1}{z}\frac{\nu P_{0,0}\rho_0 z}{A(1 - \rho_0 z)} - \{(\lambda_0 + \alpha)P_{0,0} - \alpha\}\right] \qquad (17)$$

where

$$A = \lambda + \mu_1 + b + \alpha - \lambda z - \frac{rb}{\lambda_1 + r + \alpha - \lambda_1 z}$$

$$B = \lambda + \mu_2 + b + \alpha - \lambda z - \frac{\mu_2}{z} - \frac{rb}{\lambda_1 + r + \alpha - \lambda_1 z}$$

Generating function $F(z)$ using (11), (16), and (17)

$$F(z) = \frac{P_{0,0}}{1 - \rho_0 z} + \left(1 + \frac{b}{\lambda_1 + r + \alpha - \lambda_1 z}\right)\left(F_{1,1}(z) + F_{1,2}(z)\right)$$

where

$$F_{1,1}(z) + F_{1,2}(z) = \frac{\nu P_{0,0}\rho_0 z}{A(1 - \rho_0 z)} + \frac{1}{B}\left[\frac{\mu_1}{z}\frac{\nu P_{0,0}\rho_0 z}{A(1 - \rho_0 z)} - \{(\lambda_0 + \alpha)P_{0,0} - \alpha\}\right]$$

(18)

Using $F(1) = 1$ (Normalization condition) for calculating $P_{0,0}$

$$\left[F_0(z) + F_{1,1}(z) + F_{1,2}(z) + F_{2,1}(z) + F_{2,2}(z)\right]_{z=1} = 1$$

$$\frac{P_{0,0}}{1 - \rho_0} + \left(1 + \frac{b}{r + \alpha}\right)\left(F_{1,1}(1) + F_{1,2}(1)\right) = 1$$

$$\frac{P_{0,0}}{1 - \rho_0} + \left(1 + \frac{b}{r + \alpha}\right)\left(\frac{\nu P_{0,0}\rho_0}{A(1 - \rho_0)} + \frac{1}{B}\left[\frac{\mu_1 \nu P_{0,0}\rho_0}{A(1 - \rho_0)} - \{(\lambda_0 + \alpha)P_{0,0} - \alpha\}\right]\right) = 1$$

After simplification, we get

$$P_{0,0} = \frac{-\frac{\alpha}{B'}\left(1 + \frac{b}{r+\alpha}\right) - \frac{\alpha}{B}\left(\frac{b\lambda_1}{(r+\alpha)^2}\right)}{\frac{\rho_0}{(1-\rho_0)^2} + \frac{b\lambda_1}{(r+\alpha)^2}R + \left(1 + \frac{b}{r+\alpha}\right)S}$$

At $z = 1$

$$A = \mu_1 + b + \alpha - \frac{rb}{r + \alpha}$$

$$B = b + \alpha - \frac{rb}{r + \alpha}$$

$$A' = -\lambda - \frac{rb\lambda_1}{(r + \alpha)^2}$$

$$B' = -\lambda + \mu_2 - \frac{rb\lambda_1}{(r + \alpha)^2}$$

$$R = \frac{\nu\rho_0}{A(1 - \rho_0)} + \frac{1}{B}\left\{\frac{\mu_1 \nu\rho_0}{A(1 - \rho_0)} - \lambda_0 - \alpha\right\}$$

$$S = \frac{\nu\rho_0}{A(1 - \rho_0)^2} + \frac{\nu\rho_0}{A'(1 - \rho_0)}$$

$$+ \frac{1}{B'}\left\{\frac{\mu_1 \nu \rho_0}{A(1 - \rho_0)} - \lambda_0 - \alpha\right\}$$

$$+ \frac{\mu_1 \nu \rho_0}{B(1 - \rho_0)}\left\{\frac{\rho_0}{A(1 - \rho_0)} + \frac{1}{A'(1 - \rho_0)}\right\}$$

(ii) Mean Queue Length

In this section, F′(1) is used to calculate the mean queue length.

$$L = \left.\frac{dF(z)}{dz}\right|_{z=1} = \frac{\rho_0 P_{0,0}}{(1 - \rho_0)^2} + \left(1 + \frac{b}{r + \alpha}\right)\frac{d}{dz}\big[F_{1,1}(z) + F_{1,2}(z)\big]_{z=1}$$

$$+ \frac{b\lambda_1}{(r + \alpha)^2}\big[F_{1,1}(1) + F_{1,2}(1)\big]$$

where

$$F_{1,1}(1) = \frac{\nu P_{0,0}\rho_0}{\left(\mu_1 + b + \alpha - \frac{rb}{r+\alpha}\right)(1 - \rho_0)}$$

$$F_{1,2}(1) = \frac{1}{\left(b + \alpha - \frac{rb}{r+\alpha}\right)}\left[\frac{\mu_1 \nu P_{0,0}\rho_0}{\left(\mu_1 + b + \alpha - \frac{rb}{r+\alpha}\right)(1 - \rho_0)} - \left\{(\lambda_0 + \alpha)P_{0,0} - \alpha\right\}\right]$$

$$\left.\frac{d}{dz}F_{1,1}(Z)\right|_{z=1} = \frac{\nu P_{0,0}\rho_0}{\left(\mu_1 + b + \alpha - \frac{rb}{r+\alpha}\right)(1 - \rho_0)} + \frac{\nu P_{0,0}\rho_0^2}{\left(\mu_1 + b + \alpha - \frac{rb}{r+\alpha}\right)(1 - \rho_0)^2}$$

$$+ \frac{\nu P_{0,0}\rho_0\left(\lambda + \frac{rb\lambda_1}{(r+\alpha)^2}\right)}{\left(\mu_1 + b + \alpha - \frac{rb}{r+\alpha}\right)^2(1 - \rho_0)}$$

$$\left.\frac{d}{dz}F_{1,2}(Z)\right|_{z=1} = -\frac{\left(-\lambda + \mu_2 - \frac{rb\lambda_1}{(r+\alpha)^2}\right)}{\left(b + \alpha - \frac{rb}{r+\alpha}\right)^2}\left[\begin{array}{c}\dfrac{\mu_1 \nu P_{0,0}\rho_0}{\left(\mu_1 + b + \alpha - \frac{rb}{r+\alpha}\right)(1 - \rho_0)} \\ -\left\{(\lambda_0 + \alpha)P_{0,0} - \alpha\right\}\end{array}\right]$$

$$+ \frac{1}{\left(b + \alpha - \frac{rb}{r+\alpha}\right)}\left[\begin{array}{c}\dfrac{\mu_1 \nu P_{0,0}\rho_0\left(\lambda + \frac{rb\lambda_1}{(r+\alpha)^2}\right)}{\left(\mu_1 + b + \alpha - \frac{rb}{r+\alpha}\right)^2(1 - \rho_0)} \\ + \dfrac{\mu_1 \nu P_{0,0}\rho_0^2}{\left(\mu_1 + b + \alpha - \frac{rb}{r+\alpha}\right)(1 - \rho_0)^2}\end{array}\right]$$
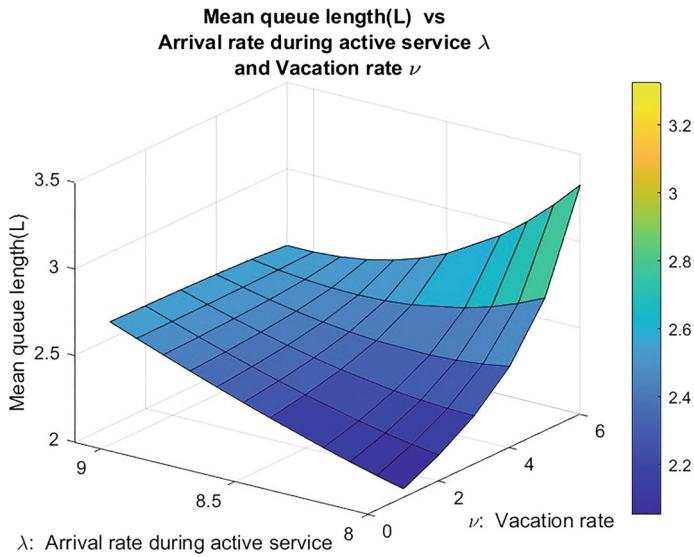
4 Numerical Illustrations

Fig. 4.1 3D Plot of mean queue length (L) versus arrival rate during active service (λ) and vacation rate (v)
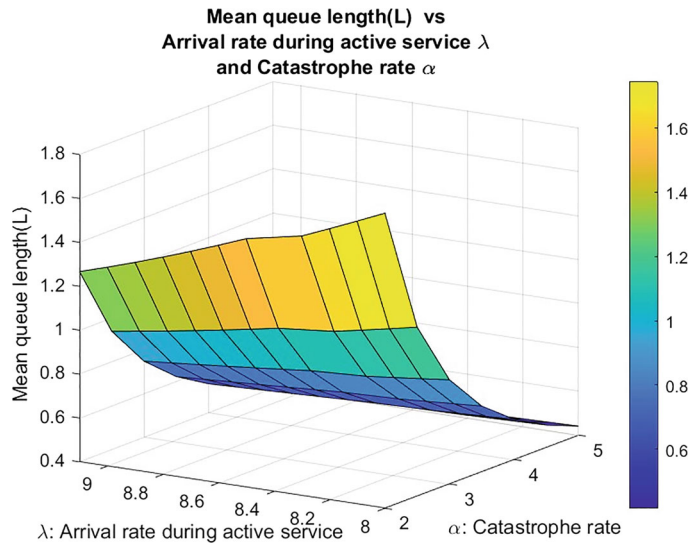
Fig. 4.2 3D Plot of mean queue length (L) versus arrival rate during active service (λ) and castastrophe rate (α)
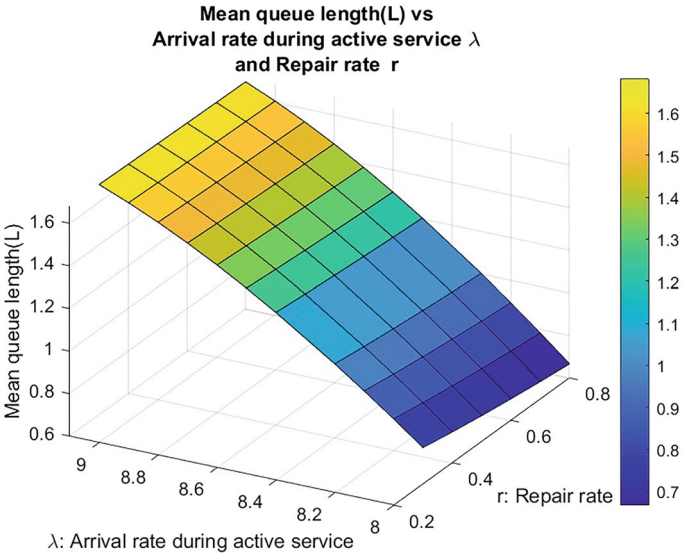
Fig. 4.3 3D Plot of mean queue length (L) versus arrival rate during active service (λ) and repair rate (r)
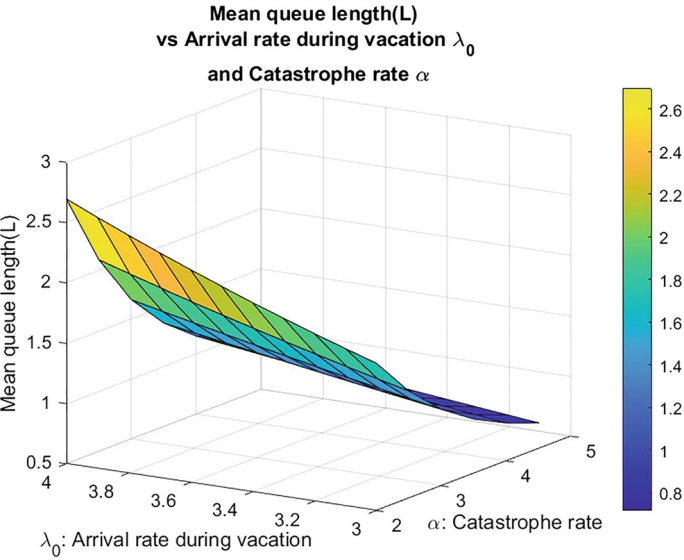
Fig. 4.4 3D Plot of mean queue length (L) versus arrival rate during vacation service (λ_0) and catastrophe rate (α)
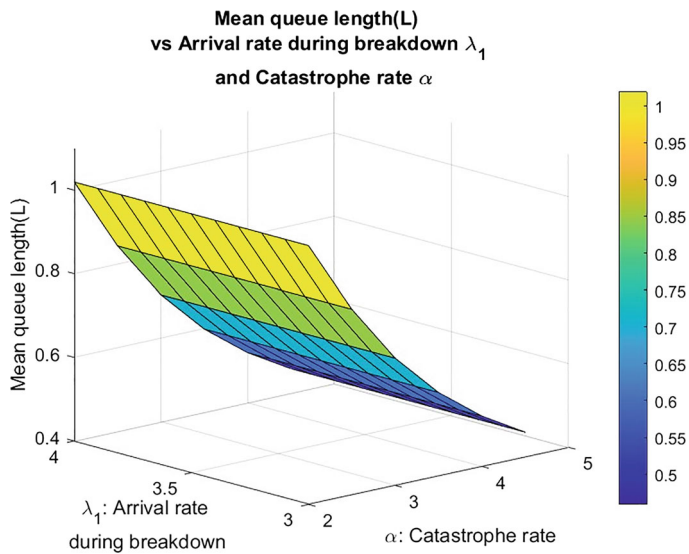
Fig. 4.5 3D Plot of mean queue length (L) versus arrival rate during breakdown (λ_1) and catastrophe rate (α)
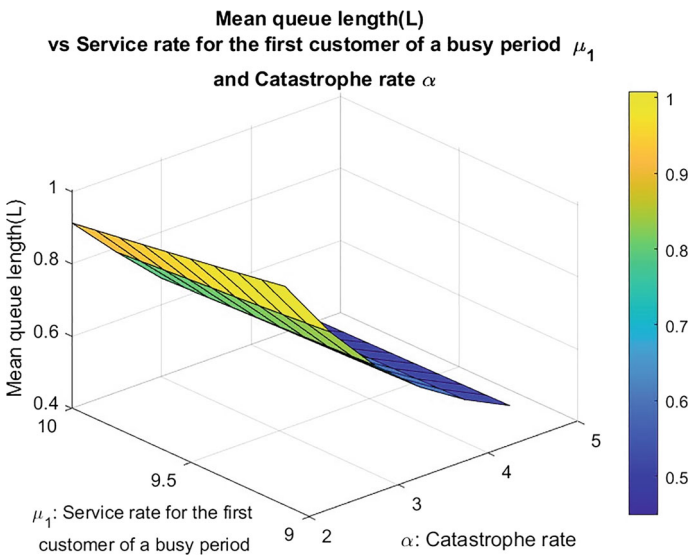
Fig. 4.6 3D Plot of mean queue length (L) versus service rate for the first customer of a busy period (μ_1) and catastrophe rate (α)
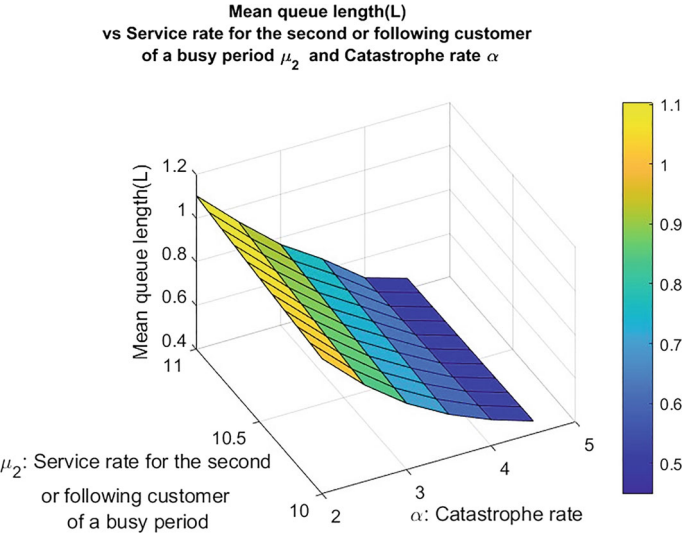
Fig. 4.7 3D Plot of mean queue length (L) versus service rate for the second or following customer of a busy period (μ_2) and catastrophe rate (α)
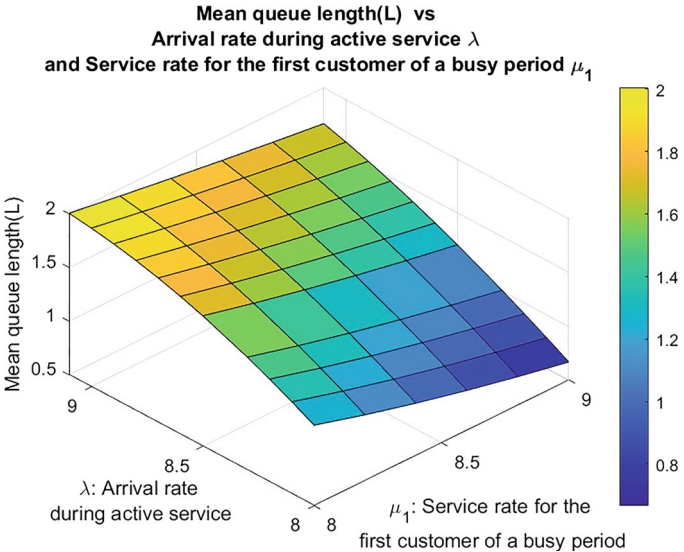
Fig. 4.8 3D Plot of mean queue length (L) versus arrival rate during active service (λ) and service rate for the first customer of a busy period (μ_1)

5 Conclusion

This paper analyzes a multiple vacation queuing system with first exceptional service, catastrophes, breakdowns, and repairs. The steady-state probabilities and mean queue length are found using generating function technique. Further, graph-based numerical analysis has been done using MATLAB. Numerical examples illustrate that MQL decreases in every case as catastrophe rate increases. As normally expected, MQL rises with the rise in arrival rates during active service, vacations, and breakdowns. In the situation of higher vacation rate, repair rate, and service rates during exceptional and normal services, MQL decreases.

References

1. Alshreef, G., Tarabia, A.: Transient analysis of chemical queue with catastrphes and server repair. Inf. Sci. Lett. Int. J. **12**(2), 541–545 (2023)
2. Ayyappan, G., Sathiya, K., Subramanian, A.M.G.: M$^{[X]}$/G/1 queue with two types of service subject to random breakdowns, multiple vacation and restricted admissibility. Appl. Math. Sci. **53**(7), 2599–2611 (2013)
3. Yutaka, B.: On M/G/1 queues with the first N customers of each busy period receiving exceptional service. J. Oper. Res. Soc. Jpn. **42**(4), 490–500 (1999)
4. Afthab, M.I., Begum, P., Fijy, J.P., Bama, S.: Mx/G/1 queue with disasters and working breakdowns. Int. J. Sci. Res. Publ. **6**(4), 275–284 (2016)
5. Boucherie, R.J., Boxma, O.J.: The workload in the M/G/1 queue with work removal. Probab. Eng. Inf. Sci. **10**, 261–277 (1996)
6. Deepa, B., Kalidass, K.: An M/M/1/N queue with working breakdowns and vacations. Int. J. Pure Appl. Math. **119**(10), 859–873 (2018)
7. Ghimire, R.P., Ghimire, S.: Heterogeneous arrival and departure M/M/1queue with vacation and service breakdown. Manag. Sci. Eng. **5**, 61–67 (2011)
8. Gray, W.J., Wang, P.P., Scott, M.K.: A vacation queueing mode with service breakdowns. Appl. Math. Model. **24**, 391–400 (2000)
9. Li, H., Zhu, Y., Yang, P., Madhavapeddy, S.: On M/M/1 queues with a smart machine. Queueing Syst. **24**, 23–36 (1996)
10. Indra, Vijay, R.: Queuing analysis of Geo/Geo/1 queue with catastrophes using Matrix Geometric technique. Int. J. Stat. Appl. Math. **3**(1), 110–114 (2018)
11. Jain, N.K., Singh, B.G.: Transient solution of an M/M/1/N queue subject to uniformly distributed catastrophic intensity with restoration. Int. J. Comput. Sci. Math. **2**(3), 277–283 (2010)
12. Rachna, K., Manju, S.: On a vacation with exceptional first service and server breakdown. J. Sci. Technol. Res. **7**, 8–12 (2017)
13. Rachna, K., Manju, S.: On M/M/1 vacation with exceptional N service and server breakdown. J. Comput. Math. Sci. **10**(5), 1061–1071 (2019)
14. Kumar, K.B., Arivudainambi, D.: Transient solution of an M/M/1 queue with catastrophes. Comput. Math. Appl. **40**, 1233–1240 (2000)
15. Krishna, K.B., Pavai, M.S.: Transient analysis of an M/M/1 queue subject to catastrophes and server failures. Stoch. Anal. Appl. **23**(2), 329–340 (2005)
16. Shanmugasundaram, S., Sivaram, G.: Analysis of M/G/1 feedback queue under steady state when catastrophes occur. Turk. J. Comput. Math. Educ. (TURCOMAT) **12**(1S), 640–646 (2021)
17. Welch, P.D.: On a generalized M/G/1 queueing process in which the first customer of each busy period receives exceptional service. Oper. Res. **12**, 736–752 (1964)

CNN-Based Mathematical Model for Sub-classification of Non-small Cell Lung Cancer into Squamous Cell Carcinoma and Adenocarcinoma

Rajendra Kumar, Aman Anand, Neetu Singh, and Masood Alam

Abstract Lung cancer is an important healthcare concern. It affects gender in different ways and men are at the greatest risk of dying from this cancer, while women are at the second highest risk. In medical science, the process of detection of lung cancer is done using low-dose CT scan (LDCT) images. For this purpose, a patient lies on a thin and flat table sliding back and forth inside a hole in the middle of the Computed Tomography (CT) scanner, which is a large, doughnut-shaped healthcare device. Doing the same using automated systems using artificial intelligence with high accuracy without human involvement is a challenging task. The main objective of this research is to design a Convolutional Neural Network (CNN) model to classify squamous cell carcinoma and adenocarcinoma with high accuracy. Around 85% of lung cancer cases belong to non-small cell lung cancer. Early detection and treatment are important to a patient's recovery. Diagnosing the various kinds of cancers of the lungs is usually a troublesome process that requires time and error. In addition to identifying lung cancer subtypes more accurately and in less time, convolutional neural networks may help in determining patients' right treatment procedures and their survival rates. Despite its complexity, even for experienced pathologists, this area of research can be challenging when it comes to adenocarcinoma and squamous

R. Kumar (✉)
School of Engineering and Technology, Sharda University, Greater Noida, India
e-mail: rajendra04@gmail.com

A. Anand · N. Singh
GL Bajaj Institute of Technology and Management, Greater Noida, India
e-mail: amananand0609@gmail.com

N. Singh
e-mail: drneetusinghmaths@gmail.com

Present Address:
A. Anand
Department of Computer Science and Engineering, ITS Engineering College, Greater Noida, India

M. Alam
Department of Mathematics and IT, Center for Preparatory Studies, Sultan Qaboos University, Muscat, Oman
e-mail: malam@squ.edu.om

cell carcinoma. This chapter proposes a mathematical model and its three-layer CNN implementation for sub-classification of non-small cell lung cancer into squamous cell carcinoma and adenocarcinoma. The proposed system is validated to classify non-small cell lung cancer into squamous cell carcinoma and adenocarcinoma. The model is trained with an accuracy of 96.89% and validated with an accuracy of 93.20%.

1 Introduction

Various mathematical models are designed and implemented for prediction, classification, regression, clustering, etc. Prediction of different cancers, skin diseases, and plant diseases are common examples. Mathematical models include details of layers in the CNN architecture and hyperparameters settings to get better accuracy. Cancer is now becoming the most common disease and lung cancer is the major reason of cancer death worldwide. It is difficult to identify because it appears and manifests symptoms only at the end of the process. Early discovery and treatment of the condition, on the other hand, can minimize the mortality rate and probability [1]. Approximately 7.6 million people worldwide die each year from lung cancer, as per reports by the World Health Organization. Also, in 2030, approximately 17 million people are expected to die from cancer. To diagnose lung cancer, there are different methods available, like MRI, CT, isotopes, and X-rays [2]. The specialists use appropriate tools to analyze images and detect and diagnose lung cancer at various levels of severity. Different laboratory and clinical approaches are used, such as chemical treatments to destroy malignant cells or stop their replications, targeted therapies, and radiotherapy. Patients must endure painful, time-consuming, and expensive treatments in order to identify and detect cancer disorders. To identify and diagnose lung cancer, image processing tools and machine learning approaches were utilized [3]. The aim is to make a CNN model which can recognize lung cancer and distinguish between squamous cell carcinoma and adenocarcinoma.

2 Related Work

Alakwaa et al. [4] presented research regarding the identification and classification of lung cancer, researchers are employing a Three-Dimensional Convolutional Neural Network (3DCNN). Data Science Bowl 2017 patient lung CT scan dataset by Kaggle was used in the research. This dataset comprises labeled data of 1397 persons that is further partitioned into a 978-patient training set and a 419-patient test set. For the model to achieve its full potential and to improve the accuracy of lung cancer

detection, extensive preprocessing techniques are used to generate accurate nodules, and this model presented detailed CNN training from beginning to end. This model produced a test set accuracy of 86.6%. Masood et al. [5] used models for training and evaluating using LIDC and medical datasets for detecting the lung cancer type using an improved RFCN method with multi-layer fusion RPN. Each CT scan set included three hundred slices with a gray-level image of 512×512 pixels, and each slice was 3 mm thick. LIDCIDRI dataset has 1018 CT scan sets in total. The multidimensional and region-based fully connected CNN was applied to construct this model. The accuracy that was achieved by this model is 97.91%.

Perumal et al. [6] detected and classified lung cancer using CT scan images and better Artificial Bee Colony (ABC) optimization. The LIDC dataset, developed by the National Cancer Institute, was used in this model implementation. This model employs the region expand method, the watershed algorithm, and the ABC algorithm. This model achieved very high accuracy. Zhang et al. [7] used a deep CNN for the detection and classification of lung cancer. This model included three datasets for various purposes. The first set of data was collected from the LUNA16 data collection and the second from thoracic CT scans provided by Guangdong Provincial People's Hospital and the third one from 50 surgical dissection patients. CNN is the algorithm used by this model to achieve an accuracy of 84.4%. Hatuwal et al. [8] demonstrated the identification of lung cancer using CNN on histographical images. This work used CNN to classify benign, adenocarcinoma, and squamous cell carcinoma. Here, the author used LC2000 dataset and achieved a training and validation accuracy of 96.11% and 97.20%. Teramoto et al. [9] utilized DCNN to automate lung cancer-type classification based on cytological images. They employed a deep convolutional neural network to classify adenocarcinoma, squamous cell carcinoma, and small cell carcinoma in this case. This work observed 71.1% accuracy on recognition. Asuntha et al. [10] detected and classified cancers based on deep learning. The author used fuzzy particle swarm optimization to pick features. Using the best techniques for feature extraction, they analyzed the data like HOG, wavelet transforms, local binary patterns, scale-invariant feature transform, Zernike moments, and histograms of oriented gradients. This work used LIDC database and got 65.62% accuracy. Makaju et al. [11] developed a technique for detecting lung cancer using CT scan images. This approach detects cancerous nodules in lung CT scan images by classifying nodules as malignant or benign using watershed segmentation and Support Vector Machine (SVM). The dataset used in this study is the image database consortium and this work got an accuracy of 92%. Tekade et al. [12] employed CNN model and trained over lung image database consortium LUNA16. The outcome of this study is to combine two methods as proposed models and U-Net subdivision to get better accuracy of prediction of lung nodule detection and further predicting malignancy levels. This technique provides an accuracy of 95.66% and a loss of 0.09. The model's detection rate was sluggish, which was a disadvantage of this work. Khan et al. [13] developed a technique for convolutional neural networks, to identify lung cancer. In this study, a deep convolution neural network is employed, and LIDC dataset is used. In this research work, the neural networks classified CT scan images of lung nodules as malignant or benign. Thus, before adding input CT

images to the network model, preprocessing was performed to ensure that the pictures were of comparable size and format. DCNN is not suitable for training large-size images because it is hard to train large-size images. Asuntha et al. [10] utilized deep learning algorithms for the detection and classification of lung cancer. This study targeted detecting malignant lung nodules and classifying lung cancer according to severity by analyzing input lung pictures. This study employed exclusive deep-learning methods for determining the position of malignant lung nodules. Here, features were classified using deep learning. An improved version of FPSOCNN, which reduces CNN's computational complexity, is suggested. The main disadvantage of this study is that interpreting CT image slices from a large number of CT scans remains difficult. Nasrullah et al. [14] suggested a technique to detect and classify lung nodules using deep learning in conjunction with a variety of approaches. They used publicly available datasets, such as LUNA16 and LIDC-IDRI, as well as data from hospitals for nodule detection training. The existence of malignant nodules was determined using a 3D lung CT scan. To determine whether nodules were present, lung CT images were first exposed to CMixNet and U-Net-like encoder–decoders. Using 3D CMixNet and GBM, they found nodules were categorized as cancerous. Finally, the DL-based nodule categorization findings were compared to a number of additional criteria, such as the patient's clinical biomarkers, family history, habits, biological behaviors, and location of the discovered nodule. There have been several experiments using the free datasets LUNA16 and LIDC-IDRI.

3   Dataset and Methods

A.   **Datasets**

In this study, LC2500 and LC25000 datasets are used which are taken from Kaggle [15]. LC2500 dataset contains 25,000 colored images which are divided into 5 classes each having 5000 image samples. Every picture is 768×768 in size and is formatted in jpeg. The size of LC25000 dataset is 1.85 GB. The lung colon folder consists of images that comprise two subfolders: lung image sets and colon image sets. The set of colon image subfolder has 2 subfolders: colon_n, which contains 5,000 images of benign colonic tissues, colon_aca, which contains 5,000 photos of colon adenocarcinomas. The set of lung image subfolder comprises 3 secondary subfolders: lung aca, which contains 5,000 lung adenocarcinomas images, lung SCC (Squamous cell carcinoma) images, which contains 5,000 lung squamous cell carcinomas images, and lung_n, which has 5,000 benign lung tissues images. The dataset LC25000 contains 5000 color images of lung squamous cell carcinoma and 5000 colored pictures of lung adenocarcinoma.

B. **Data Preprocessing**

In image preprocessing, the images in this study are cropped to the size of 299 × 299 pixels from 768 × 768 pixels to reduce the background area and 299 × 299 size is suitable for the CNN method. Then the cropped image is used for training and validation dataset on three-layer CNN. During image preprocessing author set the value of rescale as 1/255, shear_range as 0.2, zoom_range as 0.2 and validation_split as 0.2.

The deep learning models outperform classical pattern recognition by extracting features using image processing operations. It is required to use deep learning techniques, otherwise only a set of empirical rules and intuitions can be obtained. The CNN-based solutions include scattering networking [16] and tensor analysis [17]. One more important domain is the selection of size and number of filters in the CNN [18].

C. **Mathematical Modeling**

CNN architecture is utilized and it is shown in Fig. 1. In this methodology, there are three layers, each with its own specification, and each with an increased filter to extract the feature, max pooling to preserve the features, flattening, and kernels of $7 \times 7 \times 7$ dimensions. This model is obtained from a standard CNN by replacing the dense layer with a set of $1 \times 1 \times 1$ convolutional filters.

The proposed CNN is a three-layer architecture. CNN methods are used because they have good capability to extract features in images without complex preprocessing.

Layers of CNN—The first layer is convolutional followed by a pooling layer and the third layer is fully connected which comprises a three-layer CNN.

Convolutional layer—CNN's main building element is the convolution layer. It carries the majority of the computational cost on the network. After convolution, we obtain the shape of an output for more complex filter dimensions. The formulas to get the dimensions are as follows:

Dimension of image $= (n, n)$.
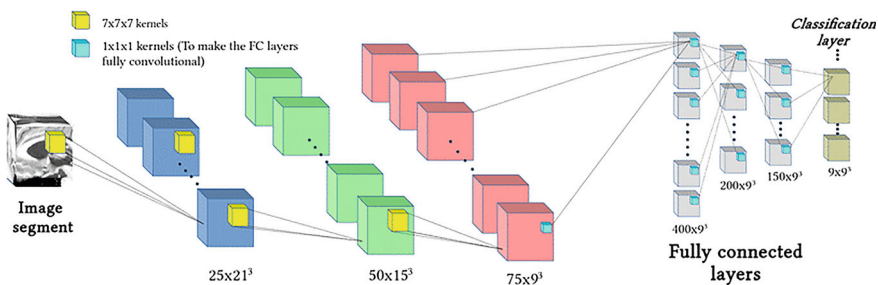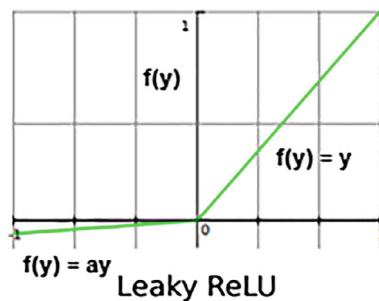Dimension of filter $= (f, f)$ such that $f < n$.

Fig. 1 The three-layer CNN architecture

Fig. 2 Leaky ReLU
activation function

Dimension of output will be $((n - f + 1), (n - f + 1))$.

Pooling layer—By computing a summary statistic of neighboring outputs, the pooling layer replaces network output at certain spots. In turn, this process reduces the size of the representation, which reduces the computational cost and weights required.

Activation functions—An activation function calculates the weighted sum of inputs and biases of a neural network, which determines whether a neuron can be activated or not. In recent research, three main activation functions mainly sigmoid, ReLU, and parameterized ReLU are commonly used in CNN implementations. The parameterized ReLU (also known as leaky ReLU abbreviated as LReLU) is presented in Fig. 2. The ReLU segregates the negative values to 0 and keeps positive values untouched. The LReLU has a role alike to the ReLU but it maps bigger negative values to slighter ones by falling the angle of the map function.

SoftMax—SoftMax is a mathematical function used for classification. It performs the operation by converting a vector of numbers into a vector of probabilities.

Fully connected layer—As in a conventional fully convolution neural network, the neurons in the fully interconnected layer are completely linked to all neurons in the preceding and following layers. The fully connected layer assists in the representation mapping between input and output.

Once the feature data is converted into a one-dimensional array, it is sent to the fully connected or dense layer. All of these individual values present separate features of the image. The dense layer performs two operations on the input data, namely (i) **linear and (ii) nonlinear transformations**.

The CNN implementation of the mathematical model takes the image, and identifies various features, dimensions and edges from the image. As per the information gathered, the objects are predicted/clustered or classified. This is quite performed by the hidden layers in a convolutional neural network. The main task of hidden layers is to extract the features of the input image. The tasks of a convolutional neural network are divided into two parts (Fig. 3):

- **First, the convolution layers** that extract the hidden patterns from the input image.

Fig. 3 Observing error in prediction

- **Second, the fully connected (also known as dense) layers** that use data from the convolution layer to generate output.

Mainly, there exist two tasks associated with the training of any neural network. First is forward propagation which receives input data, processes the feature data, and generates the output. The second is backward propagation which computes the errors and updates the parameters of the CNN.

Mathematically, a linear transformation of the data is performed using the equation:

$$Z = W^T \times X + b$$

Here, X represents the input image, W represents the weights, and b is bias which is a constant value. The dense or fully connected layer has two concerns to consider—weights and a bias matrix. The change in error concerning weights is calculated as $\frac{dE}{dW}$. As the error is not directly dependent on the weight matrix, the concept of the chain rule to determine this value. Figure 4 represents the steps of defining $\frac{dE}{dW}$.

The value of $\frac{dE}{dW}$ is calculated as follows:

$$\frac{dE}{dW} = \frac{dE}{dO} \times \frac{dO}{dZ2} \times \frac{dZ}{dW}$$

The values of the derivatives can be found separately.

Changes in Error Concerning to Output

Let the actual values for the data be D and the predicted output be O. Then the error is presented as follows:
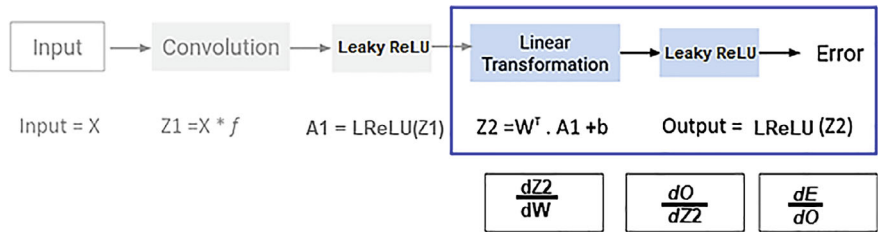

Fig. 4 Backward propagation

$$E = \frac{(D - O)^2}{2}$$

If the error is differentiated concerning the output, then we get

$$\frac{dE}{dO} = -(D - O)$$

Change in Output Concerning Linear Transformation Output

To determine the derivative of output O concerning linear transformation represented as $Z2$, we need to define O in terms of Z_2. $dO/dZ2$ is efficiently the derivative of leaky ReLU. Recall the equation for the leaky ReLU function:

$$f(x) = \max(0.1x, x)$$

Updating Linear Transformation Output Concerning Weights

The linear transformation output Z2 is the result of the linear transformation process. The equation of Z2 in terms of weights:

$$Z2 = W^T.A1 + b$$

where W is the weight, b is the bias, and A1 is calculated as follows:

$$A1 = \frac{dZ2}{dW}$$

The chain rule can be used to find the update in error concerning weights. The values in the weight matrix can be updated using the equation:

$$W_{\text{new}} = W_{\text{old}} - c \times \frac{dE}{dW}$$

The bias matrix can be updated by following the same procedure.

4   Implementation Scenario

To train the images the three-layer convolutional neural networks algorithm is used which has shown better performance on sub-classifying lung cancer than other algorithms. Before the model training, the various hyperparameter values (learning rate: 0.01, batch size: 32, activation function: leaky ReLU and SoftMax, epoch size: 15) are set, and during parameter building batch normalization is used for preventing overfitting and underfitting for every layer. Leaky ReLU and SoftMax function are used

for model training with TensorFlow, Keras framework for implementation. Leaky ReLU helps in avoiding the dying ReLU problem and ensures almost all neurons remain active permanently during training. For implementation, first, a convolution layer is applied with 64 filters. The next step is as follows: a stack of three CNN blocks, the first one of which has 32 filters, the second one and third one of which have 32 and 128 filters and dimension reduction applied on them.

5 Results

In the pre-implementation the experiments utilized LC25000 database downloaded from Kaggle and it consist of 25,000 images and the author used 5000 color images of lung squamous cell carcinoma and 5000 colored pictures of lung adenocarcinoma and the split ratio between training samples and validation samples is 80 and 20. For binary classification, the dataset consists of 8,000 images from training and 2,000 images from validation. In data preprocessing, the authors cropped the images in 299 × 299 pixels for three layers of CNN implementation. The proposed approach uses three layers of CNN which is a more efficient neural network architecture to classify the lung cancer images of LC25000 dataset. The proposed model observed 96.89% accuracy, 96.89% recall, 96.89% precision, 99.44% AUC, and 93.20% validation accuracy over 15 epochs. Post-implementation profuse and ideal results are obtained as shown in Figs. 5 and 6. The accuracy graphs present the implementation demo and a great view of action providing an advantage to automate the process of detecting lung cancer. Figures 7 and 8 present the confusion matrix of the proposed model.

Figure 9 shows the prediction of the lung cancer type present in the sample image. Here, squamous cell carcinoma is predicted.
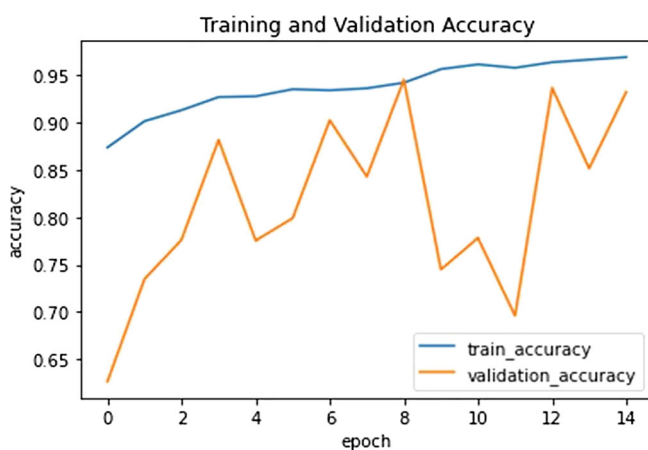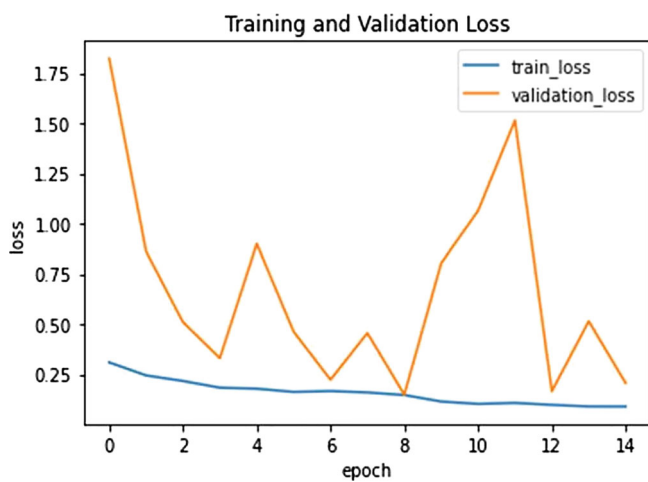

Fig. 5 Training and validation accuracies
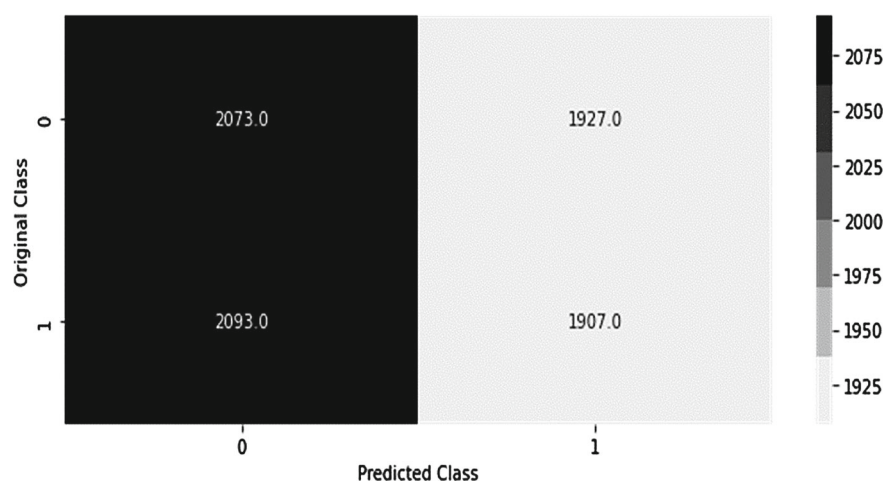
Fig. 6 Training and validation losses

Fig. 7 Training confusion matrix
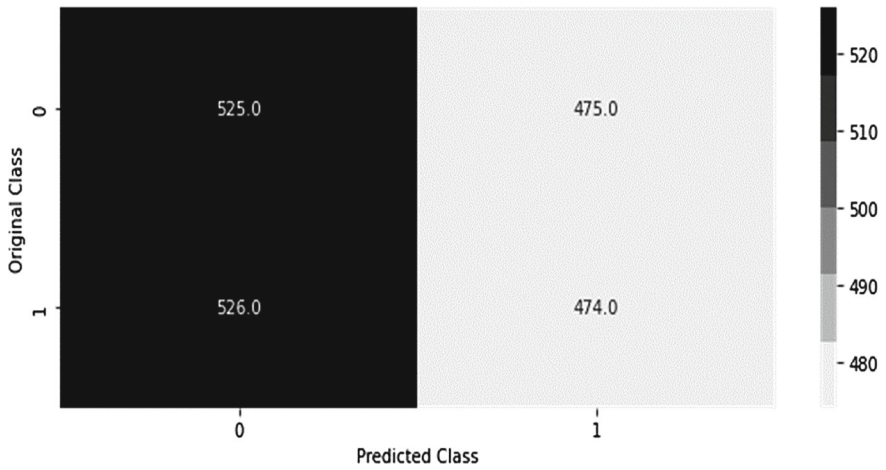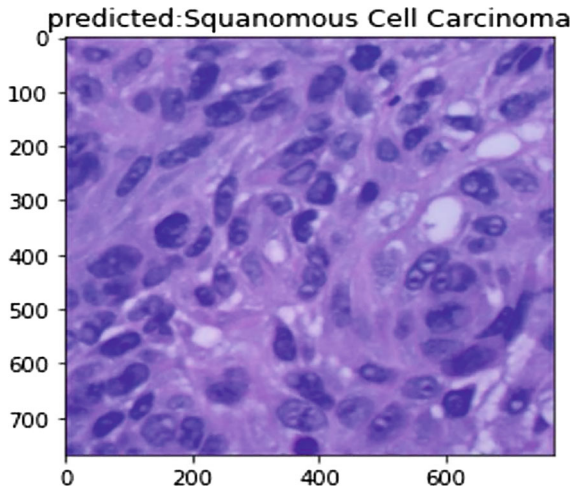
Fig. 8 Validation confusion matrix

Fig. 9 Squamous cell carcinoma is predicted

6 Conclusion

It is observed that the proposed system performed well with an image dataset containing 5000 colored pictures of lung squamous cell carcinoma and 5000 colored pictures of lung adenocarcinoma from the LC25000 dataset and obtained 96.89% training accuracy and 93.20% validation accuracy. This research work presents sub-classifying lung cancer using CNN. In this work, the training of the model on previously unseen non-small cell lung cancer images also allowed for classifying them into squamous cell carcinoma and adenocarcinoma.

References

1. Siegel, R.L., Miller, K.D., Wagle, N.S., Jemal, A.: Cancer statistics, 2023. CA Cancer J. Clin. **73**(1), 17–48 (2023). https://doi.org/10.3322/caac.21763
2. Amicizia, D., Piazza, M.F., Marchini, F., Astengo, M., Grammatico, F., Battaglini, A., Schenone, I., Sticchi, C., Lavieri, R., Di Silverio, B., et al.: Systematic review of lung cancer screening: advancements and strategies for implementation. Healthcare. **11**(14), 2085 (2023). https://doi.org/10.3390/healthcare11142085
3. Yawei Li, Xin Wu, Ping Yang, Guoqian Jiang, Yuan Luo, Machine Learning for Lung Cancer Diagnosis, Treatment, and Prognosis, Genomics, Proteomics & Bioinformatics, Volume 20, Issue 5, 2022, pp. 850-866, https://doi.org/10.1016/j.gpb.2022.11.003
4. Alakwaa, W., Nassef, M., Badr, A.: Lung cancer detection and classification with 3D convolutional neural network (3D-CNN). Lung Cancer **8**(8), 409 (2017)
5. Masood, A., Sheng, B., Yang, P., Li, P., Li, H., Kim, J., Feng, D.D.: Automated decision support system for lung cancer detection and classification via enhanced RFCN with multilayer fusion RPN. IEEE Trans. Industr. Inf. **16**(12), 7791–801 (2020)
6. Perumal, S., Velmurugan, T.: Lung cancer detection and classification on CT scan images using enhanced artificial bee colony optimization. Int. J. Eng. Technol. **7**(2.26), 74–9 (2018)
7. Zhang, C., Sun, X., Dang, K., Li, K., Guo, X.W., Chang, J., Yu, Z.Q., Huang, F.Y., Wu, Y.S., Liang, Z., Liu, Z.Y.: Toward an expert level of lung cancer detection and classification using a deep convolutional neural network. Oncologist **24**(9), 1159 (2019)
8. Hatuwal, B.K., Thapa, H.C.: Lung Cancer detection using convolutional neural network on histopathological images. Int. J. Comput. Trends Technol. **68**, 21–4 (2020)
9. Teramoto, A., Tsukamoto, T., Kiriyama, Y., Fujita, H.: Automated classification of lung cancer types from cytological images using deep convolutional neural networks. BioMed Res. Int. 1–6 (2017)
10. Asuntha, A., Srinivasan, A.: Deep learning for lung Cancer detection and classification. Multimed. Tools Appl. **79**(11), 7731–62 (2020)
11. Makaju, S., Prasad, P.W., Alsadoon, A., Singh, A.K., Elchouemi, A.: Lung cancer detection using CT scan images. Procedia Comput. Sci. **1**(125), 107–14 (2018)
12. Tekade, R., Rajeswari, K.: Lung cancer detection and classification using deep learning. In: 2018 fourth international conference on computing communication control and automation (ICCUBEA) 16 Aug 2018, pp. 1–5. IEEE
13. Khan, A.: Identification of Lung Cancer Using Convolutional Neural Networks Based Classification. Turkish J. Comput. Math. Educ. (TURCOMAT). **12**(10), 192–203 (2021)
14. Nasrullah, N., Sang, J., Alam, M.S., Mateen, M., Cai, B., Hu, H.: Automated lung nodule detection and classification using deep learning combined with multiple strategies. Sensors **19**(17), 3722 (2019)
15. https://www.kaggle.com/datasets/mysarahmadbhat/lung-cancer
16. Kumar, R., Singh, R.C., Kant, S.: Dorsal Hand Vein-Biometric Recognition using Convolution Neural Network. Springer International Conference ICICC, New Delhi, 21–23 Feb. 2020
17. Kumar, R., Bharti, V.: A critical review of finger vein recognition techniques for human identification. In: 2021 Third International Conference on Inventive Research in Computing Applications (ICIRCA), Coimbatore, India, pp. 1–9 (2021).https://doi.org/10.1109/ICIRCA51532.2021.9544906
18. Kumar, R., Singh, R.C., Kant, S., Learning, D.H.V.R.U.V.D.: Macromol. Symp. **397**(2000244), 1–13 (2021)